Graphene Tunnel Junctions for Nanoelectronics and Biosensing: Intrinsic Electronic Noise and Response to Environmental Factors

Paweł Puczkarski

A thesis presented for the degree of
Doctor of Philosophy



Oriel College
Department of Materials
University of Oxford
17 March 2018

Abstract

Graphene Tunnel Junctions for Nanoelectronics: Intrinsic Electronic Noise and Response to Environmental Factors

Paweł Puczkarski
Oriel College, University of Oxford
Hilary Term 2018

Abstract of a thesis submitted for the degree of Doctor of Philosophy

This thesis is concerned with the investigation of Graphene Tunnel Junctions (GTJs) and their applications. GTJs are fabricated by feedback-controlled electroburning, which results in the controllable formation of nanometric tunnelling gaps. Tunnelling currents have been widely used to study electron transport through single molecules, however the scope of their practical applications remains limited.

The main aim of this thesis is to assess the feasibility of the use of GTJs for biosensing. The first research chapter summarises the results demonstrating that GTJs are highly sensitive to their local electrostatic environment. Under cryogenic conditions with reduced perturbations from the environment, the devices are used to study the dynamics of nearby charge traps. Measurements show features of Two Level Fluctuation and Lorentzian Noise. This verifies that in optimum situation the junctions are capable of detecting single electron dynamics.

The second research chapter describes the emergence of $1/f$ noise resulting from the superposition of fluctuators upon the increase of temperature. This chapter also presents the impact of noise on the measurement sensitivity and resulting limits of detectable sensing signals on the order of 1-10 nA. In the next chapter the impact of a liquid environment is studied. Water polarisation effects at graphene-water interface lead to decreased current levels due to electrostatic screening, and to increased noise due to molecular fluctuations.

Next, the viability of biosensing using GTJs is demonstrated by the detection of single nucleotides at nM concentrations in water solutions. The detection of deoxy-guanine and thymine triphosphates moving around junctions due to Brownian motion is demonstrated, with specific tunnelling current spikes in the range of 1-100 nA.

Finally, I present an outlook on the development of GTJ sensing devices, including the fabrication protocol and device geometry of suspended GTJs capable of sequencing linear DNA strands. Furthermore local side-gate devices with enhanced sensing performance are proposed.

List of Publications

Articles listed below contain results described within this thesis:

1. Three-terminal graphene single-electron transistor fabricated using feedback-controlled electroburning, Applied Physics Letters **107**, 2015, Puczkarski P., Gehring P., Lau C.S., Liu J., Ardavan A., Warner J.H., Briggs G.A.D., Mol J.A.

2. Graphene Nanoelectrodes for Biomolecular Sensing, Journal of Materials Research **32**, 2017, Puczkarski P., Swett J.L., Mol J.A.

Article submitted for review:

3. Low-Frequency Noise in Graphene Tunnel Junctions, ACS Nano, Puczkarski P., Wu Q., Sadeghi H., Hou S., Karimi A., Sheng Y., Warner J.H., Lambert C.J., Briggs G.A.D., Mol J.A.

Acknowledgements

This DPhil project would not be possible without many people who helped, inspired or encouraged me along the way.

First of all I would like to thank my supervisors, Prof Andrew Briggs and Dr Jan Mol, for giving me opportunity to work in their laboratory. I am grateful to Jan for all the advice, guidance and patience that I experienced. I am also in debt to all other members of our research group.

In particular in the beginning of my DPhil I was lucky to learn fabrication and measurement methods from Dr Pascal Gehring. I was also very privileged to work with Dr Amin Karimi, who expanded my understanding of electric noise and introduced me to the obscure art of noise hunting. Work in the cleanroom would have been much more challenging, if it had not been for Paul Pattinson, who always did his best to maintain it at the highest standard, and helped to stay in a good mood even during the longest fabrication sessions.

The project has also greatly benefited thanks to our partners from Lancaster, Prof Colin Lambert and Qingqing Wu, who not only provided DFT and MD simulations, but also helped me to further develop my ideas over our long discussions. I would not be able to realise any of liquid environment measurements and nucleotide sensing without the advice of Dr Ken Healy, Dr Ping Xie, Marion Crawford and Dr Jason Hyde from Oxford Nanopore Technologies, who kindly helped me when I was working on the fluidic setup, nucleotide measurements and fabrication of suspended devices, and who were patient even if I was asking a total novice questions.

I would like to also thank Aaron Lau, who preceded me as a DPhil student and who started some of the experiments that I continued. I also thank Jacob Swett and Jasper Fried, two colleagues who joined the group to continue work that I started, and who never failed to help me find ways to further optimize my experiments and develop new research ideas. I would like to also acknowledge the assistance of Dr Carlos Rios and Dr James Thomas, who helped me with AFM imaging, and Radka Chakalova who helped with RIE.

The project was possible because of funding from EPSRC, World Templeton Charity and Oriel College.

I would like to thank all the friends from old times, who are always around and keep on supporting me, and to the new friends from Oxford who made the last few years a great adventure. In particular, I would like to thank my college, and all the people who make Oriel such a friendly and supportive community.

Finally, I would like to thank my parents who never failed to believe in me.

Abbreviations

ALD − Atomic Layer Deposition

AFM − Atomic Force Microscope

BJT − Bipolar Junction Transistor

BLG − Bilayer Graphene

cAFM − conductive Atomic Force Microscope

CMOS − Complementary Metal-Oxide-Semiconductor

CNT − Carbon Nanotube

CPD − Change Point Detection

CVD − Chemical Vapour Deposition

DOS − Density of States

DFT − Density Functional Theory

dGTP − deoxyguanine triphosphate

dTTP − deoxythymine triphosphate

dsDNA − double strand DNA

EBID − Electron Beam Induced Deposition

EBL − Electron Beam Lithography

EDL − Electric Double Layer

FEP − Fluorinated Ethylene Propylene

FET − Field Effect Transistor

FLG − Few Layer Graphene

FWHM − Full Width at Half Maximum

FIB − Focused Ion Beam

GNR − Graphene Nanoribbons

GTJs − Graphene Tunnel Junctions

HIM − Helium Ion Microscope

IPA − Isopropyl alcohol

JFET − Junction Field Effect Transistor

LFN − Low Frequency Noise

LPCVD − Low-Pressure Chemical Vapour Deposition

MCBJ − Mechanically Controlled Break Junctions

MIBK − Methyl Isobutyl Ketone

MD − Molecular Dynamics

MOSFET − Metal-Oxide-Semiconductor Field Effect Transistor

MWCNT − Multi-Walled Carbon Nanotube

PCB − Printed Circuit Board

PCR − Polymerase Chain Reaction

PDF − Probability Distribution Function

PMMA − Poly(Methyl Methacrylate)

PSD − Power Spectral Density

QD − Quantum Dot

QPC − Quantum Point Contact

RTN − Random Telegraph Noise

RTS − Random Telegraph Signal

SAM − Self-Assembled Monolayer

SEM − Scanning Electron Microscopy

SET − Scanning Electron Tunnelling

SLG − Single Layer Graphene

SNM − Scanning Noise Microscopy

SNR − Signal to Noise Ratio

SPM − Scanning Probe Microscopy

ssDNA − single strand DNA

STM − Scanning Tunnelling Microscopy

STS − Scanning Tunnelling Spectroscopy

SWCNT − Single-Walled Carbon Nanotube

TEM − Transmission Electron Microscopy

TLF − Two Level Fluctuation

UHV − Ultra High Vacuum

Contents

Abstract ii

List of Publications iii

Acknowledgments vi

Abbreviations vii

Contents xv

1 Introduction 1
- 1.1 Single Molecule Measurement Methods . . . 3
- 1.2 Graphene Electronics . . . 8

2 Methods 14
- 2.1 Materials and Equipment . . . 14
- 2.2 Device Fabrication Protocol . . . 19
- 2.3 Fabrication of Graphene Constrictions . . . 22
- 2.4 Electroburning of Graphene Junctions . . . 23

3 Random Telegraph Noise and Other Noise Forms in Nanoscale Devices 27
- 3.1 Two Level Switching in Graphene Tunnel Junctions . . . 28
- 3.2 Classification of Noise Types . . . 29
  - 3.2.1 $1/f$ Noise . . . 31
  - 3.2.2 White Noise . . . 31
- 3.3 Random Telegraph Signal . . . 34
- 3.4 Mathematical Model of RTN . . . 36
- 3.5 RTS in Semiconductor Devices . . . 38

3.5.1 Physical Origin of RTS . . . 40
3.5.2 Fluctuations in Number of Charge Carriers ΔN . . . 41
3.5.3 Fluctuations in Mobility of Charge Carriers $\Delta\mu$ . . . 45
3.6 Electric Noise in Graphene Devices . . . 49
3.6.1 Noise in Graphene . . . 50
3.6.2 Edge Induced Noise in Graphene . . . 56
3.7 RTS in Molecular Devices . . . 59

4 Random Telegraph Signal in Graphene Devices 67
4.1 Analysis of Random Telegraph Noise Signals . . . 67
4.1.1 Analysis of Noise Spectra . . . 69
4.1.2 Analysis of $I-t$ traces . . . 73
4.1.3 Comparison of Noise-Spectrum and Current-Trace Analysis Methods . . . 82
4.2 Correlations in TLF Signals . . . 89
4.2.1 ΔI Point Clusters . . . 89
4.2.2 $(\Delta I_1, \Delta I_2)$ Point Cluster Asymmetry . . . 91
4.3 Origin of TLF in Graphene Tunnel Junctions . . . 99
4.3.1 Temperature Dependence of RTN . . . 99
4.3.2 Discussion of Possible Fluctuation Mechanisms . . . 106
4.3.3 Multiple Fluctuators . . . 114
4.4 Summary . . . 119

5 Noise in Graphene Tunnel Junctions 122
5.1 Emergence of $1/f$ Noise Spectrum . . . 122
5.1.1 Lognormal Current Distribution . . . 124
5.2 Flicker Noise and Hooge Parameter . . . 130
5.3 Noise in Nanopore Measurements . . . 135
5.3.1 High Frequency Noise . . . 137
5.3.2 Low Frequency Noise . . . 138
5.3.3 Reducing Noise in Nanopores . . . 139
5.4 Noise and Sensitivity Limits in Graphene Tunnel Junctions . . . 141
5.4.1 Noise in the Measurement Setup . . . 141
5.4.2 Noise Features in Graphene Tunnel Junctions . . . 145
5.4.3 Detectable Signal Limits . . . 148
5.4.4 Temporal Resolution of Sensing Signal . . . 150
5.4.5 Detectable Signal Limits in Graphene Tunnel Junctions . . . 152
5.5 Summary . . . 157

6 Biosensing with Graphene Tunnel Junctions **158**
6.1 DNA Sequencing . . . 158
6.1.1 DNA Structure and Properties . . . 158
6.1.2 DNA Sequencing in Nanopores . . . 162
6.2 Graphene Tunnel Junction Measurements in Liquid Environments . . 167
6.2.1 Electrochemical Effects at Nanoscale Electrodes . . . 168
6.2.2 Insulation of Graphene Tunnel Junctions . . . 171
6.2.3 Electrochemistry of Graphene . . . 177
6.3 Tunnelling in Water . . . 178
6.3.1 Nanoscale Structure of Water . . . 178
6.3.2 Electric Double Layer . . . 181
6.3.3 Influence of Liquid Environment on Tunnelling Current . . . 183
6.3.4 Influence of Liquid Environment on Molecule Measurements . 184
6.4 Tunnelling in Graphene-Water-Graphene Junctions . . . 186
6.5 DNA Sensing by Tunnelling Current . . . 193
6.6 Nucleobase Sensing with Graphene Tunnel Junctions . . . 202
6.6.1 Idea of Graphene Tunnel Junction DNA sequencing . . . 202
6.6.2 Nucleotide Sensing with GTJs . . . 204
6.7 Summary . . . 217

7 Sensing Prospects **219**
7.1 Suspended Graphene Tunnel Junctions . . . 219
7.1.1 RIE of Nanopores . . . 223
7.1.2 Fabrication of Suspended Graphene Tunnel Junctions . . . 226
7.2 Three Terminal Graphene Devices . . . 228
7.2.1 Fabrication of Three Terminal Devices . . . 231
7.2.2 Electroburning of Three Terminal Devices . . . 232
7.2.3 Gating at 77 K and Room Temperature . . . 234

8 Summary **237**

Appendices **243**

A Tunnelling Distance and Simmons Model **243**

B Calculations of Noise Spectra **249**

C Scalling of ΔI Amplitude and Emergent $1/f$ noise **252**

D Limits of Change Point Detection – Simulations **254**

E Limits of Change Point Detection – Experimental traces **261**

F Measuremnt Circuit and Electronics **265**

List of Figures **268**

Bibliography **275**

Chapter 1

Introduction

Graphene Tunnel Junctions (GTJs) merge two vital fields of contemporary nanotechnology research, single molecule electronics and graphene electronics. The first of these fields is concerned with electron transport through single chemical moieties. It was initiated by the concept of a molecular rectifier introduced by Aviram and Ratner in 1974.[1, 2] Since this proposal the discipline has been developing continuously with several milestones including the observation of Coulomb Blockade, Kondo effect[3–5], Franck-Condon blockade and Fano resonance[6–8] in molecular systems.

Molecular electronics, defined as a discipline investigating properties of single molecules related to transport of electrons, and other related phenomena, such as thermoelectric effects, is now a mature field of research at the interface of solid state physics, chemistry and nanotechnology. Molecular electronics is perceived as an antidote for the dreaded limit of scaling of silicon-based electronics and unavoidable violation of Moore's law.[9] Single molecule devices, if they were produced in a repro-

ducible way, would allow for the ultimate downscaling of integrated circuits. Indeed, a single hydrogen molecule conductance has been measured[10] and a single atom switch has been implemented as a memory element in a laboratory environment.[11]

Molecular electronics, although it has not yet found any commercial applications, is already a mature field of academic research. Recently, there is rising awareness that in order to further progress, the simple study of electron flow has to extend to the study of thermal, optical, mechanical and spintronic effects in single molecules.[12]

Another direction for expansion is the shift of focus from harnessing the properties of molecules in nanodevices to the application of nanoscale devices to manipulate and analyse properties of single molecules. One such application is sensing of molecules such as DNA, proteins and carbohydrates. The sequencing of single DNA strands is highly desired as it could be a disruptive technology giving rise to the personal genome-based medicine.[13, 14]

Single molecule methods seem well-poised to address the sequencing problem, because of the efficiency in probing electronic structures of molecules. However the challenge cannot be underestimated. This goal will be realised only upon: transition from measurements of a single molecule to millions of molecules in a DNA strand; changing the measurement environment from mild ultrahigh vacuum (UHV) conditions at cryogenic temperature, to the liquid environment at room temperature, significantly disrupting the measurement process; and by changing the available measurement timescale from hours in the case of a molecule fixed in a gap, to microseconds for molecules translocating between the nanogap.

1.1 Single Molecule Measurement Methods

Ensuring electric contact between mesoscopic electrodes and a single molecule is a challenging task. In order to form a junction with just a single molecule bridging electrodes, the electrodes must be of similar size to measured molecules. Over the last few decades there emerged multiple platforms which are harnessed for the purpose of single molecule measurements, all of them are characterised with different capabilities and limitations. The common feature of all the single molecule measurement platforms is the presence of, at least, two electrodes with sharp contact points (preferably atomically sharp), which are separated by a nanometric gap. The size of the gap can be either fixed or adjustable. The distance between electrodes, if it is on the order of 1 nm, can be characterised by means of dependence of tunnelling current on applied voltage. This method of estimation of tunnelling distance is very accurate as the magnitude of tunnelling current depends exponentially on the interelectrode distance.[15–18] If the size of a small gap between electrodes is commensurate with the size of measured molecule, it allows the molecule to bridge the gap, which has a profound effect on the conduction through the junction, as it usually introduces increase in conduction and often various quantum, non-linear and gate-dependent effects, which may be used to confirm unambiguously the occupation of the gap by a single molecule.[19–21]

STM One of the natural choices for the measurement of single molecules is Scanning Tunnelling Microscope (STM), which operates on the basis of tunnelling current flowing between a conductive substrate and atomically sharp metallic tip.[22–26] This

is a method which allows for the direct and precise positioning of the tip above the substrate with piezoelectric control and feedback based on tunnelling current. The possibility of forming single-atom sharp tip enables the formation of localised probe suitable for contacting single molecules. In order to facilitate the formation of contact, molecules might be equipped with additional side groups, showing affinity to gold surface, *e.g.* −SH or aromatic side groups.[27]

As the STM approach provides a facile way of changing the tip-substrate distance, the molecular junction can be formed multiple times, on both approach and retraction of the tip from surface, allowing to gather statistically significant data.[28–30] Importantly the STM tip can be moved in all three dimensions, which allows to scan the surface of the substrate electrode and to form molecular junctions in multiple positions.[31–34]

Despite their high operational flexibility, STM molecular junctions, have a couple of disadvantages, directly related to the geometry of the junction. One such disadvantage is the high asymmetry between electrodes, which may introduce interesting effects of pinning the Fermi level of an investigated molecule to the substrate[35–37], but on the other hand this effect, if it is not desired, cannot be precluded and it unavoidably affects the molecular transport signatures. The presence of the flat substrate can affect also the conformation of a molecule in the junction. It can be envisaged that molecules with high affinity to the surface will more likely be adsorbed flat on substrate's surface than form a linear junction between the tip and substrate[38], however this effect might be mitigated by embedding analyte molecules in Self-Assembled Monolayers (SAMs), which force the analyte molecule into upright

conformation.[39–42] A difference in conformation can significantly affect electron transport through a molecule. Furthermore, because of the flexible geometry implementation of a gate electrode, tuning electron transport through a molecule is not possible in typical cryogenic setup, and only performing measurements at liquid environment with a global liquid gate electrode allows for alleviating this issue.[43–45] Although STM junctions are a powerful and flexible method of investigation of single molecule properties, their application is limited to the fundamental scientific research, without any capacity for upscaling junction fabrication and connecting the junctions into larger circuits.

cAFM A similar method of formation of single molecule junctions to STM technique is conductive-Atomic Force Microscopy (cAFM). The geometry of the formed junction is similar to STM junctions. A molecule is anchored between the conductive substrate and conductive tip, which is a modified metal-coated tip of a regular Atomic Force Microscope (AFM).[46–50] The significant difference between STM and AFM is the feedback mechanism. STM uses tunnelling current between tip and substrate, which plays a role of both the feedback mechanism and main measurement method. In the case of cAFM current between the tip and substrate is observed and constitutes main measurement method, however feedback mechanism harnesses mechanical force between the tip and substrate due to repulsive or attractive interactions. This method allows for independent investigation of molecule mechanical and electronic properties in the same measurement setup.

MCBJs A different set of methods of single molecule transport measurements relies on the formation of nanoscale junctions by mechanical deformation. Such devices are called Mechanically Controllable Break Junctions (MCBJs).[51–58] These junctions are formed in thin metallic nanowires, with a constriction on the order of 10-100 nm, located on a flexible substrate; *e.g.* phosphor bronze substrate passivated with a thin insulation layer, such as SiO_2 or polyimide.[59–62] The substrate can be bent with a micromanipulator in a three point geometry: one point located centrally at the location of the envisaged junction, below the substrate; and two points close to the edges of the substrate on its top side. Bending the substrate induces strain in the nanowire fixed on the substrate, with the constriction regions being the most susceptible to plastic deformation. The big advantage of the method is its high attenuation factor, on the order of 10^{-6}, between the vertical displacement of a pushing rod and horizontal displacement of electrodes forming the tunnel junction.[53, 56, 61, 63–65] This means that the size of the junction can be controlled with sub-picometer precision. In comparison to STM junctions, MCBJs are a symmetric system, where electrodes are suspended and molecule is detached from the substrate, which results in the suppression of any surface charge transfer effects; molecules can be characterised in their native state.[53] MCBJs are cable of performing opening and closing cycles tens of thousands of times, which allows the formation of molecular junctions multiple times.[29] As the electrodes are made of ductile metals, the atomic geometry of electrode tips can change each time the junction is formed, statistically averaged measurements allow to discriminate between effects related to the intrinsic properties of molecules and properties related to the particular geometry of the electrodes or

particular molecule connection.

MCBJs, despite being a highly successful experimental platform, their application remains limited to fundamental investigations of the molecular transport without any prospects of upscaling and implementation in more complex circuit. Another issue is obtaining gating action in MCBJ geometry. Fabricating a side gate electrode aligned with a MCBJ is possible, however, gate coupling is relatively low and allows only for small shift of the molecular energy levels.[53, 66]

Electromigration Another method of forming symmetric metal junctions relies on the electromigration of metal atoms in electric fields.[5, 11, 67, 68] In this approach thin nanowires with a narrow constriction are patterned, for example by Electron Beam Litography (EBL) process on the insulating substrate. The application of electric field to such nanowire results in narrowing of the constriction due to the momentum transfer from electrons to atomic cores; the electromigration process is effective in ductile metals such as gold or palladium.[68, 69] Typically electromigration process is aborted before the formation of a tunnel gap, when there remains a narrow metallic bridge, connecting two electrodes, with channel diameter corresponfing to just a few atomic radii. Subsequently, a gap is formed due to self-breaking mechanism: mobile atoms creating atomic bridge, due to the intrinsic rearrangement at room temperature and high strain in the constriction, eventually break the continuity of the conductor.[70, 71] This process is applied instead of continuing the bias induced electromigration till the very end, because self-breaking results in smaller and cleaner gaps. Full breaking of contacts by electromigration often results in the formation of metallic quantum dots[21, 70, 72], which contaminate the tunnel junc-

tion and lead to the transport measurement effects, which might be interpreted as signatures of molecular transport.

Electromigrated junctions, although common in early days of the development of molecular electronics, now are becoming obsolete due to much more advantageous MCBJs. Electromigrated junctions, have some advantages of MCBJs; they are sharp metallic contacts separated by a nanometric gap. However the main issue is that once the junction is formed it cannot be closed, or changed in any way. It is not possible to collect high statistics on electron transport in a single electromigrated device, in contrast to a single MCBJ. On the other hand multiple electromigrated devices can be fabricated on a single chip. A variation of the electromigration method is also sometimes applied to form tunnel junctions using a reverse process. Relatively large junctions are formed by means of EBL process and subsequently shrank by means of electrochemical deposition of metals, the process is self-terminated as the size of the junction approaches the tunnelling regime.[73]

1.2 Graphene Electronics

Single molecule measurements are often performed in metal junctions, however, carbon based-nanomaterials are emerging as an alternative electrode materials in molecular electronics.[62, 74] Such device architectures are based on carbon nanotubes (CNTs) or graphene and GTJs in particular. Graphene itself was a game changer, which, since its discovery in 2004 by Geim and Novoselov[75, 76] opened many new research perspectives in solid state physics and nanotechnology. Graphene is char-

acterised by many peculiar properties, starting with its two dimensional structure. Graphene is a single layer of sp^2-bonded carbon atoms arranged in a honeycomb lattice and it is the first member of a new family of 2D materials.[75] Graphene structure gives rise to a variety of physical properties, which pave the path for its applications. These properties include high mechanical strength and the unusual combination of high electron mobility, electric and thermal conductance, and optical transparency.[75]

Graphene atomic structure translates into unusual electron behaviour. Free electrons in graphene behave like massless quasi particles, which can be described by the equivalent of a relativistic Dirac equation.[75] Relativistic quasi particles in graphene enable the realisation of Klein paradox[77] and they allow for the observation of Quantum Hall Effect[78].[75]

Charge carriers in graphene have a linear $E(k)$ dispersion relation, as opposed to typical parabolic band dispersion of free electrons. Valence and conductance bands merge at a charge neutrality point, where carrier concentration approaches zero, however there is still non-zero quantized conductivity.[75] The absence of a bandgap in graphene allows for the observation of ambipolar transport and a smooth change of the ratio of carriers of both types.[75]

Graphene has been envisaged as a potential material for low-power, ultra-fast and miniaturized electronic devices, which would harness its high mobility[79] and long ballistic transport lengths, on the order of 1 µm even at room temperature.[80] However, the application of graphene transistors for logic electronics requires high $on - off$ ratios, which are not available in pristine graphene due to the lack of a

band gap.[81] The solution relies on opening a sizeable band gap, which can be achieved by doping, application of electric filed perpendicular to bilayer graphene or by introducing the confinement gap in graphene nanoribbons.[81] The last of these methods of band gap generation, with the band gap inversely proportional to the width of the nanoribbon[82], points at interesting size-dependent features of nanostructured graphene devices. These structures demonstrate properties arising due to the combination of nanoscale patterning and intrinsic material features of graphene. Other examples of nanoscale-patterned devices include Single Electron Transistors[83–86] and GTJs[87–89]. GTJs as well as CNT-based junctions are an increasingly important platform for electron transport investigations at the single molecule level.[90–93]

One of the methods of fabrication of gaps suitable for single molecule electronics in graphene and CNT devices is by EBL.[89, 94, 95] EBL has undergone a significant development over the recent decades with advances both in instrumentation and resist composition, which allows it to form features with sub-10 nm characteristic size[96]. EBL technique can be applied to selectively remove resist over CNT structure and use the remaining resist as a mask for etching the carbon material by means of oxygen plasma etching.[97, 98] Application of carbon nanostructures as electrode material is beneficial because of the intrinsic features of those materials and ease of their $\pi-\pi$ or covalent functionalization.[99–102] Furthermore, the EBL patterning of graphene or CNTs is advantageous as it allows for upscaling of the process in a facile manner, as opposed to the direct precise patterning of nanostructures with Helium Ion Microscope (HIM)[103], Focused Ion Beam (FIB) microscope[104] or electron

beam[105–107].[21] Nevertheless, the biggest issue of the EBL patterning is the fact that it is not possible to obtain sufficient control over the patterned geometry; gaps formed by EBL are too large to support measurable tunnelling current, and they can be used in their native state to contact only long molecules. This dimensionality problem can be resolved to some extent by the post processing of the gaps, for instance by shrinking the gap by performing a chemical reaction of amorphous carbon growth from organic precursors on the edge of the gap upon exposure to electron radiation.[21, 105] The other drawbacks of the method concern unknown termination of the graphene and CNTs edges, which can consist of oxygen-containing groups such as OH or COOH[99], due to the exposure to oxygen plasma. What is more, the edge structure is far from perfect zig-zag of armchair usually assumed in simulations; in fact it is more likely to consist of a defective combination of both of these structures.[100, 108] Despite the reports on fabrication of molecular junctions by EBL and plasma etching this method has not yet been applied to pattern molecular junctions in graphene devices.

Different approaches to carbon-based nanogaps include Electron Beam Induced Deposition (EBID) patterning of electrodes by means of electron-assisted formation of carbon electrodes from organic precursors.[109, 110] Another approach is to fabricate electrodes separated by a nanogap for single- molecule measurements by means of controlled electroburning, which for example has been demonstrated in CNTs.[111, 112] A measurement platform which recently attracts increasing interest are GTJs formed also by means of electroburning[87, 88, 90, 92, 113, 114], which is the technique considered in this thesis. One method of their formation includes EBL

prepatterning of a narrow graphene junction with successive electroburning, which is supposed to give a better control over the geometry of the device.[94]. Another modification of such method relies on patterning a series of very thin constrictions, by EBL exposure in dashed-line mode combined with overetching in oxygen plasma and subsequent electroburning.[89, 95] Despite application of GTJs for single molecule measurements their application until now has been limited to the transport measurements of molecules fixed in a junction[113, 115–117]. It is perceived that because of graphene advantageous electrical properties and high mechanical, chemical, and thermal stability GTJs can find many other applications. One distinct example is biosensing with GTJs and DNA sequencing in particular, which has been proposed theoretically[118], but there has not been any practical demonstration of GTJ-DNA interaction.

It is known that the sensitivity limits in DNA sequencing and in fact in all electrical measurements are dictated by electric noise[119–124]. The topic of electric noise in graphene ribbons has been widely investigated[125–132], however, there is no reports on such studies in GTJs. The questions that await the answer include: How noise behaviour is affected upon the downscaling of graphene devices to tunnel junctions? What is noise generation mechanism in GTJs? How electric noise defines the sensitivity limitations in GTJs? Can GTJs be used to detect bioanalytes?

This thesis describes the experimental investigation of transport properties of GTJs. Firstly, I will briefly discuss fabrication and measurement methods, followed by a theoretical and experimental study of the intrinsic electric noise in GTJs. Finally, I will analyse quantum tunnelling in aqueous environments and discuss the

biosensing capabilities and limitations of GTJs.

Chapter 2

Methods

2.1 Materials and Equipment

Substrates Devices for noise measurements and liquid measurements were fabricated on p-doped Si wafers, with 300 nm thick wet thermal oxide, purchased from University Wafers (reference number 2026). Suspended SiN membranes were fabricated by the Oxford Nanopore Technologies Ltd in a typical fabrication process[133]. Briefly, a SiN layer is deposited on both sides of a Si(100) wafer using Low Pressure Chemical Vapor Deposition (LPCVD). The deposition results in the formation of non-stoichiometric low-stress SiN films. Large square windows are subsequently opened on the back side of the wafer by means of combination of photolithography and plasma etching (CHF_3). After removal of the resist the wafer is dipped into KOH solution, capable of anisotropic etching of Si, which results in the etching of features with the decreasing cross-section profile closer to the unmodified surface of SiN. By

adjusting the etching time the area of suspended SiN membrane can be controlled. For the fabrication of devices I use wafers with the suspended membrane side length of 30 µm.

The Reactive Ion Etching (RIE) of nanopores in suspended SiN membranes is performed using substrates covered with soft polymer etching masks. RIE is performed in Oxford Instruments Plasmalab RIE-80 Plus system. The applied etching mixture consists of CHF_3 supplied at flow rate of $45\,cm^3\,min^{-1}$ and O_2 at $5\,cm^3\,min^{-1}$. Etching mixture is ionized by applying AC voltage with the following parameters: 100 V, 150 W and 13.56 MHz.

Resists In the EBL patterning process the following positive resists have been used 495 PMMA A8(Product Item # M130008 O500L1GL) and 950 PMMA A8 (Product Item # M230008 O500L1GL), anisole-based solvent to dilute them A-thinner (Product Item # M030100 1000L1GL), and developer MIBK (Product Item # M080100 40001LPE) all purchased from MicroChem.

The negative resist used for fabrication of graphene constrictions is ma-N 2405 (cyclopentanone, anisole), developer ma-D 525 (tetramethylammonium hydroxide) and resist remover mr-Rem 660 (N-methyl-2-pyrrolidone, 1-methyl-2-pyrrolidone), all purchased from Micro Resist Technology GmbH.

Fabrication of devices on suspended SiN membranes was performed using additional layer of charge-dissipating conductive polymer E-Spacer 300Z purchased from Showa Denko K. K.

Metallization Metals used for the evaporation of electrodes were used in the form of chromium coated tungsten rods (Part # EVSCRW3) for Cr evaporation and gold pallets (Part # EVMAUXX40G), Au 99.99 % purity, 150 g, purchased from Kurt J. Lesker Company. Thermal evaporation of metals was performed with Edwards 306 evaporator and thickness of the deposited layers was monitored with Edwards FTM5 Film-Thickness Monitor.

Imaging Techniques All Scanning Electron Microscope (SEM) images presented in this thesis were recorded with Hitachi S-4300 microscope at 30kV acceleration voltage. Imaging of non-conductive poly(Methyl Methacrylate) PMMA polymer substrates was performed after depositing 5 nm thick Au charge-dissipating layer, which was achieved by thermal evaporation. The AFM images of openings in PMMA insulation on devices for liquid measurements and images of features used for RIE rate test were taken with Asylum MFP-3D AFM in a noncontact mode in ambient conditions.

Graphene Growth, Transfer and Patterning Graphene used for the fabrication of the devices was synthesized by Prof Jamie Warner's group, Department of Materials, University of Oxford.[134, 135] The graphene was grown by means of Chemical Vapour Deposition (CVD) growth on Cu substrate from methane gas precursors. Pieces of Cu foil (99.8 %, 25 µm thick), 14×6 cm large were polished, cleaned from organic residue in HCl and rinsed in isopropyl alcohol (IPA). Such Cu foil pieces were placed in a quartz tube, which was inserted into a horizontal tube furnace. Cu surface works as a substrate for the reaction of graphene formation from

organic precursors, happeneing at elevated tempeartures. Graphene has been synthesised from gas mixture containing 1 % methane in argon, 25 % hydrogen in argon and 100 % argon. Temperature in the furnace was increased to 1060 °C a 50 °C/ min rate. Graphene growth was performed the same temperature with a flow rate of Ar at $600\,\mathrm{cm^3\,min^{-1}}$, H_2 at $100\,\mathrm{cm^3\,min^{-1}}$ and CH_4 at $20\,\mathrm{cm^3\,min^{-1}}$ for 1 h. Subsequently the quartz tube was removed from the furnace to rapidly cool down the substrate.

Oxygen plasma etching of graphene is performed in Diener Electronics Zepto Plasma-Surface-technology system, for 0.3 s with oxygen ionized at 13.56 MHz frequency and 50 W power.

Electric Measurements Initial characterisation of the devices and electroburning is performed on an automatised probe station (Cascade Microtech, Summit 12000M MicroChamber). The probe station allows for automatic unattended consecutive contacting of the arrays of devices with tungsten probes. The fast sweeping of voltage values and recording of the rapid changes in current through graphene constrictions during electroburning was achieved with ADwin-Gold II controller, which was also used to apply bias. In the measurements I used analog to digital input and 100 MHz event counter setting. The current signals were amplified using a Femto DPLCA 200 amplifier with variable gain adjusted with the custom written script.

Fabricated chips with graphene devices for noise and cryogenic measurements were inserted into chip carrier (Kyocera 44 LCC PB-C90577-A). The chip carriers were mounted in Winslow Straight Through Hole Mount 1.27 mm, 2.54 mm Pitch IC Socket Adapter, 44 Pin Female PLCC to 40 Pin Male DIP, which was installed in a custom made cryogenic dipper. For the cryogenic measuremnts the cryogenic

dippers were evacuated to pressure better than 1×10^{-4} mbar using a Pfeiffer HiCube turbopump.

Devices for liquid measurements were mounted on custom designed printed circuit boards (PCBs) manufactured by Newbury Electronics. Electric contact between the EBL-patterned contact pads and chip carriers or PCBs was obtained by wirebonding using Al wire (Inseto, Al/Si(1 %), 0.001) and Manual Wedge Bonder, Kulicke & Soffa, Model 4526.

Electric measurements including application of bias voltage and measurement of nano-ampere currents were performed using Axopatch 200B and Femto DPLCA 200 amplifiers and digitizer Molecular Devices Digidata 1440A digitizer. Further details of electric setup are given in section 5.4.1. No breakout-boxes or bnc cables were used. All the devices were connected directly to the amplifiers using possibly short wires, typically $10 - 20$ cm long, to reduce the electric noise level.

Liquid and Analyte Measurements The flow cells from liquid measurements were formed by filling 3D-printted moulds (printed in MakerBot Replicator 3D printer in Radcliffe Science Library, Oxford University) with Sylgard 184 silicone elastomer purchased from Dow Corning, mixed in 10:1 base to curing agent ratio. The device chips were glued to the surface of custom designed PCBs with two-ingredient kwik-Cast elasotmer ordered from World Precision Instruments. Liquid flow was achieved by connecting 1.55mm inner diameter, 1/8-inch outer diameter and 0.5 mm inner diameter, 1/16-inch outer diameter fluorinated ethylene propylene (FEP) tubing through tube fittings purchased from IDEX Health & Science LLC. Flow of water through the flow cell was controlled by automated micropump

Cavro XLP600. To avoid contamination of the pump with analyte solutions, the analyte solutions were dispensed instead through a disposable manual syringes connected to the tubing. 18 MΩ milipore water for liquid measurements was filtered using Q-Milipore Direct-Q 3 UV Water Purification System. Deoxynucleotide solutions containing 0.25 ml water solutions of deoxy- Guanine, Thymine, Cytosine and Adenosine- triphosphates at 10 mM concentration were purchased from New England Biolabs and diluted to final concentrations with milipore water.

2.2 Device Fabrication Protocol

The basic design of the devices used in the experiments presented in this thesis is shown in Fig. 2.1. The devices are patterned on a doped Si wafer with a 300 nm SiO_2 layer. On the substrate I pattern metal electrodes consisting of a thin Cr adhesion layer and Au contact layer. The last element is a graphene ribbon bridging two electrodes. The ribbon has a constriction in the middle which allows for the formation of a tunnel junction in a predefined location.

In the first fabrication step (Fig. 2.2) Si(100) wafers with 300 nm thermally grown oxide are patterned by Electron Beam Lithography (EBL, JEOL 5500FS) followed by evaporation of 10/70 nm thermally evaporated Cr/Au electrodes. Si wafers with (100) crystallographic orientation and 300 nm thick thermal oxide layer are thoroughly cleaned by means of sonication in acetone followed by sonication in IPA.

Electron Beam Lithography The EBL process relies on the direct interaction of the organic polymer resist layer with an electron beam, which is formed by field

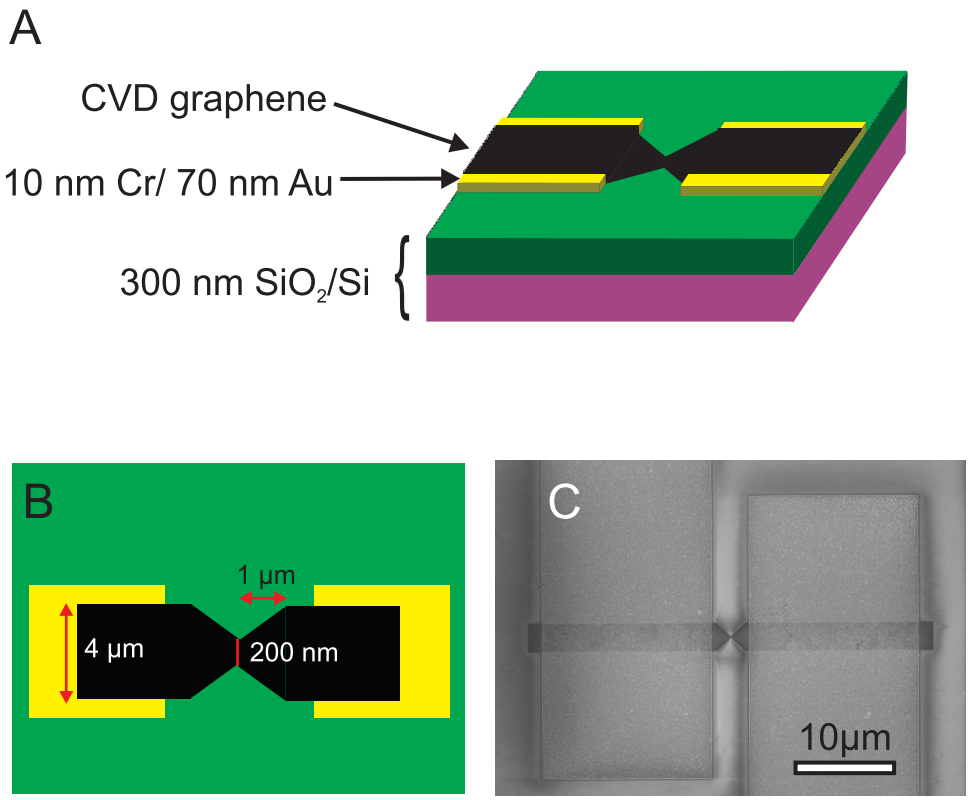


Figure 2.1: Structure of a GTJ: A) Graphene device and substrate. B) Top view of the graphene constriction with marked dimensions. C) SEM image of a graphene ribbon before the electroburning process.

emission and focused to a high degree by means of of series of condenser lens. In the case of positive resist lithography electron irradiation leads to the local damage of polymer chains, which can be easily removed. Rinsing a wafer with areas of a positive layer resist exposed with electron beams allows for the removal of exposed resist with developer, while the unexposed areas stay intact. This positive resist process is used in this thesis to fabricate gold electrodes and nanopores in electrodes in suspended SiN membranes. Patterned areas of chip are exposed to the environment and can be covered with a layer of metal or undergo etching when exposed to an etching mixture, while remaining areas are protected by the resist.

The opposite process is used in the case of negative resist lithography. Negative resist polymers become more cross-linked under exposure to electron radiation, what leads to the increase of their structural integrity. In the case of negative resist lithography rinsing the the wafer with areas exposed to electron beam leads to the removal of resist from unexposed areas, while the areas irradiated by electron radiation remain covered with cross-linked resist. This process is used in this thesis for patterning of graphene constrictions.

Two layers of a positive lithography resist PMMA are spin-coated on the wafer to fabricate gold electrodes: 1) PMMA 495, A6 and 2) PMMA 950 A3. Spin-coating is performed in Laurell-WS-650MZ-23NPP spinner, operated at the sequence of 1) $1000\,\mathrm{min}^{-1}$ RPM for 10 s and 2) $6000\,\mathrm{min}^{-1}$ RPM for 50 s. Each of the spin-coating steps is followed by 3 min annealing of the wafer on a hot plate at 180 °C. Next, the wafer with a resist layer is patterned using EBL (JEOL 5500FS) in order to define electrodes. The patterning parameters are 50 kV acceleration voltage and

$600\,\mu C\,cm^{-2}$ electron dose. After the ebeam pattering I perform the development of the exposed resist by dipping the wafers in a methyl isobutyl ketone (MIBK) and IPA, MIBK:IPA 1:3 solution for 45 s. The development process is stopped by dipping the wafer in IPA.

Finally the wafer with patterned resist layer is transferred to a thermal evaporator where I evaporate 10 nm of Cr adhesion layer and 70 nm Au layer. Lift-off of the resist and excessive gold is achieved by dipping the wafers in acetone at 40 °C for 12 h. Afterwards chips are rinsed with IPA.

2.3 Fabrication of Graphene Constrictions

Graphene used for the device fabrication is grown by Chemical Vapour Deposition (CVD) technique on a melted cooper substrate from methylene gas precursor.[134, 135] CVD graphene growth results in a multi-domain monolayer grapehene with possible regions of 2-3 graphene layers. After graphene growth a 100 nm-thick PMMA 495k layer is spincoated on top of graphene. The transfer of graphene to the chip is realised by etching the cooper substrate by placing the cooper/graphen/PMMA stack on the surface of ammonium persulfate ($(NH_4)_2S_2O_8$) solution in DI water ($0.1\,mg\,mL^{-1}$), which etches cooper. The resulting graphene/PMMA stack is transferred on a glass slide to DI water for the removal of any salt contamination adsorbed on the surface of graphene and subsequently it is transferred to the pre-patterned chip with gold electrodes. The chip is then dipped in IPA to remove air bubbles from beneath the graphene and it is dried for 1 h in ambient conditions and then for 12 h

on a hot plate at 180 °C in order to relax graphene structure, remove cresses and provide better electric contact. As the last transfer step the chip with graphene is put for 3 h into acetone at 40 °C to remove PMMA layer.

Chips prepared in this way are ready for graphene patterning. This time I spin coat a layer of a negative lithography resist ma-N 2405 on the surface of graphene at 3000 min^{-1} RPM rate for 30 s. The graphene ribbons with constrictions are patterned by by means of EBL at 50 kV acceleration voltage and 180 $\mu\mathrm{C\,cm}^{-2}$ electron dose. The development is performed in ma-D 525 for 3 min and then chips are transferred to DI water for 5 min to develop the resist.

In the result graphene surface is exposed with exception of the small areas covered by the negative resist, which correspond to the planed geometry of graphene devices. The remaining graphene is removed by means of oxygen plasma etching which leaves intact only resist-covered graphene devices on the chip. Subsequently the negative resist is removed by putting the chips into mr-Rem 660 at 150 °C for 12 h and finally rinsing them with acetone and IPA. An SEM image of a resulting device is shown in Fig. 2.1C.

2.4 Electroburning of Graphene Junctions

A crucial step in the fabrication process is formation of nanogaps at the graphene constrictions. This is achieved by means of electroburning.[87] Devices are contacted on an automated probe station. First, the resistance of the device is examined by executing a $0-100$ mV voltage sweep. Typically I observe linear IV curves with re-

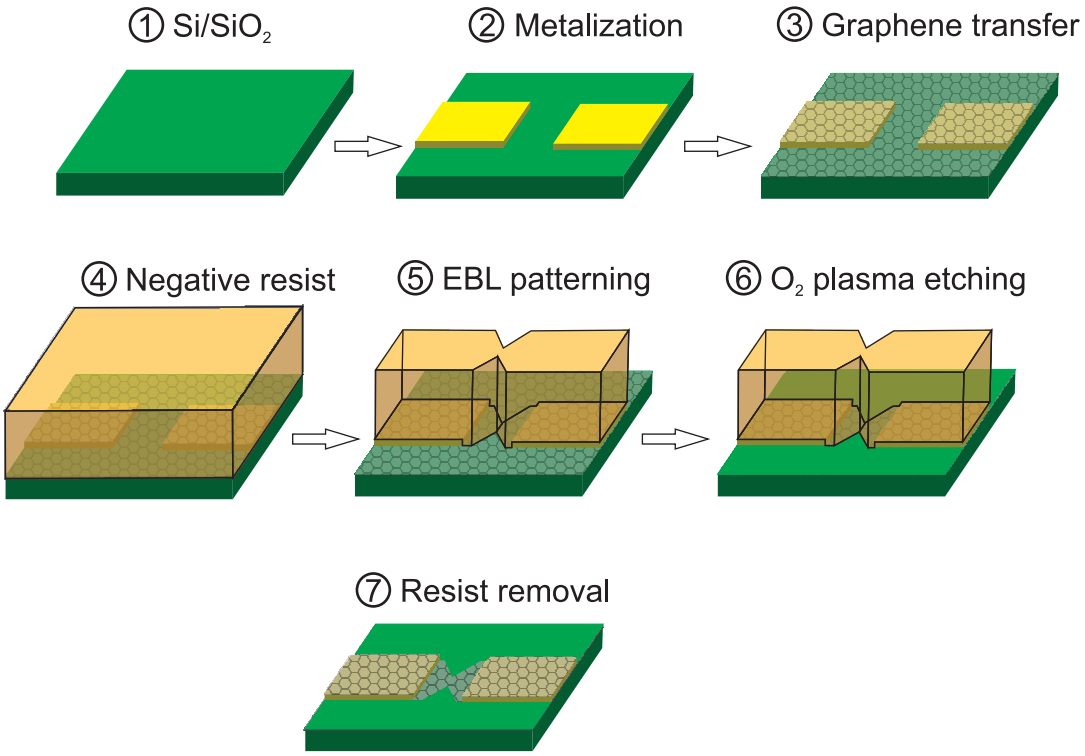


Figure 2.2: Device fabrication process: 1) Si substrate with 300 nm thermally grown SiO_2 layer 2) Patterning of 10 nm Cr adhesion layer and 70 nm Au electrodes 3) Transferred CVD graphene sheet 4) Negative resist layer 5) Exposed pattern in resist after development 6) Oxygen plasma etching leaves only graphene covered with resist F) Final device after resist removal.

sistance of $\sim 3\,\mathrm{k\Omega}$. Devices with such resistance values are selected for the feedback-controlled electroburning. A computer-controlled micro-controller (Adwin II Gold) is used to apply voltages and read current values at 100 MHz sampling rate.

A single cycle of electroburning consists of two steps. Initially, the applied voltage is ramped from 0 mV at a constant rate of $750\,\mathrm{mV\,s^{-1}}$. Current increases steadily with increasing voltage (Fig. 2.3A). At some point the slope of IV curves starts to decrease. A further increase in voltage leads to a decrease in current.[87] Whenever the feedback loop records a drop in current higher than the predefined threshold value it quickly ramps down voltage to 0 mV at a $225\,\mathrm{V\,s^{-1}}$ rate.

The interpretation of the electroburning process is that current flowing through the graphene ribbon leads to the Joule heating, $P = RI^2$. Because of the 200 nm constriction this region has high resistance and therefore is more prone to heating.[87, 88, 90] Increasing the current generates high local temperatures at the junction, reaching 600 K.[88] Such temperatures are sufficient to induce breaking of the bonds and thermal evaporation of carbon atoms.[87, 90] This process leads to a decrease in the width of the constriction, increase in its resistance and resulting decrease in the current. The process is stopped when voltage is brought back to 0 mV. In this way the constriction becomes narrower due to a single electroburning cycle. The process is repeated multiple times, leading to a higher resistance each time.

When the resistance reaches $500\,\mathrm{M\Omega}$ the process is stopped, as then the onset of tunnelling is assumed. That is, the conduction of electrons at such high resistance values is no longer mediated through the graphene ribbon but it is rather due to a quantum mechanical effect of electrons tunnelling through a vacuum potential barrier

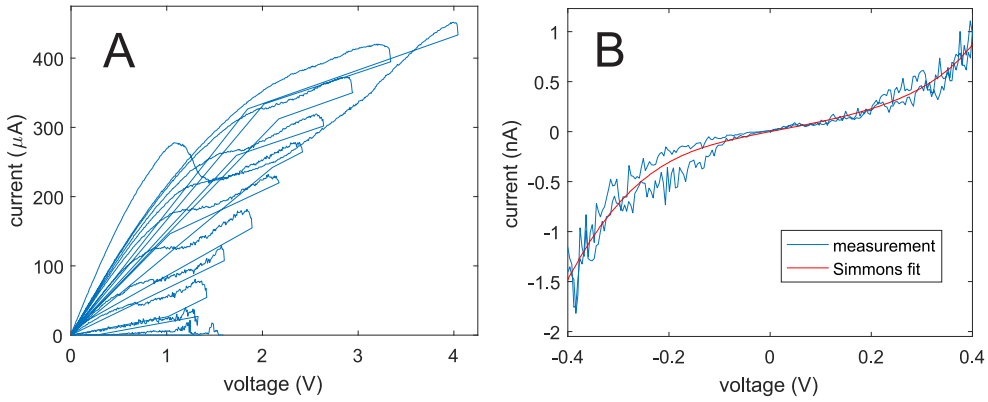


Figure 2.3: Electroburning of GTJs. A) IV curves recorded during the electroburning process. B) Tunnelling IV curve measured at ambient conditions after electroburning resulting in the formation of $d = 1.18\,\mathrm{nm}$ gap.

between two separated graphene leads. Such a tunnelling process is confirmed by the measurement of a non-linear IV curve (Fig. 2.3B). The voltage bias applied for the gap tunnelling IV characterisation and any other measurements presented in this thesis is limited to the range of $\pm 400\,\mathrm{mV}$ as higher voltages are likely to damage the tunnel junction through electric breakdown. The Simmons model is used to fit these curves in order to estimate the tunnelling distance d (Appendix A). Typically fitted values are in the $1 - 4\,\mathrm{nm}$ range.

Chapter 3

Random Telegraph Noise and Other Noise Forms in Nanoscale Devices

For all electronic and biosensing applications of GTJs it is desired that the tunnelling current in a GTJ biased with DC voltage exhibits steady time-independent characteristics. This steady current is a baseline which is altered in the course of interaction of the junction with molecules. All the fluctuations in the baseline current generated by nonspecific interactions are perceived as electric noise, which impedes the measurement process. I will start the analysis of noise by the characterisation of GTJs signal at cryogenic temperature, which will give insight into the microscopic mechanism of noise generation.

3.1 Two Level Switching in Graphene Tunnel Junctions

In the GTJs cooled down to liquid nitrogen temperature of 77 K I universally observed Two Level Fluctuations (TLFs) in the form of switching between two discrete current levels (Fig. 3.1C). Such fluctuations, also referred to as Random Telegraph Signals (RTSs), observed on short time scales on the order of tens of seconds, give rise to a bimodal current distribution, which is evident from two peaks in the current histogram (Fig. 3.1D). Both of the peaks can be fitted with Gaussian distribution. This is in contrast to the room temperature measurements where I observe a monomodal log-normal current distribution with non-specific current vs time $I-t$ traces (Fig. 3.1A-B). This is also reflected in the difference in noise spectra (Fig. 3.1E). The noise spectra at room temperature follow $1/f$ trend, with the noise magnitude proportional to the inverse of frequency, while at cryogenic temperatures there is observed the emergence of Lorentzian noise spectrum characterizing Random Telegraph Noise (RTN).

There are two main approaches to measurements of noise spectra, namely, direct measurement of the noise spectrum using a spectrum analyser or the calculation of a noise spectrum on the basis of $I-t$ traces. The advantage of the latter approach is that a single measurement allows for simultaneous recording of $I-t$ traces and the calculation of a noise spectrum. Both of these types of data are necessary to confirm the observation of RTN as noise spectrum on its own is insufficient to obtain the unambiguous $I-t$ trace.[136, 137] This is because the noise spectrum is not

sensitive to the swapping the *up* and *down* level polarity or time reversal.[136] The applied method of calculating noise spectra on the basis of $I-t$ traces following the discussion by Kirton and Uren[138] is summarised in Appendix B.

All data presented below was recorded using a voltage-clamp amplifier Axopatch 200B and a Digidata 1440A digitizer. The voltage-clamp amplifier offers noise performance superior to other types of amplifiers, as it has been developed for the purpose of extremely low-noise measurements of ionic currents flowing through cell channels. The electronic setup will be discussed in more detail in Chapter 5 and Appendix F.

3.2 Classification of Noise Types

Electric noise is an ubiquitous phenomenon in electric devices. Noise is classified on the basis of its frequency dependence, which is defined as noise Power Spectral Density (PSD), $S(f)$. $S(f)$ is in general expressed as power per unit frequency, *e.g.* $[S_I(f)] = A^2/Hz$ in the case of current noise or $[S_v(f)] = V^2/Hz$ in the case of voltage noise. Power is treated here as a reduced parameter regardless of the resistance of the device under consideration, which occurs in the typical power expression $P = U^2/R = I^2R$.

Depending on their spectral dependence various types of noise can be distinguished. I will briefly review the properties of low frequency noise types ($f < 100\,\mathrm{kHz}$) which are relevant to graphene devices.[139]

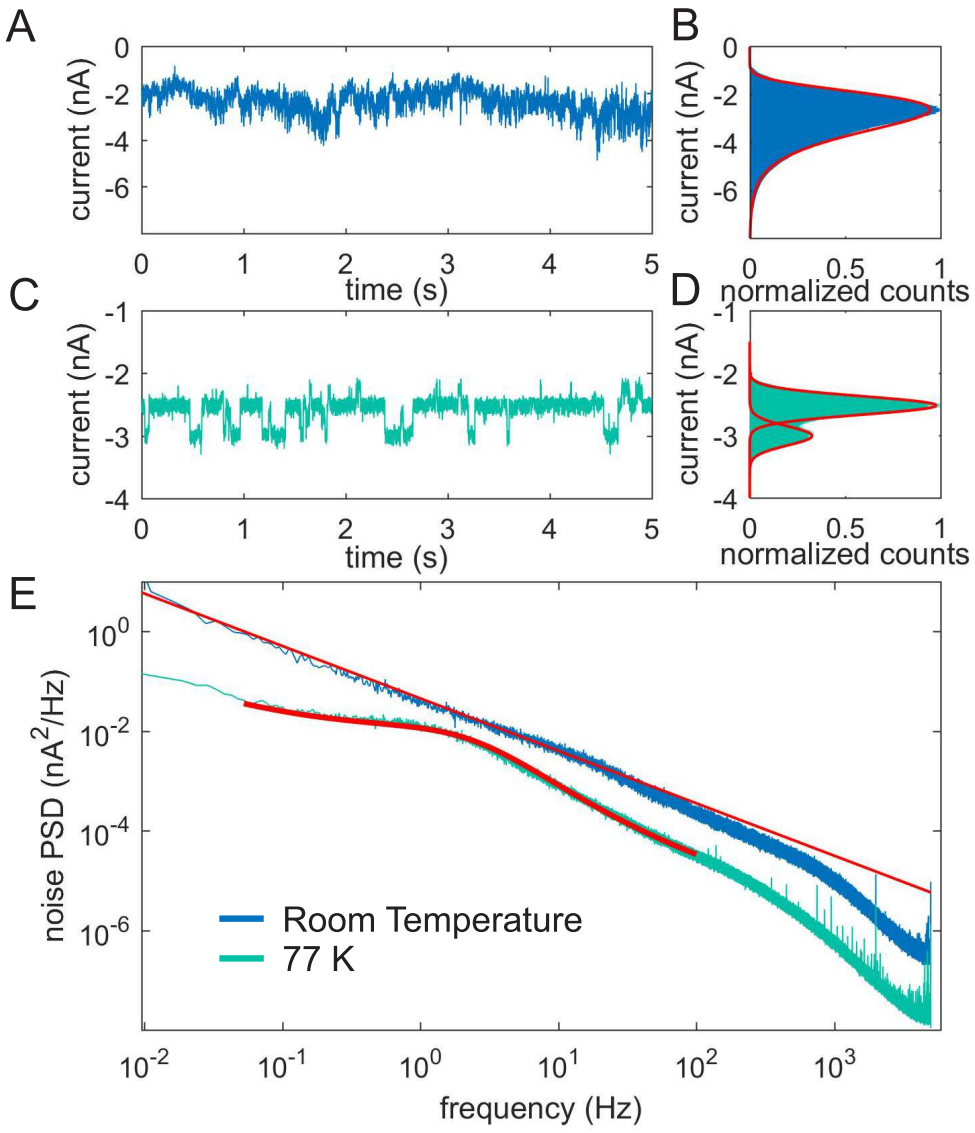


Figure 3.1: Emerging TLF and Lorentzian noise spectrum in GTJs. Room temperature data shows A) non-specific fluctuations in tunnelling current and B) corresponding log−normal distribution of current values. Upon cooling the device to 77 K it shows C) TLF in $I - t$ traces and D) bimodal current distribution with two Gaussian peaks. E) This behaviour is also found in noise PSD following $1/f$ trend at room temperature and Lorentzian noise spectrum at 77 K with lower overall noise level.

3.2.1 $1/f$ Noise

The term $1/f$ or flicker noise is applied to all noise spectra of the form

$$S(f) \sim \frac{1}{f^{\alpha}}, \tag{3.1}$$

where f is frequency and the exponent values are in the range $\alpha = 0.7 - 1.3$[140, 141] regardless of the origin of such noise spectrum. $1/f$ noise is commonly observed in natural systems and it has various origin mechanisms. Examples include fluctuations in annual temperature, river flood levels or voltage across cell membranes.[142, 143] There is a also wide range of examples where $1/f$ noise is observed in the electronic and solid state systems, such as vacuum tubes, diodes, transistors, carbon resistors, semiconductors or metallic thin-films.[142, 144, 145] I will discuss the origin of $1/f$ in more detail later in chapter 5, as it is closely related to RTN.

3.2.2 White Noise

The term white noise is used to describe all noise types whose noise spectrum is independent of the frequency,

$$S(f) = const. \tag{3.2}$$

The comparison of schematic noise spectra of $1/f$ noise and white noise is presented in Fig. 3.2. White noise can be classified as thermal noise and shot noise.

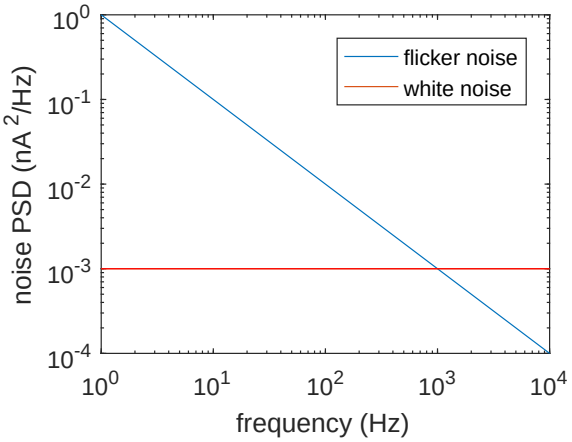


Figure 3.2: Schematic of flicker and white noise spectrum.

Thermal Noise

Thermal noise is a common feature of all conductors, and is sensitive only to the temperature and resistance of the system in which it is observed.[146] The expression describing thermal noise can be derived on the basis of fluctuation−dissipation theorem, and it has the following form[146]

$$\begin{aligned} S_I(f) &= 4kT/R \\ S_V(f) &= 4kTR. \end{aligned} \tag{3.3}$$

Since the only system parameter used here is the resistance R, white noise cannot give insight into microscopic properties of materials. However, it is important because in many cases it defines the noise floor at high frequencies obscuring other types of noise, such as $1/f$ or Lorentzian noise (Fig. 3.2).[146]

Shot Noise

Shot noise is another form of white noise, which is observed in non-equilibrium biased systems, and arises due to the discrete nature of electric charge. The number of electrons flowing through the conductor follows Poissonian statistics. In general the formula describing shot noise is given as[147]

$$S = 2eVG_0 \coth\left(\frac{eV}{2kT}\right) \sum_{n=1}^{N} \tau_n(1-\tau_n), \tag{3.4}$$

where summation is performed over N conductance channels characterized by transmission τ_n. In the case of low temperatures ($kT \leq eV$) this simplifies to[146, 147]

$$S = 2qF|I| = 2qF\frac{|V|}{R}, \tag{3.5}$$

where F is Fano factor, defined as

$$F = \frac{\sum_{n=1}^{N} \tau_n(1-\tau_n)}{\sum_{n=1}^{N} \tau_n}, \tag{3.6}$$

a parameter describing the transport state of the system. In the classical limit, of low transmission, high temperature and no correlation between charge carriers it takes value of 1. And in the case of microscopic systems it changes from 1 for a transparent channel to 0 for an open channel. Study of the shot noise and Fano factor in the mesoscopic and molecular systems provides an insight in their structure and electronic properties.[146] Fano factor can have values higher than 1 in the case of influence of Coulomb or phonon interactions on transport.[146] These interactions

point at the possible correlation of RTN at low frequencies and super-Poissonian shot noise behaviour at high frequencies, which is observed because the localized charge states changing their occupation (RTN) can influence the correlations between charge carriers (shot noise).[148]

In the next sections I will give an overview of the mathematical description of RTN and RTS. Subsequently I will discuss its occurrence in nanoscale semiconductor and molecular devices. This discussion should form a basis for the understanding of RTS in graphene tunnel junctions.

3.3 Random Telegraph Signal

RTSs are a particular form of time-dependent signal that switches immediately between two levels (*up* and *down*) without taking any intermediate levels.[138, 149] The probability of switching from *up* to *down* level is given by $\frac{1}{\overline{\tau_1}}$, while the probability of the opposite transition is given by $\frac{1}{\overline{\tau_0}}$, where $\overline{\tau_1}$ is the mean dwell time spent in *up* state and ($\overline{\tau_0}$) is the mean dwell time spent in *down* state.[149] A schematic profile of RTS in shown in Fig. 3.3. The mathematical formula for a RTS noise spectrum generated by charge traps in semiconductors has been derived by Machlup in 1954.[149]

Assuming the RTS switching probability, $p \sim \frac{1}{\overline{\tau}}$, it can be shown that the dwell times t are exponentialy distributed with a probability distribution [138, 149]

$$p_1(t) = \frac{1}{\overline{\tau_1}} \exp\left(-\frac{t}{\overline{\tau_1}}\right) \tag{3.7}$$

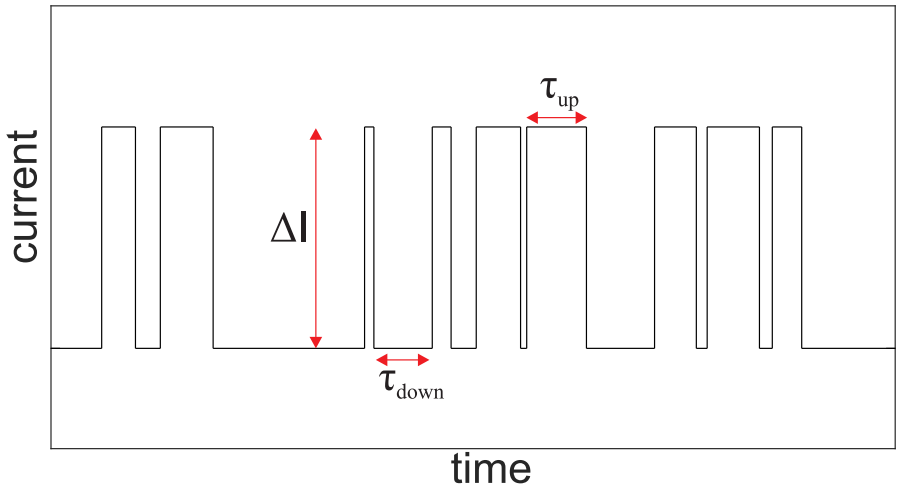


Figure 3.3: Schematic profile of RTS with marked characteristic parameters, the current step amplitude and the dwell times of *up* and *down* level.

for the *up* level and that the standard deviation of this distribution is equal to the mean dwell time[138, 149]

$$\sigma_1 = \overline{\tau_1}. \tag{3.8}$$

Analogous expressions can be obtained for the *down* level and $\overline{\tau_0}$.

The crucial assumption of Machlup's theory is the independence of charge traps and also charge carriers.[149] Occupation of a particular charge trap does not affect the charge occupancy of other traps. A similar assumption is also made for charge carriers; the capture or release of one charge carrier does not affect the probability of trapping and releasing another carriers.[149] In an analogy to holes and electrons in semiconductors, analysis of RTSs can be performed from the point of view of traps (filled/empty) or carriers (trapped/free). The assumption of independence of traps

and charge carriers allows for the calculation of an entire noise spectrum on the basis of a single trap spectrum by summation of noise contributions generated by different traps.[149]

In order to satisfy charge independence condition, large numbers of traps and charge carriers in the system are necessary.[149] In the case of a low number of traps or charge carriers the correlation can be introduced by the fact that a single trap allows only for two level fluctuation, that is it has only two possible charge states, namely filled and empty. The low number of charge traps leads to a form of exclusion principle where two carriers cannot occupy the same trap at the same time. Therefore probability of trapping charge carrier is proportional to the number of free traps.[149] Analogously, in the case of low number of carriers, change in their number by one changes the probability of filling next traps, as such probability is proportional to the number of free carriers. In the case of a system with a large number of carriers and traps, however, high changes in population are improbable and therefore the process can be treated as a random one.[149]

3.4 Mathematical Model of RTN

RTS at any moment can take only one of two possible values, namely $x_0 = 0$ for *down* level and $x_1 = \delta I$ for *up* level.[138] By rescaling, every TLF can be expressed in this way. Further the probability of the signal being in state *up* (*down*) is proportional to the mean dwell time spent in *up* (*down*) state divided by the sum of both dwell times, that is probability of finding system in the *up* state is equal to $\frac{\overline{\tau_1}}{\overline{\tau_0}+\overline{\tau_1}}$. Similarly

the probability for the *down* state is equal to $\frac{\overline{\tau_0}}{\overline{\tau_0}+\overline{\tau_1}}$.[138] Using these expressions the noise spectrum is obtained on the basis of the autocorrelation function[138, 149]

$$c(t) = \langle x(s)x(s+t)\rangle = \sum_i \sum_j x_i x_j P(s, x_i) P(s+t, x_j), \tag{3.9}$$

where $P(s, x_i)$ denotes the probability of signal at time s having value x_i. It can be shown that the resulting noise spectrum has the following form[138, 149]

$$S(f) = \frac{4(\Delta I)^2}{(\overline{\tau_0}+\overline{\tau_1})\left[\left(\frac{1}{\overline{\tau_0}}+\frac{1}{\overline{\tau_1}}\right)^2 + (2\pi f)^2\right]}. \tag{3.10}$$

If dwell times for *up* and *down* levels are equal, $\overline{\tau_0}+\overline{\tau_1} = 2\overline{\tau}$, the noise PSD formula simplifies into[138, 149]

$$S(f) = \frac{2(\Delta I)^2\overline{\tau}}{4+(2\pi f\overline{\tau})^2}. \tag{3.11}$$

Integrating this formula with respect to frequency leads to the expression for total noise power, which in the general case of arbitrary mean dwell times takes form[138, 149]

$$P = \frac{(\Delta I)^2}{(\overline{\tau_0}+\overline{\tau_1})\left(\frac{1}{\overline{\tau_0}}+\frac{1}{\overline{\tau_1}}\right)}, \tag{3.12}$$

and in the case of equal dwell times it simplifies to $P = (\frac{\Delta I}{2})^2$, which gives the maximum noise power value.[138, 149] Fig. 3.4A shows a typical RTN spectrum, which consists of two distinct regions on a log-log scale, the flat plateau for low frequencies and the step line with $\frac{1}{f^2}$ slope at frequencies above the corner frequency f_c. This kind of noise is also commonly called Lorentzian noise, due to the profile of

the noise peak on a linear scale (Fig. 3.4B).

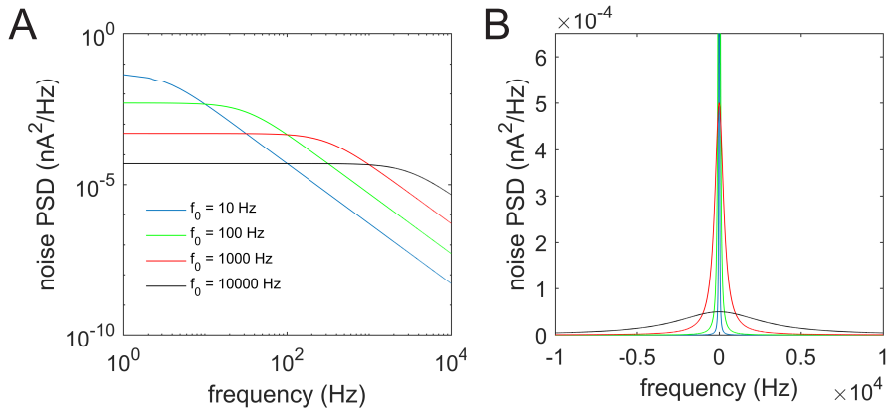


Figure 3.4: Simulated standard Lorentzian noise PSD plotted for a range of characteristic frequencies $f_0 = \frac{1}{\tau}$ on A) log-log and B) linear scale, with $\Delta I = 1\,\mathrm{nA}$.

3.5 RTS in Semiconductor Devices

The first experimental and theoretical investigations of RTSs considered switching in semiconductor devices due to the presence of charge traps. I will briefly review properties of charge trap fluctuators, because, as I will show later, they play a crucial role in TLFs observed in the GTJs (Fig. 3.1).

Since the invention of first semiconductor devices the continuous progress in fabrication methods allowed for their downscaling. This has led to the discovery of new properties of such devices related to their miniaturised dimensions. The topic of low frequency noise, such as $1/f$ noise and RTN, in silicon devices has attracted attention, firstly because of its limiting impact on the performance of analogue devices.[138, 140] The trend of miniaturization of CMOS (Complementary Metal-

Oxide-Semiconductor) devices made the noise considerations even more crucial, as with the decrease of device dimensionality the Signal to Noise Ratio (SNR) decreases.[140]

In 1950's first reports on RTS in semiconducting devices appeared. RTS has been observed in a variety of devices such as JFETs (Junction Field Effect Transistors), BJTs (Bipolar Junction Transistors), MOSFETs (Metal-Oxide-Semiconductor Field Effect Transistors), and diodes.[138, 140, 150] Reduction of the dimensionality of these devices allows to limit the effect of thermal noise and decreases the number of overlapping RTSs with different amplitudes and characteristic frequencies, resulting in a single Lorentzian spectrum. This behaviour is for example commonly observed in the drain current of MOSFETs with gate lengths smaller than 1 µm.[150]

RTS is sensitive to the conditions at which devices are operated; the fraction of devices exhibiting RTS can be increased by inspecting a range of physical conditions, changing temperature, bias voltage and measurement duration.[138, 150] The RTS at given conditions has constant characteristics independent of time. Therefore treating RTS in such devices as statistically stationary process is a good approximation.[150] The typical values of dwell times in semiconducting devices are on the order of 100 µs to 1 s, but they may even extend to tens of hours.[150] In some measurements the characteristic times up to 20 h were discovered. The ratio of observed dwell times for *up* and *down* levels $\frac{\overline{\tau_0}}{\overline{\tau_1}}$ can vary between 1 for the symmetric RTS up to 100s, for highly asymmetric dwell time distributions.[138, 150]

3.5.1 Physical Origin of RTS

RTS in semiconducting devices is commonly attributed to the capture and emission of charge carriers by charge traps.[140, 141, 145, 151]. This behaviour manifests itself in the form of Lorentzian noise spectrum and is also known as generation−recombination noise or burst noise[140]. The conductance of material can be expressed in terms of its microscopic properties through the following formula

$$\sigma = nq\mu_q, \tag{3.13}$$

where n is carrier concentration, μ_q is carrier mobility and q is electric charge. The variation in the conductance can be thus expressed as[139]

$$\delta\sigma = \delta nq\mu_q + nq\delta\mu_q, \tag{3.14}$$

Taking it into account theories describing the origin of RTS can be divided into two groups, that is theories assuming fluctuations in[140]:

- the number of charge carriers ΔN, and
- the mobility of charge carriers $\Delta\mu$

Discerning between these two possible explanations in majority of the experiments might be cumbersome as usually only current and conductance traces are measured, prohibiting the separation of ΔN and $\Delta\mu$ contributions. In practice, the correlated $\Delta N - \Delta\mu$ models are likely to provide the more accurate description of RTS.[140] I will now briefly summarise the basic concepts of these two theories.

3.5.2 Fluctuations in Number of Charge Carriers ΔN

Charge carrier number fluctuations were for the first time proposed by McWorther[140, 152], who developed a description of noise in germanium oxide interfaces. The change of conductance is caused by fluctuations of charge carriers being captured and released by charge traps. The mechanism of charge trapping depends on the nature of the traps, which can be divided into three different classes:

- charge traps in silicon
- charge traps at the silicon/silicon oxide interface
- charge traps in oxide

I will briefly describe these charge trap types.

Charge Traps in Silicon Charge traps in silicon are introduced by defects. They obtain negative charge by means of electron capture or hole release, while change to more positive state is realised by the opposite processes. For example in the case of RTS in Field Effect Transistor (FET) with n-doped (p-doped) channel, the event of capturing an electron (hole) leads to a decrease in the current, compared to its original level when trap is not occupied.[150] The initial state is restored upon the release of a carrier. The mean charge density in the neighbourhood of a trap over the distances larger than Debye screening length is not affected by the trapping event, however it changes the drain current.[150]

In the case of defect-related traps in silicon the characteristic time for the emission of both types of charge carriers, which is a thermally activated process dependent on

temperature and energy level of the trap, is given by[150]

$$\tau_e = \frac{1}{Nvc} \exp\left(\frac{E_t}{kT}\right), \tag{3.15}$$

where E_t is the energy level with respect to the band edge, N is density of states (DOS), v is thermal velocity of carriers and c is the capture cross-section. The characteristic time of capture is governed by the charge carrier concentration n, that is[150]

$$\tau_c = \frac{1}{nvc} \tag{3.16}$$

Since the emission and capture of the unlike charges are independent processes and they lead to the same change in trap charge and current affected by trap occupancy, the resulting characteristic time for negative occupation is $\frac{1}{\tau_n} = \frac{1}{\tau_{c,e}} + \frac{1}{\tau_{e,h}}$ and the characteristic time for the occupation with positive charge is $\frac{1}{\tau_n} = \frac{1}{\tau_{c,h}} + \frac{1}{\tau_{e,e}}$[150], where second indices e and h correspond to an electron and a hole respectively.

Interface Oxide Traps The second class of charge traps are traps in silicon oxide at the interface with silicon. The basic difference compared to the silicon traps is that there are no free carriers located in the oxide and therefore charge to change their occupation has to be sourced externally. There are a few possible ways of the interaction of a charge carrier in silicon with charge traps.[150] The first of these mechanisms relies on tunnelling of carriers between discrete trap levels in the oxide and the continuum of levels in the semiconductor. Interface traps provide a range

of available energy levels distributed in space and energy, which are separated from the continuum levels of the semiconductor by a potential barrier.[150]

This tunnelling process is also strongly dependent on the distance d of a trap from the interface, and therefore it influences the characteristic dwell time of a trap, which can be estimated as[140]

$$\tau = \frac{1}{4nvc} \exp(2\kappa d), \tag{3.17}$$

where $\kappa = \frac{1}{h}(2mE_0)^{\frac{1}{2}}$, m is mass of electron, E_0 is height of a tunnelling potential barrier and h is Planck constant. This indicates that faster fluctuation is induced by shallow traps lying close to the interface, while longer dwell times are caused by the more distant traps.[150]

Only traps lying sufficiently close to the interface give rise to noise which can be observed over a typical duration of a measurement[140]. In addition to that, the depth-independent $N_{ox_t}(E)$ distribution leads to a perfect $1/f$ spectrum. In contrast, the depth-dependent distribution of traps $N_{ox_t}(E, x)$ gives rise to $1/f^{\gamma}$ noise, with $\gamma \approx 1$. $\gamma > 1$ is obtained for charge concentration increasing with the distance from the interface, $N_{ox_t} \nearrow (x \nearrow)$ and $\gamma < 1$ for the charge trap concentration decreasing with the distance, $N_{ox_t} \searrow (x \nearrow)$[140, 153]

An alteration to the McWorther model which does not demand the energy alignment between the trap and charge carrier was proposed by introducing indirect interaction between the carriers in semiconductor and oxide trap levels through the interface levels[140]. In this case the trapping event is separated into two stages (Fig. 3.5B). At first free carrier is captured by the interface trap by fast thermal

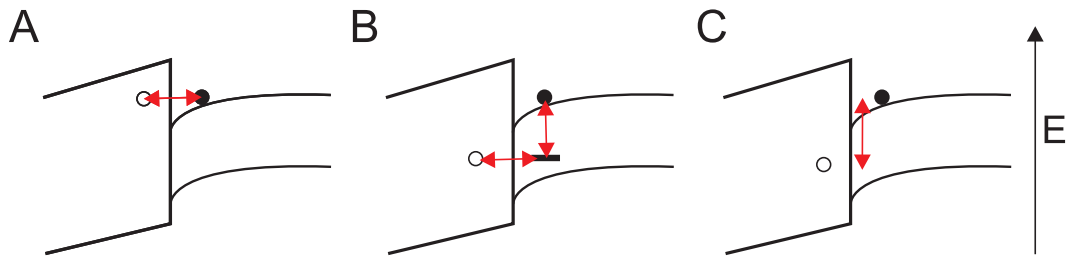


Figure 3.5: Different mechanisms of charge carrier number ΔN fluctuations at the Si/SiO_2 interface: A) Direct tunnelling B) Tunneling mediated by the oxide interface level C) Thermal phonon assisted tunnelling.[140]

capture. Second stage is tunnelling from the interface trap to oxide trap, which introduces current fluctuation and a time constant dependent on the tunnelling distance. In the second step the energy alignment between initial and final trap level is necessary as there is no phonon involved.[140, 154]

The physical realisation of a distribution of time constants may be achieved not only by the variation of tunnelling distances to oxide traps but also by the dependence of the time constant on the activation energy E[138, 140]

$$\tau_{th} = t_0 \exp(E/kT), \tag{3.18}$$

where k is Boltzmann constant and T is temperature. In this case the interaction between carriers and oxide traps is mediated only by the thermal phonons (Fig. 3.5C), without intermediate oxide interface trap [140, 145]. A $1/f$ noise spectrum can be achieved by introducing the distribution of the activation energies $D(E)$, which leads

to a noise PSD expression in the following form:

$$S_N(f) = \int_{E_0}^{E_1} \frac{D(E)\tau_{th}}{1 + (2\pi f \tau_{th})^2} dE \tag{3.19}$$

This integral also leads to the $1/f^{\gamma}$ noise spectrum. $\gamma > 1$ is achieved for the trap density increasing with energy, $D(E) \nearrow (E \nearrow)$ and oppositely $\gamma < 1$ is achieved for the trap density decreasing with energy $D(E) \searrow (E \nearrow)$.[140]

A compromise between the theories assuming the distribution of charge traps in space x and energy E are mixed models taking into account both kinds of variability. In a simple case, the trap concentration is given as[140]

$$N_{ox_t} = N_0 \exp(-\Theta|E| + \kappa d), \tag{3.20}$$

where N_0 is charge trap concentration at distance $x = 0$ from the interface and energy $E = 0$.

3.5.3 Fluctuations in Mobility of Charge Carriers $\Delta\mu$

Contrary to the charge carrier number fluctuations ΔN models another group of models are those relying on the mobility fluctuation $\Delta\mu$. In the mobility fluctuations model the observed fluctuations arise in the volume of the semiconductor, as opposed to clearly surface phenomenon of ΔN fluctuations.[140, 151] Mobility models were initially applied by Hooge for the analysis of $1/f$ noise in metals.[140, 151] These models assume the phenomenological Hooge's law, describing the scaling of noise

with the current[140, 151]

$$\frac{S_I}{I^2} = \frac{S_V}{V^2} = \frac{S_R}{R^2} = \frac{\alpha_H}{Nf}, \tag{3.21}$$

where S_I is current noise, S_V is voltage noise, I is current flowing through the device, V is bias voltage, and α_H is Hooge parameter.[140, 151] Hooge parameter is a dimensionless constant on the order of 10^{-3}. Initially it was perceived as a universal constant, however now it is clear that it is a parameter describing properties of particular material. Hooge parameter is a measure of charge scattering introduced by the defects in material.[140, 151] Materials with higher crystallinity and therfore lower scattering are characterized by lower values of Hooge parameter.[140] Value of the Hooge parameter can be expressed in terms of mobility by the following expression:

$$\alpha_H = \alpha_{latt} \left(\frac{\mu}{\mu_{latt}} \right)^2, \tag{3.22}$$

where $\alpha_{latt} = 2 \times 10^{-3}$ is a dimensionless constant, μ_{latt} is carrier mobility limited only by the lattice scattering and μ is the total mobility limited by all other scattering mechanisms present in the material, which is calculated using Matthiensen rule for the independent scattering mechanisms.[140, 151]

In the case of both ΔN and $\Delta\mu$ fluctuations the resultant noise spectrum is sensitive to the defects which can alter the number of carriers or introduce additional scattering centres influencing mobility.[140, 151] The dependence of noise on the defects in the device structure emphasizes the impact of fabrication technology, which affects the crystallinity of semiconductors.[140, 151]

It has been emphasized many times, that although Hooge's theory was successfully applied to describe various materials systems, its physical basis is unknown.[141, 145] Although I do not suspect bulk mobility fluctuations as the origin of RTSs in the GTJs, the Hooge parameter still provides an efficient way of quantifying the $1/f$ noise amplitude, which I will use in the analysis of GTJs noise at room temperature (Chapter 5).

Nanoscale Devices The observation of RTSs due to charge traps is not limited only to devices with a semiconducting channel, indeed it has been also observed in a variety of other nanoscale systems, such as Quantum Point Contacts (QPCs) defined electrostatically in two Dimensional Electron Gas (2DEG).[155] In this case charge traps adjacent to a QPC by changing their charge state shift the QPC energy levels.[155]

Another group of devices which exhibit TLF are tunnel junctions formed at thin oxide barriers, introduced between superconducting contacts (e.g $Nb/Nb_2O_5/PbAuIn$ [156] or PbBi/InO/PbBi[157]) In this case TLF is caused by the change of the occupation of traps localized within tunnelling barrier, which changes the profile of the tunnelling barrier.[156] However, conductance measurements are insufficient to discern between effects related to barrier height, length or shape.[157] In oxide barrier tunnelling systems the possibility of changing the tunnelling probability and forming charge traps intentionally by applying voltage suggested that TLFs may be caused by the electromigration of charged oxygen atoms into the tunnel junction region[157].

Similar RTS effects have been reported in both organic[159] and inorganic[158] Resistive Random Access Memory Devices (RRAM), where switching between high

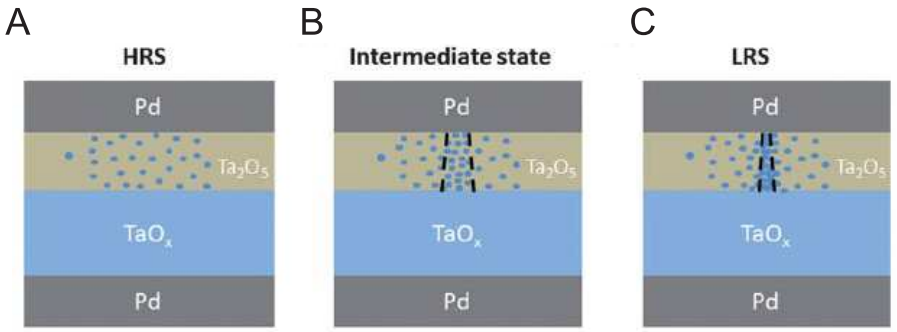


Figure 3.6: Mechanism of conductance change in the oxide-based RRAM devices. A) Device in the HRS with oxygen vacancies scattered with a large mean distance, leading to the low overlap of the electron-wave functions and effective low conductance (Mott localization). Many of traps can change their occupation giving rise to $1/f$ noise. B) Intermediate state of channel formation due to vacancy migration when forming voltage is applied. C) LRS with highly conductive channel created by the high overlap of the electron wave functions associated with various oxygen vacancies. One oxygen vacancy separated from the main channel by a relatively large distance can gate the transport through the channel by the electrostatic effect when it changes its charge state. Reprinted with permission from[158].

resistance state (HRS) and low resistance state (LRS) is attributed to the field-induced formation of a conductive channel due to the Mott localization (*e.g.* due to the oxygen vacancy V_O migration).[158] RTS in such system is caused by the change in the charge state of a single vacancy influencing electrostatically the conductance of the main conduction channel in the LRS (Fig. 3.6). In the case of the HRS such TLF was not observed as the wider distribution of the charge traps means that conductance is not sensitive to the occupation of a single vacancy and therefore charge traps introduce rather $1/f$ noise. [158]

3.6 Electric Noise in Graphene Devices

Graphene is a material which is used to form the tunnel junctions investigated in this thesis, thus it is necessary to separately discuss noise effects specific to graphene. Noise in graphene demands also a separate discussion because of its relatively recent discovery.[160] The experimental and theoretical methods of studying noise in semiconductor devices, which have been developed over last 60 years[138, 141, 145, 151, 152], have guided the analogous studies of noise in graphene systems in recent years.[139]

Like any other conductor, the noise spectrum of graphene includes thermal noise, shot noise or phonon−electron scattering induced noise.[108] However, graphene reduced dimensionality introduces special considerations when it comes to noise analysis. For single layer graphene the ratio of surface atoms to all atoms is $N_S/N_V = 1$. Therefore, noise effects introduced by the interface, which are already prominent for

miniaturized semiconductor devices, are even more important in graphene.

Graphene devices often take the form of large sheets (on the order of 10 µm) [161–167]. However the trend to miniaturize devices to obtain better sensitivity, for example for single molecule experiments, means that in-plane dimensions of these devices are reduced[90, 92, 113, 115]. This leads to a higher ratio of edge atoms to all atoms in the device N_E/N_V, and the edge effects and structure start to play role.

Different methods of graphene formation (exfoliation, epitaxy, CVD) allow for preparation of material with differing defect concentration, crystal domain size, which influence the noise levels. It is a much more serious issue in graphene compared to more mature growth methods of Si crystals and semiconductor device fabrication.[108]

CNTs have been the first carbon allotrope in which TLFs were observed. Due to the low diameter of CNTs the TLF generated by a single charge trap located close the CNT can be observed.[108, 168–170] For example, large TLFs (up to 60 %) were found in single walled CNTs (SWCNTs), which has been attributed to the possibility of fully blocking a 1D conductance channel even by a single charge trap.[168]

3.6.1 Noise in Graphene

A TLF caused by a single charge trap at a graphene interface is expected to have properties similar to the signal at a Si/SiO_2 interface, including Poisonian distribution of dwell times τ and Lorentzian noise spectra.[108] Until now TLF and Lorentzian noise spectrum in a graphene device has not been demonstrated as opposed to many examples in CNT devices.[139, 171] The interface area between the

device and substrate is typically much larger in graphene devices compared to CNTs, therefore they are more likely to interact with a high number of traps.[139]

There is no agreement yet on the noise mechanism in graphene[127]: whether it is due to carrier number ΔN[128, 129] or mobility $\Delta\mu$[131, 172] fluctuations. Two opposing pictures of graphene can be applied here. Firstly, graphene constitutes an 'ultimate surface' and all of its conduction electrons are surface electrons exposed to the interface with substrate below and adsorbates above the surface.[139] Because of the charge traps this interface noise in graphene should follow the McWorther type of fluctuations due to the change in a carrier number ΔN. On the other hand graphene can be perceived as a zero-bandgap semimetal, and therefore it should undergo conductivity fluctuations due to mobility fluctuations $\Delta\mu$ caused by the change in the occupation of scattering centres.[139, 171]

Both McWorther and Hooge approaches have been applied to graphene, with Hooge parameter values ranging from $\alpha = 10^{-5} - 10^{-2}$.[108, 128, 129, 173]. It has been proposed that current TLF in graphene devices could also be induced by the metal electrode−interface rather than underlying charge traps.[108, 130] It is likely that both graphene-dependent and electrode-dependent mechanisms are present and their relative magnitude depends on the fraction of total resistance constituted by the graphene channel and metal contact.[108]

Non-trivial Gate Dependence of Noise in Graphene A peculiar feature of graphene is its gate-dependent noise amplitude. Hooge's model predicts that the noise amplitude decreases with the increasing charge carrier concentration. However, in graphene two distinct kinds of noise dependence on gate voltage are found:

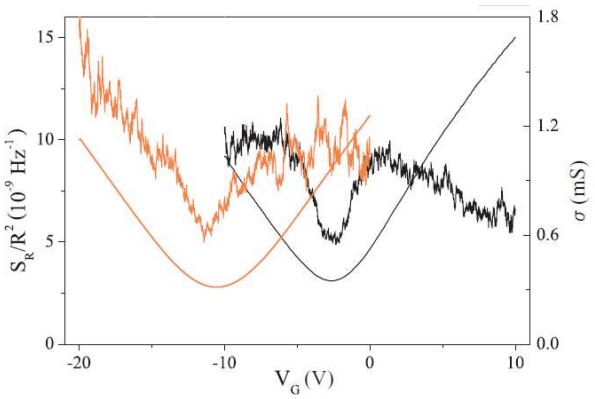


Figure 3.7: $V-$ (orange) and $M-$type dependence (black) of the normalized noise amplitude in graphene on gate voltage, caused by the interplay between short- and long range- scattering mechanisms. Smooth curves show the conductance dependence of the devices. Reprinted with permission from [129].

$V-$shape showing continuous increase in noise with increasing gate voltage and $M-$shape where after initial region of increase in noise amplitude further increase in gate voltage leads to the decrease in noise (Fig. 3.7).[129, 131] These two behaviours have been explained on the basis of Drude theory, assuming that resistance R depends on the charge carrier concentration n and the scattering impurity concentration N, that is

$$\delta R = \frac{\partial R}{\partial n}\delta n + \frac{\partial R}{\partial N}\delta N, \tag{3.23}$$

where the second term was found to determine the V vs M behaviour.[129] It has been proposed that two kinds of scattering mechanisms, namely short$-$range (being independent of concentration of scattering centres) and long$-$range (concentration dependent) can lead to this behaviour.[129]

The important feature of this model is that the time-invariant large scattering

potential gives rise to large resistance values (R), while its noise contribution is negligible ($S_R \sim (\delta R)^2$), and oppositely the small but fluctuating scattering potential may lead to the significant noise contribution without large impact on the overall resistance.[129] Considering two border cases where either long range (lr) or short range (sr) interactions dominate the resistance value and its fluctuations it has been shown that two forms of noise dependence can be obtained[129] :

$$\begin{aligned} \frac{S_R}{R^2} &\sim \left(\frac{\delta R}{R}\right)^2 \sim n^2, \text{ when } \delta R_{lr} \ll \delta R_{sr},\ R_{sr} \ll R_{lr} \\ \frac{S_R}{R^2} &\sim \left(\frac{\delta R}{R}\right)^2 \sim \frac{1}{n^2}, \text{ when } \delta R_{sr} \ll \delta R_{lr},\ R_{lr} \ll R_{sr}, \end{aligned} \tag{3.24}$$

where the first equation characterizes the $V-$type gate dependence and the latter one $M-$type dependence.[128, 129] On the basis of this analysis it was proposed that δR_{lr} fluctuations and resulting $M-$type noise curve are due to the adsorbed surface impurities such as water molecules, while δR_{sr} fluctuations and resulting $V-$type behaviour are caused by the charge traps in SiO_2 or at graphene interface.[129] This result is significant because it demonstrates that single species affect the noise performance in graphene, and that transport measurements can help discriminate between different mechanisms. It has been also shown that single molecules adsorbed on large-area graphene transistors can be identified on the basis of noise measurements.[164, 174] In the next section I will present the ways of reducing noise in graphene devices and subsequently discuss how single molecule junctions can generate RTSs.

Reducing Noise in Graphene Devices There are many strategies employed to limit the influence of charge traps distributed under and over a graphene sheet

on electric noise.[108] These methods include surface passivation[175], application of multi-layer graphene[125, 128, 176, 177], avoiding or removing surface contamination[178], engineering the substrate to limit the influence of charge traps[126, 172], or changing the measurement system from two probe configuration to four probe[155], which reduces the effect of the electrode interface on noise.

It is commonly agreed that hBN is an interesting alternative to SiO_x substrate [108, 179], due to its atomically flat structure and scarcity of dangling bonds and charge traps. The $1/f$ noise level of hBN-capped devices (Fig. 3.8) has been shown to be $5-10$ times lower compared to devices without capping layers.[172] Even better results can be obtained by fabricating suspended graphene devices[108], where it is possible to obtain the maximum graphene carrier mobility[79]. The direct evidence of substrate effect on the noise performance was provided by $in-situ$ underetching of the SiO_2 substrate under graphene FET devices.[126] Other attempts to reduce noise in graphene by applying the passivation layer on top of graphene surface were achieved with various materials including hafnium oxide [175] HfO_2 (Atomic Layer Deposition - ALD, 20 nm thick) or hBN layers.[108, 172]

Another way to decrease the influence of charge traps on noise is the application of Few Layer Graphene (FLG) instead of Single Layer Graphene (SLG), where graphene layers itself provide passivation.[108] Bi-Layer Graphene (BLG) has been shown to provide noise levels lower by one order of magnitude compared to SLG liquid-gated transistors.[125, 128, 176, 177] Reason for it may be twofold. Firstly more graphene layers effectively mean larger thickness of the conductive material, which allows for screening of the electric field induced by charge traps. A second mechanism of noise

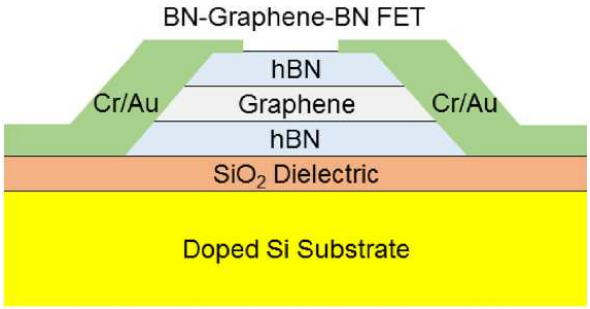


Figure 3.8: hBN − grph − hBN stack structure with a reduced noise level in a 1D-contact configuration. Application of hBN bottom and cap layers reduces noise arising due to substrate and adsorbed charge traps. Reprinted with permission from [172].

reduction may be due to the different band structure of graphene structures with varying number of layers:[108, 125, 173] SLG is a zero-bandgap semiconductor, while undoped BLG has band gap of 10 meV.[125]

A slight modification of this method is by implementing thickness-graded graphene ribbons, which change the number of layers from one in the middle of a ribbon to a few at the electrodes.[108, 130] In the sensing applications such architecture combines the advantages of both approaches, SLG (characterized by higher sensitivity to environmental factors) and FLG (lower noise introduced by graphene leads).[100, 108, 180]

At the stage of fabrication of devices the final noise level can be lowered by avoiding adsorption of contaminants on the graphene surface. One source of such contamination may be not fully removed resist, which can induce charge traps similar to those in the substrate.[108, 181] One way to circumvent this issue is to exclude resist from the process flow and substitute it *e.g.* by a nanowire hard mask.[178] Another option is to clean graphene surface after the EBL step by means of thermal

annealing in vacuum or inert atmosphere. Also oxygen plasma etching methods or graphene irradiation with electron beam can help alleviate the issue.[108, 182]

3.6.2 Edge Induced Noise in Graphene

Although there are multiple proposals of application of graphene for sensing in its pristine form its surface is low reactive due to the presence of saturated delocalized bonds.[183] Therefore for such applications it is common to use graphene oxide (GO) or reduced graphene oxide (rGO), which is highly defected and hence more prone to interact with the environment.[183, 184] It is true also for graphene edges, which treated as a defect in the perfect 2D graphene lattice, increase its sensitivity to the surrounding environment. On the other hand edges are known to afflict the charge mobility, electron and thermal conductance due to scattering.[108, 185] They also constitute a significant source of electric noise.

Edge defects in graphene can be classified into several main groups. Perfect graphene edges can either be either a zig-zag or armchair structure.[100] However, all-carbon edge composition is not energetically favourable as these edge structures have unsaturated dangling bonds, which are typically saturated by non-carbon atoms such as hydrogen, oxygen or fluorine.[108, 186] Termination with larger groups like $-$OH or $-$COOH is also possible. Because of scarcity of experimental evidence of graphene edge termination these assumptions are based predominantly on simulations.[99, 187]

For the sake of simplicity of simulations, often the ideal zig-zag or armchair configuration is assumed. In reality it is common to observe both types of edges in the same graphene structure, forming distinct regions along the edge.[100, 108,

180, 185, 188] It is also possible to obtain nanoribbons with varying width along the length of the ribbon. In the case of the large differences in width between such regions, spatially distributed, geometry-induced differences in the band structure may be achieved giving rise to Coulomb blockade.[108] Such effects may be observed in tailored bottom-up Graphene Nano-Ribbons (GNRs).[186, 189]

Another form of deviation from the perfect 2D structure at the graphene edge are lattice defects. These include point defects such as vacancies, substitiutions and interstitial atoms. There also line defects, defect loops and characteristic to graphene 5-7-5 and 5-8-5 deformed carbon ring structures.[108, 190, 191]

The studies of the effects of edge disorder in graphene devices are still at early stage. The main difficulty is in controlling the edge structure at a single atom level. Different GNR fabrication methods lead to different electric properties, affecting both the observed band gap and noise behaviour.[108, 139, 186, 192] More systematic approaches are necessary to correlate the information about fabrication methods, resulting structure and electric properties. There have been some attempts of studying the device geometry related effects on the electric properties. For example it has been found that the GNR mobility decreases with decreasing device width, suggesting the influence of scattering at the graphene edge.[108, 188] Although edges are an intrinsic feature of graphene devices it has been shown that their chemical functionalisation by exposure to HF acid may lead to the decrease in edge disorder and improvement in electron transport.[193] This treatment is expected to decrease the concentration of dangling bonds and charge accumulation at the edges.

All of these noise reduction methods are valid for large-area graphene devices,

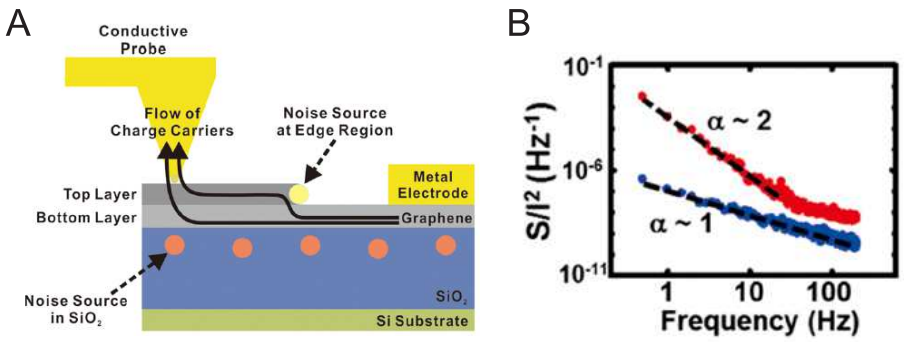


Figure 3.9: Scanning Noise Microscopy of graphene edges. A) Schematic measurement setup for SNM measurements. Current is flowing through the biased substrate, graphene and cAFM tip. The fluctuations in current, which contribute to the noise spectrum are measured with a spectrum analyzer connected to the circuit. Charge traps distributed in the underlying substrate and localized on the edges give rise to the increased noise. B) In noise measurement far from the edges of graphene the noise spectrum follows $1/f$ trend while in the case of measurement on the edges increased noise level with $1/f^2$ slope is observed. Reprinted with permission from [194].

and their effect relies on limiting the average number of charge trap fluctuators that influence electron transport. There is, however, no evidence that any of these methods is valid for ultimately downscaled devices like GTJs, whose geometry makes their particular areas more sensitive to environmental factors.

The fundamental contribution of edge states to the graphene noise spectrum has been directly confirmed by the Scanning Noise Microscopy (SNM). This measurement method, which is one of new techniques in a vast scanning probe family, relies of the measurement of electric noise spectrum in current transport between the sample and the tip of STM or cAFM (Fig. 3.9A).[194, 195] SNM has been applied to investigate the noise properties of multi-grain graphene surfaces.[194, 195] It has been shown that grain boundaries are characterized by lower conductance, possibly due to the higher defect level and presumably related opening of the band-gap. The noise level

at the edges was higher compared to the centre of the domain with additional low-frequency $1/f^2$ components compared to the sole $1/f$ component recorded in the centre of a grain (Fig. 3.9B).[194] This difference in behaviour may be attributed to a relatively large number of the charge traps embedded in the substrate underlying the graphene layer giving rise to $1/f$ noise in graphene as opposed to the single trap in the defected edge located close to the cAFM tip and therefore dominating the conductance and giving rise to $1/f^2$ noise spectrum.[194]

I expect that RTSs in GTJs are a manifestation of similar sensitivity to local environment, and that the noise contribution at the junction dominates noise originating from the large surface area. In the next section, I will present some examples showing that various tunnel junctions are characterized by the high local sensitivity and that transport through them is dominated by a single molecule in the junction. I will also show, which molecular mechanisms generate RTSs.

3.7 RTS in Molecular Devices

RTS have been recently observed in a variety of molecular systems in various device configurations and physical conditions. There are multiple proposed mechanisms that explain the emergence of TLF in molecular systems. It can be due to the effect of molecular reconfiguration[52] or binding kinetics[196]. It is also common to observe TLF effects due to charge transport modulated by the electron structure and charge traps introduced by the molecule: *e.g.* TLF can be induced by changes in the redox state of molecules.[197]

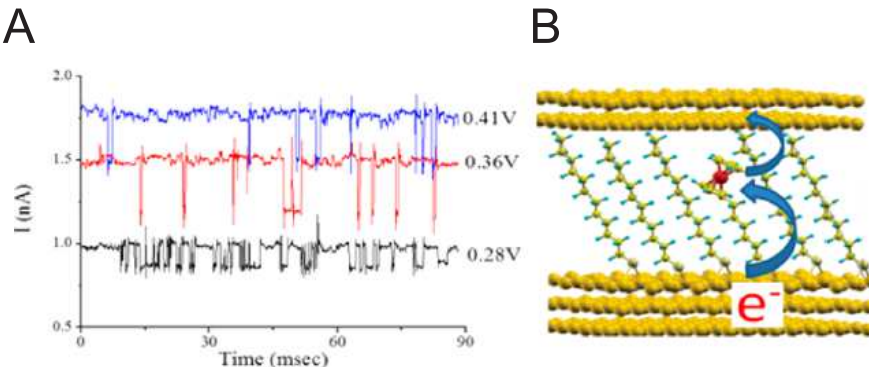


Figure 3.10: TLF in a SAM with diluted electroactive ferrocene molecules. A) TLF at different voltages. B) Diagram of the SAM junction with a conduction path. Reprinted with permission from [197].

SAM Devices TLF has been observed in Self-Assembled Monolayers (SAMs) of various molecules (*e.g.* alkanes), which were shown to introduce localized charge traps that give rise to a voltage-dependent TLF.[148] The relative position of the charge trap levels with respect to Fermi level of biased gold electrodes controls the probability of occupation of the trap. TLF in SAMs is also caused by the electrochemical activity of molecular layers containing short alkyl chains functionalized with thiol and electrochemically active ferrocene groups (Fig. 3.10).[197]

TLF in such redox systems allows to study electrochemical processes at a single molecule scale. Fluctuations are observed because there are two parallel conduction channels. First of them is a slow Marcus-type conduction process due to the localization of charge in the redox molecule. This process is slow due to the weak coupling of the electrochemical conduction channel to the electrodes. The slow change of the redox state of the redox moiety affects the second, fast conduction path, which is electron transfer with a high tunnelling rate, resulting from the strong coupling to

the electrodes.[197, 198] Purposely introduced molecules are not always necessary to observe TLF. One such example are Au microcontacts, where the switching behaviour was attributed to charge traps in a hydrocarbon layer remaining as a residue after the fabrication process or deposited directly from ambient air.[181]

TLF was also observed in a variety of single molecule systems allowing to study electron transport through a single molecule. Configurations where such phenomenon was observed included STM tips, MCBJ, single CNTs and graphene tunnel junctions.

RTS in MCBJ Molecular Devices The TLF in transport through molecules has been studied in MCBJ devices, which are commonly used for the single molecule experiments.[54, 199, 200]. TLF in such systems was attributed to the molecule reconfiguration induced by current (Fig. 3.11).[52, 201] The low amplitude of TLF and the increase of corner frequency with larger currents indicate that TLF is not caused by the repeating forming and breaking of the bond with one of the electrodes, but rather that TLF is a result of changing the configuration and coupling of the molecule within junction, however without fully breaking the connection. Current dependence is related to the local heating of the molecule and the junction tip, which increases the reconfiguration rate.[201]

Single Molecule Devices in Liquids Similar molecular rearrangement effects have been observed in single molecule measurements in liquid environments. There is a significant difference in $I - t$ traces for pure solvents and solutions of molecules functionalized to form a molecular bridge in the junction.[202] Tunnelling trough the solvent causes only low-magnitude current fluctuations, giving rise to $1/f$ noise

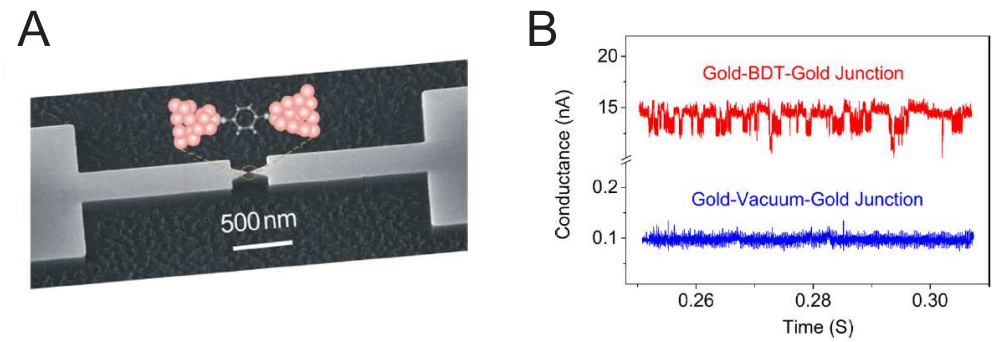


Figure 3.11: TLF in Au MCBJ with benzenditihol molecule. A) SEM image of the junction. B) Conductance vs time trace in a junction with and without the molecule. No switching is observed for the empty junction. Reprinted with permission from [201].

spectrum. In molecular solutions, at the distances small enough to allow molecule to form the bridge RTS with a higher amplitude and on the timescale of $\sim 1\,\mathrm{ms}$ is observed. The switching is attributed to the thermally driven breaking and re-forming of one of the bonds to the electrodes (Fig. 3.12).

The presence of a liquid environment also affects transport through single-tethered molecules in MCBJs.[203] In a single tethered molecule, TLF is caused by the interplay between two coupling constants Γ.[203] One of them Γ_1 is fixed by the molecular linker connected to the gold electrode and the second one (Γ_2) depends on the fullerene distance d to the electrode $\Gamma_2(d) = \Gamma_{2,0}\exp(-\kappa d)$.[203] Different solvents influence the $G-d$ conductance traces. The $G-d$ traces in good solvents (*e.g.* toluene for C60) are noisy and show low conductance values because efficient solvation allows for multiple molecular configurations.[203] On the contrary, more stable traces are recorded in bad solvents (e.g. DMSO for C60), which favour the trapping of a molecule in the junction to minimise the molecule solvation energy.[203]

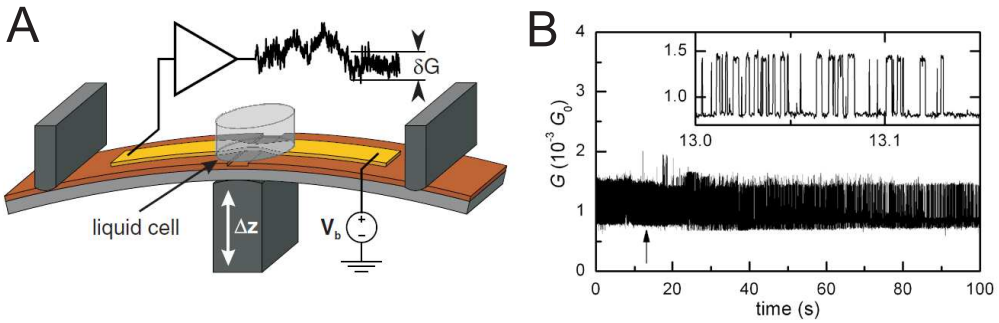


Figure 3.12: TLF in MCBJ molecular systems in liquid environment. A) Diagram of a measurement system used to measure TLF in MCBJ junctions with flow cell used to contain liquid. B) TLF signal in conductance recorded in hexanedithiol solution[202] attributed to breaking and re-forming of molecular bond with one of the electrodes. Reprinted with permission from [202].

RTN in STM Junctions TLF has been also observed in metal point contacts formed in STM configuration, without any added molecules. It is attributed to the repeated switching of surface adatoms between two metastable positions. Switching is a result of lateral motion of an atom in a double potential well of the underlying lattice, which depth is lowered by the tip-induced potential[31] The examples include switching of Au atoms on Au(111) surface[204], Zn nanowire MCBJs[205], Co atom on a Cu(111) surface between hcp and fcc positions[31] and Ag atom on Ag(111) surface[206]. TLF due to the surface atom motion is caused by the local heating of the junction, which is due to the excitation of adatom vibrations due to the inelastic interaction with tunnelling electrons.[205, 206]

Besides the thermally activated switching of atoms another mechanism that has been observed is tunnelling of adatoms between two metastable positions.[31] This has been observed at low voltages ($\sim 5\,\mathrm{mV}$) where heating effects are negligible and in contrast to the heating-activated mechanism it shows no voltage or current

dependence.[31] The local heating effects also affect the dynamics of the molecule bond formation in STM junctions, with higher currents leading to faster TLF.[207]

RTS in Molecular Graphene Tunnel Junctions TLF effects have been also observed in molecular GTJs (5 nm wide) measured in a liquid environment. The junctions were used as a measurement platform to electrically investigate dynamic formation of pseudorotaxane host-guest complexes, which was reflected in the current TLF (Fig. 3.13).[208] The observed switching behaviour with timescales on the order of 100 ms was attributed to the association−dissociation process of the host−guest complex.[208] TLF in such system can be perturbed by increasing temperature because of the thermally induced instability of this molecular complex. The analysis of TLF dynamics allows to estimate the binding constant for the molecular complex, with values is in accord with results obtained from ^{1}H NMR titration experiments.[208]

RTN in CNT-FET Devices TLF has been also observed in molecular CNT-FET devices, based on single semiconducting CNTs.[171] Pristine devices showed only $1/f$ noise, with monomodal current distribution. TLF, Lorentzian noise peak and increased amplitude of $1/f$ noise has been observed upon deposition of redox-active molecules (Fig. 3.14). The molecules gate the CNT conductance and introduce TLF by changing their redox state.[171] The corner frequency f_c of the Lorentzian peaks was different for three different molecules investigated with such CNT-FET device, allowing for their discrimination.[171] The relative difference between CNT Fermi level E_F and the molecular trap energy level E_T may be obtained from the

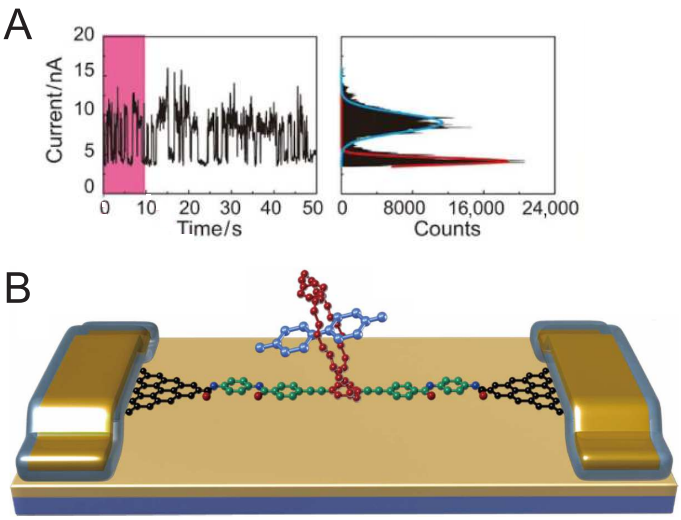


Figure 3.13: TLF in GTJs due to pseudorotaxane complexation reaction. A) Current $I-t$ trace and distribution due to the repeated formation of a molecular complex. B) Diagram of a GTJ whith a covalently bonded crown ether (red) capable of complexing MV^{2+}molecule (blue). Reprinted with permission from [208].

ratio of capture and emission dwell times[171]:

$$\frac{\tau_c}{\tau_e} = g \exp\left(\frac{E_T - E_F}{kT}\right), \tag{3.25}$$

where g is a degeneration factor.

All of these examples show that different tunnel junctions show transport features dependent on the junction-bridging single molecules, regardless of the particular mechanism (charge trapping, molecular reconfiguration, bond breaking or tip-atom thermal switching). It demonstrates the sensitivity of tunnel junctions to their local environment. I will proceed to the analysis of RTSs in GTJs, which will lead to the identification of their switching mechanism.

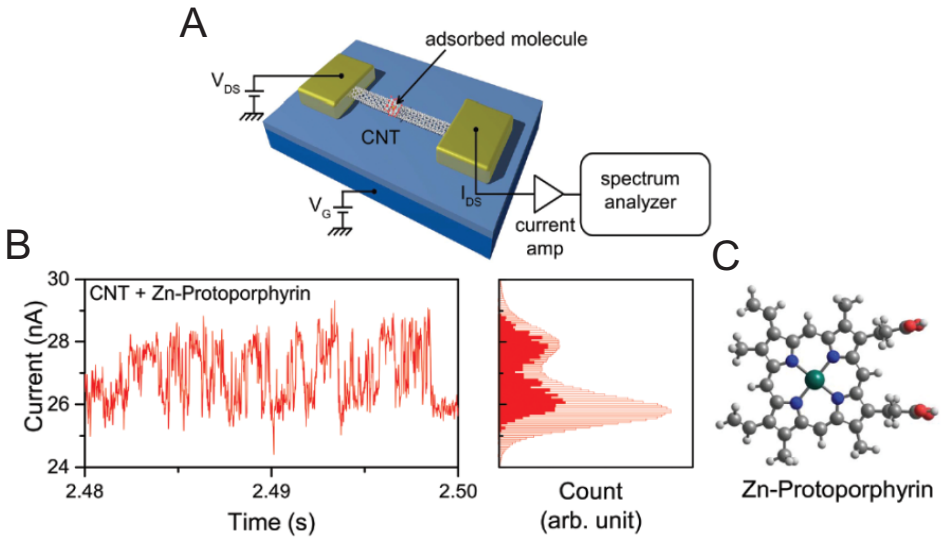


Figure 3.14: TLF in molecule-functionalized single CNT devices. A) Diagram of a single CNT device with Zn-protoporphyrin adsorbed on top. B) A resulting $I-t$ current trace and distribution C) Structure of the adsorbed molecule. Reprinted with permission from [171].

Chapter 4

Random Telegraph Signal in Graphene Devices

4.1 Analysis of Random Telegraph Noise Signals

In this chapter I focus on the analysis of RTS and RTN observed in GTJs. These results are significant, as until now there has been no evidence of a RTS and Lorentzian noise in any graphene device,[139, 171] and here I will show that due to the local sensitivity of GTJs RTS can be observed in such devices.

The investigated devices were prepared as previously described (Chapter 2) and those with tunnelling gap size in the range of $1 - 3\,\mathrm{nm}$, as estimated by Simmons model (Appendix A), were chosen. I typically applied 0 to $\pm 400\,\mathrm{mV}$ source-drain voltages and recorded the resulting current. Voltage values higher than $400\,\mathrm{mV}$ were not used as this would likely lead to the failure of device, resulting in undetectable

current levels. The biased devices exhibited TLFs over the time spans of minutes to hours. However, the statistical analysis of the traces longer than a couple of seconds is cumbersome due to the additional source of noise that can obscure the ongoing TLF. This additional noise component has a random nature, as opposed to the reproducible TLF behaviour. In order to enable the statistical analysis of the TLF in GTJs I introduce a complete methodology for extracting the physical parameters from TLF signals.

This methodology consists of the following analysis steps:

1. Calculating noise PSD curves
2. Fitting noise PSD spectra with Lorentzian peaks
3. Extracting information about the corner frequency (mean dwell time τ) and ΔI levels from the fit parameters
4. Using τ value obtained from the fit to define the maximum number of TLF switching events within a given duration of the $I - t$ trace
5. Application of Change Point Detection method to $I-t$ traces in order to extract separate current steps (with a limited number of allowed TLF switching events calculated on the basis of τ). In this way, the dwell time and mean current value for each of the current levels are extracted for the entire duration of the analysed trace
6. Grouping of the consecutive current levels in pairs. For each of these pairs the

mean current is calculated. It serves as a baseline for further analysis

4.1.1 Analysis of Noise Spectra

The set of noise spectra for a typical GTJ measured at 77 K, with an applied voltage range of 0 to 200 mV is shown in Fig. 4.1A. The 0 mV trace shows only low $1/f$ contribution at frequencies below 10 Hz and increasing capacitance noise at frequencies higher than 1 kHz. The rapid decrease of noise at frequencies higher than 10 kHz is related to the applied Bessel filter. Biasing the junction leads to the increase of noise by a few orders of magnitude. Yet devices measured at non-zero voltages are characterized by deviation from the linear $1/f$ trend. In particular in the intermediate frequency range of 10 to 1000 Hz a shoulder in the noise spectrum can be observed. I will focus my attention on this fragment and prove that nonlinearity observed in this range is due to the Lorentzian noise. In Fig. 4.1B I present one of the noise

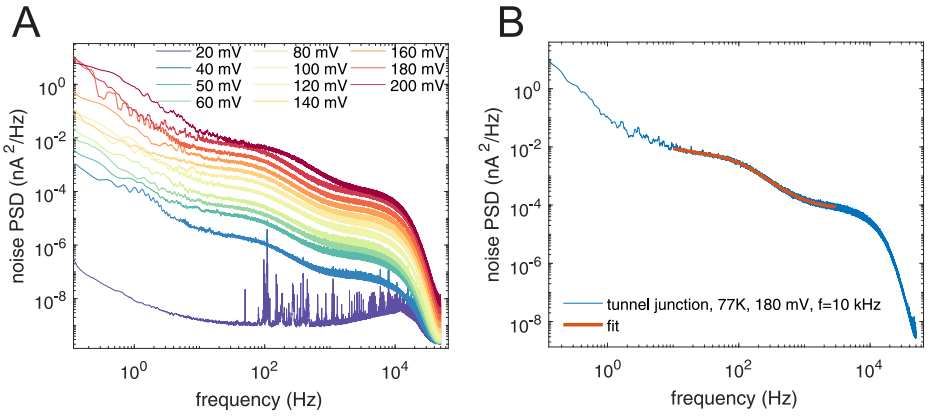


Figure 4.1: RTN spectra of tunnelling current in GTJs. A) Noise spectra obtained in the same tunnel junction for a range of applied voltages. B) Example of noise spectrum recorded at 180 mV with curve fitted over $5 - 3000$ Hz frequency range.

spectra for the device measured at 180 mV. The noise spectrum is fitted with a

three-component noise function of the following form[201]

$$S(f) = \frac{A}{f^{\alpha}} + \frac{2(\Delta I)^2 \tau}{4 + (2\pi f \tau)^2} + const, \tag{4.1}$$

where the first term describes the flicker noise contribution and is characterized by two parameters (A, the flicker noise amplitude and α , the frequency exponent). The second term is the Lorentzian formula, assuming that the mean dwell time values for *up* and *down* levels are equal $\tau_{up} = \tau_{down} = \tau$. ΔI in the Lorentzian formula is the mean amplitude of current steps. The third term of the fitting function is a constant white noise contribution. The noise spectra were fitted over the $5-3000$ Hz frequency range. The resulting fit shown in orange in the plot 4.1B yields good agreement with the experimental data. The curve fitting procedure was repeated for other voltage values and other devices. In the following sections I analyse the dependence of the three noise contributions on applied voltage and current.

White Noise The white noise contribution to the GTJ noise PSD depends exponentially on the applied bias voltage (Fig. 4.2A). The square root of the white noise contribution $S^{1/2}_{I,white}$ plotted versus mean current shows that there is a linear relation $S^{1/2}_{I,white} \sim \overline{I}$, for all voltage values. This indicates the correlation of white noise contribution PSD with $\overline{I}^2$, and consequently its correlation with the power of current flowing through the junction $P = I^2R$. The fit of the white noise contribution with the $y = ax^n + b$ function, plotted on the linear scale versus mean current, returns the exponent value of 1.86, which is close to the expected value of 2.

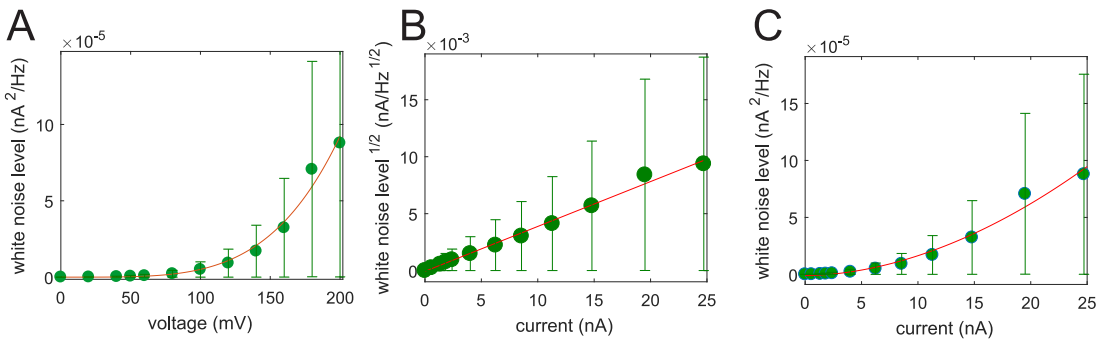


Figure 4.2: Fitted white noise contribution of PSD spectrum for a GTJ. A) Dependence of white noise contribution on applied voltage. B) Dependence of square root of white noise contribution on measured tunnelling current. C) Dependence of white noise contribution on measured tunnelling current.

Flicker Noise The $1/f$ noise contribution is characterized by two parameters, the amplitude and slope. Values of the slope coefficient (Fig. 4.3A) do not show any monotonic trend with increasing voltage and they vary between 0.8 and 1.2, which is within the limit of commonly accepted flicker noise slope.[140, 141]

The amplitude of the fitted $1/f$ noise contribution increases exponentially with the applied voltage (Fig. 4.3B), with some deviations at low voltages. The same data points plotted as a function of mean current exhibit a linear dependence of $A^{1/2}_{flicker}(I_{mean})$ within the error bars (Fig. 4.3C), indicating that the scaling with the mean current follows the same trend as in the case of the white noise contribution.

Lorentzian Noise The Lorentzian noise contribution is characterized by two parameters, the ΔI level and the mean dwell time, τ. The mean dwell time plotted as a function of voltage yields values of about 3 ms and its variation is within the error bars (Fig. 4.4A). Therefore, I conclude that there is no clear dependence of the mean dwell time on the applied voltage or mean measured current.

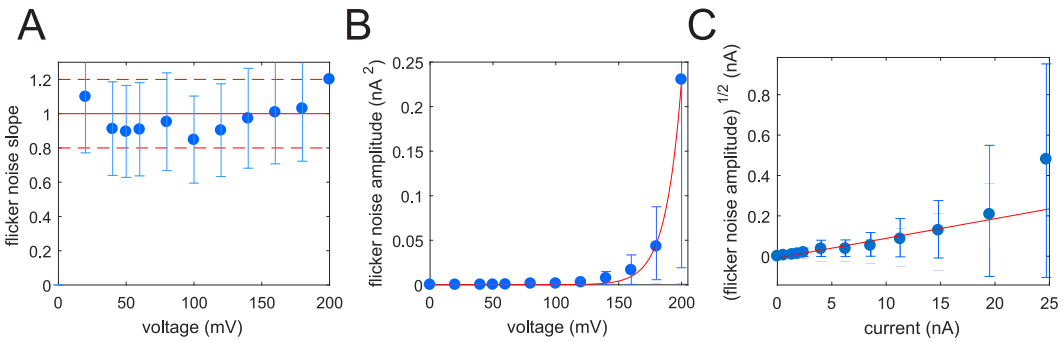


Figure 4.3: Fitted flicker noise contribution of PSD spectrum of a GTJ. A) Dependence of α slope of white noise contribution on applied voltage. Horizontal lines show $\alpha = 1$ (solid) and $\alpha = 0.8$, $\alpha = 1.2$ levels (dashed lines). B) Dependence of fitted amplitude A of flicker noise contribution on applied voltage with exponential fit. C) Dependence of fitted amplitude A of flicker noise contribution on measured mean tunnelling current.

Further, I analyse the dependence of ΔI levels on the applied voltage. The dependence of the fitted ΔI^2 level on voltage follows the exponential trend as it can be fitted with the formula $y = a \exp(x/b)$ (Fig. 4.4B) and again I find a linear dependence of the fitted ΔI levels in the function of the mean measured current. (Fig. 4.4C).

The parameters describing the amplitude of white noise ($S(f) = const$), flicker noise (A) and RTN (ΔI^2) all follow the $S \sim I^2$ scaling trend. This is a common observation in noise in electronic systems, and as it has been discussed by Dutta and Horn, it indicates that the noise generation mechanism is not driven by current.[145] Instead, the current serves only as a readout mechanism, allowing to detect independent resistance fluctuations, which are an equilibrium process.[145] The common scaling law for all three noise contributions implies their common origin. In particular, if the white noise was to be identified as thermal noise, it would scale linearly with

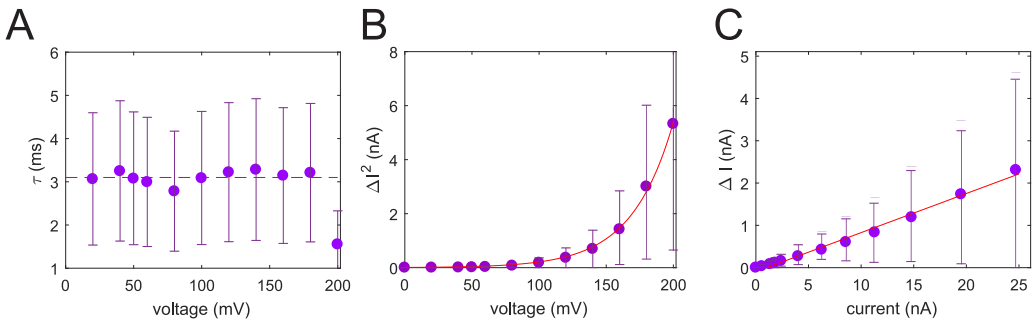


Figure 4.4: Fitted Lotrentzian noise contribution of PSD spectrum for a Graphene Tunnel Junction. A) Dependence of mean dwell time τ of Lorentzian noise contribution on applied voltage. Horizontal line shows $\tau = 3.1\,\text{ms}$ reference level. B) Dependence of fitted ΔI^2 amplitude of Lorentzian noise contribution on applied voltage with exponential fit. C) Dependence of the fitted ΔI amplitude of Lorentzian noise contribution on the measured mean tunnelling current.

resistance R which in turn scales with applied voltage as $1/R \sim \exp \alpha V$, assuming the current flow through the tunnelling junction.[15] However, to fit the experimental data a non-physical $1/R \sim V^2$ scaling law would have to be satisfied. It implies that the observed white noise is not identical to the thermal noise, which I will verify later.

4.1.2 Analysis of $I - t$ traces

On top of the noise spectra discussed above, I have also analysed the $I-t$ traces. The understanding of the statistical properties of TLFs demands the separation of the traces into individual current steps. This can be achieved by applying the method of Change Point Detection (CPD).

Change Point Detection The aim of CPD is to divide a signal into separate segments in such a way that the change of a statistical property, such as the mean

value or standard deviation, in each of the segments is minimized and the changes between segments are maximized.[209] The procedure of finding a single change point is realized by dividing signal into two segments. For each of them the mean statistical property of interest is calculated, and for each point in both segments the deviation from the segment mean statistical property is calculated.[209] Deviations for all of the points are summed. The procedure is repeated multiple times with the shifted change point. The point that minimizes the accumulated deviation from the mean statistical property for both segments is accepted as the real change point. If the signal has to be divided into segments in order to achieve best separation in terms of mean the expression to be minimized is defined as[209]

$$J = \sum_{i=1}^{k-1} \left(x_i - \frac{1}{k-1} \sum_{j=1}^{k-1} x_j \right)^2 + \sum_{i=k}^{N} \left(x_i - \frac{1}{N-k+1} \sum_{j=k}^{N} x_j \right)^2 . \qquad (4.2)$$

The same procedure can be applied to find a higher number of change points $\boldsymbol{X} = [x_1, x_2, \ldots, x_N]$ in the signal, where the expression to be minimized is a function of a change point vector $J(N)$.[209] In the case of an unknown number of change points N, it is possible to find their optimum number by introducing a penalty term into the minimized expression, *e.g.* $J(N) = J(N) + \beta N$, where the penalty term is a linear function of the number of change points.[209]

Results of Change Point Detection Analysis I performed the CPD by cutting the entire recorded $I-t$ trace into 10 s-long segments and analysed them individually. For each segment the maximum allowed number of change points is given as the duration of the trace segment t_{trace} divided by the mean dwell time $\overline{\tau}$ obtained by

fitting the noise spectra, $N_{max} = t_{trace}/\overline{\tau}$. A trace fragment with extracted levels is shown in Fig. 4.5. For each of the current steps a mean step current is calculated and plotted as a horizontal line. The visual inspection of the fragments shows that the method is able to correctly distinguish the consecutive current steps. The recorded current steps and the calculated mean step currents are in good agreement.

Subsequently, the consecutive current steps are grouped into pairs. For each of these pairs the baseline current is calculated as the mean current value of the *up* and *down* current levels. This is calculated as the mean of only 2 points, where each of the points represents a single current level, $\overline{I_b} = \left(\overline{I_{up}} + \overline{I_{down}}\right)/2$. I use this method instead of calculating a simple average of all recorded data points for two consecutive current steps, because it allows for the impartial estimation of the local current baseline, neglecting the effect of different duration lengths. By averaging all the recorded data points the mean local current would be biased towards the levels with longer dwell times.

The mean current baseline plotted in black in the Fig. 4.5 is used as a reference level to calculate the height of ΔI current steps

$$\begin{aligned} \Delta I_{up} &= \overline{I_{up}} - \overline{I_b} \\ \Delta I_{down} &= \overline{I_{down}} - \overline{I_b}, \end{aligned} \tag{4.3}$$

where $\overline{I_{up}}$ is a mean current level for a single *up* level and $\overline{I_{down}}$ for a single *down* level. The mean baseline current reflects the relatively slow and low amplitude random changes in the environment of the junction that affect the regular and fast TLF in the current. The procedure of extracting τ and ΔI values is repeated for the

next set of levels until all the levels in the trace have been analysed.

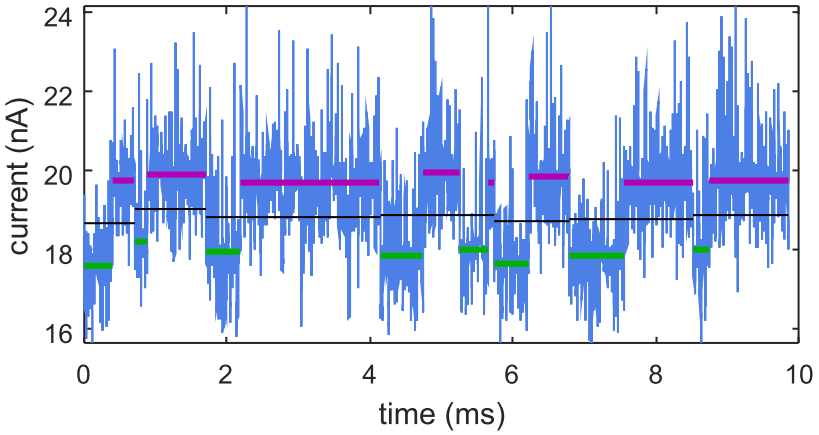


Figure 4.5: RTS observed in a GTJ at 77 K and 180 mV bias. Blue line shows fragment of an original $I - t$ trace. Red and green lines show mean current levels for individual current levels extracted by CPD method for *up* and *down* levels respectively. Black line shows the baseline current calculated as the average value of two consecutive current levels.

Baseline Current I_b Analysis In Fig. 4.6A I plot the mean baseline current $I_b(t)$ as a function of time for the duration of the analysed trace (500 s in the current example). In general the value of the mean baseline current shows a random drift, and only occasionally there are examples of rapid high-amplitude change of the baseline current lasting for $\sim 1-100$ s (for example the baseline current burst in the presented trace at $t = 70$ s), which can be interpreted as a current burst event with a long dwell time.

A histogram of the baseline current values presented in Fig. 4.6B shows a distribution of baseline current values with a dominant skewed single peak. The main peak can be fitted with a log-normal distribution, similarly to current distributions

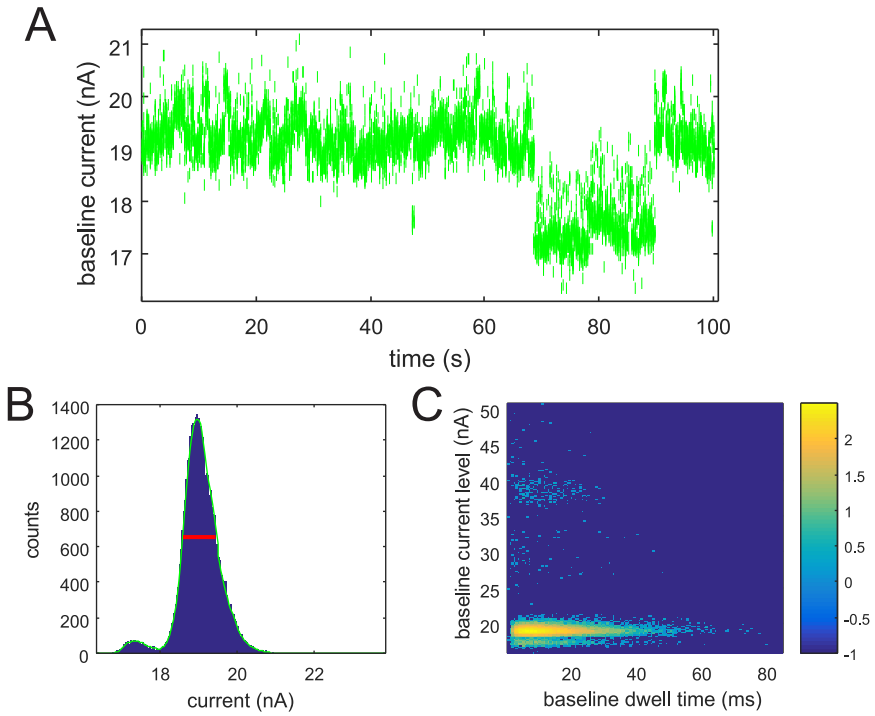


Figure 4.6: Properties of local baseline current. A) $I-t$ trace of local current baseline. B) Histogram of local baseline current values with marked FWHM value. C) 2D histogram of dwell time vs current level of local baseline levels.

recorded at room temperature (Chapter 5). A much lower satellite peak is also observed, which I attribute to the low current baseline bursts. The similarity of the I_b baseline current distribution to the log-normal current distributions measured at room temperature again indicates that there might be a common mechanism responsible for the fluctuations. Freezing the slower fluctuators at cryogenic temperatures leads to the long dwell times, manifesting as the occasional baseline current bursts, while the signal is dominated by TLF generated by a single fast fluctuator.

In Fig. 4.6C I plot the 2D histogram of the mean baseline current I_b vs its dwell time τ_b, $f(\overline{I_b}, \tau_b)$, which does not show any specific clustering. However, it contains

three main point groups centred at $\overline{I_b} = 20\,\mathrm{nA}$ and smaller point clusters centred at $\overline{I_b} = 17$ and $40\,\mathrm{nA}$. In all of these groups low dwell times are favoured, however, in the case of $\sim 20\,\mathrm{nA}$ points the time distribution is wider, while the higher and lower current values of the $\overline{I_b}$ are shorter events. This is a manifestation of the exponential distribution of dwell times for different I_b levels; the more populated levels have more long-lasting events.

In Fig. 4.7 I plot the Full Width at Half Maximum (FWHM) value of the distribution of the baseline current values $\overline{I_b}$ as a function of the mean tunnelling current. This value can be treated as a measure of fluctuations in I_b in an analogy to ΔI for TLF. The FWHM values scale linearly with the current. This scaling trend is exactly the same for the ΔI step height of TLF fluctuation, as discussed previously. Such observation provides another argument that both kinds of fluctuations have a common origin, or at least both of them are equilibrium processes not driven, but only probed by the current.[145]

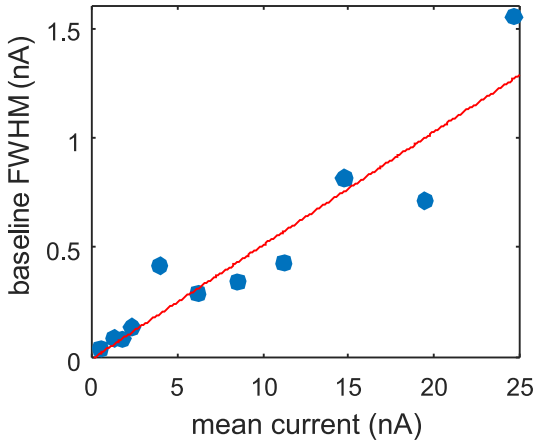


Figure 4.7: FWHM of locale baseline current plotted versus mean tunnelling current with linear fit.

TLF Current Step Analysis After extracting the values of the baseline current I_b I proceed to the analysis of TLF with respect to this baseline. Fig. 4.8 shows a few thousand initial ΔI levels as a function of the level number, removing the time duration information from the plot. This plot clearly shows spacing present between the positive and negative ΔI levels, indicating a rare occurrence of steps with a current level close to the baseline current $\overline{I_b}$. The positive and negative ΔI levels form two distinct lines, proving the successful separation of the traces into individual ΔI levels and a proper estimation of the baseline current. The *up* and *down* levels are uniformly spread over time showing no regions with detected abundance of only *up* or *down* levels, confirming that the CPD method is applied correctly.

Having confirmed the expected properties of extracted ΔI levels I analyse the histogram of ΔI current values, presented in Fig. 4.8B. the histogram shows a clear bimodal distribution of ΔI values. I fit this distribution with two Gaussian peaks. From the plot it can be seen that ΔI distribution reaches its local minimum at 0 nA current, indicating a scarcity of events which cannot be classified as *up* or *down* events. Further the mean value of the *up* and *down* levels can be extracted as the coordinate of the centre of each of the peaks, which will be used later.

Lastly, in Fig. 4.8C I plot fragments of the extracted current signals, namely the baseline current $\overline{I_b(t)}$ (centred around the global mean value of measured current) and $\Delta I(t)$ current levels (centred around 0 nA after subtracting the baseline current). The first of the signals shows random fluctuations without any repeating pattern, contrary to the latter one, which demonstrates clear form of TLF, resembling the TLF signals known from literature.[31, 181, 197, 201–203, 210]

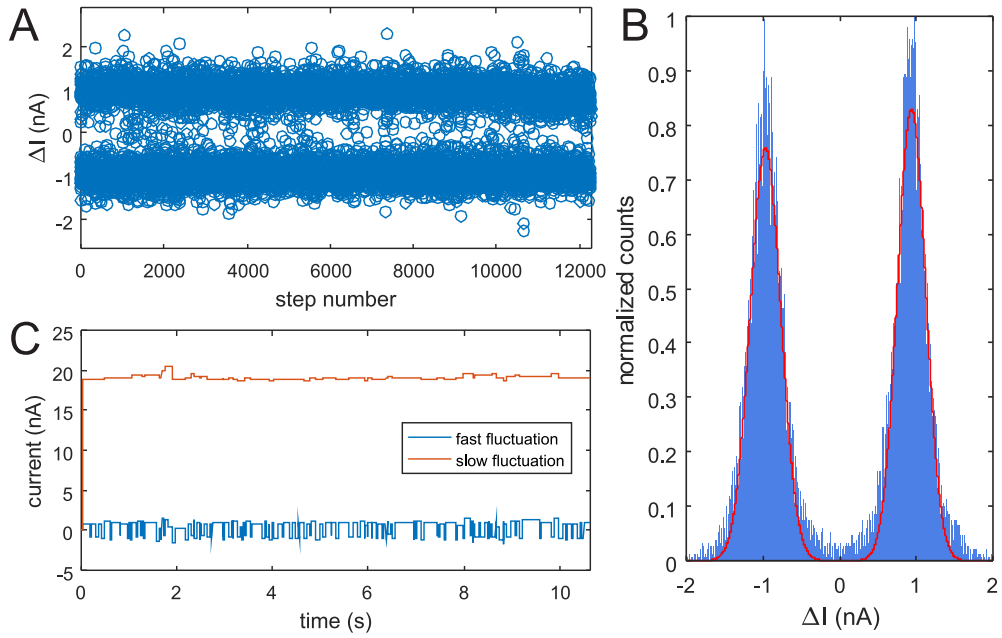


Figure 4.8: ΔI level analysis in GTJ signal. A) ΔI values plotted versus step number, showing good separation between *up* and *down* levels. B) Distribution of ΔI values showing good separation into two current levels. Peaks are fitted with Gaussian function (red line). C) Plot of the initial part of the trace showing signal separated into slow $\overline{I_b}(t)$ and fast contributions $\Delta I(t)$.

Temporal Properties of TLF Signal For each of the ΔI levels besides the current step height I also extracted the dwell time τ. The distribution of such dwell times plotted separately for *up* and *down* levels on a semi-logarithmic scale is shown in Fig. 4.9. The dwell time count statistics follow an exponential decay trend. From the linear fit of the dwell time count number with the following function $N = A\exp(-t/\tau) \rightarrow \ln(N) = \ln(A) - t/\tau = b - at$, I can obtain the mean value of τ as the reverse of the slope coefficient $\tau = 1/a$. The fitted values show asymmetry between the mean dwell time for *up* ($\tau_{up} = 13.0\,\text{ms}$) and *down* levels ($\tau_{down} = 4.3\,\text{ms}$) for measurements at 180 mV. Such distribution of dwell times is similar to the TLF

dwell time distribution found in molecular MCBJs.[207]. The averaged dwell time for both levels, calculated as the mean value of dwell times for *up* and *down* levels, $\tau = \left(\frac{1}{\tau_{up}} + \frac{1}{\tau_{down}}\right)^{-1}$ shows good agreement with mean dwell time values obtained by means of the fitting noise spectrum (Fig. 4.10A).[211]

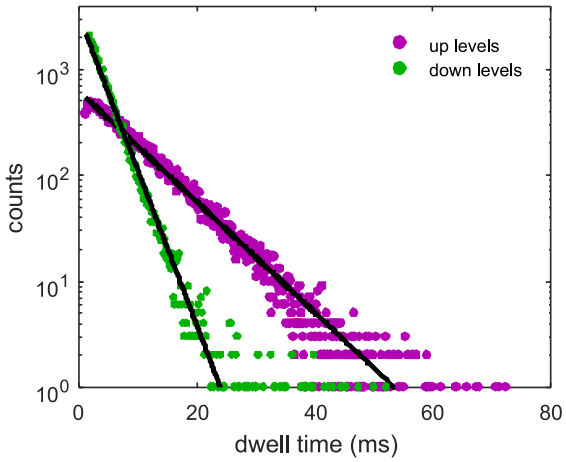


Figure 4.9: Distribution of dwell times τ for *up* and *down* levels.

A histogram showing the distribution of the level dwell time values as a function of the mean current of the level is presented in Fig. 4.10B. I do not observe any specific clustering, showing that regardless of the particular current level all of the current steps follow the Poissonian distribution, favouring short dwell times, which is also evident from Fig. 4.9. The histogram shows two separate regions, reflecting the switches between *up* and *down* levels. The dwell time values for the *up* level are distributed over a wider range compared to the dwell time values for the *down* level. But again as in the case of the τ_b distribution it is only a feature of a longer exponential tail of τ_{up}.

I find similar histograms for lower voltages, where the only difference is that there

is no clear spacing between the high count regions for *up* and *down* levels. Instead, the highest number of counts is observed in the region of transition between peaks $\Delta I \sim 0$. For low voltages ($< 40\,\mathrm{mV}$) these are, however, only short levels ($\tau < 1.5\,\mathrm{ms}$), indicating that some of the detected switching events might be incorrectly triggered by a noise form different to TLF. I emphasize that the long dwell times are observed only for the current values corresponding to the mean *up* or *down* current step level, indicating that switching events are correctly extracted from the measured traces.

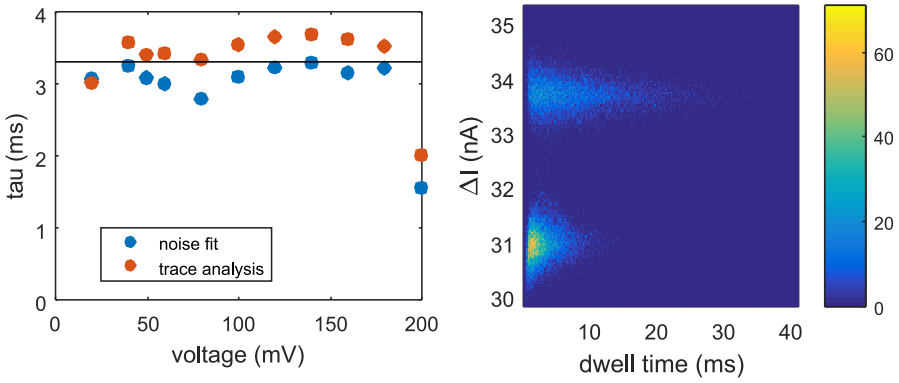


Figure 4.10: A) Voltage dependence of mean dwell time τ obtained on the basis of noise and trace analysis. Black reference line is plotted at $\tau = 3.3\,\mathrm{ms}$.) B) 2D histogram of ΔI values vs τ current steps extracted from analysed $I - t$ trace.

4.1.3 Comparison of Noise-Spectrum and Current-Trace Analysis Methods

Having analysed the $I-t$ traces I further use the data extracted from them in order to understand the origin of features observed in the noise spectra. As it was described previously in section 4.1.2 I separated the measured traces into two contributions

(Fig. 4.8C): the random slowly fluctuating baseline $I_b(t)$ and the faster TLF $\Delta I(t)$. For both of these contributions I calculate a noise spectrum on the basis of the $I-t$ profile following the procedure described in Appendix B. In Fig. 4.11A I show the original measured noise spectrum and the decomposed contributions: TLF and baseline fluctuation. The former shows a clear Lorentzian frequency dependence with a flat plateau below the characteristic frequency and $\frac{1}{f^2}$ slope above.

At low frequencies the noise spectrum is dominated by the baseline contribution. It follows a linear trend with the intermediate slope exponent in the range of $1 < \alpha < 2$. This suggests that beyond the frequency range of the current measurement there is another Lorentzian peak with a slow time constant, which roll-off arm is superimposed over the plateau of the observed Lorentzian peak. For higher frequencies the RTN dominates and the baseline noise contribution has a clear $\frac{1}{f^2}$ roll-off arm. This can be understood if the extraction of the TLF from the raw trace is perceived as a way of filtering. The noise spectrum for the measured trace after removing TLF information is filtered above the frequency where the noise spectrum was dominated by the TLF.

On the opposite side of spectrum, at frequencies above 1 kHz there is another region where discrepancies between the measured noise spectrum and the noise spectrum for the extracted TLF can be observed. In this region there is another plateau, which further transforms into a steep slope due to the applied 8-pole Bessel filter at 10 kHz frequency. The first assumption is that this is the thermal noise contribution related to the resistance of the junction. In order to assess this hypothesis I calculate the mean current and the mean conductance of the junction, $G = I/V$

(Fig. 4.11C) as a function of voltage. The obtained conductance is used to calculate the expected level of thermal noise by applying the Johnson-Nyquist formula $S(f) = 4kT/R = 4kTG$ (Fig. 4.11C).[145] I plot it also as a reference level in the figure showing the noise spectrum (Fig. 4.11A). It is, however, several orders of magnitude lower than the observed high frequency plateau. Also, as I discussed previously in section 4.1.1, the scaling of the white noise component obtained by noise fitting does not follow the $1/R \sim \exp V$ trend expected for the thermal noise in a tunnel junction.

As an alternative I look closer at the recorded $I - t$ traces, focusing in particular on the fast fluctuations observed within individual ΔI levels. For each of the ΔI levels I calculate the noise spectrum. A few of these noise spectra are presented in Fig. 4.12A. As the duration of the traces used to calculate these traces is on the order of $\sim 1\,\mathrm{ms}$ each of them contains only several dozens of points. Still, two distinct regions may be distinguished, a roll-off at frequencies above 10 kHz due to the applied 8-pole Bessel filter, and a flat region below this frequency. I use all the data points below the 5 kHz frequency to calculate the average white noise level for each of the ΔI levels. The values of the white noise levels are subsequently averaged for all ΔI levels detected at a particular voltage.

The white noise level obtained from the Lorentzian fit of the noise spectra and the mean white noise level have similar values and they scale identically with the measured tunnelling current, and their scaling trend differs from the scaling of the calculated thermal noise. Therefore, I conclude that the observed high frequency noise plateau is related to the fast fluctuations within individual ΔI levels and its

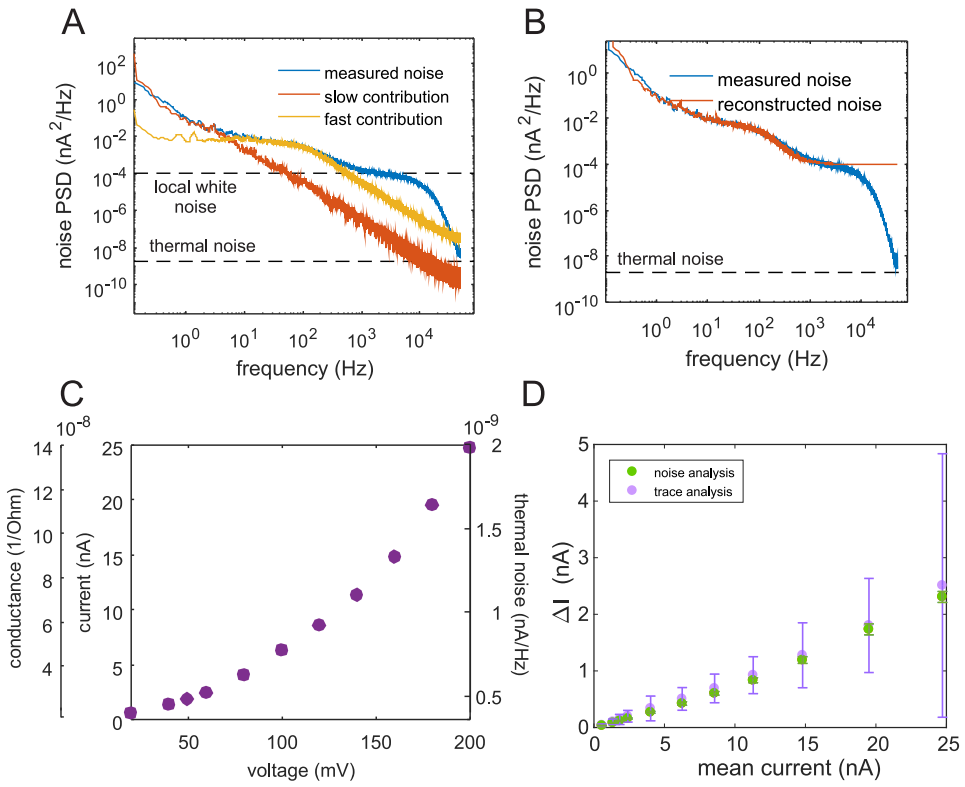


Figure 4.11: Separation of the noise in graphene tunnel junction into separate contributions. A) Noise PSD showing originally measured noise and its extracted contributions together with marked local white noise level and thermal noise calculated for this junction. B) Comparison of the original and reconstructed noise spectrum. C) Mean tunnelling current, calculated conductance values and expected values of thermal noise in the GTJ, as a function of voltage. D) Comparison of the ΔI values obtained by the noise and trace analysis.

origin is not due to the thermal noise related to the varying resistance of the tunnel junction. Because of the limited bandwidth of the measurement setup I cannot unambiguously characterize the nature of the high frequency plateau. Excluding the thermal noise I note that shot noise of this level has not been reported before.[147] Therefore the possible scenario is that I observe a part of another Lorentzian peak with a characteristic frequency higher than the bandwidth of measurement.

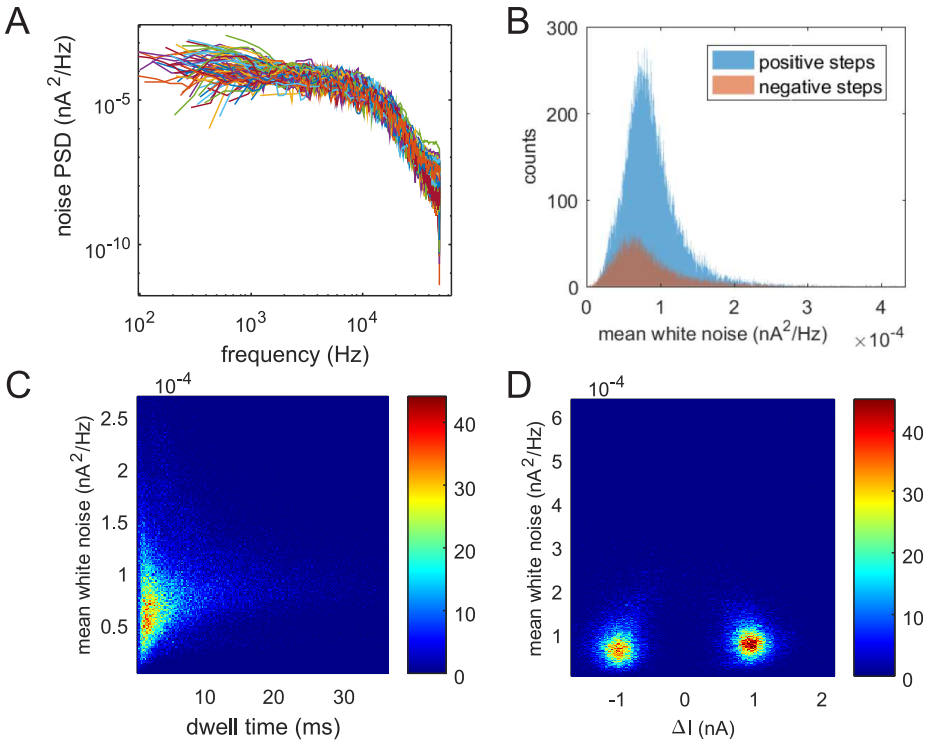


Figure 4.12: Local white noise analysis: A) A couple of noise spectra calculated for individual ΔI steps. B) Distribution of the average noise values for these current steps. C) 2D histogram of noise PSD values and relevant step dwell time τ. D) 2D histogram of ΔI values and relevant noise PSD.

Finally, I look at the statistical properties of extracted white noise levels. First, I plot the distribution of their values for the positive and negative ΔI levels (Fig. 4.12B).

For each of the ΔI step polarities the mean white noise level distribution has a skewed log-normal distribution. I note that the apparent number of noise points (histogram area) is lower for the *down* state. This is because the *down* levels are on average shorter than *up* levels and the higher ratio of them is too short to calculate the noise spectrum. Fig. 4.12C shows the 2D histogram of the mean white noise levels plotted against the dwell time of a particular current step. There is a particular noise value around which a long tail of high dwell time values is centred and where the majority of the noise values are located. This value corresponds to the mean noise level, which can be estimated with better precision for longer levels, while levels with short dwell times are more likely to be disturbed by the erroneous level identification by CPD method, leading to a higher deviation in noise from its mean value.

The same argument holds for the histogram of the mean white noise levels as a function of the ΔI levels in Fig. 4.12D. There is a distribution with two concentric (on a chosen scale) regions centred at the mean ΔI level and the mean value of white noise. It proves that there is not any characteristic correlation between ΔI level and noise. In the histogram there are two diagonal lines starting at the main point clusters and extending in the direction of low ΔI values and high noise levels. This can be again explained by a higher uncertainty of the noise estimation for low ΔI values, which are more prone to the error in CPD method and therefore are characterized by the higher noise levels. Thus it can indicate that the white noise distribution as well as ΔI distribution have Gaussian profiles, and the long tail observed in Fig. 4.12A is only an artefact.

Importance Until now no clear TLF signal has been observed in pristine graphene devices, although some deviations from flicker noise spectrum were observed due to the molecule adsorption on carbon nanostructure-based devices[171] and TLF was recorded in graphene junctions functionalized with state-switching molecules[208]. In the case of large surface area graphene devices it is unlikely to observe the effect of a single charge trap (either due to an adsorbed molecule or a substrate). To the best of my knowledge I demonstrate for the first time the unambiguous TLF and RTN in a graphene device. I assume that it is due to a high local sensitivity of the tunnel junction to its electrostatic environment. In the case of CNTs it has been shown that charge traps closer than 3 nm to their surface are capable of inducing RTS.[171, 212] Only the closest of the charge traps have a dominant effect on the switching and noise behaviour.

Here I show that the TLF in the $I - t$ traces is also reflected in Lorentzian contribution to noise spectrum. The good agreement between τ and ΔI values obtained by the trace and noise analysis further supports the claim that the observed features are a real TLF. As expected ΔI values have Gaussian distribution, while τ values follow Poissonian statistics. The scaling behaviour of the current steps $\Delta I \sim I$ indicates that the fluctuations occur independently of the current flow.[145] Current is not the driving force but only a readout mechanism of the TLF present in the device at equilibrium. This scaling behaviour is also confirmed by the lack of dependence of τ values on the applied voltage.

Besides the Lorentzian noise component I observed also $1/f$ and high frequency white noise contributions. The origin of the former was identified as the slow fluctu-

ations in the baseline current $I_b(t)$ while the latter one is due to the fast fluctuations within the individual ΔI levels, as opposed to the expected Johnson-Nyquist thermal noise contribution, which turned out to be lower than the observed noise level by a few orders of magnitude. Both $1/f$ and white noise contributions scale with $\sim I^2$ as confirmed on the basis of noise fit and FWHM values of the relevant current distributions. This indicates that these noise contributions may have the same origin as TLF.

4.2 Correlations in TLF Signals

4.2.1 ΔI Point Clusters

After analysing the statistical properties of ΔI levels subsequently I will look at the correlations between consecutive current steps. In order to analyse the correlations between two consecutive switching events ΔI_n and ΔI_{n+1} I will focus on their difference $\Delta I_{n,n+1} = \Delta I_{n+1} - \Delta I_n$, which corresponds to the absolute height of a current step. In the analysis of pairs of transitions between three consecutive levels ($\Delta I_n \rightarrow \Delta I_{n+1} \rightarrow \Delta I_{n+2}$) there are two possible scenarios:

- *up* transition followed by *down* transition with a positive $\Delta I_{n,n+1}$ value and a negative $\Delta I_{n+1,n+2}$ value (Fig. 4.13A). This corresponds to the $(\Delta I_{n,n+1}, \Delta I_{n+1,n+2})$ point located in the fourth quadrant of a ΔI point cluster plot (Fig. 4.13C)

- *down* transition followed by *up* transition with a negative $\Delta I_{n,n+1}$ value and a positive $\Delta I_{n+1,n+2}$ value (Fig. 4.13B). This corresponds to the $(\Delta I_{n,n+1}, \Delta I_{n+1,n+2})$

point located in the second quadrant of a ΔI point cluster plot (Fig. 4.13D)

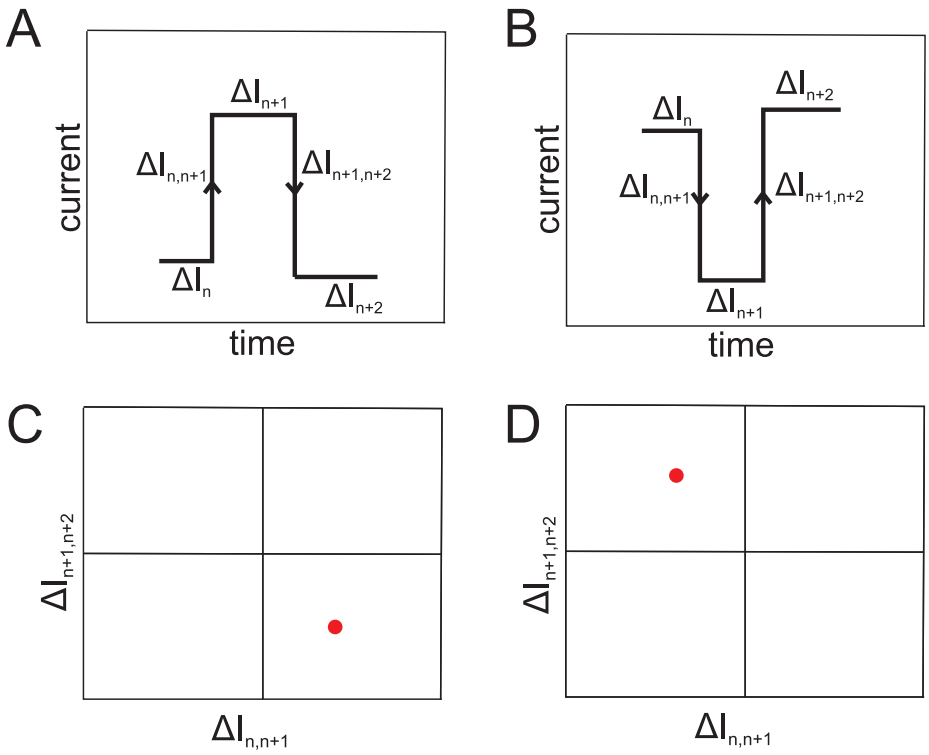


Figure 4.13: Diagram showing two possible pairs of transitions in TLF A) *up* transition ($\Delta I_n \rightarrow \Delta I_{n+1}$) followed by *down* transition ($\Delta I_{n+1} \rightarrow \Delta I_{n+2}$) and B) *down* transition ($\Delta I_n \rightarrow \Delta I_{n+1}$) followed by *up* transition ($\Delta I_{n+1} \rightarrow \Delta I_{n+2}$). C) and D) Location of the $(\Delta I_{n,n+1}, \Delta I_{n+1,n+2})$ in the point cluster point for transition sequences plotted in Fig. A and B respectively.

These plots, called also time-lag diagrams[137], are a common method of analysing correlations in TLF signals. This method was applied to analyse correlations in conductance of metallic break junctions[213, 214], or switching in organic memory devices[159]. Recently it was also applied to analyse the memory effects in switching of molecules such as cysteine in MCBJ between metastable positions, which led to TLF.[74] In Fig. 4.14 I present an example of a correlation plot which I obtained

for one of the $I - t$ traces in a GTJ. As expected, there are two main point clusters located in the second and fourth quadrant. There are no additional clusters which could indicate specific correlations in the consecutive current levels. There is however an interesting asymmetry in the shape of the point clusters. The top cluster (in the second quadrant) has elongated shape, while the bottom quadrant (in the fourth quadrant) is more circular. I postulate that this asymmetry originates from the electrostatic repulsion between the charge carriers occupying charge traps, which I will discuss further in the next section.

In Appendix D and E I also use the ΔI point cluster plots as a tool to validate the accuracy of the previously performed CPD in the $I - t$ traces. The separation of the plot in the separate zones described in Fig. 4.14 allows distinguishing between genuine transition pairs and the analysis artefacts.

4.2.2 $(\Delta I_1, \Delta I_2)$ Point Cluster Asymmetry

I will now analyse the asymmetry of point clusters in ΔI point cluster plots (Fig. 4.15A). There is an asymmetry in the distribution of pairs of points corresponding to negative step followed by a positive one $(-\Delta I, \Delta I)$ − second quadrant. The distribution of these points is elongated along the diagonal axis (Fig. 4.15B, C), while the distribution in the direction perpendicular to the diagonal axis (off-diagonal distribution) appears to be narrower. This is in contrast to the second cluster of points corresponding to a step *up* followed by a step *down* $(\Delta I, -\Delta I)$ − fourth quadrant, which seems to be more circular (Fig. 4.15D).

To quantify this asymmetry I extract the two data clusters and rotate them by

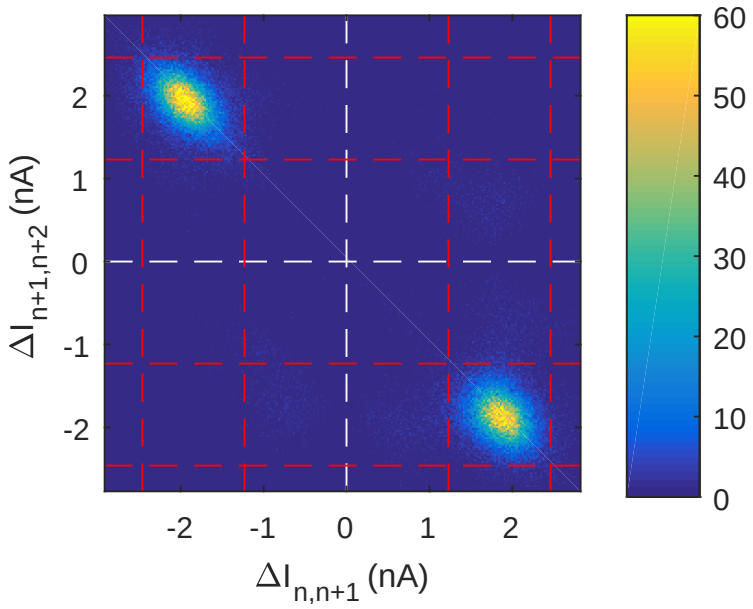


Figure 4.14: Example of ΔI point cluster plot obtained for a GTJ measured at 77 K at 180 mV bias. Dashed red lines indicate the reference levels separating the point cluster into zones. The lines are equally spaced in both directions $x = n*\Delta I_{max},\ y = m*\Delta I_{max},\ n, m = 1,\ 2$, with ΔI_{max} adjusted to contain majority of points belonging to both point clusters within two zones.

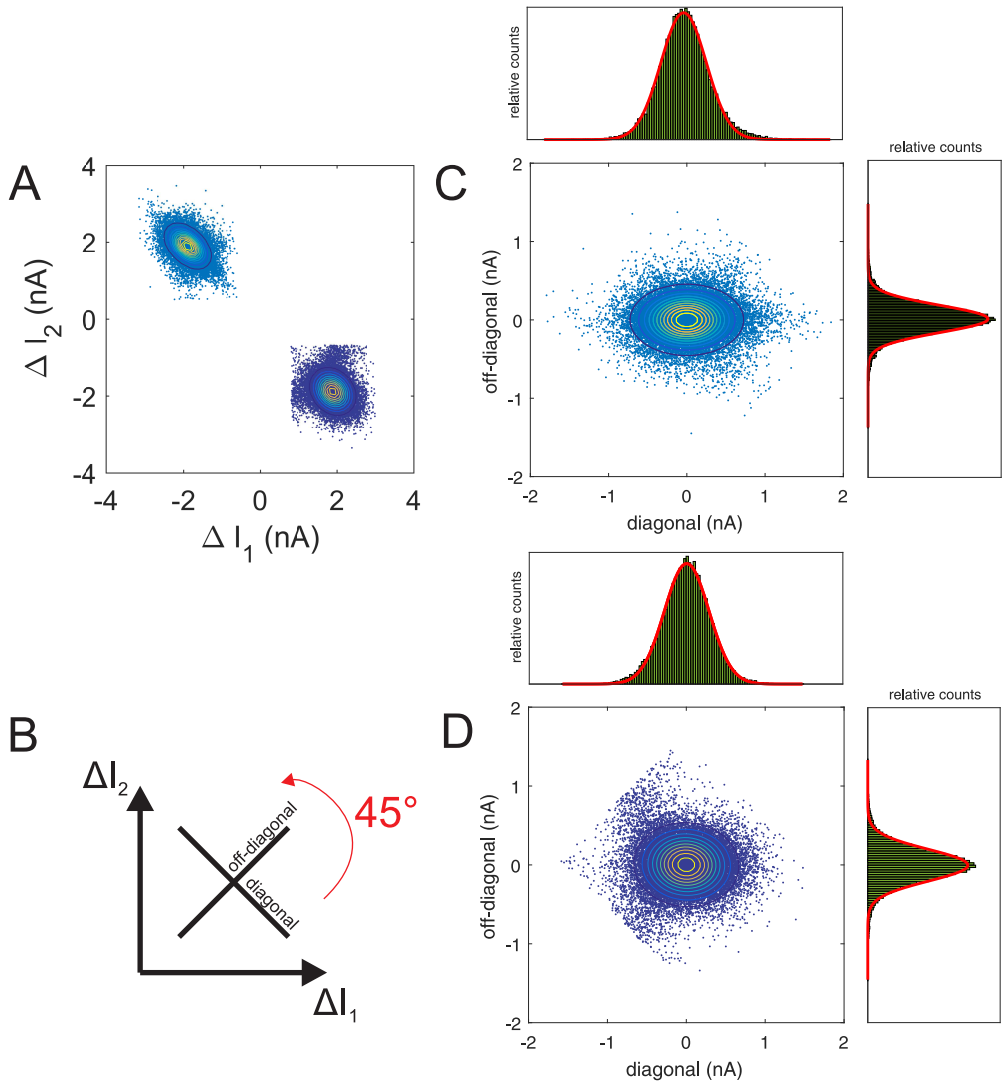


Figure 4.15: A) distribution of $(\Delta I_1, \Delta I_2)$ points showing clustering into two main groups of points highlighted in different colours. B) Labelling of axis and schematic of data rotation direction used for the asymmetry analysis. Rotated point clusters and distributions of data projected on the diagonal and off-diagonal axes fitted with Gaussian functions for C) top $(-\Delta I, \Delta I)$ and D) bottom $(\Delta I, -\Delta I)$ point clusters respectively.

45°, so that the diagonal axis is now aligned with the new x axis of the new coordinate system and the new off-diagonal axis is aligned with the y axis (Fig. 4.15B, C and D). Further I calculate the projection of data on x and y axis obtaining two histograms with a Gaussian distribution for each of the data clusters. Subsequently I fit these distributions with Gaussian peaks obtaining the mean value $\mu \approx 0$ and the width of the distribution σ.

The asymmetry factor of the data clusters is calculated as a ratio of the Gaussian distribution width of the diagonal and off-diagonal elements $\alpha = \frac{\sigma_{diag}}{\sigma_{off-diag}}$. As shown in Fig. 4.16A the bottom data cluster (located in the fourth quadrant) has asymmetry factor equal to ~ 0.75, consistent across all the measured voltages. In contrast the asymmetry factor for the top data cluster (in the second quadrant) has a lower asymmetry factor value of ~ 0.55, consistent across all the measured voltage values. This indicates that the bottom cluster is more symmetric, and closer to circular distribution compared to the top cluster.

As an alternative method I fit the rotated data clusters with a multivariate Gaussian distribution of the form

$$f_{\mu,\Sigma}(\boldsymbol{X}) = \frac{1}{(2\pi)^{\frac{1}{2}}|\boldsymbol{\Sigma}|^{\frac{1}{2}}} \exp\left(-\frac{1}{2}(\boldsymbol{X}-\boldsymbol{\mu})^T\boldsymbol{\Sigma}^{-1}(\boldsymbol{X}-\boldsymbol{\mu})\right), \tag{4.4}$$

where $\boldsymbol{X}$ is a random vector of size two in the case of bivariate distribution, $\boldsymbol{\mu}$ is a vector of expected values and $\boldsymbol{\Sigma}$ is a covariance matrix, which diagonal elements correspond to the variance of each of the expected values and off-diagonal elements correspond to the covariance between different elements of $\boldsymbol{\mu}$ vector.

The rotated data clusters and the contour of the fitted bivariate Gaussian dis-

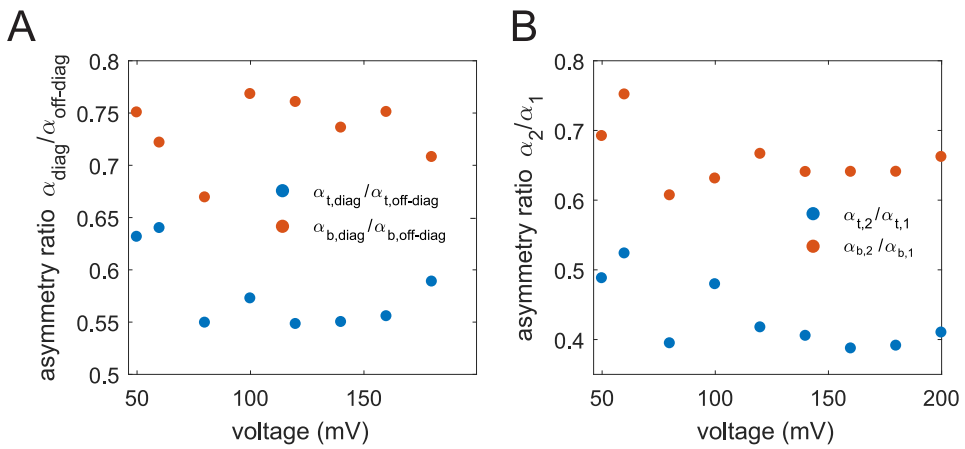


Figure 4.16: Asymmetry factor of the point distribution for *up* and *down* point clusters obtained as a ratio of the widths of the point clusters rotated by 45° by A) 1D Gaussian fit and B) 2D bivariate Gaussian fit.

tribution is plotted in Fig. 4.17A, B. As the result of the fitting procedure for each of point clusters I obtain two variance values σ_{11} and σ_{22}, which are the diagonal elements of the covariance matrix

$$\mathbf{\Sigma} = \begin{bmatrix} \sigma_{11}\sigma_{12} \\ \sigma_{21}\sigma_{22} \end{bmatrix}. \tag{4.5}$$

The asymmetry factor in the case of a bivariate Gaussian fit of data is defined as $\alpha = \frac{\sigma_{22}}{\sigma_{11}}$. The values of the fitted asymmetry factor in the function of voltage are plotted in Fig. 4.16B. Comparing these values to the asymmetry factor values obtained by a 1D Gaussian fit of data projections it is clear that both of them have exactly the same trend and show the higher (lower) asymmetry factor for the top (bottom) data cluster. Also the off-diagonal elements of the covariance matrix $\mathbf{\Sigma}$ denoting the covariance between two peak variables have low values on the order of 10^{-3}, indicating no cross-correlation between data points distributed along x and y axis after the rotation.

Finally, I plot the original non-rotated top and bottom point clusters with overlaid contours of the bivariate Gaussian peaks (Fig. 4.17A, B)

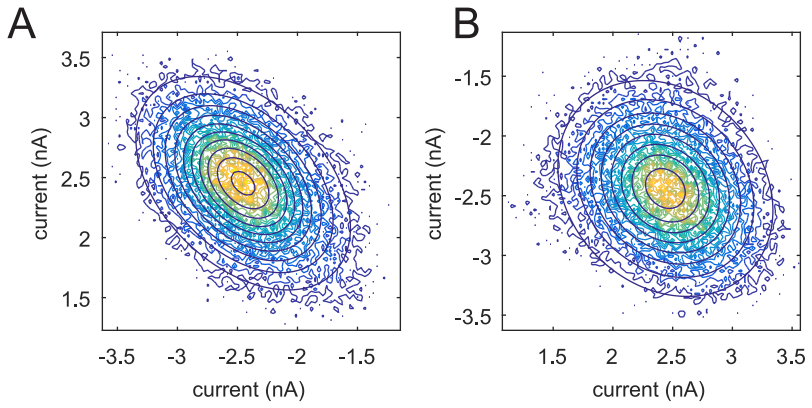


Figure 4.17: Contour plot of non-rotated matrices with overlaid contour of fitted bivariate Gaussian peak for A) top and B) bottom point cluster.

In order to understand the origin of the asymmetry observed in Fig. 4.18A I simulate the $(\Delta I_1, \Delta I_2)$ point distribution and reproduce the asymmetry of both clusters. It is achieved by assuming a slightly wider distribution of current values for *down* transition compared to *up* (Fig. 4.18B). The probability of finding each of the $(\Delta I_1, \Delta I_2)$ points in the bottom cluster is given as a product of three Gaussian distributions:

$$P(I_0, \Delta I_1, \Delta I_2) = P_1(I_0)P_2(I_0 + \Delta I_1)P_1(I_0 + \Delta I_1 - \Delta I_2) = \frac{1}{\sqrt{2\pi}^3 \sigma_1 \sigma_2^2} \times$$
$$exp\left(-\frac{1}{2}\left[\left(\frac{I_0 - \mu_2}{\sigma_2}\right)^2 + \left(\frac{I_0 + \Delta I_1 - \mu_1}{\sigma_1}\right)^2 + \left(\frac{I_0 + \Delta I_1 - \Delta I_2 - \mu_2}{\sigma_2}\right)^2\right]\right), \quad (4.6)$$

where I_0 is the initial current value for a particular switching sequence and it can take values in the $(-\infty, +\infty)$ range, μ_1, μ_2 and σ_1, σ_2 are mean values and standard deviations for *up* and *down* current Gaussian distributions respectively. An analogous equation may be found for the top cluster $P(I_0, \Delta I_1, \Delta I_2) = P_2(I_0)P_1(I_0 + \Delta I_1)P_2(I_0 + \Delta I_1 - \Delta I_2)$. After summing all the contributions in the entire range of I_0 I obtain the final distribution of the $P(\Delta I_1, \Delta I_2)$, which is plotted in Fig. 4.18A.

This analysis reproduces well the features of the experimental data and shows that a slight difference in the width of a current distribution for *up* and *down* levels can explain the observed asymmetry. As it was discussed by Rogers *et al.* a single charge trap located in a tunnelling barrier in oxide-based tunnel junctions can give rise to TLF.[156] The repulsion between multiple closely located and energetically equivalent traps allows only one of them to be occupied at a given moment.[156] A charge carrier having freedom to move between these charge traps introduces slight

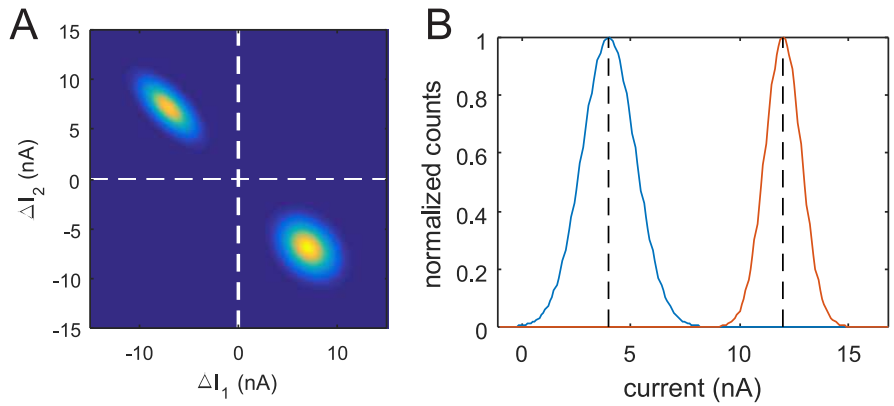


Figure 4.18: A) Simulated distribution of $(\Delta I_1, \Delta I_2)$ points showing the asymmetry between point clusters. B) Two current Gaussian distributions differing in the distribution width, used to simulate ΔI point clusters.

changes in the tunnelling barrier, resulting in the electronic noise, however without significantly changing the tunnelling probability and therefore not introducing the TLF signal.[156]

I postulate that this explanation can be also applied to the GTJs. The difference in current distributions can be obtained for example if *up* level corresponds to the empty charge trap. If there are more than one charge trap at the similar distance from the junction, trapping an electron by one of them would lead to a decrease in the current and the observation of the *down* level. Also an electron moving between these two equivalent traps would lead to slight changes in the current giving rise to a wider Gaussian distribution. So the observed asymmetry of ΔI point clusters is a result of a Coulomb repulsion between charge carriers occupying traps in the vicinity of the junction.

This interpretation is supported by the fact that slightly wider distributions of ΔI peaks for *up* levels are found in the ΔI values obtained by CPD method. The

ratio of distribution widths for *up* and *down* levels is ~ 1.1 for voltages higher than 120 mV. While I see the opposite trend for lower voltages I assume that in this region the distributions are widened by the erroneous detection of the current levels, which is more likely at lower voltages.

4.3 Origin of TLF in Graphene Tunnel Junctions

4.3.1 Temperature Dependence of RTN

Having discussed the RTS dynamics in GTJs I subsequently proceed to the identification of the switching mechanism. In order to identify this mechanism I analysed the temperature dependence of TLF in the $4.2 - 77$ K range. I performed the measurements at temperatures equally spaced on a logarithmic scale. For the entire temperature range I observed a typical behaviour characterised by TLF and Lorentzian noise spectrum. The aim of these experiments was to identify the role of thermal excitations in TLF.

The recorded $I-t$ traces were analysed using the protocol described previously in section 4.1, including calculation of noise spectrum and its fit with three-component model, namely white noise, $1/f$ and Lorentzian noise contributions. As can be seen in Fig. 4.19 in the low temperature regime the fitted values describing these three noise components show little dependence on temperature. The $1/f$ noise slope and amplitude and also the white noise level are constant within the errorbars over the inspected temperature range. The slight fluctuations in the value of mean current and FWHM of the baseline current are also within the error bars (Fig. 4.19D, E). In

the low temperature range the current, white noise and flicker noise parameters do not show clear dependence on temperature.

In Fig. 4.20A, B I plot the values of ΔI and τ as a function of temperature. There is good agreement between values obtained by the trace analysis and the Lorentzian noise spectrum fit. ΔI values seem to be constant over the investigated temperature range. On the contrary τ values change in a consistent way, decreasing by $\sim 0.5\,\mathrm{ms}$ with the increase in temperature, which is a very small change compared to the high range of the investigated temperatures. The values of both τ_{up} and τ_{down} dwell times change in the same direction (Fig. 4.20B). At temperatures above 10 K the observed dependencies on temperature were not as clear as at lower temperatures, with much more scatter in the data points. I believe that this behaviour was caused by the onset of additional charge traps with higher activation energies, although TLF was observed up to 77 K temperature.

Estimation of Activation Energy Assuming a thermally activated switching process the mean dwell time of *up* and *down* level can be expressed as[31, 204]

$$\begin{aligned} \tau_{up} &= \frac{1}{\nu_0} \exp\left(\frac{E_{up}}{kT}\right) \\ \tau_{down} &= \frac{1}{\nu_0} \exp\left(\frac{E_{down}}{kT}\right), \end{aligned} \tag{4.7}$$

where ν_0 is an attempt frequency equal to average phonon frequency and E_{down}, E_{up} are the energy barriers for *down* and *up* states respectively.[31, 204] Such exponential dependence means that even a slight variation in the energy barrier leads to the changes in the switching frequency over many orders of magnitude. Using this type

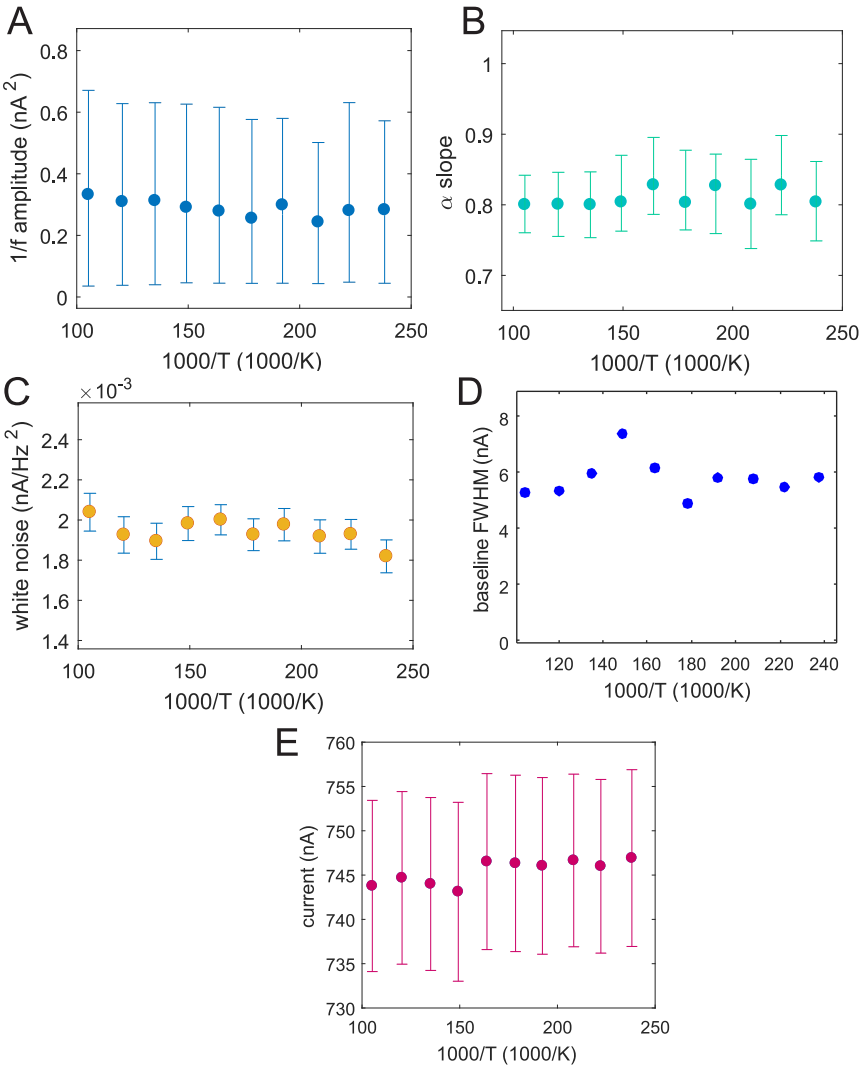


Figure 4.19: Results of the noise fit with three components A) and B) fitted $1/f$ noise amplitude and slope, respectively, as a function of temperature. C) Fitted white noise level in the function of temperature. D) Current baseline FWHM values as a function of temperature. E) Mean current value as a function of temperature.

of Arrhenius formula I obtain very low activation energy values, $E_A = 0.14\,\mathrm{meV}$ on the basis of Lorentzian fit and $E_A = 0.16\,\mathrm{meV}$ on the basis of $I - t$ trace analysis (Fig. 4.20C). Also the fitted prefactors in the equation 4.7, which correspond to high temperature limit of the attempt time, are low, on the order of $0.6 - 0.7\,\mathrm{ms}$. Similar values were obtained for the fits of separate τ_{up} and τ_{down} contributions. The values of the activation energy are very low considering that the typically found energy barriers for TLF due to the atom switching in metal atomic contacts are on the order of $0.1 - 10\,\mathrm{eV}$.[205] The monotonous increase of the time constants τ_{up} and τ_{down} was for example also found in TLF caused by the charge state fluctuations of the molecules adsorbed on CNTs.[171] Although the extracted activation energy in this case was higher ($0.376\,\mathrm{eV}$) than in the presented measurements.

Assuming that the attempt frequency is the same for both states the expression for the energy difference may be also obtained in the form[31]

$$\Delta E = E_{up} - E_{down} = kT \ln\left(\frac{\tau_{up}}{\tau_{down}}\right). \tag{4.8}$$

Using this equation I obtain the energy difference values on the order of $6\,\mathrm{meV}$ (Fig. 4.21)

These two results $E_A \approx 0.14\,\mathrm{meV}$ for both *up* and *down* states, and $\Delta E \approx 6\,\mathrm{meV}$ energy difference between them are inconsistent. Therefore I assume that the unphysical values of activation energies obtained from the temperature dependence are not correct and the process in not thermally activated. It suggests a tunnelling process as the origin of switching in this particular device. There are reports of the transition from the temperature-independent tunnelling process at low temperatures

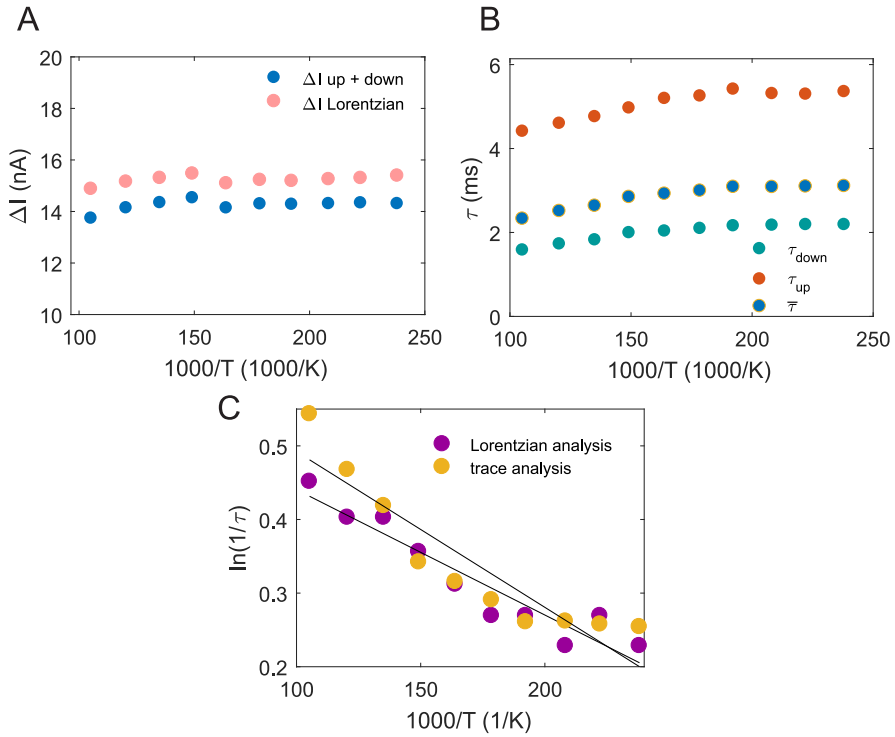


Figure 4.20: Temperature dependence of TLF: A) ΔI values extracted from Lorentzian fit and from trace analysis as a sum of mean *up* and *down* current levels. B) Temperature dependence of mean τ and separated mean dwell times for *up* and *down* levels obtained on the basis of $I-t$ trace analysis. C) Fit of τ values obtained on the basis of $I-t$ and Lorentzian noise analysis used to extract the activation energy as a slope of the data points (black lines).

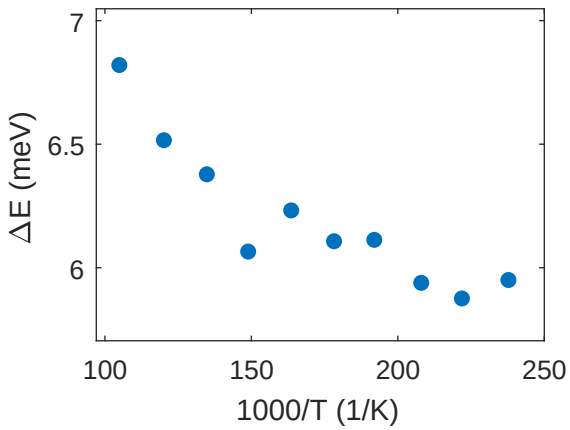


Figure 4.21: Energy difference between *up* and *down* states.

to the temperature driven TLF at higher temperatures observed for example in the switching of a metal atom at the STM tip.[31] Arrhenius plots showing no temperature effect on the mean TLF dwell time were also found in Au−pentacene−Au junctions[207], although the reason for that was not discussed. Before further discussing of the proposed physical mechanisms of fluctuations, I will look at the scaling of asymmetry factors with temperature.

Temperature Dependence of $(\Delta I_{n,n+1}, \Delta I_{n+1,n+2})$ Point Cluster Asymmetry

The ΔI point cluster analysis has been performed in order to obtain the distribution of the point clusters as a function of temperature. In Fig. 4.22 I present a typical 2D histogram of $(\Delta I_{n,n+1}, \Delta I_{n+1,n+2})$ transitions with two asymmetric point clusters, varying in the asymmetry degree (top one more and bottom one less asymmetric). As previously, the asymmetry level was analysed by means of the bivariate Gaussian distribution and 1D Gaussian fits of data points rotated by 45° and projected on the x and y axes.

Both of the methods of analysis yield similar results, showing that there is a constant, temperature-independent higher asymmetry (lower asymmetry ratio ≈ 0.5) for the top cluster and lower asymmetry (higher asymmetry ratio ≈ 0.8) for the bottom point cluster (Fig. 4.23C and D, respectively). This observation is in agreement with the previous measurements in the function of voltage, where the asymmetry ratio was constant regardless of the bias.

It is however interesting to plot the widths of the point cluster distributions rather than their ratios, in the function of temperature (Fig. 4.23A and B). A temperature increase causes a monotonous increase in the width of the distribution in both directions, diagonal and off-diagonal. But from the asymmetry ratios it is known that the rate of this increase is equal for both axes of each of the point clusters. With the increasing temperature there is an increasing random contribution which is added to the value of ΔI step, which does not depend on the polarity of the switch.

As I discuss in Appendix D, the increased level of white noise leads to the widening of the distribution of the ΔI point clusters, which I observe with increasing temperature. This can explain the observed trend of widening of the distribution with the increasing temperature; however as it can be seen in Fig. 4.19A and C there is no significant increase in the fitted white noise level with the temperature. Assuming that there is a slight increase in $1/f$ noise amplitude in Fig. 4.19A and that $S \sim I^2$, the change of $1/f$ noise amplitude on the order of $0.1\,\mathrm{nA}^2$ is not sufficient to explain the change in the width of the distribution on the order of 1 nA over the same temperature range. Therefore I speculate that because of the lower bandwidth of the measurement system in this measurement (7 kHz), the high frequency white

noise plateau may not be fully resolved between the Lorentzian $1/f$ arm and the filter roll-off; therefore the white noise fitted values are underestimated and in reality this high frequency noise can be increasing with the temperature increasing the current distribution width.

The lack of influence of temperature on the analysed features of noise spectra and the fact that obtained thermal activation energies are unphysically low (sub-meV range) indicate that the mechanism responsible for TLF and the Lorentzian noise peak is tunnelling. I speculate, however, that at the temperatures above the measurement range (77 K), in analogy to other reports, such tunnelling process may be dominated by a temperature dependent mechanism.[31]. The presence of a thermally activated background processes, although not directly observed in the noise spectra, may be indirectly deduced from the widening of the ΔI point cluster distributions. In the next section I will discuss the different scenarios of the tunnelling process which could lead to TLF.

4.3.2 Discussion of Possible Fluctuation Mechanisms

Tunnelling Following the idea presented in ref. [31] I will describe the tunnelling process in terms of a Wentzel-Kramers-Brillouin (WKB) approximation, which provides the expression for a switching rate in the following form[31]:

$$\nu = \nu_0 \exp\left(-\frac{d(2mE_B)^{1/2}}{\hbar}\right), \tag{4.9}$$

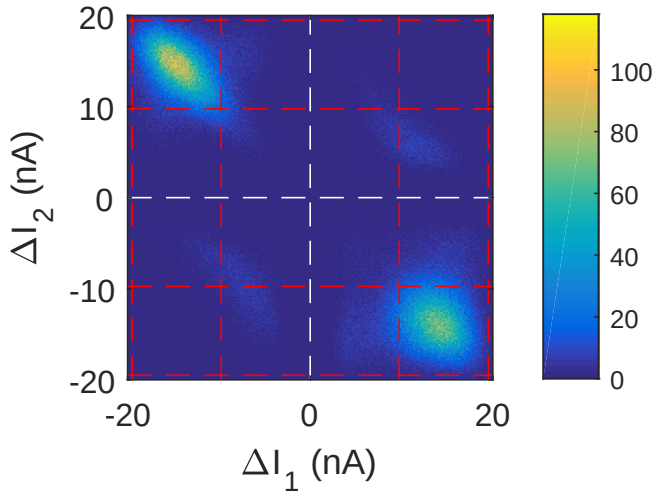


Figure 4.22: $(\Delta I_1, \Delta I_2)$ point histogram for TLF measured in graphene tunnel junction at 4.2 K.

where d is a tunnelling distance, ν_0 is the attempt frequency usually assumed to be equal to the average phonon frequency taken as 10^{12} Hz and m is mass of the tunnelling entity. This formula can be rewritten in order to obtain the expression for the tunnelling barrier height:

$$E_B = \frac{1}{2m}\left(\frac{\hbar \ln \nu_0 \tau}{d}\right)^2 \tag{4.10}$$

I used here $\nu = 1/\tau$ identity relating the switching rate and the mean dwell time, which is the value known from the noise and $I - t$ trace analysis.

Now I will consider two scenarios, namely tunnelling of

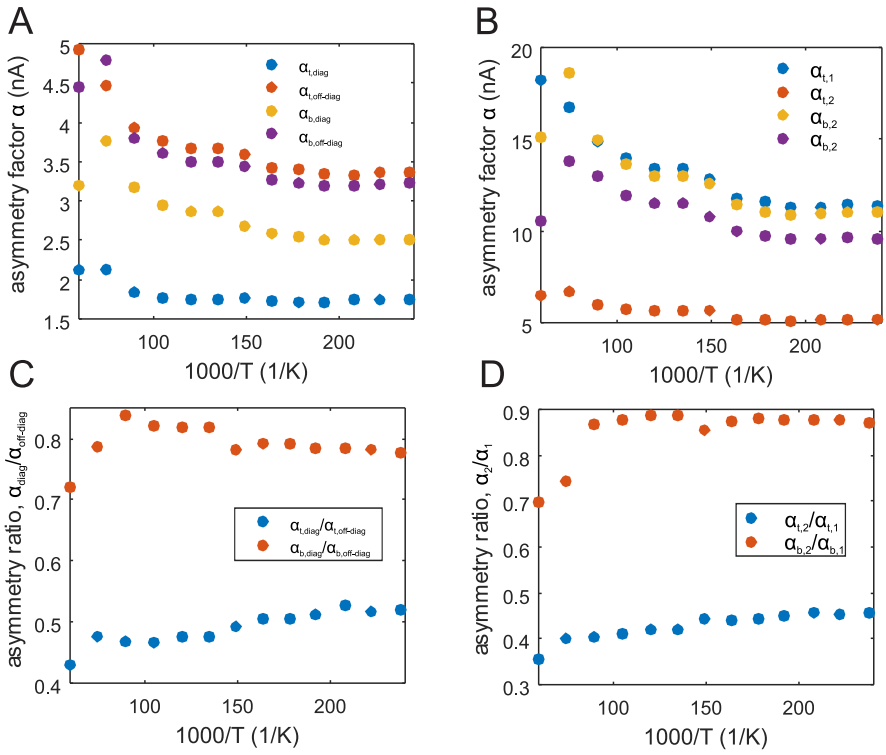


Figure 4.23: Analysis of asymmetry of $(\Delta I_1, \Delta I_2)$ point clusters as a function of temperature. A) Asymmetry factors calculated as the the width of 1D Gaussian fit of the diagonal and off-diagonal elements of both, top and bottom point clusters. B) Asymmetry factors obtained on the basis of bivariate Gaussian fit of both, top and bottom point clusters. C) Asymmetry ratio for *up* and *down* $(\Delta I_1, \Delta I_2)$ point clusters calculated as ratio of 1D Gaussian asymmetry factors. D) Asymmetry ratio for *up* and *down* $(\Delta I_1, \Delta I_2)$ point clusters calculated as ratio of bivariate Gaussian asymmetry factors. Higher values mean more symmetric point cluster.

1. Electron

2. Charged carbon atom

In the first case the electron mass is equal to $m_e \approx 9.11 \times 10^{-31}\,\mathrm{kg}$. In order to estimate the tunnelling barrier it is assumed that the tunnelling distance is equal to the spacing between charge traps in SiO_2, which is proportional to the concentration of charge traps n, $d \approx n^{1/3}$. Taking a typical value $n = 10^{18}\,1/\mathrm{cm}^3$ [215] (or equivalent surface density $n_S = 10^{12}\,1/\mathrm{cm}^2$ [131]) I obtain $d = 10\,\mathrm{nm}$. Calculating the energy barrier value for such process using the equation 4.10 I obtain $E_B = 0.426\,\mathrm{eV}$, which is a reasonable value for charge traps in SiO_2.[138, 216]

The second proposed mechanism is the tunnelling of a charged carbon atom with mass $m_C \approx 1.99 \times 10^{-26}\,\mathrm{kg}$. I assume that the tunnelling distance is equal to the length of a $C-C$ bond in graphene, $d = 0.142\,\mathrm{nm}$.[217] Resulting energy barrier is equal to $E_B = 0.11\,\mathrm{eV}$. This value is low compared to the energy of a single $C-C$ bond $E = 4.9\,\mathrm{eV}$[218, 219]. However, it is known from the investigation of adsorption of adatoms[220, 221] and molecules[222–224] on a graphene surface, that the potential barrier for their sliding motion is low. For example the energy barrier for sliding of carbon adatom on the graphene surface $E = 0.25 - 0.61\,\mathrm{eV}$[225, 226], other atoms adsorbed on the graphene surface have similar barriers for sliding. This energy is similar to the energy values obtained in my calculation, indicating that switching of a charged atom or molecule between two metastable positions can lead to the observed dynamics.

Electrostatic considerations Having checked that tunnelling dynamics of a carbon atom or electron can lead to the observed frequency of the fluctuations I look at their influence on the tunnelling current. For this purpose I will treat the fluctuating moiety as a point charge of value e which generates the distance-dependent spherical potential

$$V = \frac{1}{4\pi\epsilon\epsilon_0}\frac{e}{r}, \tag{4.11}$$

where ϵ_0 is vacuum permittivity and I take $\epsilon = 3.9$ for SiO_2 relative permittivity, d is the distance from the point charge. The external source-drain voltage applied to the device in the equilibrium situation has value V_B. Now I assume that placing the point charge in the distance R from one of the graphene electrodes shifts the applied voltage to

$$V_{B1} = V_B + \frac{1}{4\pi\epsilon\epsilon_0}\frac{e}{R}$$

I assume that the potential of only one of the electrodes is affected by the introduction of the point charge. Subsequently the charge changes its distance from the electrode by dR, what leads to the new bias value

$$V_{B2} = V_B + \frac{1}{4\pi\epsilon\epsilon_0}\frac{e}{R+dR}$$

The presence of the point charge will effectively shift the applied bias.

These voltage values are used as a crude estimation of the envisaged gating of transport through the graphene junction by a point charge. I assume here the simple

exponential tunnelling current model of the form[15]

$$I = I_0 \sinh\left(\frac{V}{\beta}\right) \tag{4.12}$$

Two different positions of the point charge lead to different IV curves. I consider two previously discussed situations, assuming that dR distance is equal to the tunnelling distance of 1) electron between two charge traps and 2) charged carbon atom sliding between two lattice positions on the graphene surface (Fig. 4.24C). It is known what are the possible distance shifts dR in the point charge position, and the ratio of observed current fluctuations to mean tunnelling current in the investigated voltage range is roughly $\frac{\Delta I}{I} = 0.1$. I checked which distances R of the point charge from the graphene electrode can lead to such $\frac{\Delta I}{I}$ values.

In the case of a charge trap in SiO the distance $R = 10\,\mathrm{nm}$ gives reasonable ΔI values (Fig. 4.24A). I plot there the original symmetric IV curve simulated for V_B voltage and two tunnelling IV curves for voltage shifted due to different positions of a charge trap. Curves affected by the point charge potential are asymmetric, as voltage is shifted in the positive direction, assuming the switching of a positive charge. Symmetric IV curves may be also obtained (Fig. 4.24B) assuming that the sign of the trapped charge is defined by the sign of applied bias. This is a reasonable assumption as charge traps in the oxide layer need external source of charge carriers to change their occupancy, because there are no free charge carriers in the oxide. In this scenario the filling or emptying of the trap is realised by the tunnelling of a charge carrier from the conductor.[140] This scenario is also supported by the reasonable values of R and $\Delta R = 10\,\mathrm{nm}$, which are equal to the assumed spacing between charge

traps.[215] In the end of the next section I will compare the experimental results of the IV curve asymmetry between positive and negative voltages with the simulated curves discussed here.

In the second scenario − tunnelling of a charged carbon atom, the distance between two metastable atom positions $\Delta R = 0.142\,\mathrm{nm}$ is small. In order to obtain a sizeable voltage shift such atom would have to be close to the junction, because the spherical potential value decays as $\frac{1}{R}$ and large differences are observed only near the centre of the field. Expected $\frac{\Delta I}{I}$ ratios can be obtained for $R \approx 2\,\mathrm{nm}$, however such location of the charge would lead to unrealistically high current values $\sim 1\,\mu\mathrm{A}$. Larger distances $R \approx 10\,\mathrm{nm}$ would lead to the current values in expected nA-range, however at such distances the change in potential between R and $R + dR$ positions is not sufficient to induce detectable ΔI values. Therefore I conclude that electron tunnelling between two charge traps is a more probable explanation of the observed TLF.

Graphene Edge Besides effects related to the electrostatic influence of electric charge, following the ref. [210], I consider the change of the tunnelling gap width due to the switching of a carbon atom at the tip of the junction as a reason of observed TLF. I will analyse a simple distance-dependent model of tunnelling conductance of the form $G = G_0 \exp(-\beta d)$, where $\beta = 10\,\mathrm{nm}^{-1}$ is the tunnelling decay constant of vacuum, d is the tunnelling distance and $G_0 = \frac{2e^2}{h}$ is a quantum of conductance.[73] The change in the conductance of the junction can be defined as $\Delta G = G_1 - G_2 = G_1 \exp(-\beta \Delta d)$, where G_1 is the equilibrium high conductance level and G_2 is the shifted conductance after moving of the atom at the tip of the junction by the

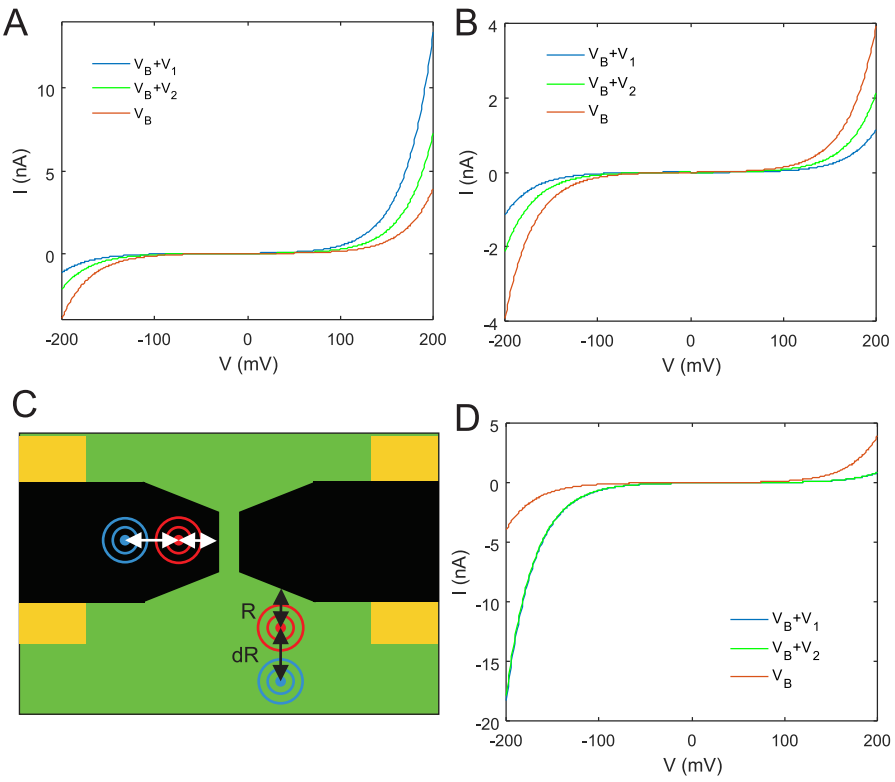


Figure 4.24: Simulated IV curves showing a symmetric IV curve due to applied bias V_B and curves modified by the presence of charge in the distance R (V_1) and $R + dR$ (V_2) from the junction for the case of A) positive charge $+e$ with distance $R = dR = 10\,\text{nm}$. B) Symmetric IV curves assuming that sign of the trapped charge depends on the applied bias $sgn(e) = sgn(V_B)$. C) Diagram of a GTJ with an adsorbed carbon adatom and a point charge switching between two charge traps giving rise to TLF. D) Tunnelling IV for the scenario of a carbon atom in the distance $R = 10\,\text{nm}$ and $dR = 0.142\,\text{nm}$ leading to asymmetric profile of IV and small ΔI values.

distance Δd.[210] Taking values $G_1 = 10^{-3}G_0$ and $\Delta G = 10^{-4}G_0$ typically observed in the junctions leads to $\Delta d \approx 0.01\,\mathrm{nm}$, which is low compared to the C−C bond length in graphene (0.142 nm). Two level switching in graphene junctions was also attributed to the formation of carbon atomic chains bridging the gap[227] In the case of formation of such chains the change in conductance is even higher, each chain increases it by G_0.[227] I conclude that the TLF origin due to the formation of carbon chains or carbon atom switching at the tip of the junction is unlikely.

4.3.3 Multiple Fluctuators

In the case of a typical TLF a change in the state of the fluctuator causes switching between two conductance levels. A larger number of fluctuators may lead to a higher number of observed current levels (4 levels for two independent traps). This model is only valid if fluctuators do not interact, *i.e.* it assumes large spacing between independent fluctuators. However, if the distance between them is sufficiently small there might be correlations between the state of the fluctuators. The mechanism of the interaction may be, for instance, by electrostatic interactions. Correlated charge traps will lead to more than two current levels, for example three current levels may be observed if one of the charge traps controls the occupation of the other one.[138] Correlations between traps were reported in CNTs[228] and silicon devices[137].

Two Fluctuators with Similar Dwell Times In GTJ measurements I also observed fluctuations with a higher number of levels, although such observations were quite rare ($< 10\,\%$). In Fig. 4.25 I plot the $I - t$ traces and current histograms

for one such device. For each of the bias polarities there are two main fluctuation levels with relatively low ΔI values, and long dwell times on the order of $\sim 0.1\,\mathrm{s}$. In addition to that there are also levels characterised by larger ΔI values and shorter dwell times. The current histogram in Fig. 4.25C shows that for each trace there are 4 current levels that can be attributed to 2 fluctuators governing transport through the device.

An interesting feature of these current peaks is the asymmetry in their distribution when opposite bias polarities are compared. As can be seen in Fig. 4.25C, for the negative bias the low conductance peaks at $\sim 1\,\mathrm{nA}$ are much more frequent than the two peaks at $\sim 2.5\,\mathrm{nA}$. For the positive bias the absolute values of the current peaks are similar, although the ratio of counts of two low and two high conductance peaks is opposite. Here peaks at $\sim 3\,\mathrm{nA}$ are more frequent, however, the difference in population of various states is not as clear as for the negative voltages.

Such difference between currents for the positive and negative voltages is observed over the entire voltage range of the measurement. I measured 1 min traces at voltages in the range of -400 to $400\,\mathrm{mV}$ with $5\,\mathrm{mV}$ increments and subsequently constructed current distribution histograms for each of the traces (Fig. 4.26A). It can be clearly seen that for the entire range of positive voltages two high levels are more frequent, while for the negative voltages two peaks with lower conductance values are more prevalent. This is further confirmed in Fig. 4.26B where I plot the mean IV curve which is highly asymmetric (red curve). It is however possible to recover two symmetric tunnelling IV curves. This is achieved by finding the 5th and 95th percentile value of the current distribution for each of the voltage values. Then I merge the

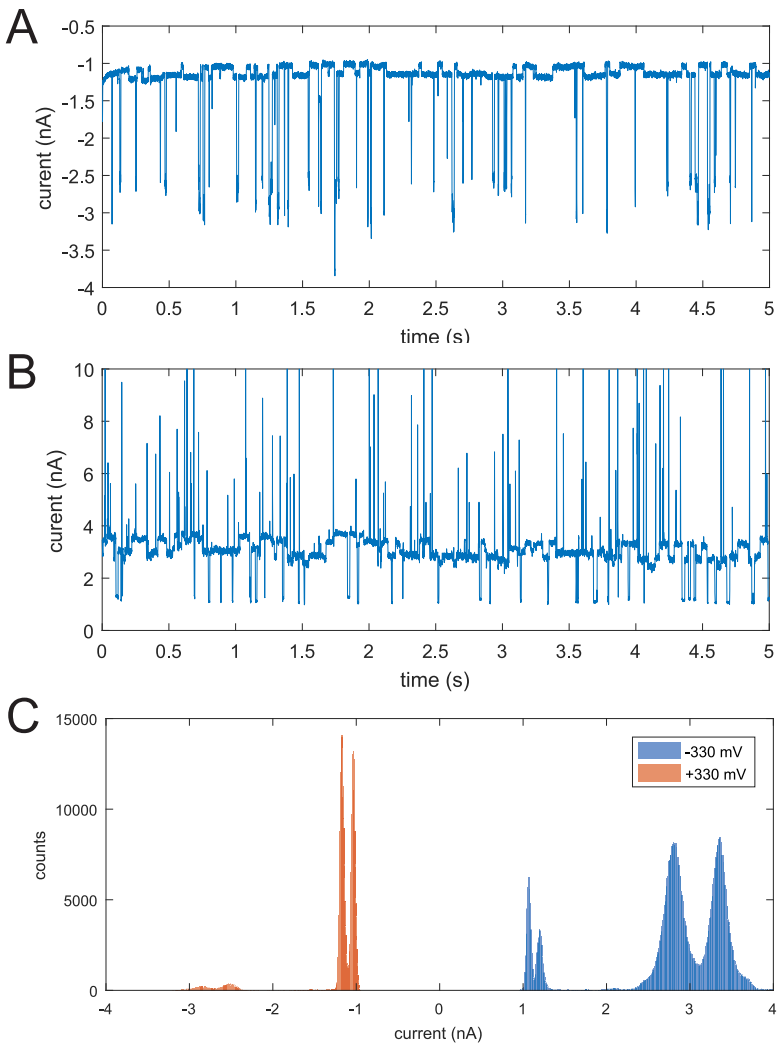


Figure 4.25: Current switching due to multiple fluctuators: A) and B) $I-t$ traces measured in graphene tunnel junction at 77 K temperature at -330 mV and 330 mV respectively. C) Current histograms for the same bias values.

95th current percentile values for the positive voltages with the 5th percentile current values for the negative voltages to obtain the high conductance symmetric IV curve (green curve). Similarly I merge the 5th percentile current values for the positive voltages with 95th percentile current values for the negative voltages to obtain the low conductance symmetric IV (black curve). Both of these curves can be fitted to the Simmons model (Appendix A).

The other way to look at these IV curves would be to treat the mean IV curve as a result of a positively occupied charge trap shifting the bias in the positive direction. The 5th percentile, less probable state with a larger current at negative biases would then correspond to a negatively occupied charge trap, leading to the shift of bias in the negative direction. Two IV curves separated in this way bear resemblance to the curves simulated in the previous section.

The exponential increase in current for both states as a function of voltage is consistent with the previously described linear dependence of ΔI on the mean current. Further the asymmetry in the population of states can explain the often observed asymmetry of tunnelling IV curves in GTJs. I propose that one of the fluctuators governs the large conductance jumps, while the second one, presumably more distant from the junction, has lower impact on conductance as it changes current by only $\sim 0.1\,\mathrm{nA}$ at $330\,\mathrm{mV}$ and its ratio of high and low counts is less sensitive to the bias. This could be explained by the previously discussed electrostatic model and a larger distance R from the junction. Mean dwell times for the levels with high ΔI values are also lower compared to dwell times for the levels with lower ΔI, this is consistent with the dependence of the dwell time of the level on the tunnelling distance between

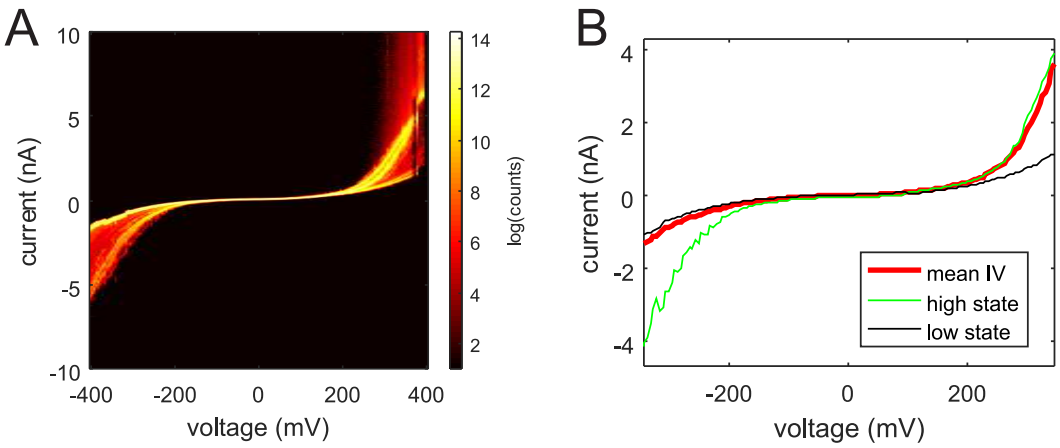


Figure 4.26: Separation of the asymmetric tunnelling IV into 2 symmetric curves. A) 2D histogram of tunnelling current distribution for a range of voltages, counts are plotted on a logarithmic scale. B) Mean tunnelling current IV curve and extracted curves for high and low conductance state.

two metastable sites (ΔR).

Two Fluctuators with a Large Difference of Dwell Times The two traps governing the TLF in the previously discussed device have similar dwell times. However, assuming the exponential dependence of the dwell times on the inter-trap distance dR it should be possible to spot the devices with completely different dwell times, as in silicon devices, where dwell times up to 20 h were observed.[150] I ran the measurement at a constant bias of ± 400 mV for up to 6 h.

In Fig. 4.27A I present 6 h-long traces for the previously discussed device showing an excellent stability of fluctuations over the measurement duration. The observed current levels and the ratio of the point counts at each of them do not vary over the time, implying that switching frequencies governed by both of the fluctuators stay constant.

However, as expected in other devices measured for long times, I observed a typical fast switching behaviour with time constants on the order of $1 - 100\,\mathrm{ms}$ convoluted with slow switching between two different current levels (Fig. 4.27B-D). Such long dwell times had values on the order of hours. Both cases of correlated (Fig. 4.27B and D) and independent amplitudes (Fig. 4.27C) generated by multiple oscillators were found.

The observation of multilevel fluctuations with a large difference of dwell times is a another indication that the observed fluctuations can be caused by electrostatic gating by the charge traps. The large distribution of dwell times can be also related to the intertrap tunnelling distances dR. If gating was induced by the adsorbed adatoms it would be more difficult to justify the existence of potential barriers leading to such a high range of switching frequencies.

4.4 Summary

I have investigated RTSs and RTN noise in GTJs. The presented results show that the origin of the switching are single charge traps located in the vicinity of the tunnel junction, most likely in the SiO_2 substrate. The process below $77\,\mathrm{K}$ has features of intertrap electron tunnelling, while thermal excitations at higher temperatures are also possible. The amplitude of the RTS scales with the mean tunnelling current indicating that switching is not driven by the current, which serves only as a readout mechanism. The analysis of the ΔI point clusters allows to obtain insight into interactions of the adjacent traps, due to the Coulomb repulsion. These results show

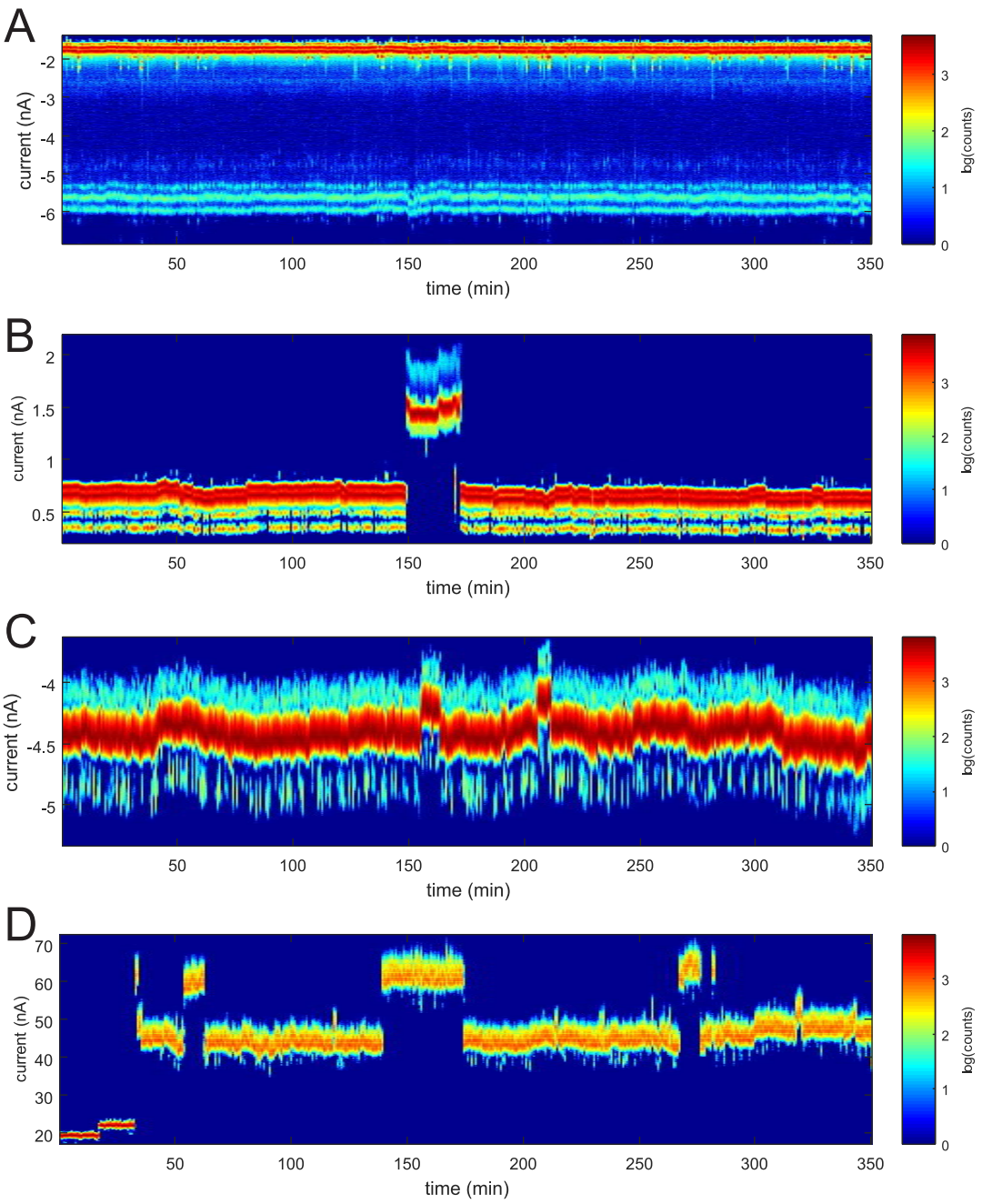


Figure 4.27: Long $I-t$ traces recorded for different devices exhibiting current levels controlled by more than one fluctuator. A) $I-t$ trace for a device showing four current levels controlled by fluctuators with similar switching frequencies (trace recorded at $-400\,\mathrm{mV}$). B-D) Traces for devices showing four or more current levels controlled by fluctuators with large difference of dwell times (traces recorded at B) $+400\,\mathrm{mV}$ C) $-400\,\mathrm{mV}$ D) $+70\,\mathrm{mV}$).

that GTJs are capable of probing the single charge traps dynamics, and that they are highly sensitive to their local environment.

Chapter 5

Noise in Graphene Tunnel Junctions

5.1 Emergence of $1/f$ Noise Spectrum

In the previous chapter I have focused on the analysis of a single fluctuator that dominates the transport in GTJs at 77 K. I continue the analysis with the investigation of the tunnel current at room temperature, where the effect of multiple thermally excited fluctuators is expected. At first I will quantify the room temperature noise in order to use it later to discuss the possible temporal and current limitations of the GTJ sensing method. I will also discuss how the sensitivity of the junction to the local environment containing a small number of fluctuators leads to similar noise behaviour of different devices.

It is commonly agreed that the superposition of many TLF contributions with cor-

ner frequencies distributed uniformly on a logarithmic scale gives rise to a $1/f$ noise spectrum.[136, 141, 145, 150, 229] This idea was first put forward by McWhorter in the context of MOSFETs[150], and is sometimes referred to as the McWorther, Dutta-Horn[136, 141, 145], or Van der Ziel model[229]. In Fig. 5.1 I plot an example of the formation of $1/f$ noise spectrum from the separate Lorentzian peaks. The four fluctuators are sufficient to observe the spectrum similar to $1/f$ spectrum over 4 orders of magnitude of frequency[229], corresponding to a frequency range typically investigated in the experiments. The validity of the McWorther model has been only recently unambiguously demonstrated experimentally using electric circuits consisting of a varying number of fluctuators in the form of magnetic nanodots with different characteristic frequencies.[229]

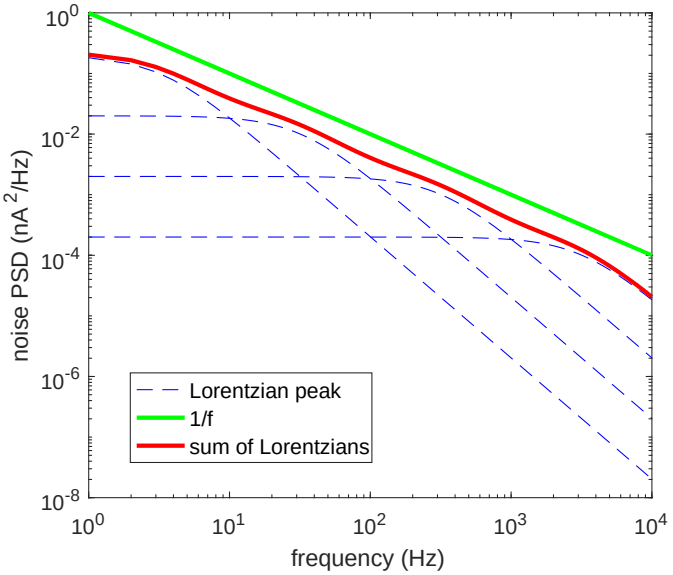


Figure 5.1: Formation of a $1/f$ noise spectrum as a superposition of individual Lorentzian peaks with exponentially distributed time constants $\tau = 0.1,\ 0.01,\ 0.001,\ 0.0001$ s.

In the McWorther model, thermal excitations of additional fluctuators are proposed as the reason of transition from Lorentzian to $1/f$ noise spectrum at higher temperatures.[138, 141, 145, 150] At low temperatures only fluctuators with low activation energies produce a detectable switching signal. At higher temperatures more fluctuators are activated and mean dwell times continue to decrease shifting the corner frequency up.[138, 141, 145, 150] Although in the measurements at $T < 77\,\mathrm{K}$ I observed features pointing at inter-trap tunnelling rather than thermal activation as a perceived switching mechanism, it is expected that at higher temperatures thermal excitations start to play larger role in the switching behaviour.

In most models of $1/f$ noise it is assumed that the dwell times of the individual Lorentzian peaks are distributed uniformly on a logarithmic scale ($t = 10^{-n},\ n = 1,\ 2,\ 3,\ 4, ...$) and $\Delta I = const$ for all of the Lorentzians[138, 139, 141, 229] (as in Fig. 5.1), however, as discussed in Appendix C the ΔI scaling trends can also lead to $1/f$ noise.

In Fig. 5.2A I plot noise spectra recorded for a GTJ at room temperature for a range of voltages. All of the spectra show a $1/f$ trend regardless of the applied voltage. The only difference is the increase in the absolute noise level with increasing bias. Before analysing the noise spectrum in more detail I will look at the properties of $I - t$ traces.

5.1.1 Lognormal Current Distribution

In Fig. 5.3A I present a typical $I - t$ trace recorded for a GTJ at room temperature. There are fast oscillations in the current on time scales below 1 ms. These fluctua-

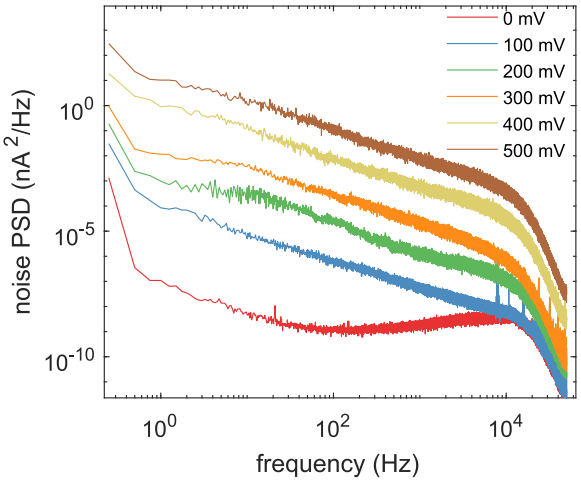


Figure 5.2: Noise spectra recorded for a GTJ at room temeparature for a range of voltages.

tions, as opposed to cryogenic temperature measurements, do not form any distinct, repetitive switching pattern. No correlations are observed there, which is typical for signals with a $1/f$ spectrum.[138, 229]

The current histogram for a 10 s-long segment in Fig. 5.3B has a characteristic asymmetric shape with a long tail towards large (absolute) current values. I fit the current histogram to a lognormal distribution

$$P = \frac{1}{\sqrt{2\pi}x\sigma} \exp\left(-\frac{(\ln x - \mu)^2}{2\sigma^2}\right). \tag{5.1}$$

(To be accurate the fitted distribution is a current probability density function obtained as a distribution of the current counts normalised by the area under the curve)

For a given set of values X with a normal distribution its exponential function $Y = \exp(X)$ has a lognormal distribution. A clear physical intuition can be drawn

there if I assume a simple tunnelling current model $I = I_0 \sinh(\alpha V)$[15], for large voltages only one of the exp functions in sinh will contribute significantly to the current. If I further assume that either the tunnelling barrier α or the voltage value V has a normal distribution centred at its mean value, the resulting current distribution will have a lognormal distribution.

A lognormal distribution Y plotted on a logarithmic x scale has a normal distribution with parameters μ and σ corresponding to the mean and standard deviation of Gaussian distribution. The parameters defining the lognormal formula 5.1 can be used to calculate the mean value and standard deviation of the lognormal distribution in the following way

$$\begin{aligned} \mu_{lognormal} &= \exp\left(\mu + \sigma^2\right) \\ \sigma_{lognormal} &= \left(\exp\sigma^2 - 1\right)\exp\left(\mu + \sigma^2\right). \end{aligned} \tag{5.2}$$

I have performed the $I-t$ measurements for a total of 35 devices (at varying voltage ranges within $\pm 500\,\mathrm{mV}$). All of the current distributions had a similar lognormal shape regardless of the applied voltage and the measured mean current value. The mean current values, covering two orders of magnitude, plotted in the function of bias for all measured voltages are presented in Fig. 5.4A. Each of the measured $I-t$ traces was divided into 10 s-long segments and its normalised current distribution was fitted with the lognormal function. The average values of μ and σ fit parameters for each of the $I-t$ traces were calculated as a mean for all 10 s fragments of a given trace. The calculated mean fitted current values show excellent agreement with the measured mean current values at both high (Fig. 5.4B) and low current range (Fig

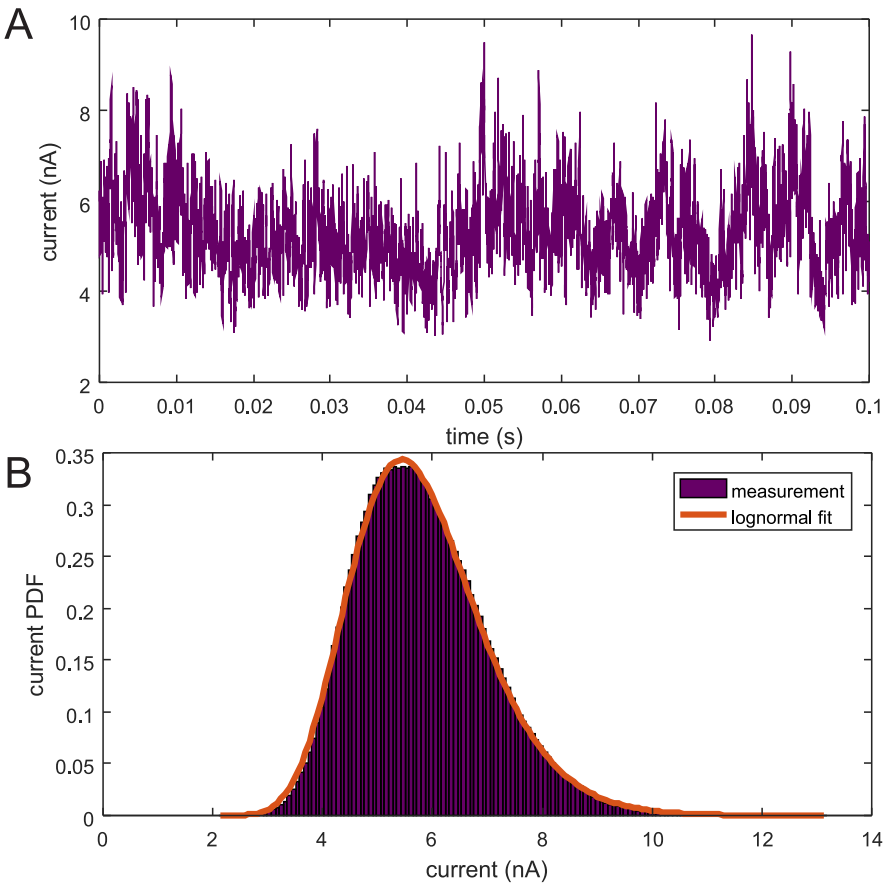


Figure 5.3: Tunnelling current in a GTJs at room temperature measured at +400 mV bias. A) Typical $I - t$ trace recorded in GTJs. B) Normalised current distribution with lognormal fit.

5.4C).

Similarly in Fig. 5.4D I present a plot of the standard deviation $\sigma_{lognormal}$ based on a lognormal fit plotted versus the standard deviation calculated directly for the $I-t$ trace. There is a linear relation between the parameters obtained by both methods. Slightly lower values of $\sigma_{lognormal}$ compared to measured σ may be attributed to the difference between calculating standard deviation for short fragments of trace ($\sigma_{lognormal}$) and averaging them, and calculating the standard deviation for the entire trace (measured σ). Such discrepancy may be related to the presence of switching events with long dwell time.

Another important feature of the fitted $\sigma_{lognormal}$ values is their linear dependence on the mean measured current $\sigma_{lognormal} \sim I$ (Fig. 5.4E). The same holds true for the measured σ values. This is in accord with the previously discussed linear dependence of ΔI levels, as well as the width of distribution of fast and slow contribution to RTN noise spectra at 77 K on the mean current (section 4.1.1). As stated before it means that the observed fluctuations are not driven by current, which serves only as a readout mechanism[145].

The linear $\sigma_{lognormal} \sim I$ dependence can be justified, however it does not explain low scatter of $\sigma_{lognormal}$ values. As can be seen in Fig. 5.4E for a given current value I obtain similar values of $\sigma_{lognormal}$ for all of the measured devices. Such universal behaviour indicates a common origin of the current fluctuations regardless of the tunnelling gap size and the particular junction geometry.

I hypothesize that this observation may be understood in the framework of previously discussed electrostatic model 4.3.2. At elevated temperatures thermal tran-

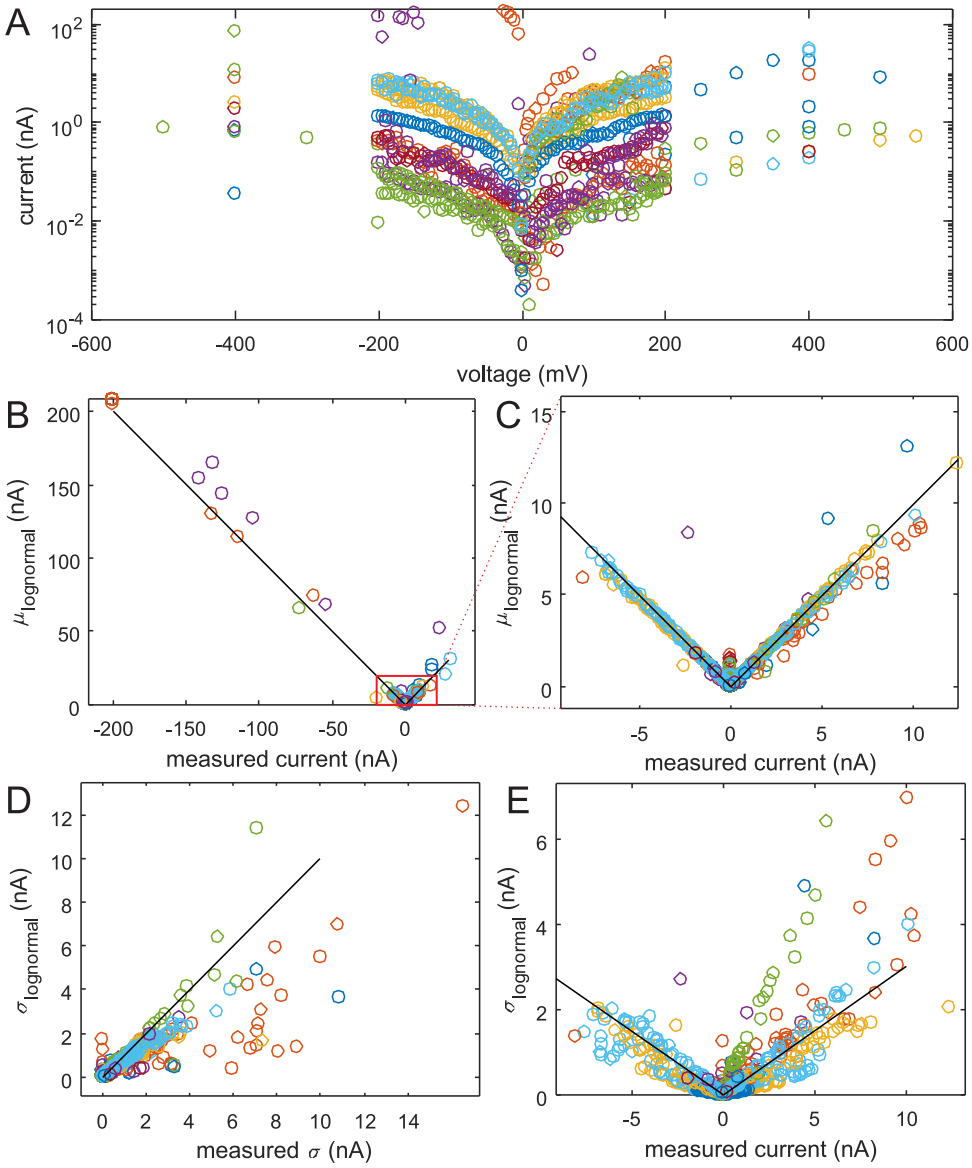


Figure 5.4: Tunnelling currents in GTJs at room temperature. A) Mean tunnelling current as a function of voltage for 35 inspected devices. B) Dependence of the fitted mean value $\mu_{lognormal}$ of a lognormal distribution in a function of mean tunnelling current (Fig. C shows zoomed in plot for a typically observed current values). D) Dependence of the mean fitted standard deviation $\sigma_{lognormal}$ value of a lognormal distribution on a standard deviation obtained directly from the $I-t$ trace. Straight lines in all the previous plots show $y = x$ functions with slope equal to 1. E) Dependence of the mean fitted standard deviation $\sigma_{lognormal}$ value of a lognormal distribution on a mean tunnelling current.

sitions between higher number of traps are allowed, and there are many available traps in the vicinity of the junction with the normal distribution of the inter trap distances centred at $d = 10\,\mathrm{nm}$.[138, 150, 215] I assume that such a distribution of tunnelling distances leads to the similar distribution of the electrostatic voltage values V induced due to the traps. Because of the relation $I \sim \exp V$[15] the resulting current distribution has a lognormal profile.

As well as at low temperatures, at room temperature there is also evidence of the single fluctuators with long dwell times. In Fig. 5.5 I show examples of 6 h-long traces recorded at room temperature. Traces at room temperature are characterised by a lognormal current distribution. These current distributions can be steady and were sometimes measured over many hours without any switching events, as in Fig. 5.5A. However, for the majority of the devices long-term two level switching events with dwell times on the order of minutes to hours were observed. Such TLF switching events differed in the amplitudes, dwell time ratio for *up* and *down* levels, and also their effect on the resulting width of the lognormal current distribution (Fig. 5.5B-E). According to the proposed mechanism of the charge traps switching, leading to the TLF, these events are caused by the charge traps with large activation energies compared to the kT energy at room temperature.

5.2 Flicker Noise and Hooge Parameter

I will now focus on the analysis of the properties of $1/f$ spectra obtained for the 35 GTJs, measured at room temperature at different voltages in the $\pm 500\,\mathrm{mV}$ range

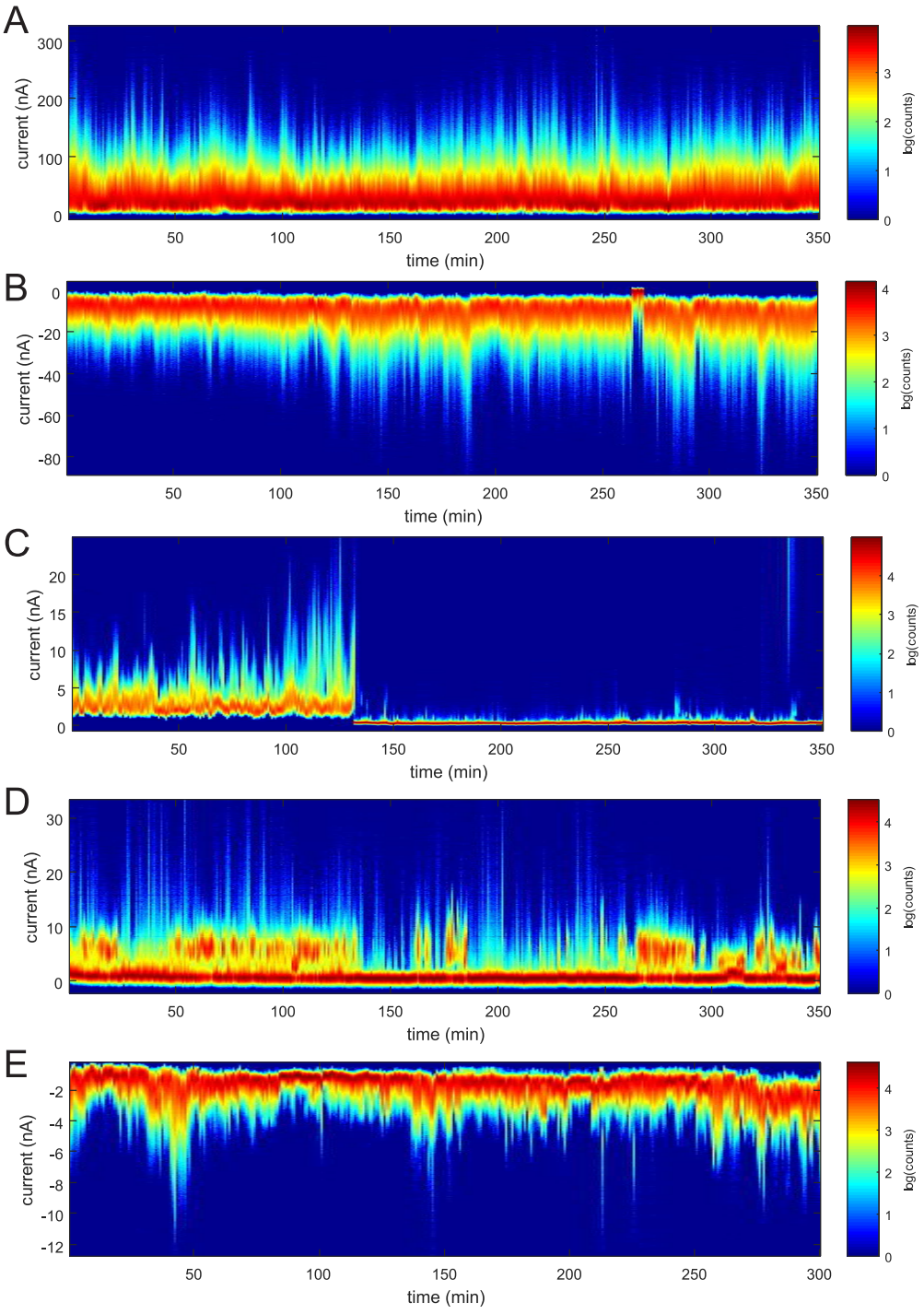


Figure 5.5: 6 h long $I - t$ traces recorded at room temperature showing lognormal current distribution superimposed over the slow TLF. Device A shows clear current asymmetry between A) +400 mV and B) −400 mV voltages with overall uniform lognormal current distribution over time with exception of a brief discrete switching event at −400 mV. Three other devices show lognormal current distribution convoluted with different TLF with long dwell times. Devices were measured at +400 mV (C and D) and −400 mV (E).

(the same data was used for the lognormal current analysis in the previous section). All of the measured noise spectra had a linear frequency dependence on a log−log scale. I fitted them with a simple flicker noise model $S(f) = A/f^{\gamma}$ in the $10-3000\,\mathrm{Hz}$ frequency range. The typical examples of the noise spectra along with fitted curves are shown in Fig. 5.6A. The fitted noise slope γ values as presented in the Fig. 5.6B are within $0.8 - 1.3$ range, with the most frequently observed γ close to one, which is appropriate for the accepted definition of $1/f$ noise[140, 141, 145]. In Fig. 5.6C I show that there is no particular dependence of the noise slope on the mean tunnelling current.

For the purpose of amplitude analysis I apply a parameter α, relating the noise spectrum $S(f)$ to the mean measured current I[128, 130, 131, 164, 172, 176]

$$\frac{S(f)}{I^2} = \frac{\alpha}{f}. \tag{5.3}$$

Parameter α is simply a scaled amplitude of the flicker noise spectrum $S(f) = A/f$, $A = \alpha I^2$ at $1\,\mathrm{Hz}$. Because of its similarity to the Hooge parameter I will refer to it as pseudo-Hooge parameter. A real Hooge parameter would require taking into account the number of free charge carries, which does not seem to be a critical parameter in the case of tunnel junctions. The pseudo-Hooge parameter is a convenient figure of merit for analysis of noise regardless of the measured current and it is often used in graphene research.[127, 128, 130, 131, 172, 173, 177]

Usually α value at a particular frequency (*e.g.* 1 or $10\,\mathrm{Hz}$) is analysed[127, 128, 131, 132, 172, 173], however a more robust method is to define the α averaged over all measured frequencies[182]

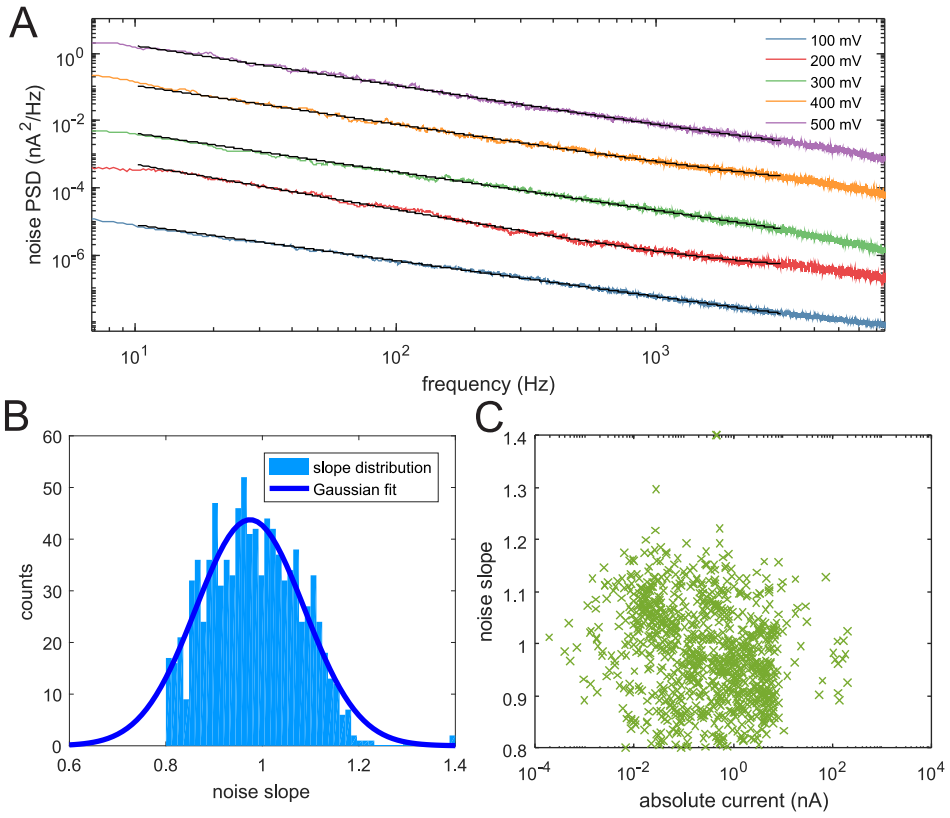


Figure 5.6: Results of fitting of $1/f$ noise spectra recorded at room temperature. A) Typical noise spectra recorded for a single devices at different voltages with fitted $1/f$ lines (black). B) Distribution of fitted γ slopes of $1/f$ noise spectra for all of the characterised devices. C) Distribution of fitted γ slopes of $1/f$ noise spectra versus mean current values for all of the characterised devices.

$$\alpha = \frac{1}{N}\sum_{i=1}^{N}\frac{S(f_i)}{I^2}f_i, \tag{5.4}$$

where averaging is performed for all N frequency points f_i and corresponding noise levels $S(f_i)$. I applied this approach to calculate α values for all of the measured $I-t$ traces. The values of calculated α parameter in the function of mean current are plotted in Fig. 5.7A. They are characterised by a low spread of the values, with most of the points located in the $10^{-3} - 10^{0}$ range. This values are very high compared to the typical values in graphene FETs $\alpha = 10^{-5} - 10^{-2}$[108, 128, 129, 173]. I presume that this is the indication of a higher sensitivity of graphene tunnel junctions to their local environment and it can indicate that GTJs are not only more sensitive to the noise sources but also to the sensing signals.

I do not observe any particular dependence of the α parameter on the mean tunnelling current. Its values are relatively constant for a given device over the recorded current range and they change only from a device to a device. Thus I expect that the variance in α values is related to the variability in the device structure, including a particular form of the tunnel junction and its surrounding. The histogram in Fig. 5.7B presents the average values of pseudo-Hooge parameter for each of the measured 35 devices, the number of data points is insufficient to draw any conclusions about the pseudo-Hooge parameter distribution, however a single peak is probable.

In the next section I will first discuss noise in nanopore experiments what will allow me to draw an analogy to GTJs, in the end of the chapter I will use the extracted α values to estimate the sensitivity limits of GTJs.

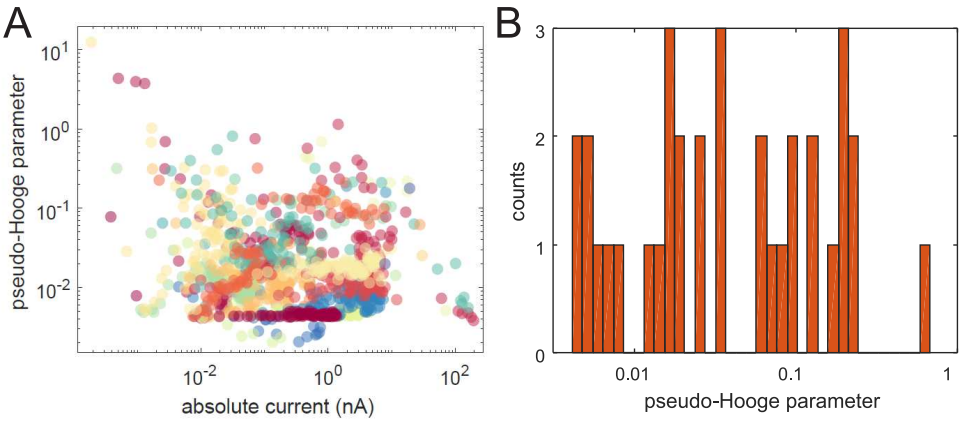


Figure 5.7: Pseudo-Hooge parameter values. A) Plot of the pseudo-Hooge parameter values as a function of mean current. Different colors correspond to different devices. Applied bias was in the ±500 mV range. B) A histogram showing the same data averaged for each of the 35 measured devices.

5.3 Noise in Nanopore Measurements

Nanopores are now a well understood method of sensing and sequencing of bioanalytes, which will discussed in more details in section 6.1.2.citeKasianowicz1996,Merchant2010,Schneider2010 There is also a significant literature discussing noise performance of such devices.[119, 122, 124, 230–232] I will briefly discuss these results, which will stand for a convenient analogy in the further discussion of noise in GTJs.

Noise spectrum has a fundamental influence on the sensitivity of devices. Nanopore sequencers can exhibit a couple of distinct noise regions (Fig. 5.8). Typicaly the frequency dependent noise amplitude in nanopores is described as[119, 121, 231–234]

$$S(f) = a_1 \frac{1}{f^\beta} + a_2 + a_3 f + a_4 f^2. \tag{5.5}$$

These four noise spectrum components correspond to:

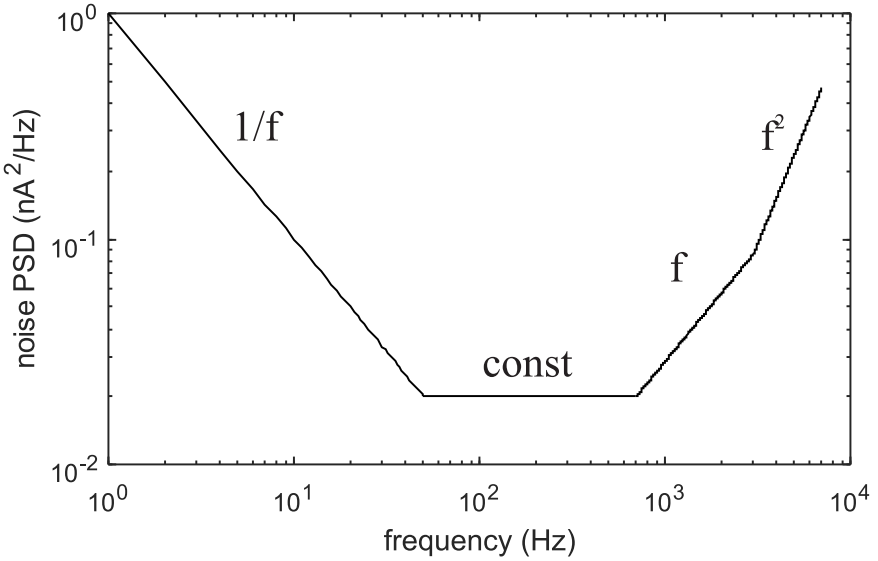


Figure 5.8: A schematic noise spectrum in nanopore measurements with four distinct regions.

- $1/f$ noise with exponent $\beta = 0.7 - 1.4$[119, 230]
- Thermal Johnson noise $S = \frac{4kT}{R_P}$, related to the resistance of a nanopore R_P[119, 231, 233]
- Dielectric loss noise term due to the imperfect lossy dielectric of the membrane[119, 230]
- Capacitance noise induced by the interaction of amplifier voltage noise with the net capcitance at the input[121, 234]

In the next sections I will discuss these noise contributions, beginning with high frequency noise. Details of the amplifier circuit and related noise are given in Appendix F.

5.3.1 High Frequency Noise

The noise components at intermediate and high frequencies are related to the total capacitance present in the system at the amplifier input.[121, 123, 233, 235] This capacitance includes capacitance C_m due the capacitor created by the insulating membrane in contact with two reservoirs filled with electrolytes, wiring stray capacitance C_w and the amplifier input capacitance C_A.[120, 121, 123, 231, 233] The total capacitance $C_{tot} = C_m + C_w + C_A$ at the differential input of the amplifier leads to the current noise PSD defined as[121, 231, 233]

$$S_I(f) = (2\pi f C_{tot})^2 e_n^2 \ [\mathrm{A}^2/\mathrm{Hz}], \tag{5.6}$$

where e_n is the characteristic amplifier input voltage noise.[233] The amplifier voltage noise itself is modelled as a sum of thermal and flicker noise[236]

$$e_n^2 = V_{n,thermal}^2 + V_{n,flicker}^2.$$

The resulting noise current is given as[121, 234, 237]

$$I_{RMS} = \frac{2\pi}{\sqrt{3}} B^{\frac{3}{2}} e_n C_{tot} \tag{5.7}$$

where B is bandwidth.

At lower frequencies a $S \sim f$ noise component can be observed. It is attributed to the noise related to the energy dissipation in a lossy dielectric medium of the nanopore membrane.[230] The energy dissipation is caused then by a complex capacitance

$C' = C(1 + j\omega D)$, where D is a dielectric loss coefficient.[231] Instead of losses in a nonideal dielectric of thin membranes the energy loss can occur also in the Electric Double Layer (EDL).[231] Another alternative is the interaction of flicker noise $V_n = A/f$ of the amplifier with the input capacitance[231, 234]

5.3.2 Low Frequency Noise

High frequency noise components depend only on the capacitance of the membrane or amplifier input, however there is much more scatter in the low frequency noise values, which reflect the properties of nanopores.[230] Such noise conveys information about the dynamics of process in the volume of a nanopore, but it is also sensitive to the differences in geometry of nanopores.[230] These differences might be elusive, even similar pores, as inspected by Transmission Electron Microscopy (TEM) may have $1/f$ noise spectra differing by three orders of magnitude.[230]

The origin of $1/f$ noise in nanopores still remains disputable, although it is agreed that initially fabricated inorganic nanopores had higher overall noise levels compared to their organic counterparts.[119, 121, 232] On the other hand the inorganic nanopores provide multiple opportunities for alleviating the noise issues by engineering of their properties, as opposed to organic pores, which are less prone to simple surface modifications.[121]

The flexible structure of the organic α-hemolysin nanopores was at first suspected of inducing current fluctuations due to change of shape of the conducting channel.[238] Another proposed mechanism, which can cause $1/f$ noise in both organic and inorganic nanopores, is the formation of asymmetric potential wells in a

nanopore due to specific ion configurations, resulting in the dynamic electrostatic environment for ionic current.[239].

Inorganic nanopores tested in a range of salt concentrations, which defines the effective concentration of carriers, have been shown to obey the Hooge's law[230]: increasing salt concentration led to an increase in the conductance. Nevertheless, the normalized noise power was decreasing and the average Hooge parameter was on the order of $\alpha = 10^{-4}$, close to values obtained for semiconductor devices.[230, 232] Excessive noise over the level predicted by Hooge formula and independent of the carrier concentration has been attibuted to the formation of nanobubbles in the nanopores.[230, 240]

Another possible source of noise is the effect of surface charge in the nanopore due to the surface charge traps.[241] Recently a study of nanopores with large and small diameters showed that both of the surface and volume noise generation mechanisms are involved at the same time.[232], with surface noise (controlled by the pH level) dominating in small nanopores and Hooge-type bulk noise (controlled by the salt concentration) dominating in large nanopores.[232] The particular geometry of the pore and its surface properties have the dominant effect on low frequency noise. For instance nanopores in graphene have been shown to follow bulk, Hooge type noise behaviour without any surface contribution.[122]

5.3.3 Reducing Noise in Nanopores

The detrimental effect of electric noise on the measured signals is a strong incentive to decrease its level. It is significant because even efficient sensing mechanisms with

high signal amplitudes will eventually be dominated by the rapidly increasing noise level at high frequencies.[121, 123, 231, 234, 236] Therefore it is necessary to limit the noise amplitude. As it was shown in Eq. 5.6 high frequency $S \sim f^2$ noise is defined by two variables e_n and C_{tot}. One way to decrease noise is to reduce the amplifier input voltage noise e_n which can be achieved by using a battery as a low noise voltage source.[123]

The other option is to focus on the reduction of capacitance. The major contribution is the membrane capacitance C_m, which can be reduced by decreasing the area of a membrane exposed to electrolyte.[121, 233, 234] It has been shown that by increasing the thickness of the insulation layer around the nanopore to 1000s µm, by adding layers of SiO_2, glass and silicone, the membrane capacitance C_m can be reduced to the level of 1 pF when other circuitry-related capacitances dominate.[121] Further progress can be achieved by moving from the casual discrete amplifiers like Axopatch 200B to custom build amplifiers, where nanopores are integrated into the amplifier die.[121, 123, 231, 233, 236]

The effect of membrane thickness is ambivalent: a pore in a thinner membrane leads to a higher signal ΔI, on the other hand a thinner membrane increases capacitance noise.[234] Therefore more challenging fabrication methods are applied in order to obtain µm-sized neighbouring regions with a highly different dielectric layer thickness (Fig. 5.9). Current state-of-art nanopore systems in nanometrically thin membranes surrounded with a thick dielectric layers, with minimized parasitic capacitances and chip-integrated amplifiers can achieve temporal resolution up to 5 MHz.[234]

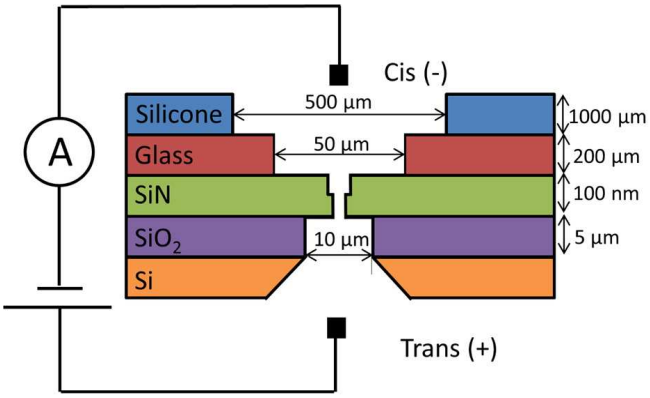


Figure 5.9: Multilayer dielectric stack used to reduce the capacitance of nanopore membrane. Reprinted with permission from [121].

Discussed methods are related to the reduction of high frequency capacitance noise, which can be addressed by means of the engineering of the capacitance properties of the membrane. On the contrary the low frequency $1/f$ noise is more difficult to eradicate and it imposes the ultimate sensing limit.[140, 241]

In the next section I will analyse the electronic setup used in the experiments as well as the noise levels in GTJs.

5.4 Noise and Sensitivity Limits in Graphene Tunnel Junctions

5.4.1 Noise in the Measurement Setup

In the measurements two different amplifiers were used, namely Femto DPLCA-200 which is a common transconductance amplifier used to detect nanoampere currents, and Axopatch 200B, which is a more specialised voltage-clamp amplifier, originally

developed for applications in the field of electrophysiology and characterised by low noise.[120] In order to fully understand the noise spectrum and resulting limitations I characterised noise levels intrinsic to the used amplifiers.

Femto DPLCA-200 Characterisation

First, I tested a Femto DPLCA-200. Its gain, which can be set in the range from $10^3 - 10^9$, influences other parameters such as 3 dB bandwidth, maximum current and input voltage noise spectrum. The characteristic values taken from the data sheet are summarised in Tab. 5.1.

Table 5.1: Femto DPLCA-200

Gain ($\mathrm{V\,A^{-1}}$)	$B_{3\,\mathrm{dB}}$ (kHz)	t_{10-90} (µs)	I_{max}(nA)	I_{in}^2 ($\mathrm{fA}/\sqrt{\mathrm{Hz}}$)
10^9	1	300	10	4.3
10^8	7	50	100	13
10^6	200	1.8	10000	130

The amplifier is characterised by measuring the $I-t$ traces in a circuit containing a resistor with different resistance values. Resistors can be treated as a reliable source of thermal noise defined by their resistance. On the basis of $I-t$ traces for three different resistors I obtained noise spectra which are plotted in Fig. 5.10A. I also calculated the theoretical value of thermal noise for these resistors (horizontal lines). There is good agreement between the measured and calculated noise level values up to the cut-off frequency of the amplifier.

Measurements in Fig. 5.10A were taken at gain = 10^9 corresponding to a 1 kHz

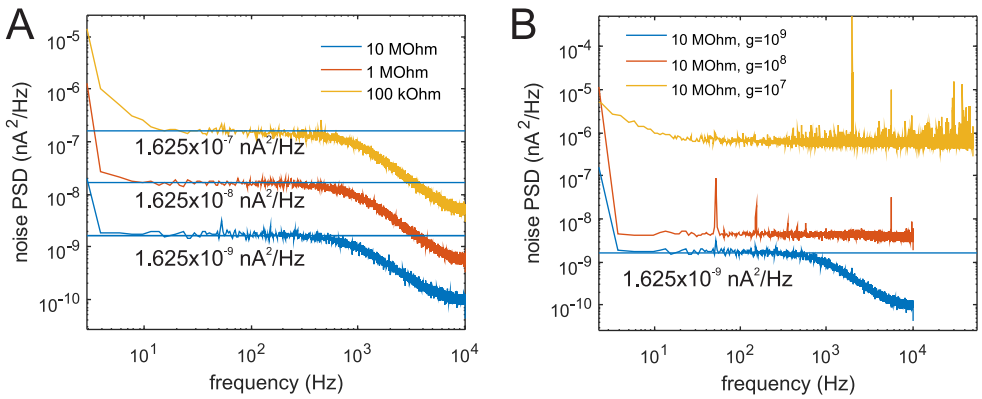


Figure 5.10: Noise levels in Femto DPLCA-200 amplifier. A) Noise spectra recorded for different resistors with maximum gain gain = 10^9. Horizontal lines indicate the calculated noise level for each of the resistors. B) Noise spectra recorded for a 10 MΩ resistor with different amplifier settings.

bandwidth. This bandwidth might not be sufficient in the case of fast sensing applications, and the maximum current value of 10 nA might be too low to resolve the sensing signal as I will show later in Chapter 6. Therefore settings with lower gain may be necessary. They are beneficial because they offer a larger bandwidth and higher current range, however it comes at the cost of increased noise levels.

Next, I tested the amplifier with a large resistance of 10 MΩ, which is similar to the resistance values expected from GTJs. I measured the noise level recorded at lower gain settings (10^8 and 10^6). As can be seen in Fig. 5.10 B lower gain settings, increase the bandwidth, but they also increase the white noise level above the theoretical noise level of the resistor. Such increase cannot be attributed only to the increase of voltage input noise of the amplifier, which is on the order of fA/$\sqrt{\text{Hz}}$.

Axopatch 200b Characterisation

Axopatch 200b has a variable gain in the range $0.05 - 500\,\mathrm{mV\,pA^{-1}}$ with the maximum current input of 200 nA at the lowest gain. Importantly, gain setting does not affect the bandwidth, which is set by the 4-pole Bessel filter in the range $1 - 100\,\mathrm{kHz}$. I performed the calibration of the instrument according to the manufacturer's procedure and measured I_{rms} values, using inbuilt amplifier functionality. Recorded values were similar to those specified in the datasheet (Tab. 5.2). This characterization was performed with maximum bandwidth $B = 100\,\mathrm{kHz}$.

Table 5.2: Axopatch 200b

	$I_{rms,specified}(pA)$	$I_{rms,measured}(pA)$
Whole cell $\beta = 1$ (R feedback)	0.55	0.46
Whole cell $\beta = 0.1$ (R feedback)	0.074	0.045
Patch $\beta = 0.1$ (C feedback)	1.55	1.60

I obtained the open circuit noise spectra at different filter settings for two gain values $g = 500$ and $g = 1$ (Fig. 5.11A and B respectively). The noise spectrum was flat and characterised with a low noise level at $4 \times 10^{-11}\,\mathrm{nA^2\,Hz^{-1}}$, similar to the minimum noise specified in the datasheet ($\sim 1 \times 10^{-12}\,\mathrm{nA^2\,Hz^{-1}}$). As I show in Fig. A and B neither gain, nor filter setting shift the noise spectrum. At high frequencies I observe an increase in noise, which I identify as a capacitance noise contribution. Subsequently I also recorded noise spectra in circuits containing resistors of different values (Fig. 5.11C and D). There is good agreement between the measurement and calculated thermal noise. Contrary to Femto DPLCA-200 measurements, changing

bandwidth and gain does not lead to the deviation of measured thermal noise from the theoretical values.

Because of the better noise performance and flexibility in the choice of gain and bandwidth parameters in the further measurements I will use the Axopatch 200b amplifier.

5.4.2 Noise Features in Graphene Tunnel Junctions

Before I consider the influence of the $1/f$ noise on the sensing limits in GTJs I will briefly discuss the high frequency noise levels. In the previously shown spectra of GTJs the noise spectrum was dominated by a $1/f$ contribution up to 10 kHz. However, in measurements with a higher bandwidth I observe the increasing capacitance noise (Fig. 5.12A). The level of this noise is relatively high, which implies high capacitance of the device. I expect that measurements of devices at high frequencies will be dominated by this contribution. On the contrary I also obtained devices with a lower $1/f$ noise level and the high frequency noise dominated by the noise of the amplifier rather than the device. In Fig. 5.12C I show one such example with overlapping noise spectra for the open circuit, GTJ at 0 mV and 500 mV, which indicates a negligible capacitance contribution of the device. Noise behaviour of this kind was observed in low-conducting devices (Fig. 5.12D).

In this way I show that it is possible to select devices with low noise levels, where high frequency behaviour is dominated by the measurement setup. As I discussed before in the section 5.3.3 such noise sources can be eradicated *e.g.* by using a chip integrated amplifier rather than a discrete one. Thus I will make a working assump-

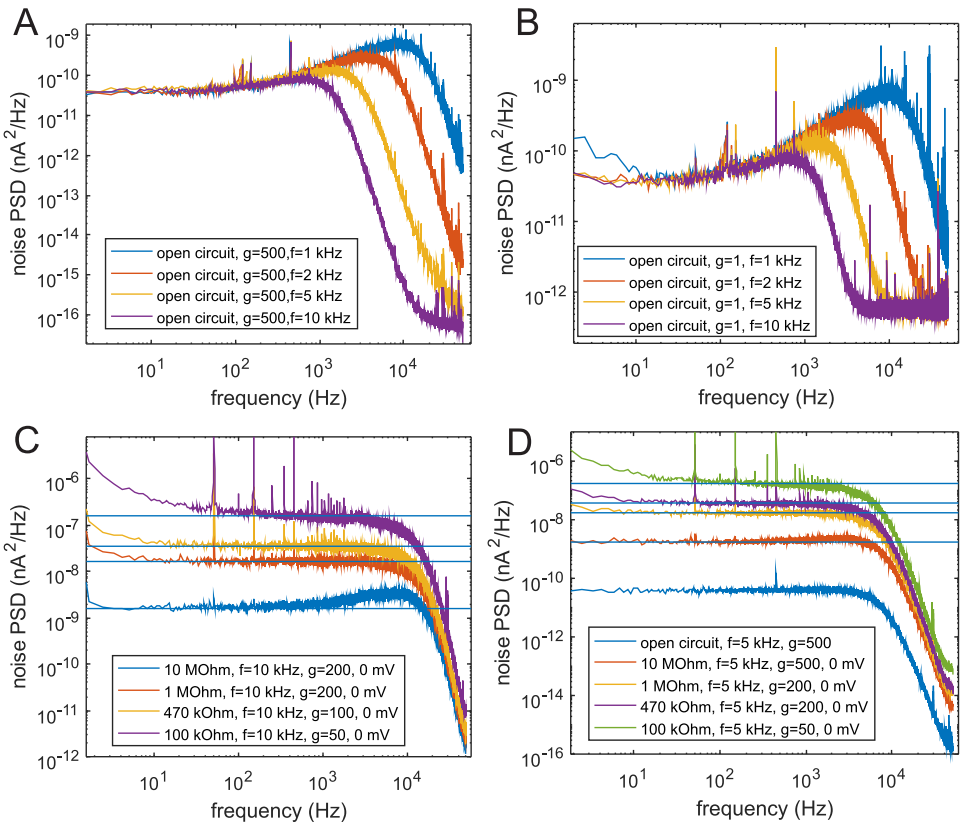


Figure 5.11: Noise in Axopatch 200b. A) and B) Open circuit noise spectra measured at various bandwidths for gain $g = 500$ and $g = 1$ respectively. C) and D) Noise spectra measured in for different resistors at different gain setting with bandwidth $B = 10\,\mathrm{kHz}$ and $B = 5\,\mathrm{kHz}$ respectively (blue horizontal lines indicate the calculated thermal noise levels).

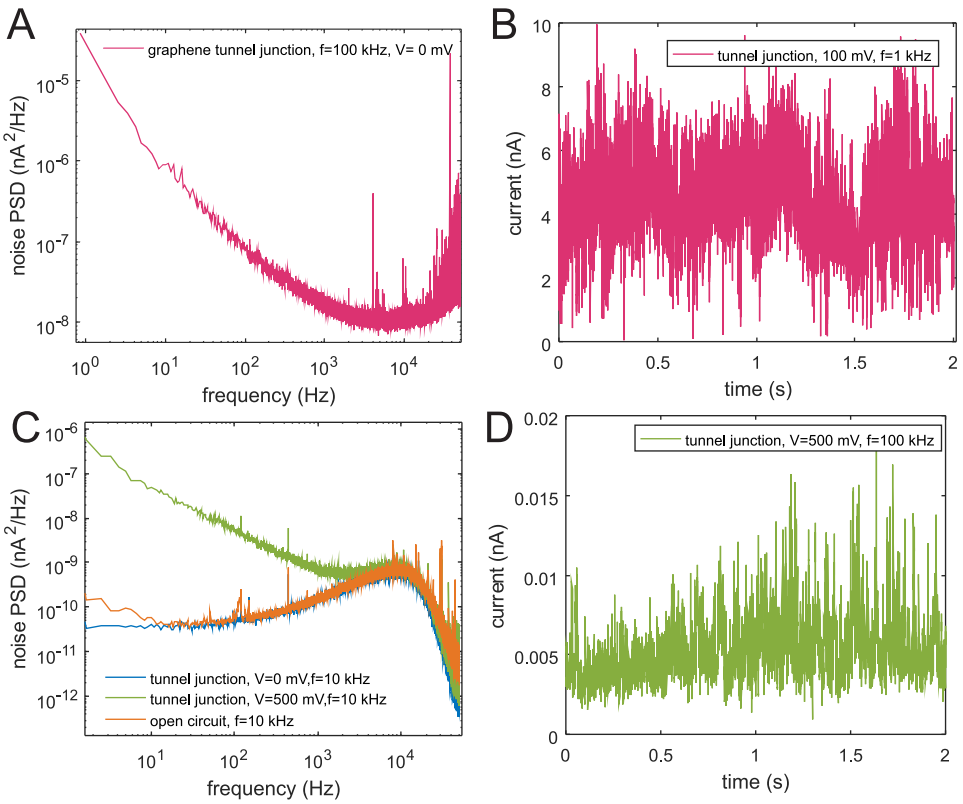


Figure 5.12: High frequency noise in GTJs. A) A noise spectrum of a typical GTJ dominated by the $1/f$ noise at low frequencies and high capacitance noise at higher frequencies. B) Corresponding $I-t$ trace of the same device recorded at 1 kHz frequency showing features of flicker noise and lognormal current distribution. C) An example of device characterized by the low $1/f$ noise level. High frequency capacitance noise is defined by the intrinsic response of the amplifier. D) The corresponding $I-t$ trace showing low current level.

tion that it is possible to perform the measurement under such conditions that the only limitation to the sensitivity of a GTJ is its $1/f$ noise spectrum. I will further discuss what detection levels can be achieved under such conditions.

5.4.3 Detectable Signal Limits

The limiting factor from the point of view of sensitivity of nanopores or GTJ sensors is their noise spectrum.[120, 231, 233–235] The flicker noise spectrum observed at room temperature constitutes a severe limitation to the sensitivity, as it cannot be improved just by recording and averaging signal for longer time if the exponent value $\alpha > 1$ in the flicker noise spectrum $S = \frac{A}{f^\alpha}$.[139] Flicker noise introduces such limitation because the energy E accumulated in the noise spectrum is proportional to the noise $E \sim S(f)^2 df = \left(\frac{A}{f^\alpha}\right)^2 df$, where df is the frequency range.[139] This energy divided by the measurement time, which is $t \approx 1/f_{min}$ is an increasing function of measurement time, which means that the average noise power is increasing.[139]

The absolute value of ΔI does not contain entire information about measurement. Proper analysis has to take into account the Signal to Noise Ratio (SNR). SNR which defines the sensing capability in a measurement depends on the spectral density of noise source $S(f)$ and the bandwidth of measurement B. It is defined as [120, 234]

$$SNR(B) = \frac{\Delta I}{I_{RMS}} = \frac{\Delta I}{\sqrt{\int_{f_{min}}^{B} S(f) df}}, \tag{5.8}$$

where ΔI is the amplitude of a detected current peak, and I_{RMS} is the root-mean-square value of the measured current.[120] ΔI value depends on the mechanism of

interaction of the analyte with the sensing device. Regardless of this mechanism the given formula estimates how high signal amplitude can be detected with a given device, characterized by a particular I_{RMS} and assuming acceptable SNR value. In nanopore measurements the minimum reasonable $SNR_{min} = 5$ is commonly assumed.[150, 231, 234] As evident from the equation 5.8, since the I_{RMS} value depends on the bandwidth, the amplitude of noise observed in $I-t$ traces will increase monotonically with the increasing B.[120] The value of SNR and therefore the detectable current peak amplitude ΔI depend not only on a measurement bandwidth but also on the profile of a noise spectrum. Increasing the bandwidth of measurement may not always be beneficial. It is the case if there is a flat noise spectrum but signal fluctuations are restricted to the bandwidth B_0. The increase of the measurement bandwidth beyond B_0 will result in decrease of SNR.[235]

A molecule tranlsocating through a nanopore induces a transient current blockade with duration τ and amplitude ΔI. An important distinction in nanopore measurements is the meaning of the observed ΔI signal. Large ΔI is obtained in the case of observation of just the difference in ionic current between open and closed pore configuration. If the differences in ionic current caused by different nucleotides are analysed, the δI of interest will be lower (Fig. 5.13).[121] A large advantage of the single molecule measurements with high bandwidth is an opportunity to observe real time dynamics, which in the case of ensemble measurements are obscured.[235] On the other hand, if the aim of the sensing process is just the detection of the presence or absence of a molecule its additional degrees of freedom allowing for different orientations of the molecule in the nanopore will lead to distorted current values, which

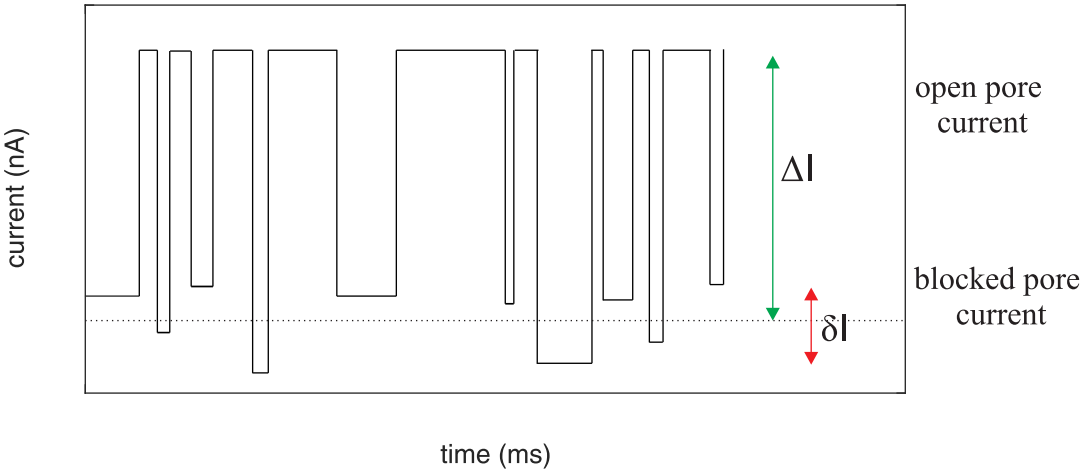


Figure 5.13: Differences in meaning of signal amplitude in nanopore measurements, which can correspond to either difference between open and closed nanopore ΔI or rather small difference between current level for different molecules or molecule configurations.

may be interpreted as noise.[235]

5.4.4 Temporal Resolution of Sensing Signal

In molecule sensing the main aim is to detect short signals generated by the interaction of a molecule with a junction. Duration of such events is dictated by the free diffusion of molecules or electrophoretic drag if molecule motion is controlled by an external field, or by a specific interaction such as adsorption of a molecule in the junction. Typically bases can pass through pores at rates higher than 1 base per ms, such rates dictate the minimum bandwidth necessary for base detection.[121, 233, 234]

The measurement bandwidth is often limited by filters which limit the high frequency current noise level.[237] The limited bandwidth B introduces the limited rate

of a current signal rise. For an instantaneous current step it is estimated as[237]

$$\frac{dI}{dt} = 2\pi B \Delta I_{step}. \tag{5.9}$$

The maximum rise time can be roughly approximated as $t_r \approx 0.33/B$.[119] This effect is critical for the detection of events with short dwell time $\tau < t_r$, which will appear in the measured trace with longer dwell time and lower amplitude.[123]

The presence of current noise affects also the uncertainty of the dwell time estimation by introducing random error of[237]

$$\Delta t_{RMS} = \frac{I_{RMS}(B)}{2\pi B \Delta I} = \frac{1}{2\pi B SNR(B)}. \tag{5.10}$$

This indicates the importance of the particular form of *SNR(B)* dependence. If the current noise is increasing with bandwidth faster than $I_{RMS} \sim B$ the temporal uncertainty Δt_{RMS} will increase (for high frequency capacitance noise $I_{RMS} \sim B^{\frac{3}{2}}$).[237] Conversely the scaling lower than $I_{RMS} \sim B$ will lead to a decrease in temporal uncertainty with an increase in bandwidth (for white noise $I_{RMS} \sim B^{\frac{1}{2}}$).[237] Because of these considerations the optimum bandwidth B is often assumed to be equal to the onset frequency of capacitance noise $S \sim f^2$.[231, 237] That is why the exact value of γ exponent of $1/f$ noise is revealed. Value of $\gamma = 1$ is the border between signals which will improve or deteriorate with an increasing bandwidth. Electronic noise causes the limitation of the time resolution of the resolved signal, assuming that all the other technical limitations related to high frequency capacitance noise may be removed the $1/f$ noise of the nanopore is the ultimate sensing limit.[241]

The detrimental effect of flicker noise of the form $S = AI^2/f$ on the measured signal is fully manifested in long measurements, as noise PSD increases for low frequencies, which are related to the duration of the measurement. The long duration of the measurement leads to increased noise power.[120] By analytically calculating the *SNR* for flicker noise the expression for the maximum bandwidth of measurement given the minimum tolerable value of SNR_{min} can be expressed as[120, 230]

$$B_{max} \approx f_{min} \left(\exp \left[\frac{1}{AI^2} \left(\frac{\Delta I}{SNR_{min}} \right)^2 \right] - 1 \right). \tag{5.11}$$

This parameter is important as it defines the duration of a current peak which can be detected with a given device.

5.4.5 Detectable Signal Limits in Graphene Tunnel Junctions

Sensing performance is compromised by the SNR and temporal resolution. Two major factors hindering these properties are small signal frequency response and the accumulated power of the electric noise in the signal.[119, 120] Now I will estimate what are the limits of bandwidth and minimum measurement frequency for a given noise spectrum observed in GTJs, allowing to obtain acceptable SNR levels.

Bandwidth is a crucial parameter, because it defines how fast the device can react to the molecule translocation. Fast tranlsocation rates are desired to reduce time necessary for sequencing. If an (unlikely) assumption that it is sufficient to obtain one data point per molecule is made, then the bandwidth in Hz can be read as a

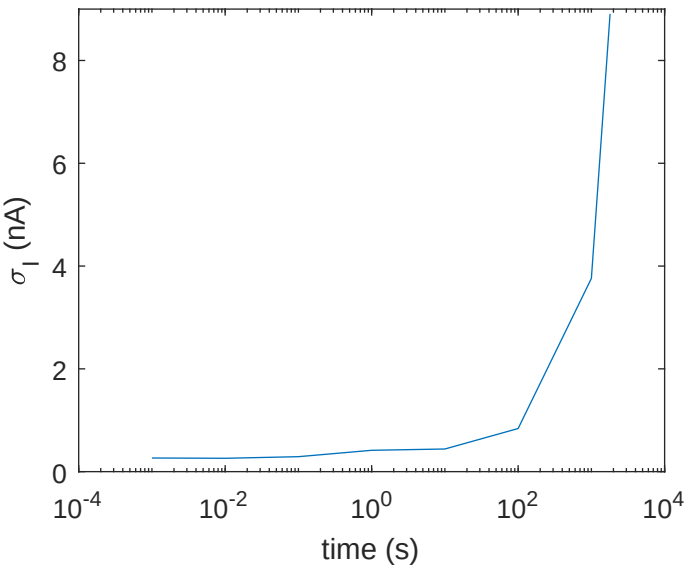


Figure 5.14: Current standard deviation in a GTJ as a function of measurement time.

maximum allowed translocation rate in molecules/second.

Similarly the minimum measured frequency f_0 is proportional to the the measurement time. The duration of the measurement defines the length of a DNA strand which can be read during a single measurement, which is given as $N \sim \frac{B}{f_0}$. As I discussed the long measurement of a signal with $1/f$ noise leads to the accumulation of noise, which results in the increase of current noise I_{RMS}. In Fig. 5.14 I show how measured current standard deviation increases in the function of time.

In section 5.2 I found a relatively narrow distribution of the pseudo-Hooge parameter in the range $10^{-3} - 10^{0}$. I will now analyse how idealised $1/f$ noise spectra based on these α values will affect the expected device sensitivity. As proposed before I will take into account only the $1/f$ noise contribution. In Fig. 5.15A I plot

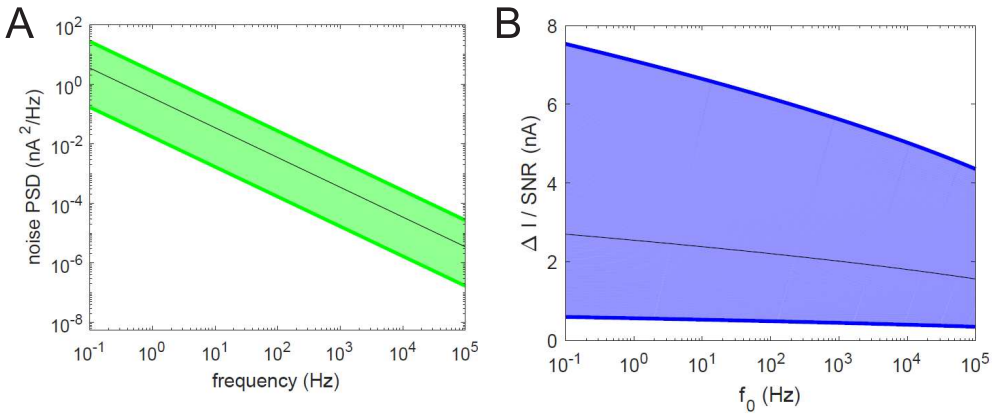


Figure 5.15: Idealised $1/f$ noise spectrum in graphene tunnel junctions. A) $1/f$ noise spectrum calculated for the the obtained pseudo-Hooge parameters. The black line corresponds to the average $\alpha = 0.0867$ value while top and bottom green lines are calculated for the maximum and minimum recorded $\alpha = 0.6765$ and $\alpha = 0.0042$ respectively. Calculations were done assuming current value $I = 2\,\mathrm{nA}$. B) Corresponding signal detection limit defined as $\Delta I/SNR$, calculated on the basis of noise PSD curves in Fig. A, assuming $B = 10 \times 10^6\,\mathrm{Hz}$.

the expected $1/f$ noise spectrum range for graphene tunnel junctions at example, arbitrarily chosen 2 nA current, calculated as $S(f) = \alpha I^2/f$. The maximum and minimum values of this range are calculated as $1/f$ noise curves for maximum and minimum recorded pseudo-Hooge parameter values.

As I discussed in the previous section the noise spectrum and measurement frequency range ($f_0 \sim \frac{1}{t}$ - minimum frequency corresponding to the measurement duration t, and bandwidth B) define the minimum detectable ΔI level. Here I propose to take as a figure of merit the ratio

$$\frac{\Delta I}{SNR} = \sqrt{\int_{f_{min}}^{B} S(f)df}, \tag{5.12}$$

which allows for the analysis of a detectable signal level in a facile way. In order to obtain the real ΔI it just has to be scaled by the tolerable SNR value, which is usually equal to 5, however it can be different for different applications. Such normalised detection limits for the idealised noise spectra at 2 nA current and assuming the reasonable value of measurement bandwidth $B = 1 \times 10^6$ Hz are plotted in Fig. 5.15B as a function of minimum frequency f_0. As can be seen there the pseudo-Hooge parameter and the corresponding noise level as well as frequency f_0 have significant impact on the detection limit.

The particular observed ΔI will depend on the mechanism of the interaction of the analysed molecule with the junction. As I show in Fig. 5.15B in the case of the $I = 2\,\mathrm{nA}$ and assuming $SNR = 5$ the detectable range will be $\Delta I \approx 10 - 15\,\mathrm{nA}$ over the analysed f_0 frequencies and for an average GTJ. This value is reasonable comparing to the sensing measurements discussed in the Chapter 6.

I note that high values of the $\frac{\Delta I}{SNR}$ detection limit at low f_0 frequencies may not be the ultimate limit. It is envisaged that analysis of the traces may be performed in the way similar to the analysis of RTN at 77 K, discussed previously in section 4.1.2, that is by dividing the recorded trace into separate segments and analysing the ΔI current peaks with respect to the resulting local baseline. In such way the minimum f_0 frequency limit would be increased decreasing the integration range in formula 5.12 and lowering the resulting minimum detection limit.

The other way to understand it is to remind that I assume the emergence of $1/f$ noise spectrum due to the superposition of individual TLFs with different frequencies. In long measurements presumably fluctuators with large dwell times can be

observed. Dividing signal into short sections and analysing it with respect to the current baseline effectively would remove the effect of the slow fluctuators.

I visualise the effect of a change in f_0 frequency in Fig. 5.16A, where I plot the signal detection limit as a function of both f_0 and B frequencies. The figure shows that relatively large changes in the size of the noise integration window within experimental parameters affect the change by varying the detectable signal limit over $2\,\frac{\mathrm{nA}}{\mathrm{SNR}}$.

In Fig. 5.16B I look at the dependence of the detectable signal limit in the function of f_0 frequency and mean tunnelling current I, I stress that this noise generating current is an empty gap current. Because of its influence on the noise level, increasing the mean current significantly affects measurable ΔI values. However this effect is less significant for shorter measurements (larger f_0).

In order to achieve lower detection limits it is beneficial to limit the time of measurement and decrease the mean tunnelling current. However the analyte system has to be taken into consideration. Shorter measurements times will mean fewer detected interactions between the junction and molecule. Measurement time is therefore a trade-off between higher noise level and lower number of detected events dictated by the molecule length, analyte concentration in the solution, and its kinetics due to Brownian motion or electrophoresis. In terms of the current impact on noise, the current flowing through the tunnel junction is not a parameter which can be freely adjusted; it is a function of applied voltage, and therefore the relevant question is if the detected signal scales faster or slower with increasing voltage compared to the empty gap tunnel current.

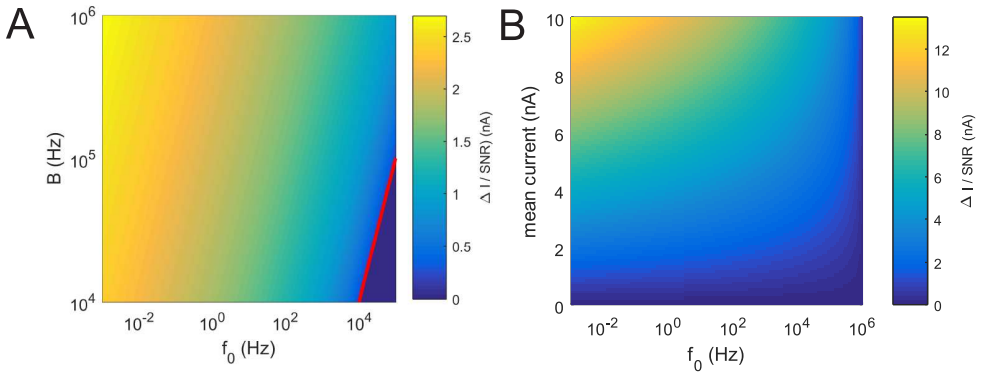


Figure 5.16: 2D maps of signal detection limits. A) Calculated dependence of the signal detection limit on the minimum frequency f_0 and bandwidth B assuming $I = 2\,\mathrm{nA}$. The red line corresponds to $f_0 = B$, below this region none noise can be observed. B) Dependence of the signal detection limit on the minimum frequency f_0 and mean tunnelling current assuming bandwidth $B = 1 \times 10^6\,\mathrm{Hz}$.

5.5 Summary

In this chapter I described the emergence of $1/f$ noise spectrum in GTJs at room temperatures, which is attributed to the thermal activation of a larger number of charge traps. This process results in the high values of the pseudo-Hooge parameter. This parameter is high compared to graphene FETs, which is a drawback but it can be also treated as a sign of high sensitivity of GTJs to the local fluctuating environment. I have discussed how increase in the bandwidth and measurement duration lead to noise power accumulation, limiting the SNR. The sensing limit at the target bandwidth is on the order of $10 - 15\,\mathrm{nA}$. In the next chapter I will discuss the measurements in liquid environment and GTJ biosensing measurements.

Chapter 6

Biosensing with Graphene Tunnel Junctions

6.1 DNA Sequencing

6.1.1 DNA Structure and Properties

The cheap and efficient methods of DNA sequencing would enable the advent of personalized medicine based on the DNA sequence. The statistical comparison of alternations in the genome sequence would allow for identification of correlations between specific mutations and the risk of particular illnesses.[13] After understanding such correlations individual patients could be screened to asess the potential risks to their health. DNA sequencing methods could also enhance cancer research[13] and besides the benefits of DNA sequencing of living organisms other applications such as information encoding in DNA strands could develop.[242]

DNA is encoded with four fundamental units, divided into two groups, purine bases (adenine-A and guanine-G) and pyrimidine bases (cytosine-C and thymine-T). All of these bases are connected to deoxyribose sugar creating nucleosides (Fig. 6.1A).[13] The RNA strand instead of deoxyribose is built with ribose sugar groups. Nucleotides form a single strand DNA (ssDNA) when bridged by a single phosphate group, while single nucleosides in cells before joining the strand are in the form of triphosphate nucleosides (Fig. 6.1B).[243] DNA structure is complete when it forms a double strand DNA (dsDNA) helix with a complementary strand running in the opposite direction, creating weak hydrogen bridges between $A-T$ and $C-G$ base pairs.[13]

At physiological pH the DNA phosphate backbone is negatively charged, with approximately one extra electron per nucleotide.[13] The electric neutrality is obtained because of the accompanying counterions in solution (Na^+, K^+, or Mg^+)[13] The negative charge of the backbone allows for the electrophoretic manipulation of DNA strands by means of applied electric potential.[13, 244–246]

The classical sequencing technique (Sanger method) relies on the amplification (copying) of DNA strand by means of Polymerase Chain Reaction (PCR).[13, 247] The amplified analyte is subsequently cut at random points, tagged with fluorescent labels at the end, and detected by the combination of optical detection methods and gel electrophoresis.[13, 247] The Sanger approach generates high costs and is relatively slow.

The complete human genome has approximately 6 billion bases.[247] Sequencing of the full human genome was for the first achieved in 2001 by the International Human Genome Sequencing Consortium[13, 247–249] The state-of-art *de novo* se-

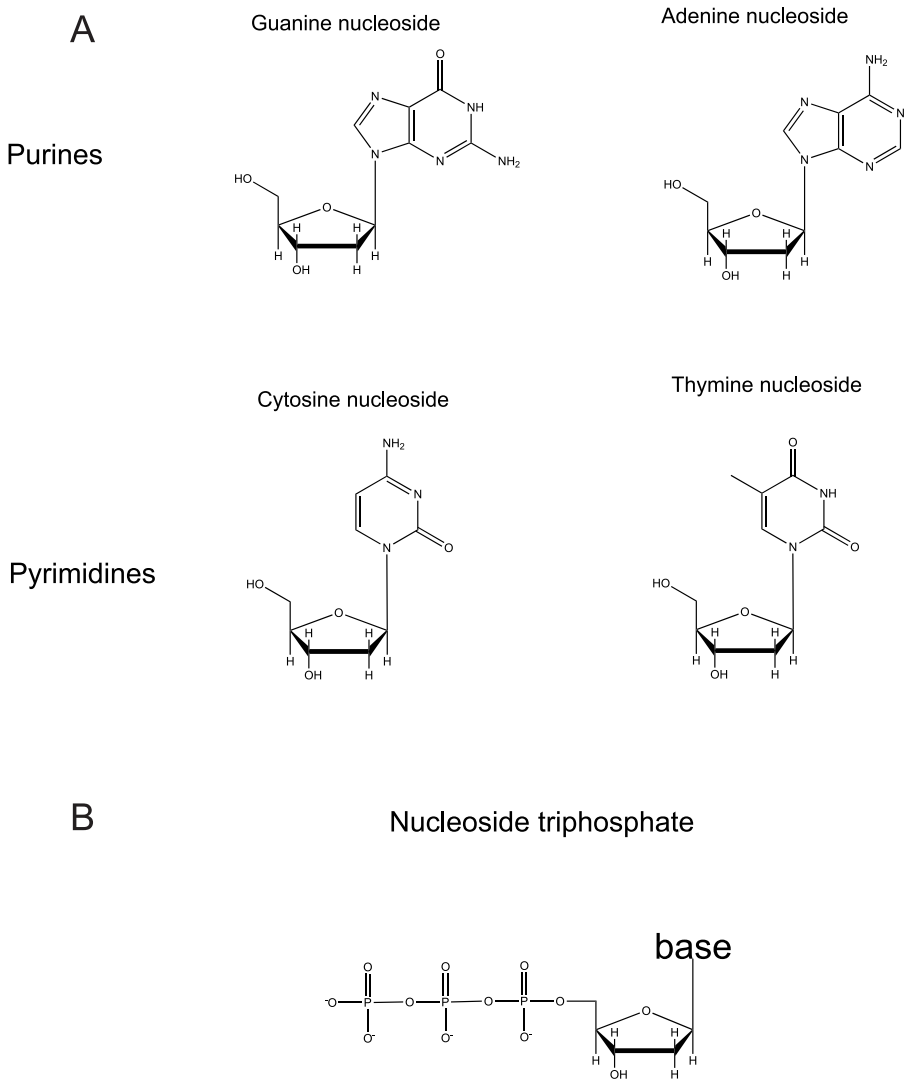


Figure 6.1: A) Chemical structures of nucleosides forming DNA strands. B) Structure of a nucleoside triphosphate, where base can be replaced by A, T, C or G.

quencing of a human genome using Sanger method is estimated to take a couple of months to one year and would cost around 1 000 000 $.[13, 247] The National Institute of Health sets the goal of sequencing the entire genome in less than 24 h for less than 1000 $[13, 14], which would allow for the development of personalised medicine. To achieve this ambitious goal, novel methods have to be developed in order to achieve fast, label-free sequencing at a single molecule level.[13] In particular, methods allowing for continuous sequencing with long read-lengths are necessary. The read-length limit for Sanger method is set at approximately 1000 base pairs[250]

Any envisaged sequencing method has to be sensitive to the differences in physical properties of the individual bases. Approaches relying on the differences in the nucleotide size such as sequencing in nanopores have been proposed. The relatively small differences in volumes of the nucleotides, in the range of $\sim 320 - 360\,\text{Å}^3$ allows for the sequencing in nanopores with similar size. New approaches to DNA sequencing rely on identifying differences in electronic structure of the bases.[13] The existence of a transport gap in DNA was first proposed on the basis of Density Functional Theory (DFT) simulations[13, 251] and subsequently proved in STM measurements showing the gap of $\sim 2.5\,\text{eV}$ with a reproducible conductance peak structure (Fig. 6.2).[252, 253] Other factors such as different dipole moments of bases ($p_A \approx 2.5\,\text{D}$, $p_T \approx 4.1\,\text{D}$, $p_G \approx p_C \approx 7\,\text{D}$[13]), which are large compared to the water dipole moment ($p_{H_2O} = 1.83\,\text{D}$[254]) are also envisaged to affect electron transport in a single base tunnelling experiments.[255]

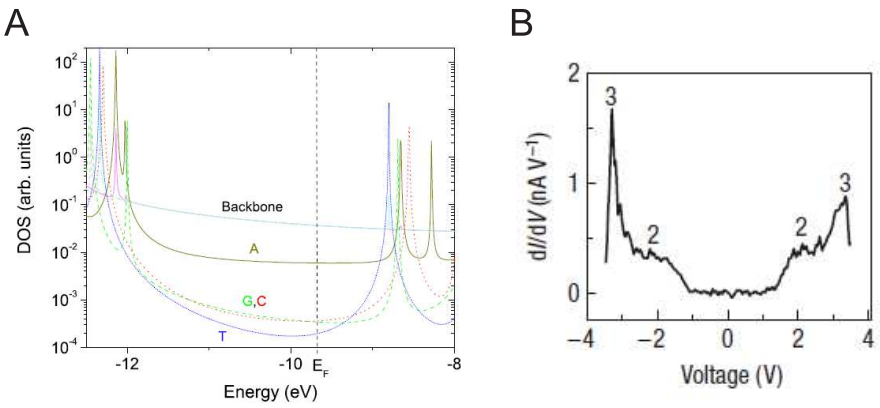


Figure 6.2: Electron transmission of nucleotides. A) DFT simulations of DOS of the individual nucleotides and phosphate backbone in a gold nanojunction. Reprinted with permission from [13]. B) Differential conductance spectrum recorded for a base in dsDNA in an STM junction. Reprinted with permission from [252].

6.1.2 DNA Sequencing in Nanopores

The new generation of sequencing techniques relies on the signal detection from single DNA strands.[250, 256] The first of this type of new-generation techniques was realised in the form of resistive pulse sensing inspired by the Coulter counter used in blood characterisation.[257, 258] The method relies on the detection of changes in ionic current flow through a single pore defined in a membrane separating two chambers (*cis* and *trans*) filled with salt solution, Fig. 6.3A.[13, 14, 258–260] Upon application of the transmembrane voltage the ionic current flows though the pore, with positive ions (*e.g.* K^+ in KCl solutions) attracted to the cathode and negative ions (Cl^-) attracted to the anode.

The conductance of a nanopore is given as[109, 241, 260, 261],

$$G = [\mu_K + \mu_{Cl}] n_{KCl} e \left(\frac{1}{d} + \frac{L}{\pi d^2} \right)^{-1}, \tag{6.1}$$

where d and L are the pore diameter and length respectively, μ_K and μ_{Cl} are ion mobilities and n_{KCl} is total ion concentration. The first term describes the pore access resistance and the second one resistance of the cylindrical pore.[249, 260] At low electrolyte concentrations also the surface conduction term ($\sim \mu_K \frac{4\sigma_S}{d}$) has to be taken into account.[249] If the pore diameter d is decreased the current values will be lowered; typical values in nanopores are on the order of $1 - 100\,\mathrm{nA}$. Nucleotides entering the nanopore limit the pore cross-section available for the ion transport and in the end reduce the ionic current. Decreasing the length L of the nanopore makes its volume commensurate with the size of nucleotides, allowing for their sequencing by analysing the levels of ionic current blockade.

The first realisation of translocation detection protocol has been achieved with organic nanopores by Kasianowicz *et al.* in 1996.[262] The constriction for ionic transport was formed by embedding a pore in a lipid bilayer (Fig. 6.3A).[263, 264] The most commonly used pore is α-hemolysin (α-HL), Fig. 6.3B, which is a toxin produced by the *Staphylococcus aureus* bacteria.[258, 265]

One of the issues of such nanopores is the length of the channel which can accommodate up to 10-12 nucleobases at the same time leading to the convolution of ionic signal.[250, 266] Attempts have been made to resolve this issue, *e.g.* by engineering the protein to make its channel shorter using biotechnology methods[267], or by functionalizing the pores with specific bonding sites[268]. Alternatively a molecular motor (DNA exonuclease enzyme) located at the entrance of α-HL can control the translocation process.[259, 266, 269] The exonuclease enzyme cleaves DNA strand releasing single nucleotides one after another at the controlled rate. It allows for

the full sequencing of the DNA strand.[266] It is also possible to use other pores such as MspA with a lower length and diameter of the constriction (0.6 nm and 1.2 nm respectively), which allows to detect signals from only four bases occupying the nanopore simultaneously.[250, 256, 269]

Despite the success of experiments with organic nanopores they have many drawbacks, which could be alleviated by fabricating pores in thin inorganic membranes (Fig. 6.3C). Inorganic pores are easier to fabricate with flexibility in length and diameter and, as opposed to α-HL, they are compatible with CMOS fabrication process used in semiconductor industry.[230, 232, 241, 255, 260, 271–273] Inorganic pores are also characterised by higher stability allowing to tune experimental parameters such as temperature, salt concentration, pH and electric field in a wider range compared to the organic nanopores, which facilitates the detection of translocation events.[13, 256, 260, 272, 273]

Materials used for the deposition of inorganic membranes include SiN[271, 274, 275], SiO_2[274], Al_2O_3[276], ZnO[277], HfO_2[278] and SiC.[260, 273] The fabrication methods of sub-10 nm nanopores include focused electron beam drilling in TEM; or alternatively FIB microscope usually using heavy Ga^+ ions or helium ion microscope (HIM).[260] After drilling the size of the nanopore can be further shrunk either by means of the electrodeposition of a metal layer[279] or by ion beam sculpting leading to the plastic deformation of the membrane upon bombardment with ions[280, 281].

Despite the advanced fabrication techniques developed, inorganic nanopores are usually lager than their organic counterparts, and they result in a couple of orders of magnitude higher translocation rates, which prevents single base readout due to

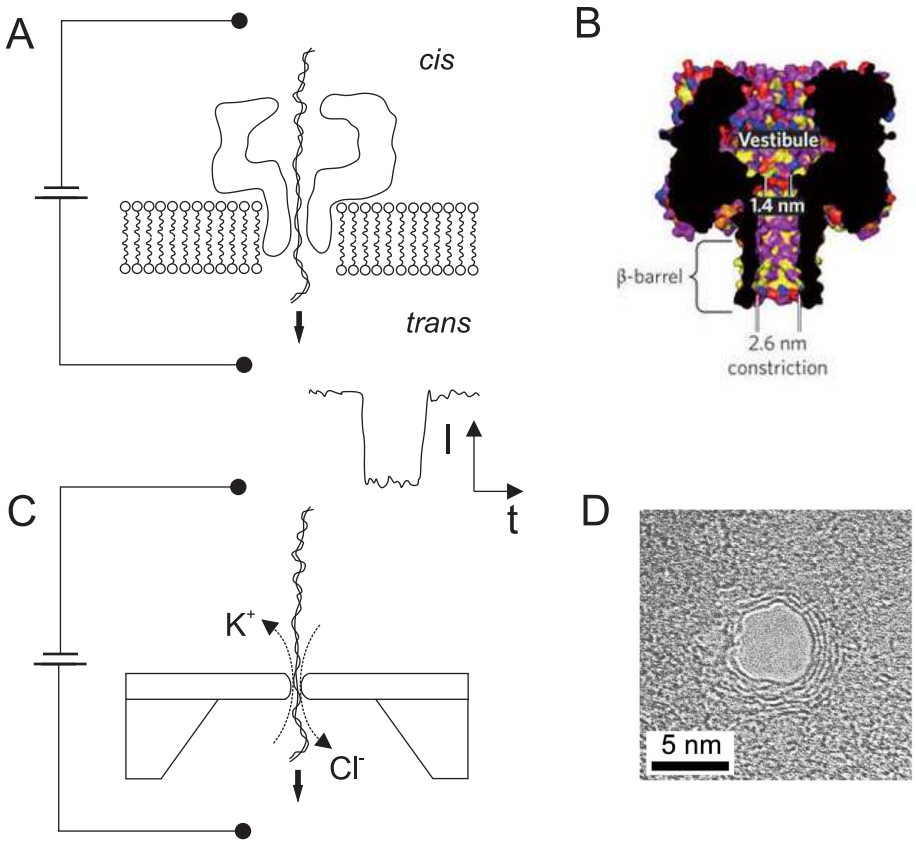


Figure 6.3: Resistive pulse sensing in organic and inorganic nanopores. A) Translocation through an organic α-HL nanopore embedded in a lipid bilayer. B) MD simulation of the α-HL structure. Reprinted with permission from [259] C) Translocation through a nanopore in an inorganic membrane. D) TEM image of a nanopore in a multilayer graphene membrane. Reprinted with permission from [270].

bandwidth limitation.[259] Various experimental parameters[282] such as electrolyte temperature, salt concentration[283], viscosity or pH[284] can be used to decrease fast translocation rates in solid state nanopores. Additionaly trapping DNA strand in two adjacent nanopores[277] or functionalisation of the pore with molecules allows the decreasing the translocation rates.[285, 286]

It has been envisioned that the ultimate spatial resolution would be achieved in the nanopores formed in a single-atom thick membrane.[256, 259] In 2010 three independent groups reported DNA translocation through nanopores in suspended single-layer graphene membranes (Fig. 6.3D).[270, 287, 288] The translocation events were detected in TEM-drilled nanopores with diameters down to 5 nm.[270, 287, 288] Since then, also other 2D materials, such as MoS_2, have been used as membrane materials.[289] Despite theoretical predictions of possibility of achieving single-base resolution in such devices[290] a sequencing operation has not been demonstarated yet[291]. The possible explanation is high sensitivity of the graphene nanopores to the orientation of nucleotides.[290]

Despite the atomic thickness of graphene membranes the possibility of single base resolution in such nanopores is debatable, also due to a highly localized electric field that is generated in such nanopores ($E \sim \frac{V}{L}$).[292] This field extends beyond the geometrical volume of the pore[293] rendering the ionic current sensitive to the volume beyond the geometric volume of the nanopore occupied by a base.[291] Therefore, other methods are necessary to obtain single base resolution. The tunnelling sequencing protocol is one of them, as will be discussed in section 6.5.

6.2 Graphene Tunnel Junction Measurements in Liquid Environments

All practical methods of detection of DNA require it to be dispersed in liquid environment. This is true also for the tunnelling sequencing protocol.[13, 294–296] In order to make GTJs compatible with measurements in liquid environments I designed a flow cell (Fig. 6.4) attached to a PCB. A chip with graphene devices is glued to the surface of the PCB with biologically inert Kwik-cast elastomer. Wirebonds are made in order to connect device contact pads to the leads of the PCB. Subsequently a PDMS (polydimethylsiloxane) flow cell is attached to the surface of the PCB. The flow cell has a chamber with 0.9 mL volume aligned with the chip. The flow cells were prepared in house by filling the 3D-printed moulds with PDMS and curing it at ambient conditions. Flow cells are disposable and for each set of devices I use a new one to prevent cross-contamination.

The flow cell is connected to three external tubes. One of them (Inlet 1 in Fig. 6.4) is connected to the automated pump (Cavro XLP 6000) capable of controlling liquid flow with µL precision and flow rates on the order of $1 - 1000\,\mu\mathrm{L\,s^{-1}}$. Two additional outlets allow for filling the flow cell with analyte solution and rinsing it with solvent or dry:

- Filling is achieved by closing the Outlet 1, opening Outlet 2 and pumping the liquid until flow cell is filled
- Rinsing with solvent is achieved by closing the Outlet 2, opening Outlet 1 and pumping solvent

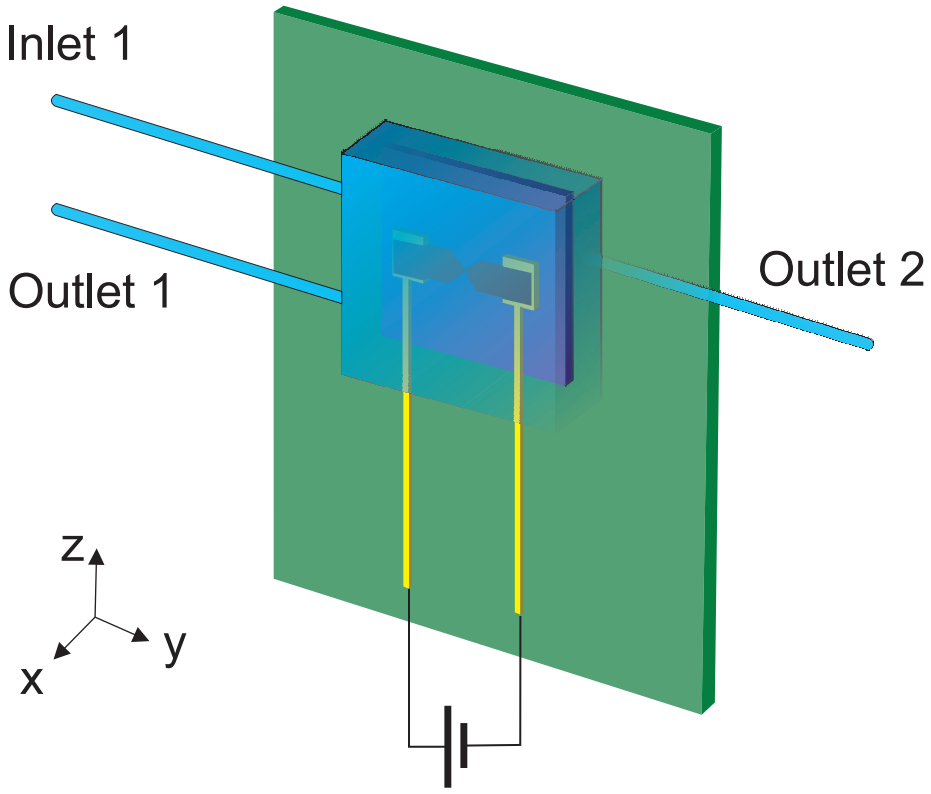


Figure 6.4: Diagram of a PCB and flow cell for liquid measurements.

- Emptying of the flow cell is achieved by closing Outlet 2, opening Outlet 1 and pumping air until the flow cell is empty

6.2.1 Electrochemical Effects at Nanoscale Electrodes

At the interface of a conductive phase in electrolyte solutions there occurs a specific interaction: if the electrode material is not inert, its ions may be released by means of electrochemical etching.[297] Conversely, the inert electrodes, allows for the charge transfer through the interface without affecting the electrode structure.[297] This process can lead to the oxidation or reduction of ions in the solution, for example

oxygen and hydrogen. The kinetics of this process are determined by the work function of electrodes and the energy level structure of ions.[297]

If transport in water includes an ionic contribution it is due to the water splitting reaction[298], which involves reduction at a cathode $H^+ + e^- \rightarrow H$ and oxidation at an anode $OH^- \rightarrow OH + e^-$.[298] On the large interelectrode distances, where tunnelling is not observed, the charge transport relies solely on ionic processes, which are limited by the electron trasfer rate at the solid-liquid interface and by the diffusion constant of H^+ and O^- ions in water.[298] In the equilibrium the net flux of charge in both direction is zero, however the application of external bias can disturb the equilibrium.[297]

Like many other physical phenomena, electrochemical processes at micro- and nanoscale have different characteristics compared to their bulk counterparts. This effect has been harnessed in Scanning Electrochemical Microscopy.[299–301] The miniaturization of electrodes for liquid measurements leads to a qualitative change in electrochemical processes. For electrodes with a characteristic size less than 20 µm the ion-diffusion mode changes from planar to high density, 'ultramicroelectrode' ion transport (Fig. 6.5).[299] This change of the transport regime leads to extremely high ionic current densities at microelectrodes, which are governed by the electron transfer rates at the interface rather than ion diffusion rates in the solution.[299] Very fast diffusion processes around microelectrodes mean that electrochemical signals can be detected even in solutions with very low concentrations of electroactive species.[299] In the result it is often difficult to unambiguously distinguish between tunnelling or electrochemical transport in STM measurements.[300]

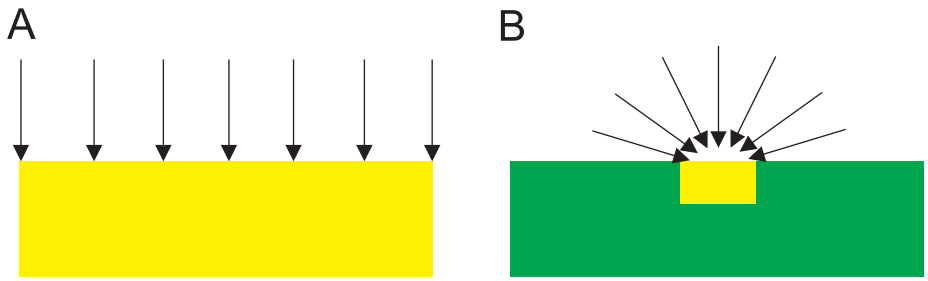


Figure 6.5: Comparison of ion diffusion modes: A) Planar diffusion mode typical for macroscopic electrodes. B) Non-planar diffusion for micrometer electrodes with high diffusion rate[299].

Beasuse of electrochemical effects the insulation of the electrodes is a crucial aspect of measurements in liquid environments. Electrochemcial effects and ultramicroelectrode ion transport mode may be a problem in GTJs, which consist not only of nanoscale graphene electrodes, but also micron-size gold leads. This can give rise to spurious ionic currents[302] and introduce increased levels of capacitance noise[303]. Since the early studies on STM in electrochemical environments it is known that the electrodes have to be properly passivated and electrochemically inert, with reduced area of the electrodes exposed to the liquid environment, in order to decrease the spurious Faradaic currents.[304–306] Unprotected electrodes in electrolytes give rise to high ionic currents, which can obscure the molecule signatures.[61, 62] Different kinds of passivation have been used including electrophoretically applied paint[305, 306] and Apiezon wax.[304, 307] Nanoscopic lithography-defined gold electrodes have been covered with a sputtered SiO_2 layer[307]

Insulation has been also applied to Au MCBJs by CVD of SiO_2 layers[58, 61] and ALD of Al_2O_3 layers[62]. The passivation layer is applied prior to the formation of a junction, meaning that almost the entire metallic surface is coated. Upon breaking of

the junction, a small area of $\sim 1\,\mathrm{nm}^2$ is released, supporting tunnelling current.[61, 62] It has been found that increasing the thickness of the insulation layer L leads to a decrease in I_{RMS} noise values as $I_{RMS} \sim \frac{1}{L}$[58] This shows that the capacitance of the electrode-insulation-electrolyte system couples to the the voltage noise of the amplifier, giving rise to capacitance noise in analogy to the noise behaviour in nanopores.[58] Using the low-k materials (i.e. SiO_2 instead of Al_2O_3) decreases noise further.[58]

6.2.2 Insulation of Graphene Tunnel Junctions

To prevent leakage currents in GTJs, I investigated possible insulation methods. Comparison was made between two approaches, using electron-beam evaporated layer of SiO_2 (50 nm thick) and positive resist PMMA 495 (100 nm thick). The tests of insulation were performed on typical devices consisting of a SiN substrate and gold electrodes, however without graphene ribbons. The rationale was to verify if there are any spurious current contributions in a system without a tunnelling conduction path. Besides two kinds of passivation I also tested non-insulated devices as a control experiment.

The fabricated devices were tested in three environments: dry, DI water and buffer solution (1 M KCl, 7.5 pH HEPES buffer). The insulation layers were characterised by means of measurements of the current response to triangular voltage waveforms with 50 Hz sweeping frequency and ± 100 mV amplitude. The resulting $I - t$ traces were turned into current histograms, which are presented in Fig. 6.6

As can be seen in Fig. 6.6A, D and G, dry devices with different insulation types

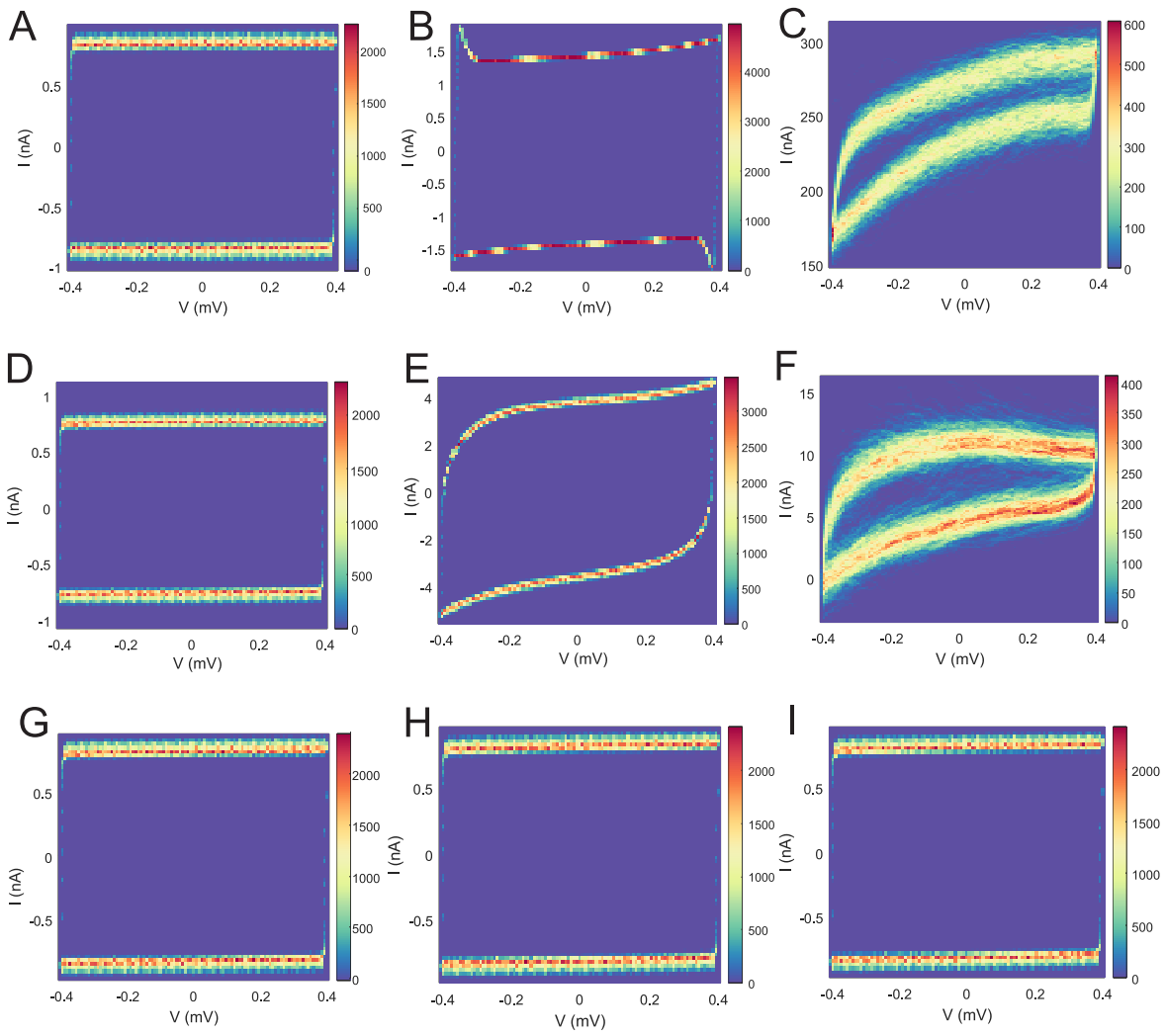


Figure 6.6: Results of insulation study showing histograms of parasitic currents measured in response to 50 Hz and ±400 mV amplitude triangular voltage waveform. Measurements were performed on devices in dry, DI water and buffer solution environment (from left to right) with A-C) no insulation D-F) 50 nm SiO_2 insulation and F-H) 100 nm PMMA 495 insulation.

exhibit the same level of current, $\sim 0.8\,\mathrm{nA}$. Its flat profile with respect to voltage, taking into account the steady voltage increase rate, points at the clearly capacitative mechanism of this current. Assuming that the relation between applied voltage $U(t)$, capacitance of the electrodes C and the resulting charge q is given by $C = \frac{q}{U(t)} \rightarrow q = CU(t)$, and using the definition of current $I = \frac{dq}{dt} = \frac{dCU(t)}{dt} = C\frac{dU(t)}{dt} = const \times C$,[298] these results indicate that different insulation layers do not increase the estimated inter-electrode capacitance ($20\,\mathrm{pF}$).

The differences between examined insulation methods are revealed in traces obtained for DI water, presented in Fig. 6.6B, E and H. While the PMMA-insulated device shows current at exactly the same level as the dry device (Fig. 6.6 G and H), the bare and SiO_2 insulated devices show an increased level of the parasitic current. I tested ten devices with each insulation type. Similar IV curves to the presented were obtained for all devices without insulation and with PMMA insulation. There was more variability in SiO_2 insulated devices (three out of ten did not show any increase of current compared to the dry state.

Finally in Fig. 6.6C, F and I there are presented IV histograms for devices tested in buffer solution. Large parasitic current values were obtained for all bare devices and eight out of ten SiO_2-insulated devices (the precise shape and current level differs from device to device). I attribute these currents to non-faradaic or Faradaic ionic currents resulting from redox processes due to reduction/oxidation of buffer molecules. Lower values of the current obtained in the case of SiO_2 insulation may indicate that although the insulation layer is applied it may not be continuous and it can contain cracks or pinholes allowing solution to penetrate it and access the

electrode surface.

In contrast, in the case of PMMA insulation I rarely observed the increase in parasitic current and the majority of the devices (eight out of ten) exhibited unaltered level of parasitic current compared to the dry devices even in the buffer solution. Therefore the PMMA insulation layer was used for subsequent measurements.

The use of the PMMA insulation layer impedes wirebonding, preventing the bonded wire from making a good contact with the device contact pad. Therefore additional EBL step was added to remove the insulation layer over the contact pads (Fig. 6.7B). Since wirebonds and contact pads are not insulated and could give rise to the spurious ionic effects I manually covered those elements with PDMS layer (Fig. 6.7C). In order to prevent the PDMS from spreading over graphene devices I used longer electrodes (Fig. 6.7A). 1.2 mm-long electrodes were patterned, leaving enough space for the carefully applied insulation (Fig. 6.7C). A very thick PDMS layer should also have a positive effect on decreasing capacitance of the devices. Devices prepared in this way are fully passivated with the exception of self-aligned pore over the graphene junctions.

Using soft organic resist is beneficial because of the ease of exposing the tunnel junction area to the analyte solution. It is necessary to remove the insulation from the junction area in order to detect the influence of liquid environment or analyte on the tunnelling current. In the case of SiO_2 insulation it would be necessary to include an additional lithography step to pattern the openings in insulation. A PMMA insulation layer provides an easier opportunity to proceed. The electroburning process generates high temperature in the constriction area, on the order of ~ 600 K.[87, 88,

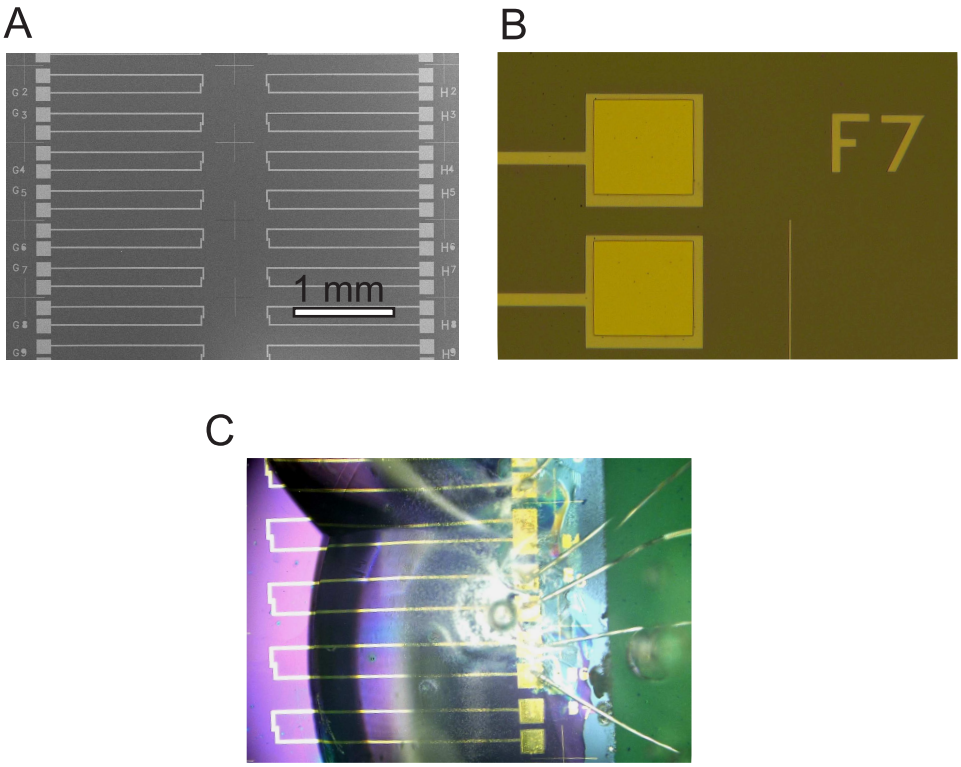


Figure 6.7: Chip design and insulation for liquid measurements. A) SEM image of the remote electrodes chip. B) Optical microscope image of the chip with PMMA passivation layer and openings over contact pads. C) Optical image of wirebonded devices with wires insulated with PDMS.

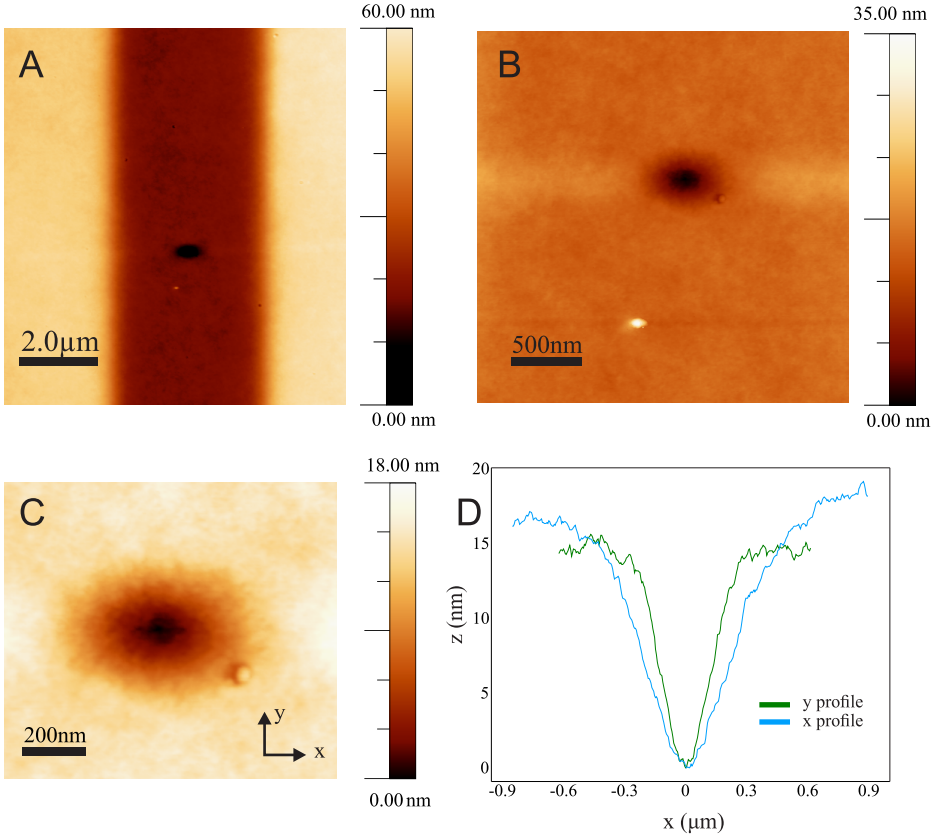


Figure 6.8: A-C) AFM images of the opening in the PMMA insulation layer. D) Extracted profile of the opening in the PMMA layer in x and y direction.

308] This temperature is sufficient to locally remove the resist by thermal decomposition and evaporation.[308] I can thus fabricate an opening in the PMMA insulation layer self-aligned with the tunnelling junction (Fig. 6.8A-C). I confirmed the formation of openings in the resist by AFM technique. The typical size of the pore is on the order of $600 - 700\,\mathrm{nm}$ (Fig. 6.8D). I confirmed that IV curves measured for PMMA insulated devices did not differ in any aspect from the curves for unmodified devices.

6.2.3 Electrochemistry of Graphene

Minimizing the area of graphene exposed to ionic solution is important, becasue electrochemical processes can occur also at the surface of graphene. Studies of electrochemical activity of CVD graphene have shown that graphene has on average one order of magnitude faster electron transfer rates than a graphite electrode, which is attributed to the surface corrugations increasing activity of graphene.[309] I therefore expect that the electrochemical processes could influence the transport in non-passivated GTJs in electrolyte solutions.

In fact, it has been shown that the ionic current at graphene edges is much higher compared to the basal contribution.[310] Measurements of the ionic current in HCl solution at the edge of graphene sandwiched between two Al_2O_3 layers, to prevent basal currents, showed that the edge contribution can be significantly higher than basal current ($10^4\,\mathrm{A\,cm^{-2}}$ compared to $10^{-8}\,\mathrm{A\,cm^{-2}}$ for basal currents).[310]

What is more the redox potentials found for bulk reactions can be reduced by the high density of the adsorption sites at a graphene edge. The resulting voltage shifts can be on the order of 0.1 eV.[310] The electroburning process is also expected to leave the oxygen terminated graphene edges.[88] The electrochemical studies of graphene oxide proved that in this inhomogeneous material consisting of graphene clusters decorated with oxidation debris, the latter is the major contribution to electrochemical processes.[311] Graphene oxide is characterised with intrinsic electrochemistry, meaning that it can undergo redox process on its own without additional redox active species in the system. Because of the nanoscale size of the investigated graphene electrodes and presumably a defected edge structure the electrochemical effects can

play role in the measurements in electrolyte solutions. I will verify later in section6.4 if electrochemical effects due to the intrinsic electrochemical activity are present in water environment without any purposely added electroactive species.

6.3 Tunnelling in Water

6.3.1 Nanoscale Structure of Water

Implementing efficient insulation allows to reduce electrochemical effects. However the liquid environment can still have a significant impact on tunnelling current. In order to understand the observed analyte signal and to prove that it is not a side effect of water presence I will first analyse the impact of the liquid environment on GTJs.

I start by giving an overview of the water structure at the nanoscale and at graphene interface, which is qualitatively different to its bulk properties[312, 313], and which can influence dynamics of the observed tunnelling processes. The water-graphene interface is weakly hydrophobic with a wetting angle of $\sim 90°$.[312] The wetting angle may be increased by introducing structural defects in the graphene lattice, or it may be turned more hydrophilic by introducing polar functional groups such as -OH.[312]

The simulations of water adsorbed on the graphene surface show a high level of ordering of molecules into the planar layers parallel to the graphene surface (Fig. 6.9A).[312] This indicates a dominant interaction at the interface and with the increasing distance, further than three layers from the interface, water adopts

random bulk-like structure.[312] Within the first three layers, the structure is random without any preferred orientation of molecules. The separation of water into layers allows for relatively high in-plane diffusion rates, while out-of-plane diffusion is impeded.[312] Such ordering in nanoconfined water allows for flow rates orders of magnitude higher compared to the bulk values.

In GTJs the tunnelling distance between graphene electrodes is similar to inter-plane distances in the mentioned simulations. It is therefore expected that GTJs may facilitate the formation of stable layered water structures in the gap. Some water structures can lead to the formation of charge traps at water-electrode interfaces.[73] I assume that the nanoconfined water structures can stabilise such charge traps on time scales detectable with the bandwidth available in the presented measurements, as opposed to the water molecular motions at time scales of fs[314].

Molecular Dynamics (MD) simulations of water confined between two graphene sheets separated by $7 - 20\,\mathrm{nm}$ distance have shown that the water layers adjacent to grahene always have the highest density of water molecules (Fig. 6.9B).[313, 315] It has been also found that the slight change of inter-plane distance, by $1\,\text{Å}$ significantly changes the structure of water layers and the resulting viscosity changes by orders of magnitude. The highest viscosity is obtained for the graphene inter-plane distances commensurate with the relaxed water-layer distances, while at distances where interlayer water molecules occur, mixing between layers is enhanced leading to the decrease in viscosity.[313]

I expect that these effects will also lead to the variability in the environment of GTJs. Junctions with different gap size can accommodate various water structures

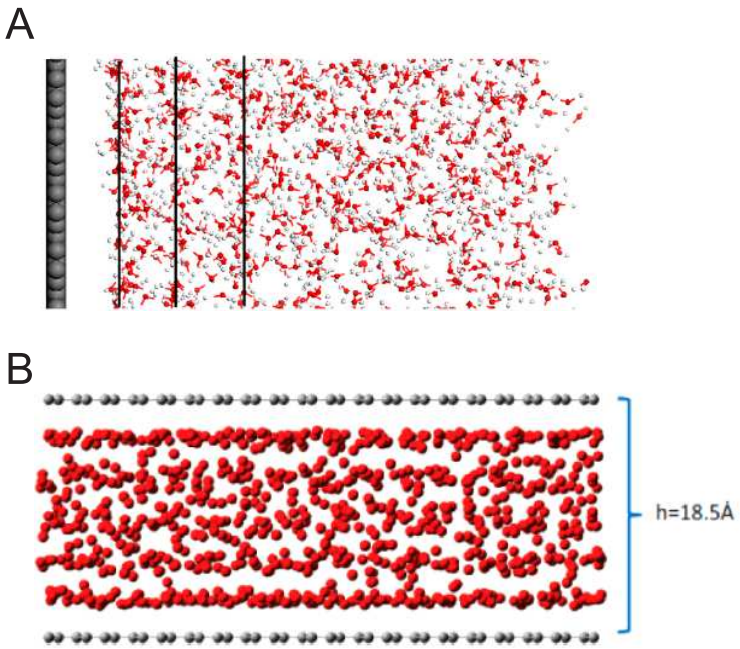


Figure 6.9: Water nanostructure at graphene interface. A) Ordering of water into layers at the graphene interface. With the increasing distance water molecules take random orientations. Reprinted with permission from [312]. B) Structure of water layers formed in a narrow channel between two adjacent graphene planes. Black lines corresponding-to high-density water planes are located at 3.2, 6.2, and 9.6 Å from the graphene surface. Reprinted with permission from [313].

characterised by different levels of stability and structural fluctuations affecting the electrostatic environment.

6.3.2 Electric Double Layer

In solutions containing free ions their particular arrangement is observed at charged surfaces of conductors. These interfaces consist of surface charge in the conductor and oppositely charged ions in the solution (Fig. 6.10A)[316] and are known as Electric Double Layers (EDLs). EDLs contribute to the screening of electric potential at the electrode (Fig. 6.10B), however they are insufficient to fully screen the surface charge and the area of increased ion concentration extends beyond the first ion layer.[316] The ion concentration decreases exponentially in the form of a diffusive layer with the distance from the interface. The ion concentration decay is characterised by the Debye length[316]

$$\lambda_D = \sqrt{\frac{\epsilon\epsilon_0 kT}{2nz^2e^2}}, \tag{6.2}$$

where n is bulk ion concentration. Typically $\lambda_D = 1 - 100\,\mathrm{nm}$, depending on the ion concentration. In the absence of ions the water dipole polarisation is responsible for charge screening.[301] EDLs can be induced by either applying a voltage to the conductive electrodes or by changing the pH of solution.[317] Even at the neutral pH, water is characterised by non-zero concentration of dissociated ions ($6 \times 10^{13}\,\mathrm{cm}^{-3}$ for OH^- ions), which can be polarized and develop an EDL upon application of a voltage to the electrodes.[318] In the case of graphene, EDL effects and induced potentials can have significant impact on the transport. Because of the low density

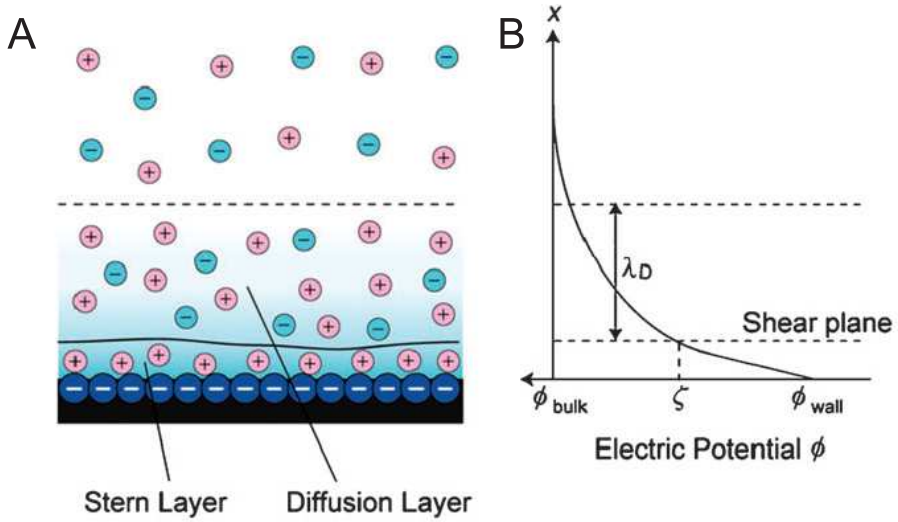


Figure 6.10: Electric Double Layer in ionic solution formed at a negatively charged surface with a negative charge layer confined to the conductor and oppositely charged ions grouping at the surface. A) Schematic diagram of an EDL. B) Corresponding electric potential decay due to EDL screening effects. Reprinted with permission from [316].

of states around Fermi level, graphene is not efficient in screening external electric fields. DFT calculations have shown that ions adsorbed at graphene surface generate fields extending deeper than five graphene layers in the direction perpendicular to its plane.[319] Similar results were found for the measurements of EDL capacitance on graphene.[320]

On the basis of tunnelling currents measured in MCBJ it has been hypothesized that EDLs can influence the tunnelling barrier. Steeper $I-d$ tunnelling current decay curves have been observed in water, which has been attributed to the alignment of water dipoles around electrodes so that they screen the applied voltage.[61] In contrast, tunnelling in the non-polar organic solvent has been shown to yield slower

decay of the tunnelling current over distance compared to air, indicating enhanced tunnelling through the intermediate molecular states.[61] The efficiency of water EDL screening mechanism depends on the ratio of tunnelling distance and the thickness of the Debye layer.[61] Large Debye lengths allow for a larger number of possible interelectrode ion configurations, and increase the variability of the current values.[61]

Measurements of tunnelling currents in junctions in non-polar organic solvents yield negligible levels of leakage currents, comparable to the noise in air measurements, implying that the ionic or EDL-related effects are dominant sources of noise in water measurements.[58] The high frequency noise in such systems will scale as $\sim C_{EDL}^2$, with the capacitance of a EDL given as

$$C_{EDL} = \epsilon_E \epsilon_0 \frac{S}{\lambda_D}, \tag{6.3}$$

where ϵ_E is the is relative permittivity of electrolyte and λ_D is the Debye screening length.[58] As I will show later the presence of water and induced EDL at the GTJs surface affect both tunnelling current and electric noise.

6.3.3 Influence of Liquid Environment on Tunnelling Current

The topic of tunnelling in liquid environments is relatively new, with the first experiments on STM imaging under such conditions dating back to 1980's.[300, 304] To date, there is no agreement about the particular transport mechanisms involved or the relevant components of the system affecting it. The simplest approach is to

treat the tunnelling medium filling interelectrode gap as continuum characterised by a macroscopic work function, which affects the tunnelling probability.[321–323] Measurements in large area gold cross-bar junctions have shown that an ensemble-averaged tunnelling barrier is dependent on the strength of interactions between liquid molecules rather than their electron structure or ionization potential.[323, 324] It has been shown that liquids with large cohesive energies have lower tunnelling barriers and in general can be divided into three groups, hydrogen bonding, polar and non-polar solvents in the order of increasing tunnelling barrier.[323, 324] In break junction measurements it is assumed that on nanometric distances the dielectric continuum approach is insufficient and the particular structure of the solvent molecules affects the tunnelling current.[73, 321, 322] The investigation of such effects in single molecule junctions is more cumbersome as both the analyte and solvent molecules can form a molecular junction. Also both transport mechanisms, Simmons tunnelling through the energy barrier and Landauer resonant transport through the molecular level, can produce similar IV curves impeding discrimination between these two processes.[325]

6.3.4 Influence of Liquid Environment on Molecule Measurements

The presence of polar liquids in the transport through a polar single molecule leads to the effective gating action.[315] Water dipoles surround the charge-transport mediating organic molecule in order to compensate for its intrinsic dipole moment. Simulations show that such configurations are robust with alignment observed also

in the second solvation layer, making it similiar to a minatiurized molecular EDL. The arrangement of water dipoles around the central molecule induces a net electric field, which shifts the transmission spectrum towards lower energies.[315, 326, 327] The overall shape of the transmission spectrum is conserved with the only addition of sharp peaks due to the resonant transport through water states.[315] The simulations have shown that the time-averaged gate potential due to water molecule field is equal to 0.6 eV reducing the current through a benzenedithiol moleclue by 35 % and at the same time giving rise to $\sim$ 20 % fluctuations in the value of current due to water structure dynamics.[315] The described mechanism is not observed in non-biased and non-polar carbon structures, as they do not induce any alignment of water dipoles around themselves. However, the effect of current fluctuations is stronger in insulating CNTs, where transport is dominated by interband-tunnelling.[315]

The experimental investigation of the solvent effect on transport through a benzenediamine molecules in MCBJs implied a similar mechanism, however gating was assumed to shift the workfunction of gold electrodes rather than molecular levels.[322, 328, 329] The explanation involves adsorption of the analyte or liquid molecules at the binding sites on the gold surface. Such process is accompanied by charge transfer which shifts the electrode work function.[322, 328] The gold Fermi level shifts with respect to the benzenediamine Highest Occupied Molecular Orbital (HOMO) level and leads to the increase or decrease in current up to 50 %[322, 328, 329]

In general the liquid environment can lead to the dipole polarization effects on mesoscopic scales at electrode surface or on nanoscale when solvent molecules screen the dipole moment of the molecule present in the junction. The third option is the

formation of a molecular junction by the solvent molecules. In the next section I will verify which of these scenarios is realised in GTJs in the liquid environment.

6.4 Tunnelling in Graphene-Water-Graphene Junctions

To check the influence of the liquid environment on a tunnelling current in GTJs I characterised, at first, all of the devices in a dry state by measuring 120 s long traces at DC voltages from −200 mV to 200 mV in 5 mV increments. Measurements were performed with Axopatch 200B at 100 kHz sampling rate and with 10 kHz low-pass filter. Immediately afterwards 18 MΩ cm DI water from the Milli-Q water filter system was introduced to the flow cell by means of the Cavro automated pump. After flushing the tubing and flow cell with 10 mL of water the flow was stopped and measurements were repeated for devices in the DI water environment.

On the basis of recorded $I-t$ trace I calculated the mean current and plotted it as a function of applied bias. In Fig. 6.11A-D I show typical mean IV curves for four different devices. All of these curves were fitted with Simmons tunnelling curves[15], indicating tunnelling as a probable transport mechanism. In ∼70 % of the measured devices I have found that for a given device, the current level recorded in water is lower compared to the initial dry state, which in agreement with the observations of Arima *et al.*[61] I hypothesize that the formation of EDL because of the polarization of water molecules on the graphene surface partially screens the applied voltage and increases the tunnelling barrier. The decrease in current is in contrast to the increase,

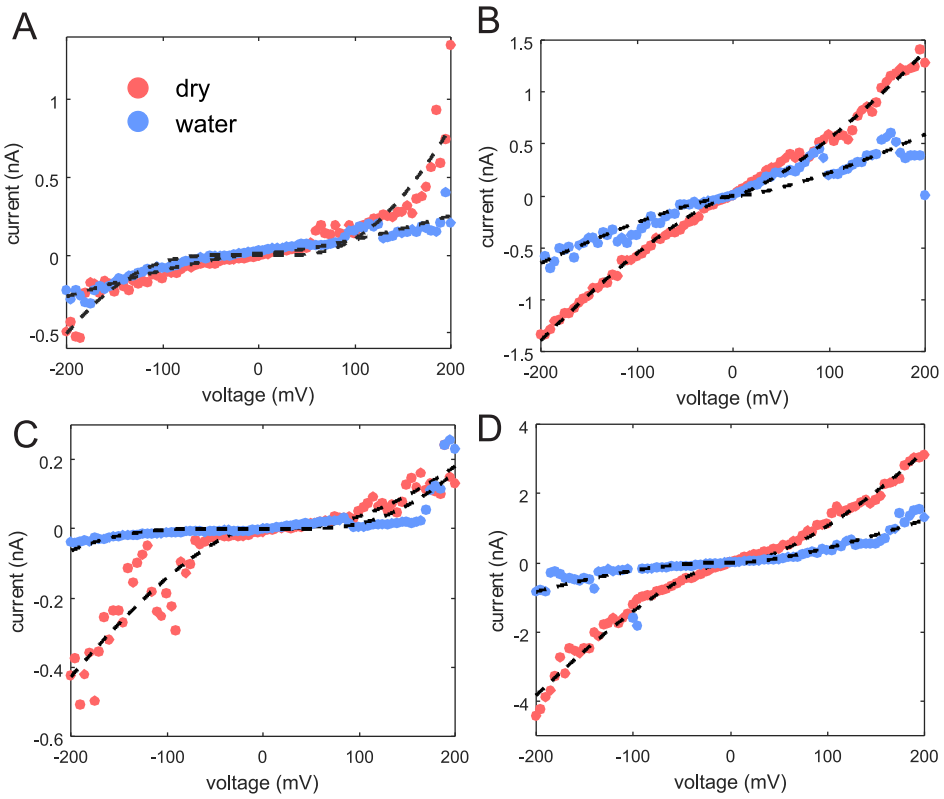


Figure 6.11: Comparison of the IV curves measured for four different devices in dry state (red points) and after wetting in water (blue points). Dashed lines show Simmons model fitted curves (See Appendix A).

which would be expected in the case of the electrochemical effect. It allows me to think that at least in DI water the PMMA insulation method with a pore over a GTJ is sufficient to prevent electrochemical effects.

$I - t$ traces recorded for different devices and at different voltages were subsequently used to calculate noise spectra, which in majority yielded the linear $1/f$ profile. I performed the least-square fit to obtain the γ exponent values. The distribution of the fitted parameter is plotted in Fig. 6.12. For devices in a dry state I observed a single peak with the maximum around $\gamma = -1$ in agreement with the

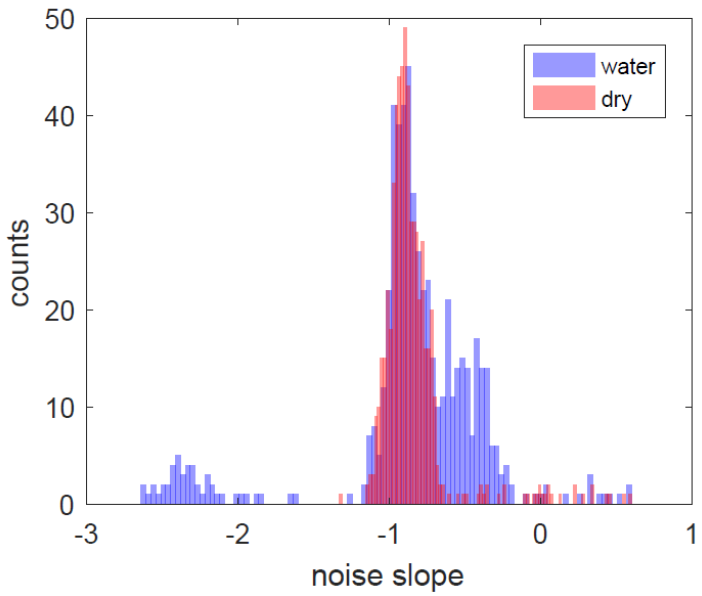


Figure 6.12: Distribution of the γ slopes of fitted f^{γ} noise spectra, measured at different voltage in $-200\,\mathrm{mV}$ to $200\,\mathrm{mV}$ range for seven devices in dry conditions and in water environment.

previously presented discussion of $1/f$ noise in graphene devices at room temperatures. A similar peak was observed for measurements in water. For the noise spectra recorded in water the distribution is wider and there are additional slope peaks at $\gamma \approx -2$ and $\gamma \approx 0.5$.

At first I will look at noise properties of the devices with a well-defined $1/f$ slope $\gamma = -1$. Current values for a given device at a particular voltage are usually lower after introducing DI water. The opposite trend is observed for the current standard deviation σ_I plotted versus mean current, data for devices B and D from Fig. 6.11 are presented in Fig. 6.13A and C. As I observed before, the scaling of σ_I with current is linear, indicating that current serves as a readout method to probe the existing

noise but it does not generate it.[145] The slope of $\sigma_I - I$ dependence for devices measured in water is higher compared to the dry devices, indicating the additional source of noise in water environment. The same conclusion may be drawn on the basis of the flat distribution of normalised noise spectra S_I/I^2 plotted as a function of voltage (Fig. 6.13B and D). As in dry devices, also for devices in water there is no dependence of the normalised noise amplitude (pseudo-Hooge parameter) on voltage, however, there is a systematic difference in the noise level for dry and wet devices, with devices in water exhibiting increased noise.

Increased noise might be related to the molecular rearangement of water molecules in EDL introducing variability by changing the electric field in the vicinity of the junction. EDL in electric circuit analysis is treated as a capacitor[297], which may lead to an increase in high frequency noise. Until now the presented analysis is valid for the traces with slopes $\gamma \approx 1$. However, it does not explain the observation of traces with either higher or lower noise slope values.

In order to understand the widening of the noise slope distribution and slope values $\gamma \neq -1$ upon introducing DI water I look at the individual current noise spectra. In Fig. 6.14A I plot typical noise spectra for a dry and wet device. Both of these curves follow the linear $1/f$ trend with a similar slope and only differ in the absolute noise level. In Fig. 6.14C I plot a noise spectrum for the device with a low slope $\gamma \sim -0.5$. The corresponding dry device noise spectrum again has a usual $1/f$ noise spectrum. The device in water, however, is characterized by a relatively flat noise spectrum. In many noise spectra I also observe a small bump indicative of the superposition of a Lorentzian peak and a $1/f$ noise spectrum. I assume that the

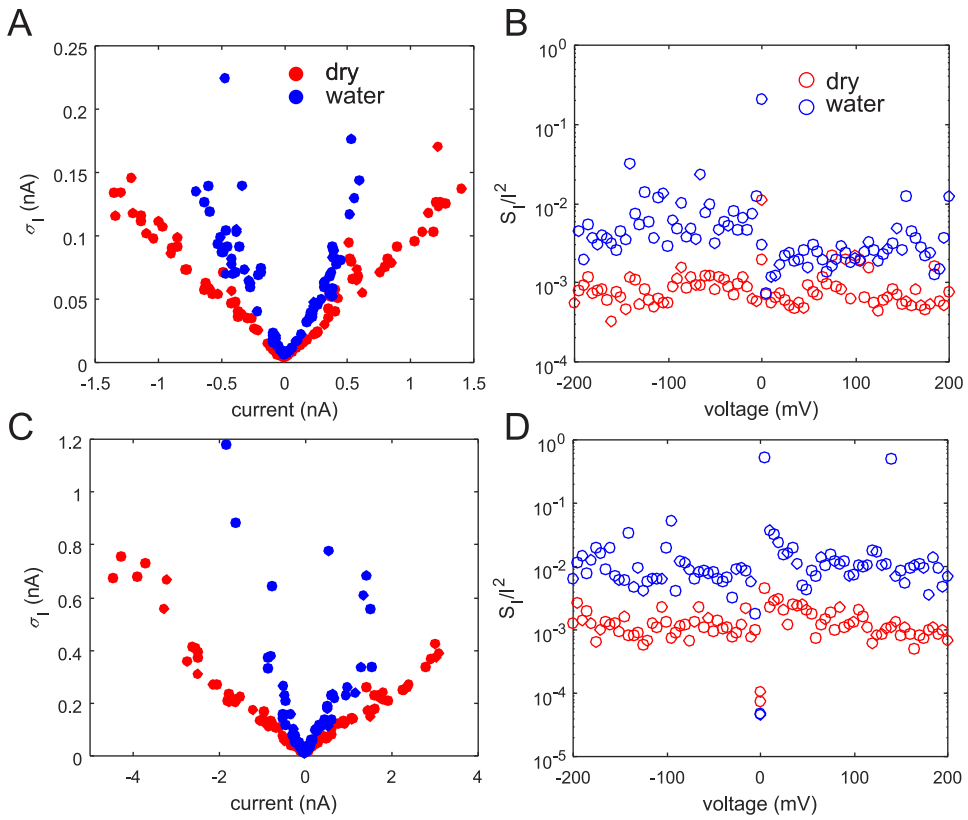


Figure 6.13: Noise comparison in ambient and water environment. A) and C) Standard deviation of current traces measured in dry devices and in water plotted versus mean current. B) and D) Normalised noise amplitude plotted in the function of applied voltage. A and B are results for device B from Fig. 6.11, C and D are results for device D from Fig. 6.11.

spectra with γ slope different to 1 are the manifestation of Lorentzian noise. Noise slopes $\gamma \sim 2$ would correspond to the slow fluctuations with low corner frequency, which in the measured frequency range would show only the steep roll-off and $\gamma \sim 0.5$ corresponds to the fast fluctuators with high characteristic frequency and plateau observed for the majority of the recorded frequency range (as in Fig. 6.14C).

To verify this hypothesis I looked at the $I - t$ traces and corresponding current histograms. An $I - t$ trace for the device showing typical $1/f$ noise in Fig. 6.14A is shown in Fig. 6.14 E. The trace shows typical featureless fluctuations characteristic of $1/f$ noise.[138, 145] The only difference between the dry device and the device in water environment is different current level. The corresponding normalized current distribution is shown in Fig. 6.14B. The histograms for ambient and water environments were successfully fitted with a lognormal distribution, as expected from the tunnelling current at room temperature.

The same device measured at different voltage and different time showed a qualitatively different, transient behaviour. In some fragments of the $I - t$ trace I found signatures of perturbed TLF in water trace, while I have never observed such features in dry devices at room temperature (Fig. 6.14F). TLF current traces give rise to a bimodal current distribution as shown in Fig. 6.14D, note that the relative height of the second peak is low due to the low number of RTS peaks counts.

I emphasize that I have not observed the features of Lorentzian noise in dry devices at room temperature. Such features can be observed only in DI water. In contrast to the 77 K measurements, where a given type of fluctuation could last for many hours, in water measurements TLF is observed for short time periods on the

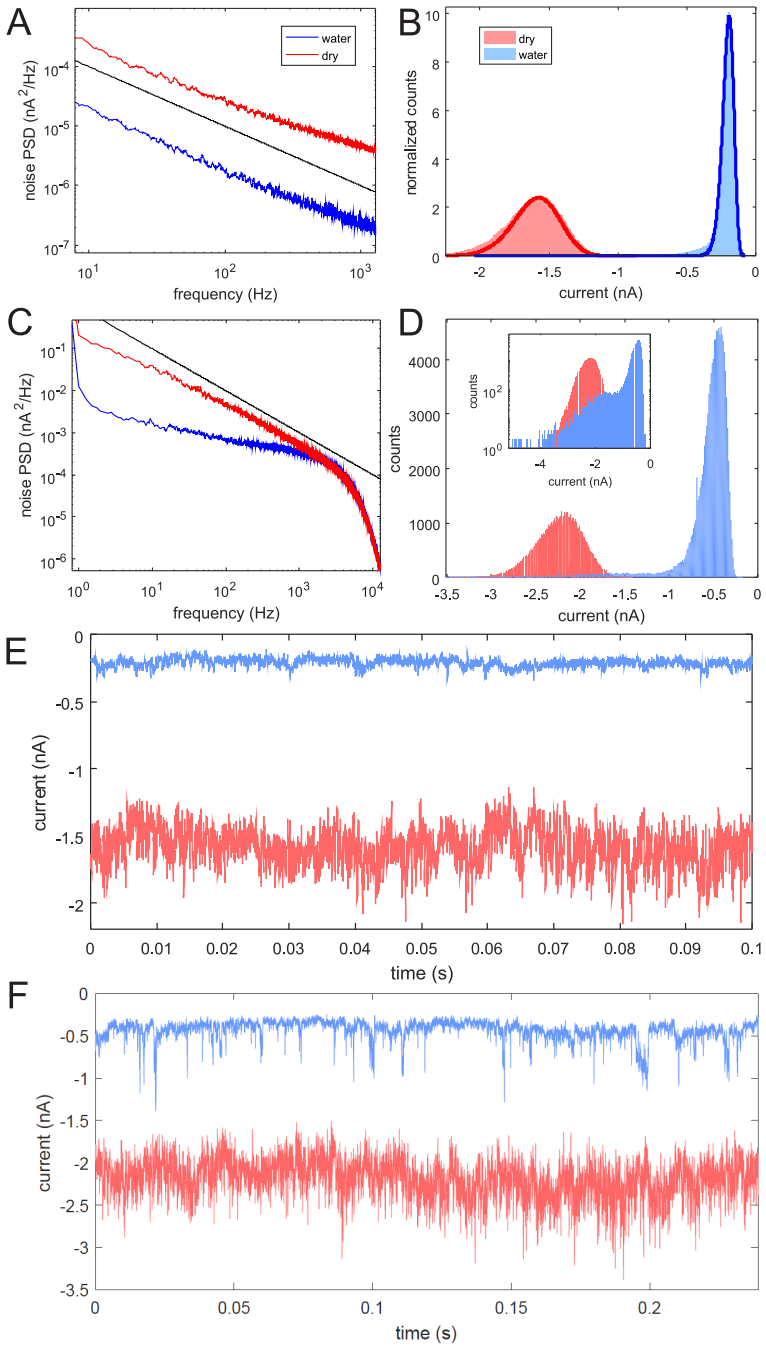


Figure 6.14: Comparison of noise spectra and tunnelling $I-t$ traces for devices in dry and water environment. Typically observed A) $1/f$ noise spectra (black line shoes $1/f$ slope) B) Lognormal current distribution (solid lines show lognormal fit) and E) $I-t$ trace for a device measured in dry and water conditions. Presented data were recorded for the device D in Fig. 6.11 at $-110\,\mathrm{mV}$. F) Tunnelling current $I-t$ fragment recorded for the same device at $-140\,\mathrm{mV}$ showing the TLF in water and D) current distribution for the same current trace fragment with double current peak (inset shows the same data plotted on a logarithmic scale). C) Comparison of noise with different slopes for dry devices and measured in water (black line shoes $1/f$ slope).

order of $\tau \sim 0.1\,\mathrm{s}$. In these cases none or very small bump in the overall noise spectra is observed. In the case of traces showing longer periods with TLF it is reflected in the profile of noise spectrum showing significant deviation from the $\gamma \sim -1$ slope.

The low-amplitude TLF signal in graphene−water junctions is consistent with the results of tunnelling through water in MCBJ gold junctions reported by Boussaad *et al.*[73] They reported the relatively low occurrence of such observations in less than 10 % of recordings.[73] The independence of the probability of observation of TLF signals on applied voltage, pH, ion concentration and its dependence on the tunnelling distance in their case has been explained as a result of the formation of localized trapping states within a junction.[73] The fluctuations of water structure shift such trap energy level with respect to the Fermi level of electrodes allowing for trapping and detrapping processes. I hypothesise, taking into account the similarity of the results, that the mechanism involved in the measurements is similar. The nature of such trap states is not known, but hydrated electrons or resonant states due to image charges at electrodes have been suggested.[73, 301] The robust water molecule structures formed in the nanoconfinement situation, which can be envisaged in GTJs, can stabilize such traps over longer time periods.

6.5 DNA Sensing by Tunnelling Current

Now I will proceed to the analysis of tunnelling biosensing signals in GTJs, starting with a brief summary of results obtained in gold junctions. The first steps towards tunnelling-based DNA sequencing have been made in STM configuration at cryogenic

temperatures and were a simple extension of imaging experiments.[330, 331] In the Scanning Tunnelling Spectroscopy (STS) approach the first STM scan records the sample topography at constant bias. This is used to locate positions of bases and subsequently record full conductance spectra $\frac{dI}{dV}$.[252, 253] The existence of a structure of conductance peaks separated by the transport gap has been experimentally proved in 2008.[252] Subsequently partial sequencing of ssDNA has been achieved by distinguishing guanine from other nucleotides.[332]

The details of transmission spectrum are influenced by the orientation of a nucleotide in the gap and the strength of its interaction with the substrate.[253] Simulations have shown that using graphene as a substrate may decrease this variability by enforcing flat arrangement of bases on the surface due to strong $\pi-\pi$ interactions.[38] It has been also shown that the base-calling accuracy can be increased by combining machine learning data analysis algorithms (naive Bayes classifier) with STS measurements in different pH environments.[42] Similarly STM-MCBJ experiments benefited from the alteration of experimental bias and pH conditions allowing to control the onset of transmission curve features, increasing the reliability of analysis.[333]

One alteration to the STM sequencing experiments is the recognition tunnelling method in junctions functionalized with reader molecules capable of specific interactions with DNA bases (Fig. 6.15), a method intensively developed in Stuart Lindsay's group.[286, 334] The role of reader molecules is to limit the number of possible base orientations, probe specific chemical interactions with the bases, reduce the effect of residue and water molecules on tunnelling, and simplify fabrication by shrinking the tunnelling distance between electrodes after implementation of the reader

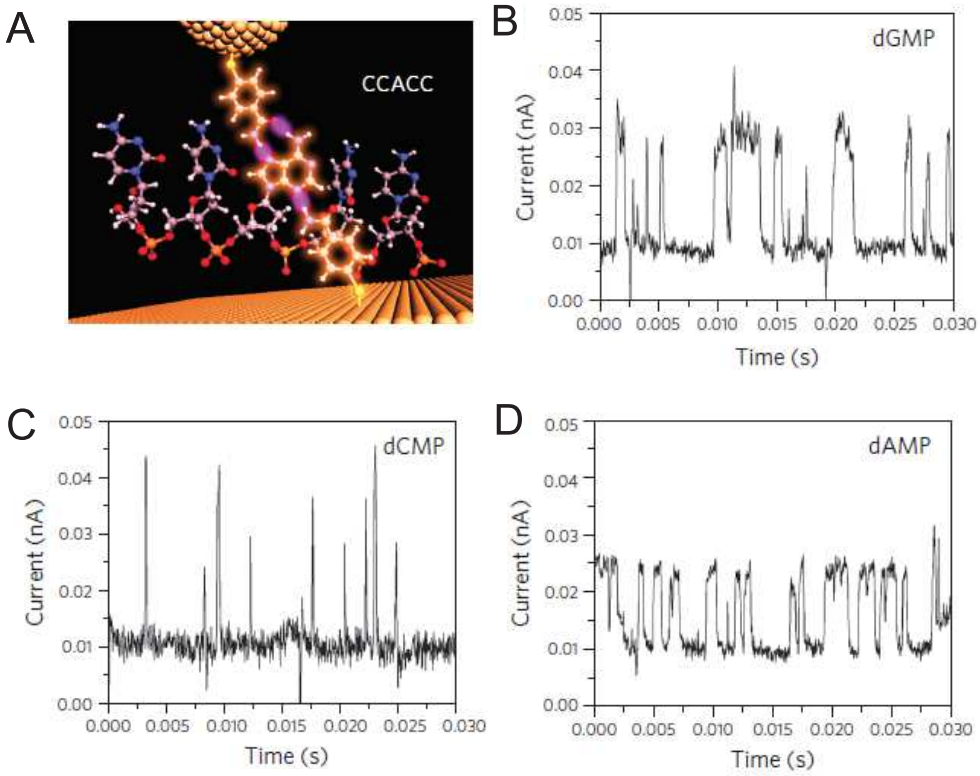


Figure 6.15: Recognition tunnelling signals recorded with a universal reader molecule (mercaptobenzamide). A) Diagram of a short oligomer trapped between two reader molecules. B-D) Typical recognition tunnelling signals for guanine, cytosine and adenosine monophosphates respectively. Reprinted with permission from [296].

molecule.[255, 286, 335, 336]

Reader molecules can take the form of bases complementary to the detected analyte and anchored to gold surface by $-$SH groups.[40, 334] Appropriate reader molecules have been found to enhance the interaction with SAMs of nucleosides adsorbed on gold surface, which was evident from the elongated $I-d$ current decay curves.[40, 47] The longer decay distances have been recorded for the base pairs creating three hydrogen bonds as opposed to pairs with only two bonds. Together with the asymmetry between $I-d$ curves for approach and retract it indicates that the recognition mechansim is not limited to tunnelling and mechanical properties of the hydrogen bonds also play significant role.[47] It has been proposed that recognition is achieved due to the longer time of the persistence of molecular bonds, which leads to higher charge transfer and in the effect allows for distinguishing bases.[334] Noise in the signals has been limited by using palladium tips[337] and by constricting the molecule orientations by dispersing them in alkanethiol SAMs on gold surface.[41]

In order to sequence real DNA strands a universal reader molecule, capable of specific bonding to all four bases through hydrogen bonds is necessary.[296]. Effective trapping of bases on timescales of seconds has been realised in geometry where both tip and substrate are functionalized with the same universal reader molecule instead of a complementary bases.[296, 336] Such junctions have generated reproducible current traces and allowed for stochastic sequencing of short oligomers.[296] Recently it has been proposed that in the case of some nucleosides universal reader molecules capable of $\pi-\pi$ stacking instead of hydrogen bonding can provide increased base-calling probabilities.[338]

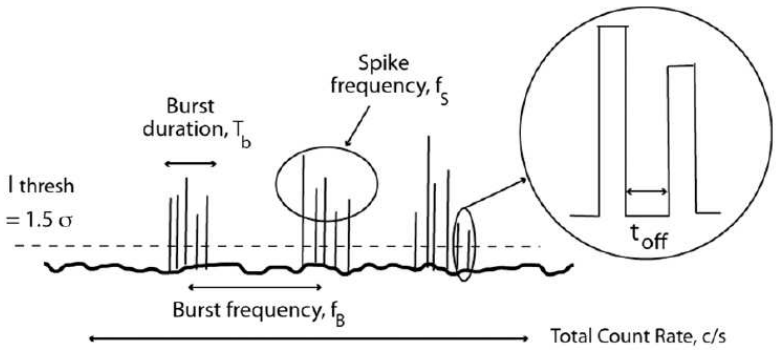


Figure 6.16: A diagram showing typically observed features of tunnelling signals in DNA sequencing, showing groups of peaks with different frequencies of occurrence. Reprinted with permission from [335].

In recognition tunnelling experiments it is commonly observed that current peaks attributed to a molecule tunnelling come in bursts (Fig. 6.16). All of the peaks within one burst are attributed to a single capture event and the ongoing reconfigurations of a base.[255, 286, 335–338] The commonly observed TLF is attributed to the slight change in the molecular orientation.[334] It has been argued that mechanical connection does not have to be broken in order to observe zero-transmission.[296, 334]

The analysis of simple parameters like current peak height, duration and frequency is insufficient for unambiguous base calling.[255, 286, 335] It is necessary to apply a machine learning approach, like Support Vector Machine, using dozens of parameters describing signal, including those simple parameters but also parameters describing shape and spacing obtained by Fourier and wavlet analysis of the signal.[255, 335–339] Information about the signal surrounding a given peak is necessary for base-calling with increased accuracy.[335]

Nanopore-Embedded Tunnel Junctions One serious drawback of STM configuration is the impossibility to direct the translocation of bases through the nanoconfined volume. As an alternative, the fixed MCBJ-based nanogaps were investigated. The sole fabrication of nanometric pores in thin membranes is a challenging task. The device consisting of tunnelling electrodes aligned or embedded in a nanopore is still a significantly more complex issue.[340, 341] The idea of nanoelectrodes-base sequencing protocol has been proposed by Zwolak and Di Ventra in 2005 (Fig. 6.17), together with the MD and DFT calculations showing feasibility of this approach.[251, 342]

The first realisation of nanopore-embedded nanogap geometry has been reported by Gierhart *et al.* in 2008.[340, 343] The devices have been fabricated by drilling a pore in a 10 nm-wide metal nanowire on a thin silicon nitride membrane using focused electron beam in TEM.[343, 344] The devices were used to detect the translocation of gold nanoparticles as a test analyte.[343] Similarly a nanochannel perpendicular to nanowires was fabricated by FIB.[345] The same method has been used to pattern nanopore in carbon electrodes.[346] Electrodes patterned by Electron Beam Induced Deposition[109, 110] or EBL patterning [303, 340] can be also precisely aligned with a nanopore after its formation.

The use of transverse electrodes for sensing allows to decouple the transmembrane voltage driving the translocation of a strand through the nanopore from the transverse voltage used to read the sequence by means of tunnelling.[347] This allows for better control over the translocation pace. The additional benefit of using the transverse readout mechanism is a possibility to verify the observation of transloca-

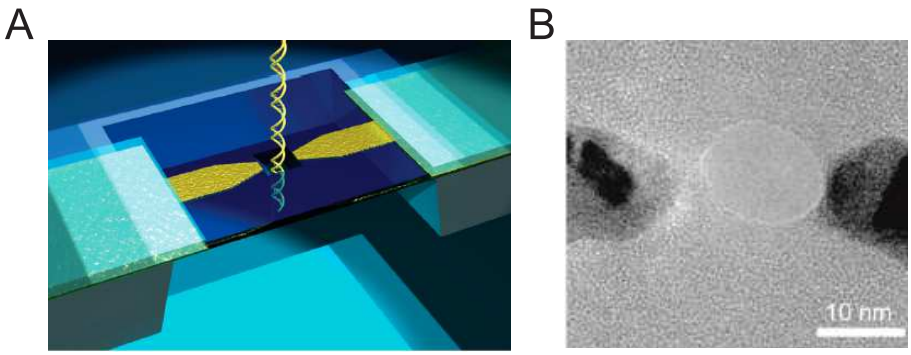


Figure 6.17: Tunnelling electrodes aligned with a nanopore. A) Conceptual diagram and B) TEM image of electrodes patterned with EBL in the vicinity of the nanopore. Reprinted with permission from [340].

tion events by comparing the signals recorded in ionic and tunnelling signal.[109, 340, 346] The presence of additional conducting surface may, however, result in increased capacitance noise and crosstalk between both measurement channels.[303]

The most significant progress in DNA sequencing using MCBJs has been reported in a series of papers by Tsutsui, Taniguchi and Kawai.[60, 295, 348–352] They presented the first instance of the statistic discrimination between single nucleotides moving stochastically around the nanogap in water solution (Fig. 6.18). The nanogap has been formed in the uninsulated gold MCBJ.[295] Subsequently the method has been utilised to show capability of differentiating between methylated and nonmethylated nucleotides (methylation state is important marker of epigenetic information).[349] They also formed an in-plane nanopore between the substrate and insulation layer with embedded electromigrated nanogap, where detection of both randomly diffusing [350] and electrophoretically dragged analyte[351] was realised. It has been also shown that randomly diffusing short strands of nucleotides (seven-base-long) can be sequenced by the break junctions without any nanopore.

This method called random resequencing relies on the statistical analysis of randomly recorded fragments of the sequence.[60] Other examples include discrimination between peptides.[352]

An interesting alteration of tunnelling nanogap sequencing is fabrication of planar junctions separated by thin dielectrics. Nanopore drilled in such a tunnelling stack, where two electrodes are bridged by a reader molecule has been demonstrated to detect nucleotides.[353] Another version of such device, with two graphene sheets as electrodes has been also proposed theoretically.[354]

Research efforts are currently focused on improving the methods of DNA sequencing, however, other applications are also attractive.[334] One of the examples is protein sequencing, which is even more challenging compared to DNA sequencing because the analyte cannot be easily amplified to obtain larger concentrations, and proteins are built with 20 different amino acids.[336] Despite these difficulties first experiments in functionalized STM junctions proved the existence of unique features, which could serve as a differentiation mechanism in protein sequencing. Similar provisional results showed that sequencing of carbohydrates is feasible. At least two research groups have shown that it is possible to differentiate monosacharides.[255, 355]

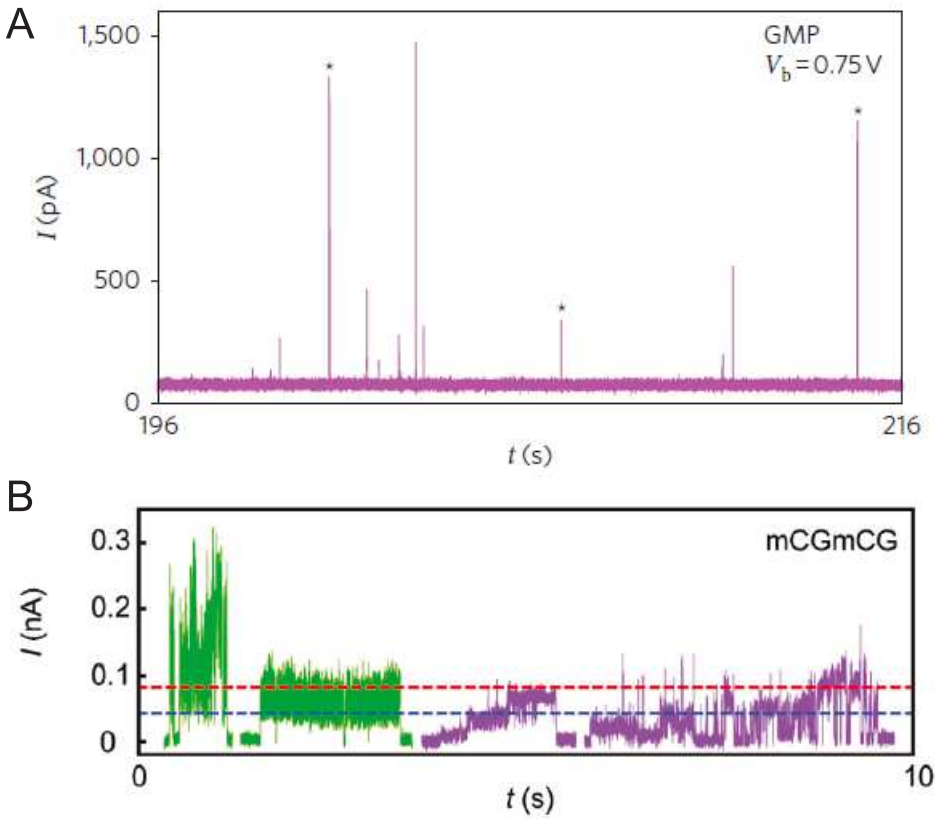


Figure 6.18: Examples of tunnelling signals of stochastically trapped DNA in MCBJ junctions. A) Tunnelling signal obtained in 5 µM guanine monphospate water solution in a stochastic gold MCBJ. Reprinted with permission from [295]. B) A signal sequence in MCBJ tunnnel junctions recorded for the specified short oligomer sequence. Reprinted with permission from [349].

6.6 Nucleobase Sensing with Graphene Tunnel Junctions

6.6.1 Idea of Graphene Tunnel Junction DNA sequencing

The alteration in Zwolak's tunnelling readout mechanism for DNA sequencing by implementing atomically thin graphene electrodes has been proposed theoretically by Postma in 2010.[118] The main advantage of GTJs is the possibility to generate a highly focused tunnelling probe. The thickness of a graphene monolayer is equal to $\sim 0.3 - 0.6\,\mathrm{nm}$[356] including solvation layer (estimated on the basis of graphene nanopore measurements[288]); comparing this to the spacing of 0.33 nm between nucleotides in a DNA strand, allows to expect a single-base resolution in graphene tunnelling sequencing. Since Postmas's proposal numerous DFT studies predicted the possibility of sequencing DNA in GTJs[357–362], with quantum transport effects such as Negative Differential Resistance[363], Aviram-Ratner molecular rectification effect[360] and quantum interference effects, such as Fano resonance.[361] Some issues have been also identified including changes in transmission spectra by a few orders of magnitude due to the rotation or shift of nucleotides in the gap.[357, 361, 362] The control over the termination of graphene edges is expected to increase the sensitivity. It could be achieved through hydrogen termination, which allows to form weak hydrogen bonds with nucleobases and increases coupling.[364]

An alternative approach of using graphene to sequence DNA, different to Postma's idea of tunnelling current measurement has been proposed in 2011 by Saha *et al.*[365] It comprises a narrow graphene nanoribbon with nanopore drilled in the middle.[365]

The nanopore in the suspended nanoribbon allows for translocation of DNA. Sensing is achieved through a modulation of the in-plane current flowing through the nanoribbon due to its gating by the DNA charge.[365] One advantage of a nanoribbon approach is a high current level, which is less sensitive to noise, however high sensitivity of GNRs to local charge still allows for effective sensing.[365] The simulations, however, usually do not include the effect of the environment, which can lead to the increase in noise levels.[294] DFT simulations have also shown that mechanical effects of bending of graphene membranes due to the interaction with a translocating DNA strand affect the in-plane electron transport.[366, 367] Such readout protocol has been also simulated in bow tie-shaped, nanopore-containing graphene quantum point contacts, similar in geometry to the GTJs.[368] It has been shown that the constriction in the translocation region increases the sensitivity of the device to DNA.[368]

DNA translocation through graphene nanogaps has been investigated[369] and there have been numerous theoretical studies of DNA sequencing in graphene nanogaps, however it has not been realised practically yet. Here I make the first attempt to obtain measurable signal from mononucleoside triphosphate solutions in GTJs. I proceed, taking inspiration from the development of gold STM and MCBJ DNA sensing, which started with the random sensing of analyte entering the gap due to the Brownian motion.[295, 296] In this section I summarise the results of sensing experiments and in the next chapter I will present ideas for the future development of sequencing-compatible GTJs.

6.6.2 Nucleotide Sensing with GTJs

All deoxynucleotide triphosphate solutions were purchased from New England Biolabs in the form of water solution at physiological 7.5 pH level and 100 mM concentration. The solutions were diluted to 10 nM concentration unless otherwise stated. The first analysed analyte was deoxyguanine triphosphate (dGTP), which has been found to give the highest signals in some experiments and simulations[60, 295, 357, 361, 365], although I note that opposite trends have been also reported[251].

After filling the flow cell with dGTP solution I measured four 10 s-long traces at -20 mV, 20 mV, -100 mV and 100 mV bias. Signals were sampled at100 kHz rate and the Bessel filter frequency was set to 10 kHz. After the measurement the flow cell was flushed with 10 mL of DI water in order to remove analyte. At this point the same measurements were performed in order to verify that the observed signal is not an artefact. This measurement cycle of measuring in dGTP and water was repeated up to seven times for each measured device.

A typical signal recorded for the dGTP solutions is presented in Fig. 6.19. For both voltage polarities a clear difference between the signal recorded in water and in dGTP solution is observed. In dGTP I observed peaks with the average amplitude higher compared to signal in water. This tendency is preserved for the consecutive analyte and water measurements, indicating that although nucleotides can strongly adhere to graphene[370] the lower signal is reinstituted in water; this allows me to assume that water rinsing cycle strongly reduces the concentration of the analyte.

Closer analysis of the peaks recorded in dGTP solution reveals their characteristic square profile. In agreement with the measurements of single nucleotides in

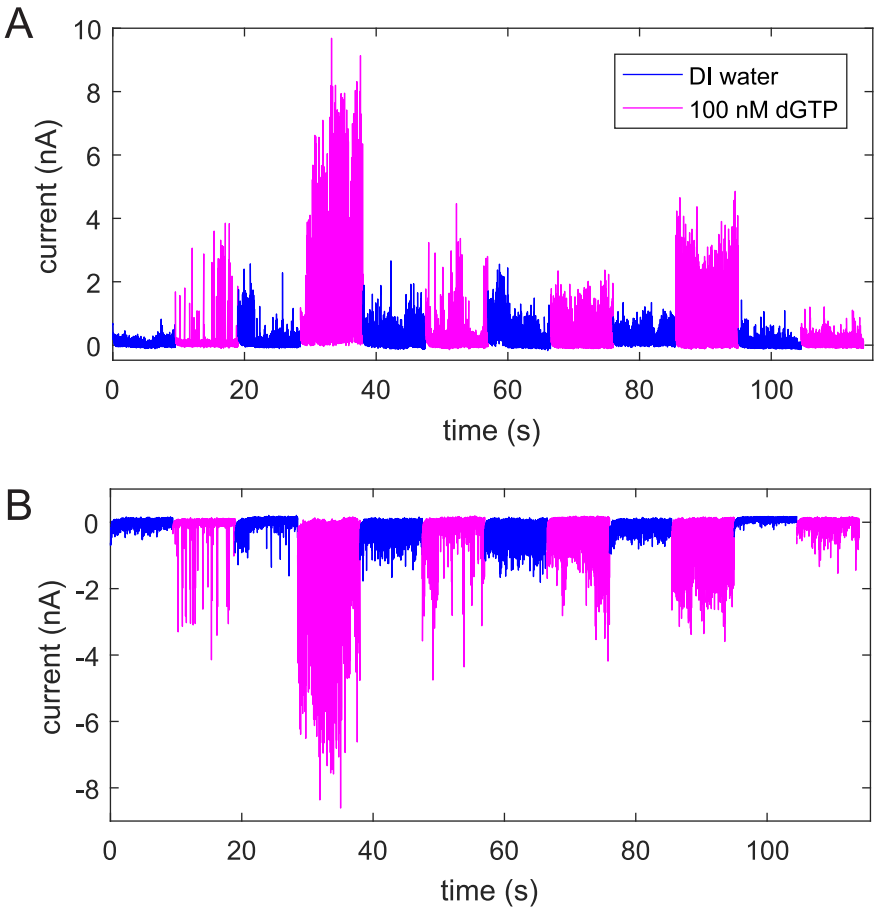


Figure 6.19: Tunnelling signal in 10 nM dGTP solution at A) 20 mV and B) −20 mV for six consecutive water/dGTP cycles.

STM junctions I observe sharp peaks with steep rise and decay curves and with a flat maximum (Fig. 6.20), which is interpreted as a signature of interaction of the nucleotide with the junction.[60, 296, 335, 336, 349–352] Furthermore, I observe the occurrence of peaks in bursts, reported earlier in STM tunnelling recognition experiments.[296, 335, 336] That is I observe periods with high peak coverage separated by long periods of featureless low-current signal (Fig. 6.20). Each burst of peaks can be interpreted as a single binding event of a nucleotide in the junction.[296, 335, 336] The series of peaks correspond to its molecular rearrangement. The current comes back to the water baseline level once the molecule is released.[296, 335, 336] Taking into account similarity of signal in GTJs to signal in MCBJs I provisionally accept this explanation in GTJs.

In the signals recorded in water I also observed current peaks in agreement with the results reported in the previous sections. The amplitude and duration of these peaks is, however, significantly lower compared to the peaks recorded in the dGTP solution (Fig. 6.20 E). The peaks profile in water is different, without a clear plateau at the maximum of the peak. I rarely observe the TLF fluctuation in water measurement, and the amplitude of such signal is just a fraction of the amplitude of the signal in dGTP solution. Rarely observed large peaks in water measurements can be attributed to the presence of remaining dGTP molecules.

These observations are in agreement with the results of STM recognition tunnelling measurements[335], where small changes in tunnelling current were reported in phosphate buffer environment; this has been attributed to the effect of water and thermal fluctuations.[286, 335] Around 50 % of the features analysed by the Support

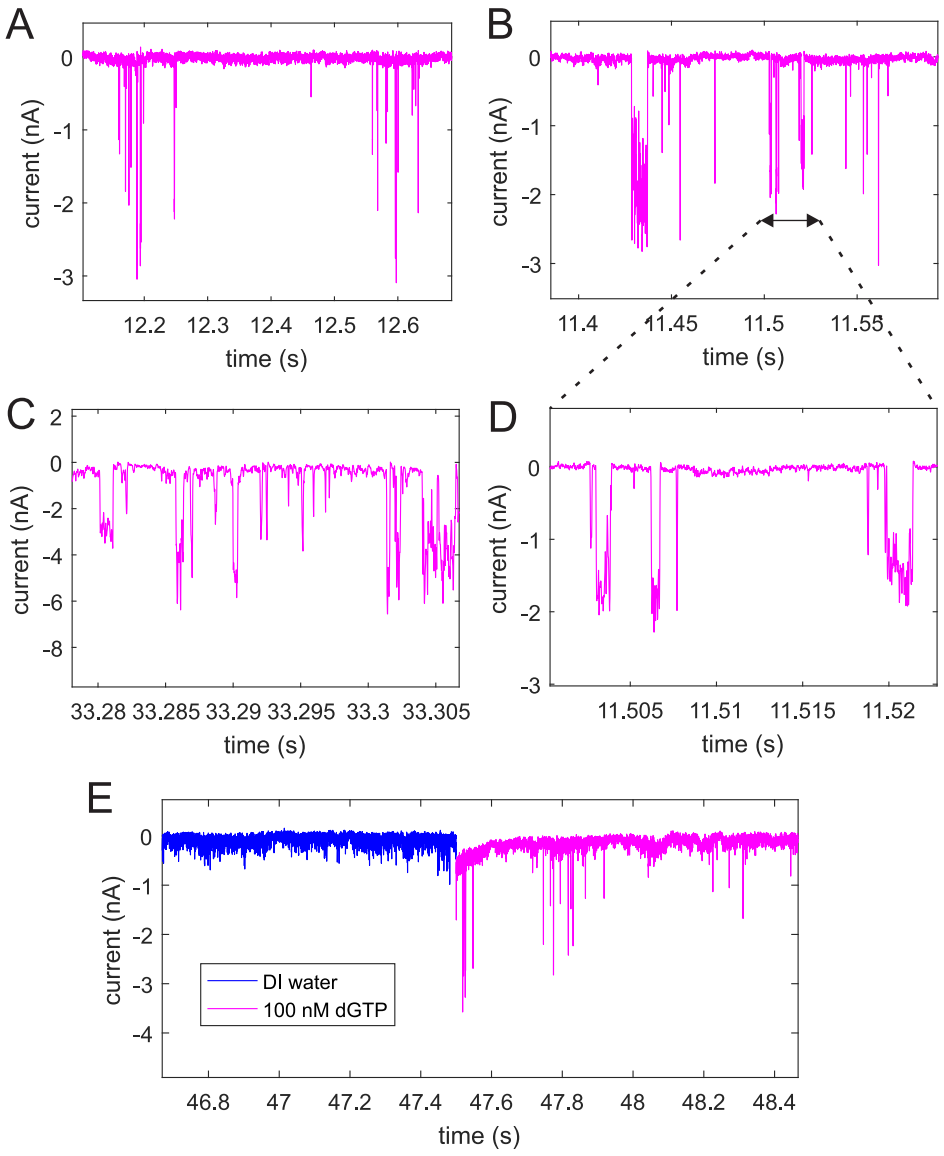


Figure 6.20: Signal peaks in dGTP solution at −20 mV (A-D), E) Comparison of the zoomed in signal recorded in clear water and in dGTP solution.

Vector Machine algorithm, in studies of other groups, are common among the different bases and can be attributed to their common transport features or due to solvent effect.[255, 336]

Signal in dGTP solution and water can be clearly distinguished. The high current peaks are observed for the majority of measurement cycles in dGTP solutions, however, I also observe high variability in the peak duration, height and occurrence frequency between consecutive cycles. These differences are evident from the comparison of the consecutive $I-t$ traces and the corresponding noise spectra (Fig. 6.21). The noise spectra for dGTP solutions show features of RTN and increased noise level compared to the spectra in water. However, I observe a significant variability in the noise spectra, preventing the identification of a single signal feature characteristic to a given analyte. Assuming that peak bursts are related to the binding of a single nucleotide to the junction or its adsorption in the vicinity of a junction it is resonable to assume that such variability is a result of the sensitivity of the junction to slight changes in its environment and in molecular orientation[286, 336]

In order to extract more information for each trace I defined the maximum baseline current level $I_{B,max}$ and calculated the mean baseline current $\overline{I_B}$ and standard deviation σ_I for all points in the range $0 < |I(t)| < I_{B,max}$. Further, I calculated the signal threshold level assuming low $1.5\sigma_I$ threshold value, $I_T = \overline{I_B} + 1.5\sigma_I$.[296] All data points above the I_T level are identified as signal peaks.

I further investigated the statistical properties of peak distributions (typical plots are shown in Fig. 6.22). The distributions of current peak amplitudes for all measured dGTP traces have a lognormal profile (Fig. 6.22A), while the peak duration is

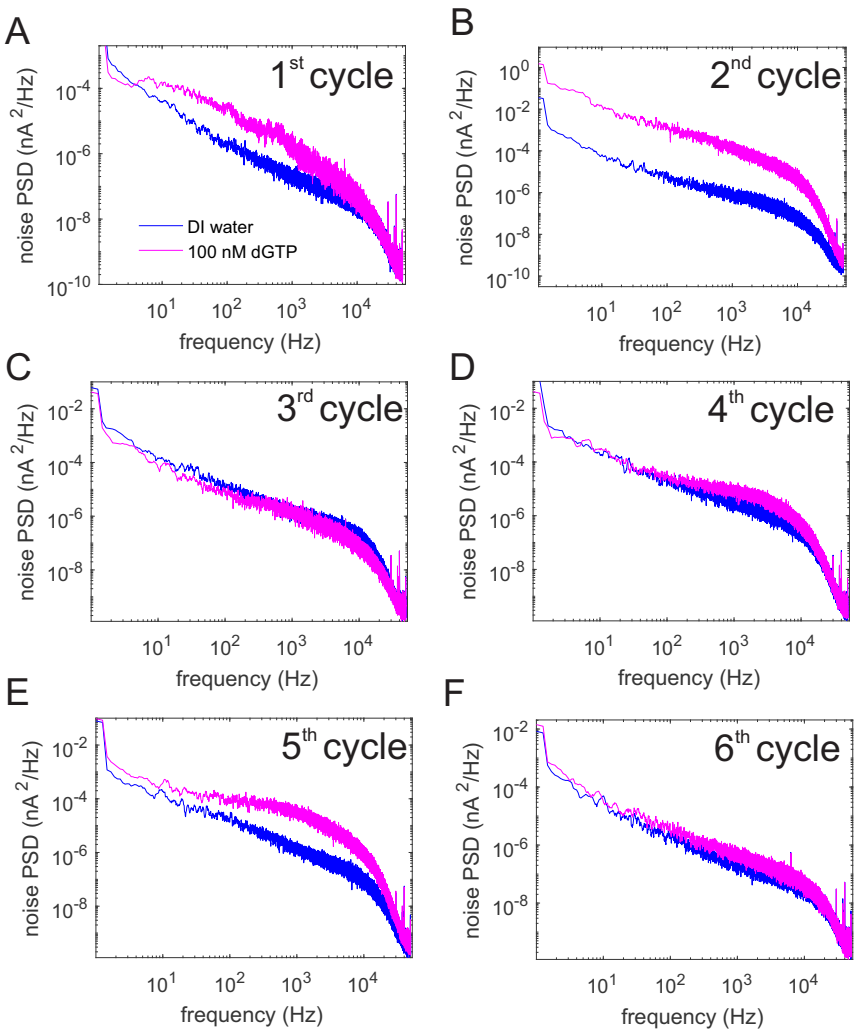


Figure 6.21: Comparison of the noise spectra for traces recorded in water and dGTP solutions at the bias of 20 mV. Figures A-F correspond to the consecutive cycles of measurement in water and dGTP solution plotted in Fig. 6.19A.

distributed exponentially (Fig. 6.22B). Such properties were also found in the STM recognition tunnelling measurements.[243, 296] In Fig. 6.22C I plot the correlation histogram of peak amplitudes and durations. For all analysed traces I observed increase in the current amplitude values with increasing duration, which can be attributed to the smoothing effect of low-pass filter, which decreases the height of the peaks above its critical frequency.[234] Increasing the bandwidth of the measurement should result in the increase of the amplitude of peaks with short dwell times.[234]

I also calculated the occurrence frequency of peaks defined as the mean number of current peaks per unit time (Fig. 6.22D).[335] Traces of peak frequency as a function of time confirm the observation of peaks in discrete bursts separated by regions of no nucleotide signal, where occurrence frequency drops down to zero. The occurrence rates covered a range of $10 - 1000\,\mathrm{Hz}$, which is similar to rates reported for junctions functionalised with reader molecules ($300 - 1300\,\mathrm{Hz}$[296], $1 - 40\,\mathrm{Hz}$[335]). Although I did not introduce purposely any functional groups capable of capturing nucleotides I assume that the low occurrence frequencies may be due to the strong interaction of nucleobases with graphene surface by $\pi - \pi$ stacking.[370]

Signal Comparison for Different Nucleosides Subsequently I analysed in the same way current signal in deoxythymine triphosphate (dTTP) solutions, which is supposed to be the least conductive base according to MCBJ measurements and DFT simulations.[60, 295, 357, 361, 365] In Fig. 6.23A and B I plot the $I - t$ traces for measurement cycles in dTTP solution and water. Similarly to the enhancement of current in dGTP, also for dTTP solutions I observed high amplitude peaks with flat plateaus (Fig. 6.23C), which were not observed in clear water.

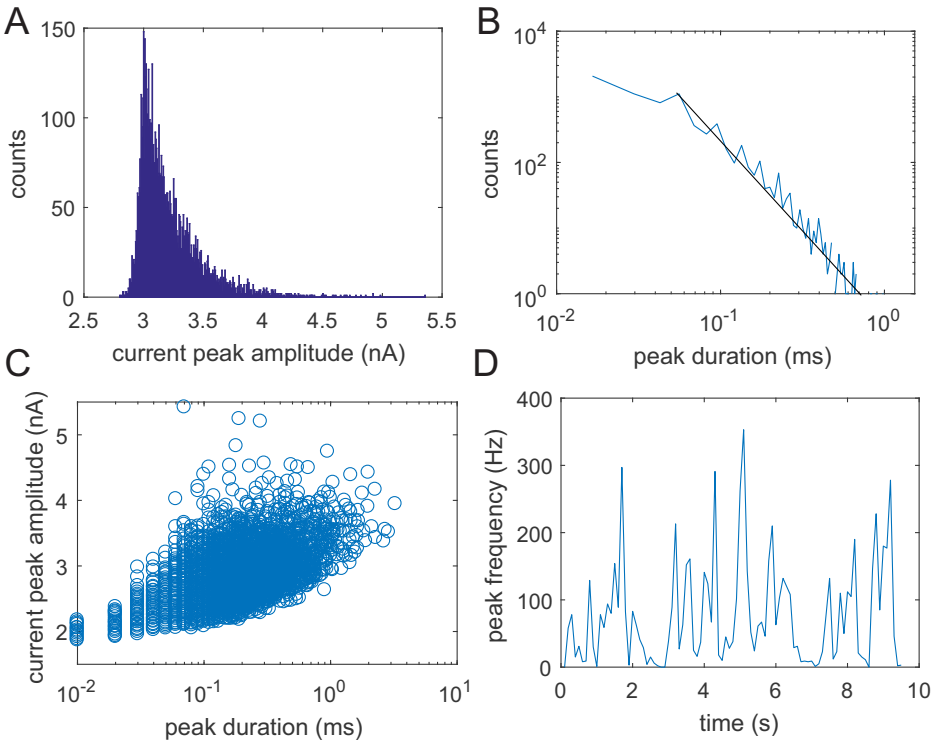


Figure 6.22: Features of dGTP signal peaks showing A) Peak height distribution B) Peak duration distribution C) 2D histogram of peak amplitude and duration correlation D) Peak occurrence frequency.

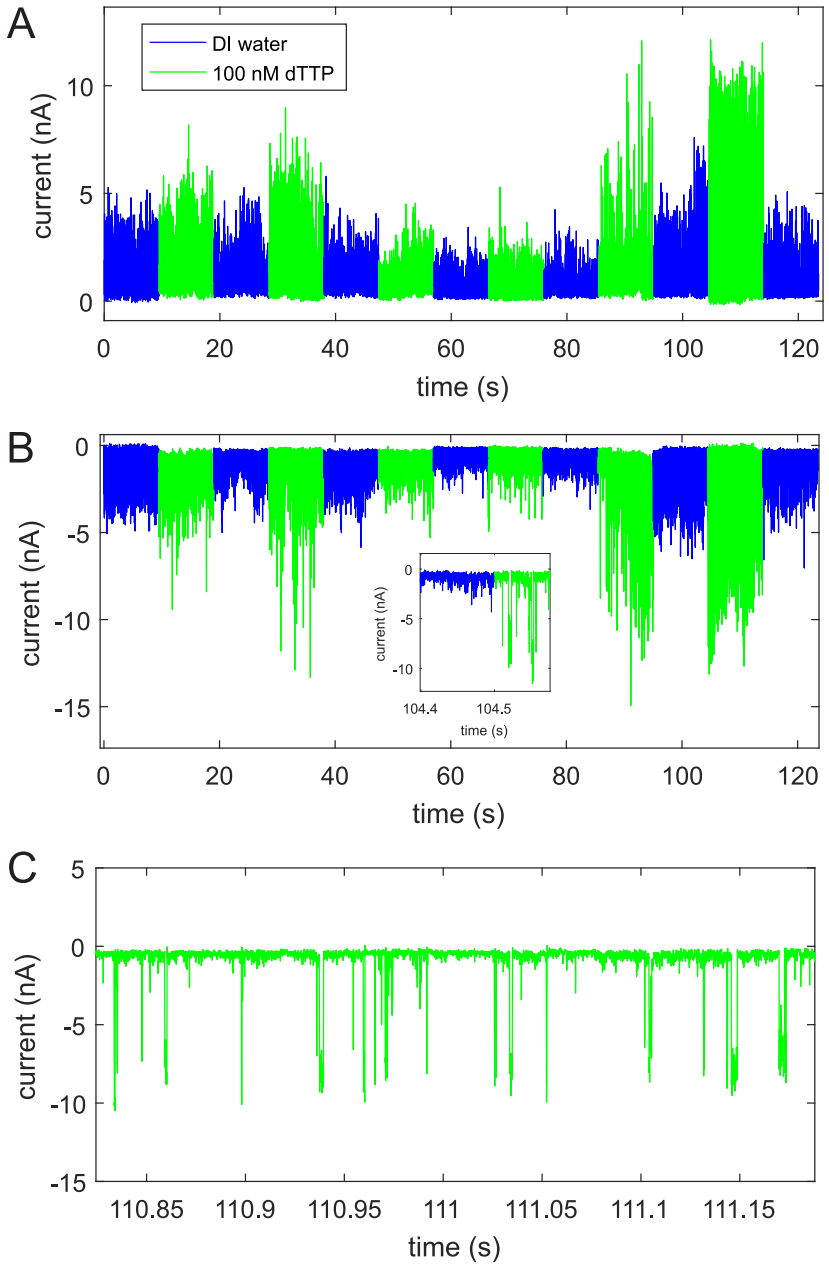


Figure 6.23: Tunnelling signal in 10 nM dTTP solution at A) 20 mV and B) −20 mV for six consecutive water/dTTP cycles (Inset shows comparison of zoomed in trace for water and dTTP solution). C) Zoom of the one on dTTP traces showing the characteristic square profile of peaks/

My goal here is to verify if statistical discrimination between solutions of different bases is possible. In order to do so I performed more measurements according to the previously described protocol of interchangeable measurement series in water and in analyte solution. The only modification is that now I initially measure a few signal sequences in dTTP 10 nM solution and then another few traces in dGTP 10 nM solution. Typical traces for three different devices measured at 100 mV and 20 mV are presented in Fig. 6.24. Both types of nucleotides give rise to discrete current peaks. However, it is clear that there are more differences between measurements of different devices, than between signals obtained from different analytes measured in the same device. This is expected, as the particular arrangement of the tunnelling gap is likely to alter the response of the junction to the environmental factors. Indeed, even the change of a single atom in the junction geometry or its surrounding can introduce measurable changes in the signal.[294] It is also possible that the observed signal is not induced by the bases but it might be induced by the negatively charged triphosphate group, which would explain the similarities in signal for different nucleotides.

To analyse the difference between dTTP and dGTP solutions I look at the correlation between their peak amplitude and duration. Three plots showing the signal distributions measured in three different devices during the last dTTP cycle before rinsing the flow cell with water, and the first dGTP cycle after rinsing the flow cell with water are plotted in Fig. 6.25C-E. The distributions show the trend of higher current amplitude for dTTP solutions. However I also note that a similar comparison for all the dGTP cycles from Fig. 6.19 shown in Fig. 6.25A and for all the dTTP cycles from Fig. 6.23 shown in Fig. 6.25B confirms that even for the same

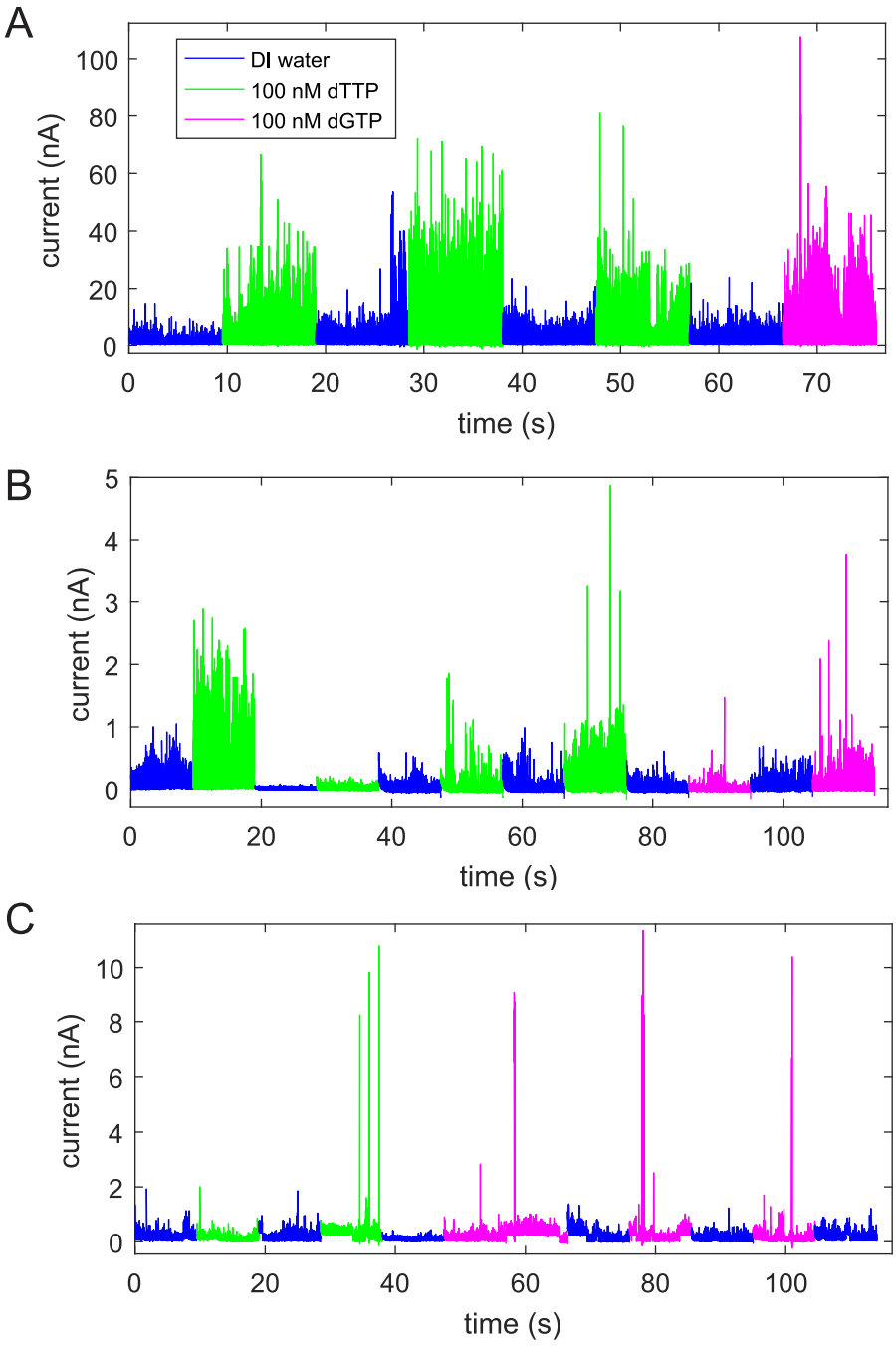


Figure 6.24: Tunnelling signal in 100 nM dTTP and dGTP solution at A) 100 mV and B-C) 20 mV for three different devices.

analyte measured with the same device there is high variability in the signal between consecutive cycles.

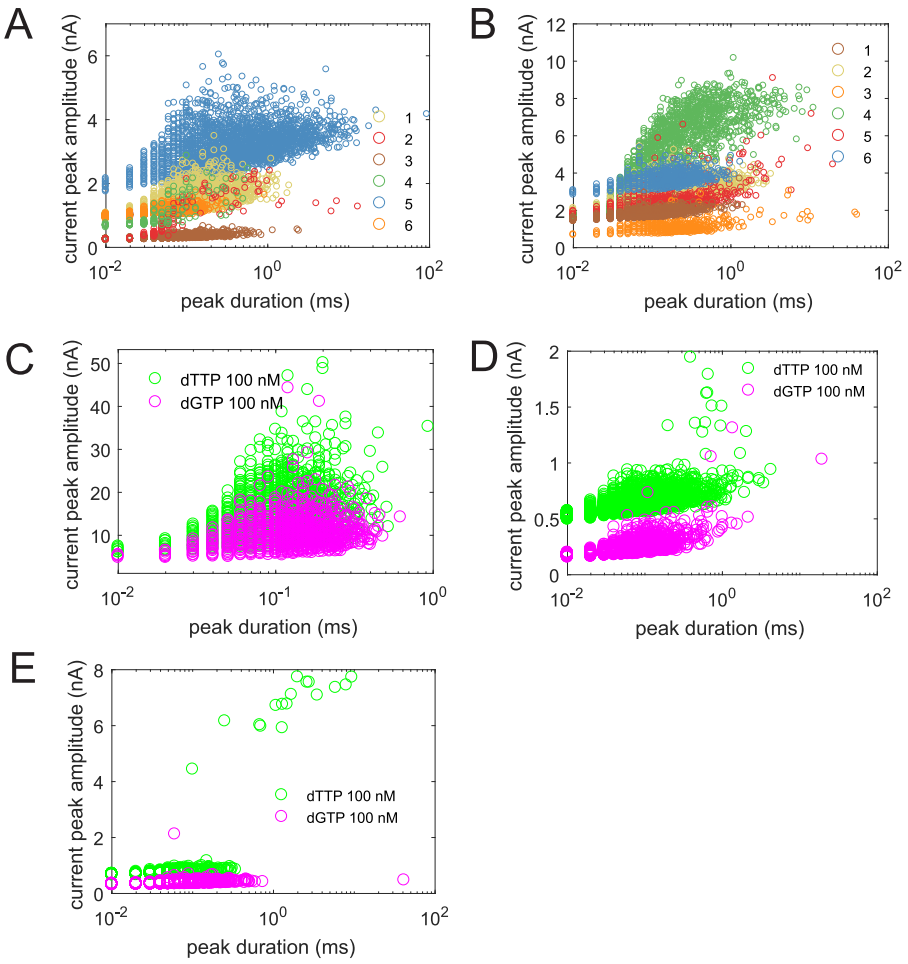


Figure 6.25: Comparison of peak amplitude-duration histograms for signals in dTTP and dGTP solutions. Histograms in Fig. C-E correspond to the traces from Fig. 6.24. A and B Correlation histograms for all analyte traces from Fig. 6.19 and 6.23 respectively.

6.7 Summary

In this chapter I have presented an efficient, PMMA-based insulation method, which allows for the reduction of spurious electrochemical effects in liquid measurements. I investigated the influence of water on GTJs, and observed decrease in tunnelling current and increase in noise at given voltage, compared to the dry state. I attribute this to the formation of EDL at graphene surface in the effect of polarisation of water molecules due to applied bias. The fast oscillations of the water molecules increase noise due to fluctuating electrostatic environment of the junction. In rare cases I observed low amplitude RTSs in water measurements, which I attribute to a transient charge traps formed by water molecular levels in the vicinity of a GTJ. These trap structures may be stabilised by the stable water clusters formed in the nanoconfined space of the GTJ.

I was able to detect the characteristic signal peaks arising from the interaction of dGTP and dTTP nucleobases with graphene junctions. The lack of characteristic high peaks with a flat-plateau profile in water measurements indicates the nucleotides as the signal origin. The relatively long dwell times on the order of ms are an indication of strong interaction of graphene with the bases. I showed the possibility of detection of low concentrations of analyte (10 nM), much lower compared to the initial concentrations necessary to obtain signal in non-optimized gold junctions (10 µM[296, 335]). I assume that the development of the devices could decrease this concentration even further. I was not able to present statistically significant difference in the signal between dGTP and dTTP molecules. I assume that aligning the tunnel junction with a nanopore, using the methods described in the next chapter,

will allow to probe the molecular interactions in a more specific way, limiting the randomness factor present in the current approach and eventually will lead to the base discrimination. In the next chapter I also describe a method of fabrication of local gate electrodes, which are envisaged to enhance base discrimination by changing the energy level alignment.

Chapter 7

Sensing Prospects

7.1 Suspended Graphene Tunnel Junctions

In the measurements presented in the previous chapter, the detection of nucleotides was realised by means of random trapping of the analyte molecules by the junction. In order to make GTJs applicable for DNA strand sequencing the movement of the analyte has to be directed and restricted in order to force the consecutive bases to translocate between graphene electrodes. This can be achieved by embedding the tunnel junction in a nanopore. Practical applications of devices for DNA sequencing demand having multiple devices capable of sequencing in parallel on a single chip in order to increase the sequencing reliability and yield.

I developed a method of fabricating arrays of nanopore-aligned GTJs meeting these criteria. As a substrate I used suspended 30 nm thick SiN membranes, with suspended area of $\sim 30 \times 30\,\mu m$ (Fig. 7.1).[371] The SiN membrane is placed on a

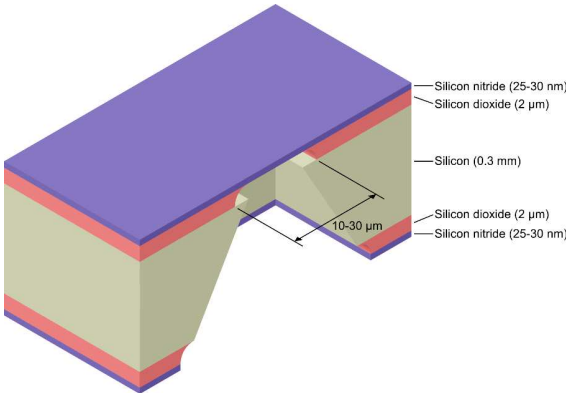


Figure 7.1: 30 nm thick SiN membrane used for fabricating suspended GTJs. Reprinted with permission from [303].

SiO_2 which decreases the membrane capacitance and main Si wafer support. Such wafers are commonly used for fabrication of inorganic pores for DNA sequencing.

The goal was to develop a process of fabricating arrays of GTJs aligned with nanopores on a wafer scale on such substrates. Nanometric pores for DNA sequencing are typically fabricated by means of an electron beam in TEM[372, 373] or a FIB[280, 281, 374] microscope. These methods allow for the lowest possible sizes of the nanopores, however they cannot be easily upscaled to fabricate nanopores on a wafer scale.[272, 375]

Another approach is to use etching mask and Reactive Ion Etching method (RIE) capable of etching SiN substrate. This allows for the fabrication of large arrays of nanopores.[272, 279, 376] The method relies on directing ionised gas capable of chemically etching the substrate.[377] As an etching mixture I used CHF_3 (at 45 $cm^3\,min^{-1}$ flow rate) and O_2 (5 $cm^3\,min^{-1}$). The addition of low O_2 flow increases the etching rate.[377] Prior to etching the membranes were loaded into RIE system with sample holder cooled down to 0 °C and the chamber was evacuated. Cooling can help

increase etching selectivity. This is especially important in the case of photoresist masks, which at high temperatures generated in the etching chambers become more prone to etching.[377] After adjusting the flow of the etching gases, ionization was achieved by applying a voltage of 100 V at 150 W and 13.56 MHz.

The selectivity in etched areas may be achieved by masking the areas which are not supposed to be modified.[133, 377] In the case of RIE fabrication of nanopores hard masks are usually used.[377–379] I decided to alter this procedure by means of soft PMMA etching mask.[133, 380, 381] Also negative resists such as SU-8 can be used.[375] The soft mask was used because of the ease of removal of PMMA layer by oxygen plasma etching as opposed to hard mask which can be removed only by another selective wet etching step.[377] The drawback of a soft mask might be its low resistance to RIE and resulting low achievable aspect ratio of patterned structures.[377] As the etching mask I used 100 nm thick PMMA 950k layer.

To calibrate this new approach the etching rate test was performed. This was achieved by patterning large features with $2 \times 2\,\mu m$ side length on the suspended membranes (Fig. 7.2C) and etching them in the RIE system in 30 s time intervals. After RIE, the remaining etching mask was removed by oxygen plasma etching, which does not affect SiN. The difference in height between etched and mask regions was measured using AFM for each of the etching durations (Fig. 7.2B). In the result a linear etching rate dependence of $\sim 0.3\,nm\,s^{-1}$ was obtained. Since the mean specified membrane thickness was 30 nm the etching time of 120 s was chosen to ensure overetching and pore formation.

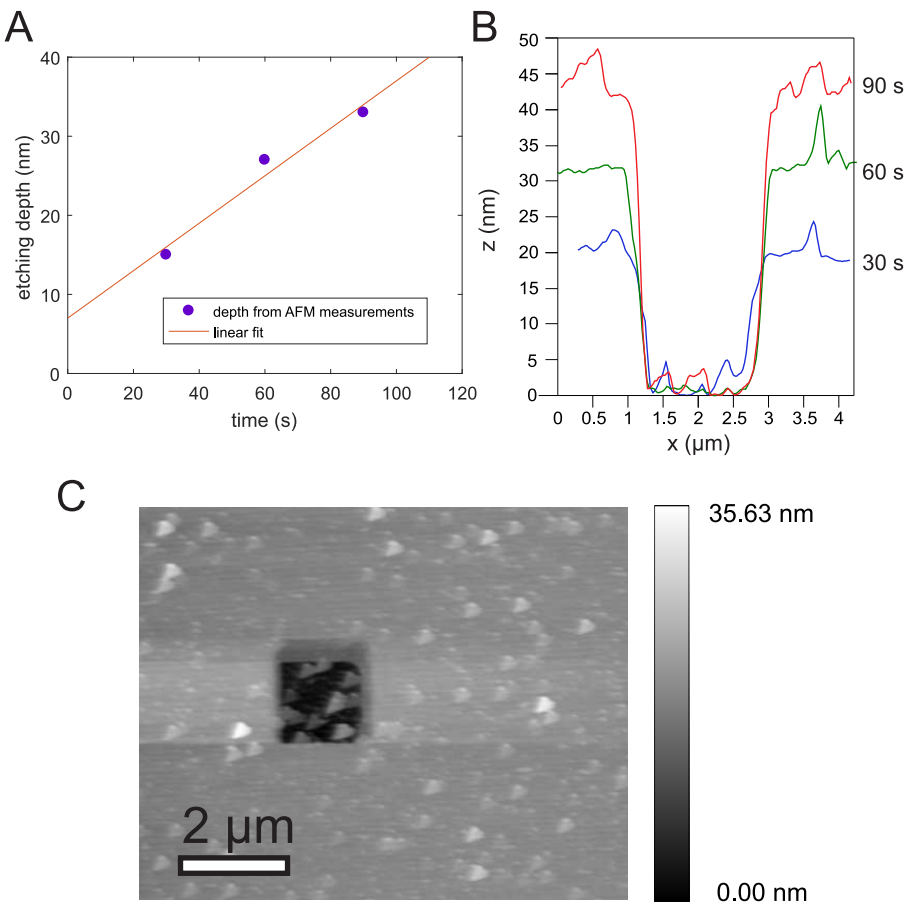


Figure 7.2: SiN membrane RIE etching rate analysis. A) Plot showing the dependence of the depth of features patterned by RIE as a function of etching time after removal of the PMMA mask. The depth of the features was estimated on the basis of B) non-contact AFM profiles of C) etched areas.

7.1.1 RIE of Nanopores

After determining the average etching rate I proceeded to the nanopore fabrication. Using the the same parameters as for graphene patterning described in Chapter 2, I patterned arrays of square pores with side length varying between 10 µm−200 nm. SEM imaging of the patterned membranes after removing the etching mask proved that transfer of the pattern to the membranes was successful. Pores were fully etched in the membrane and even at the highest SEM contrast setting I did not observe any scattering from the pore area. The large features had the expected size and shape. However, with the decreasing size of the investigated features the deviation from the expected square size and shape was observed. The smallest observed features were circular pores with $\sim$ 1 µm diameter (Fig. 7.3A-B). These features were obtained after exposing squares with 200 nm side length. In order to learn if the broadening of the features occurs at the stage of EBL patterning or RIE I evaporated a 10 nm-thick layer of gold on the developed PMMA layer before they were exposed to RIE. Results for the smallest features shown in the Fig. 7.3C-D reveal that the smearing of the pattern was present already at the stage of EBL patterning, resulting in circular openings with $\sim$ 700 nm diameter.

The low thickness of the suspended membrane results in high beam scattering and broadening of the patterned features due to electron accumulation in the non-conductive SiN[382], which can defocus the electron beam. In order to mitigate such effect on top of the PMMA mask, before EBL patterning, I applied a layer of commercially available conductive polymer (E-spacer 300Z).[382], which dissipates the excessive charge. The SEM images of gold-covered openings in PMMA proved

that features obtained with the E-spacer were in good agreement with the size and shape of the exposed pattern (Fig. 7.3E-F). The fabricated features were on par with features reported in literautre[376, 381] Further decrease in the size of nanopores can be achieved for example by perfroming EBL process in a single-dot exposure mode with low electron doses.[279] The ultimate downscaling of nanopores is achieved by the ion track etching technique[272] Pores with $\sim 1\,\mathrm{nm}$ diameters can be obtained by irradiating the SiN membranes with highly energetic ($\sim 1\,\mathrm{GeV}$) heavy ions (Bi or Xe).[383] The ions passing through the membrane leave behind them defected tracks with higher etching rate compared to non-irradiated material, which leads to the formation of pores.[383]

The results of the dose test for the pattern created without conductive polymer indicated that high electron doses of $1200\,\mu\mathrm{C\,cm^{-2}}$ were necessary to observe the smallest features after RIE (Fig. 7.3G). On the contrary, in the case of pores patterned with E-spacer sharp and properly resolved features were obtained for the entire range of investigated electron doses (Fig. 7.3H). On this basis I continued fabricating 200 nm large square pores with low electron doses of $700\,\mu\mathrm{C\,cm^{-2}}$ and with the applied conductive polymer layer. The exposure parameters are similiar to those used for patterning sub-10 nm features on thin SiN membranes.[384]

It has to be noted that despite the use of exactly the same parameters I observed variability in RIE performance. In some cases the pores were partially blocked after etching, either by not fully etched SiN, or by the fluorine based polymers (such as $Si_xO_yF_z$) formed and re-deposited during RIE[133, 377, 378, 380] (Fig. 7.4A). Redeposition of these polymers can be prevented by increasing the oxygen content in

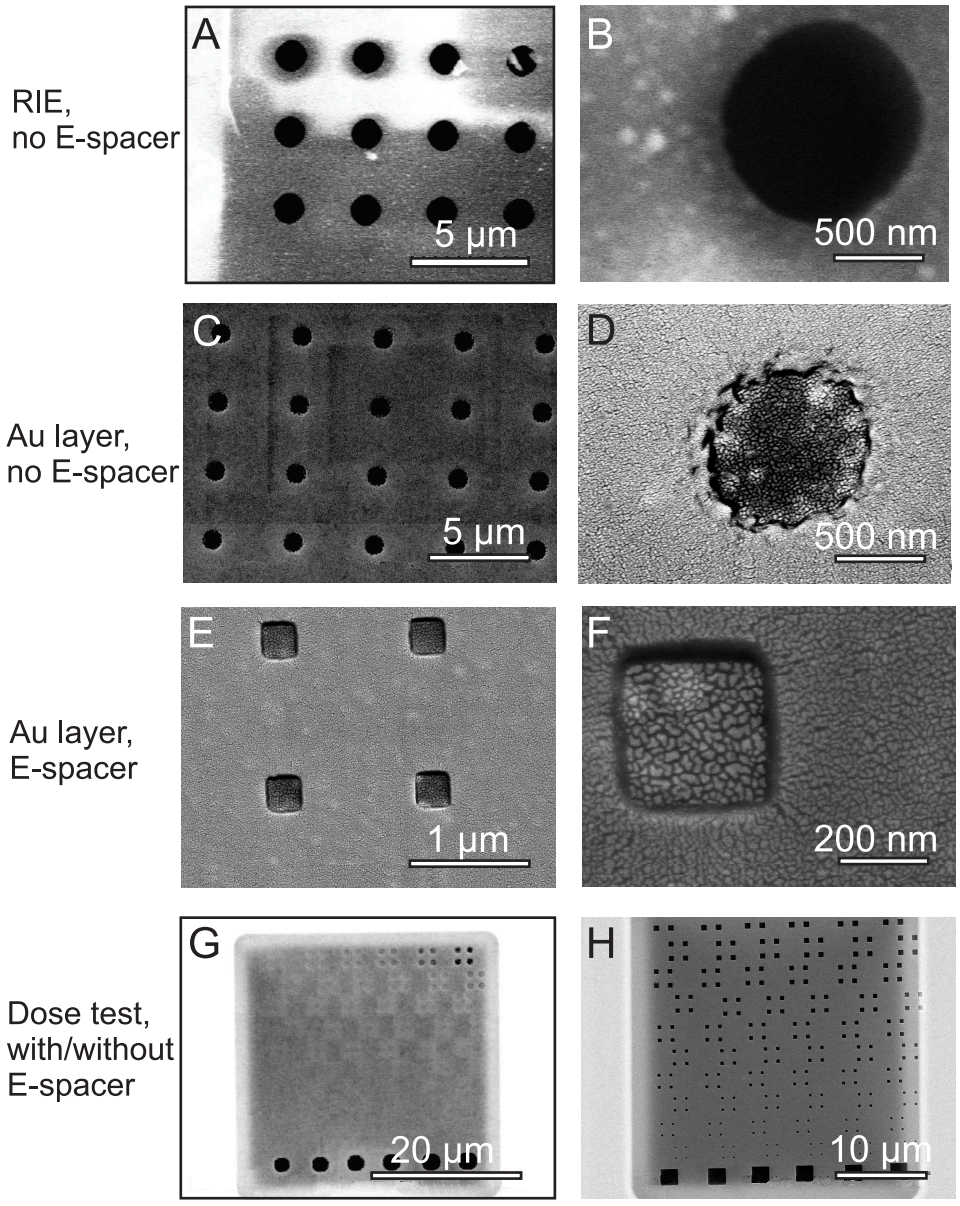


Figure 7.3: SEM images of nanopores patterned in SiN by RIE. A-B) The smallest features obtained in SiN after RIE − circular pores with diamater 1 µm. Pattern exposed by the EBL in PMMA was a square with side length 200 nm. C-D) The same pattern in PMMA. The etching mask directly after EBL patterning and before RIE was covered with 10 nm of evaporated gold. Resulting smallest openings in PMMA layer have diameter of ~ 700 nm, while the pattern exposed by the EBL in PMMA was a square with side length of 200 nm. E-F) The same pattern defined in PMMA layer by EBL, prior to the exposure a layer of conducting polymer (E-spacer) was applied. Smallest obtained features are squares with side length of 200 nm. G-H) Results of the EBL dose test on the membrane with and without deposited E-spacer layer. Each of the membranes was patterned with the same set of square openings with decreasing sizes. The six columns of these features in each of the membranes were exposed with different electron dose varying between $600 - 1200\,\mu C\,cm^{-2}$ in $100\,\mu C\,cm^{-2}$ increments.

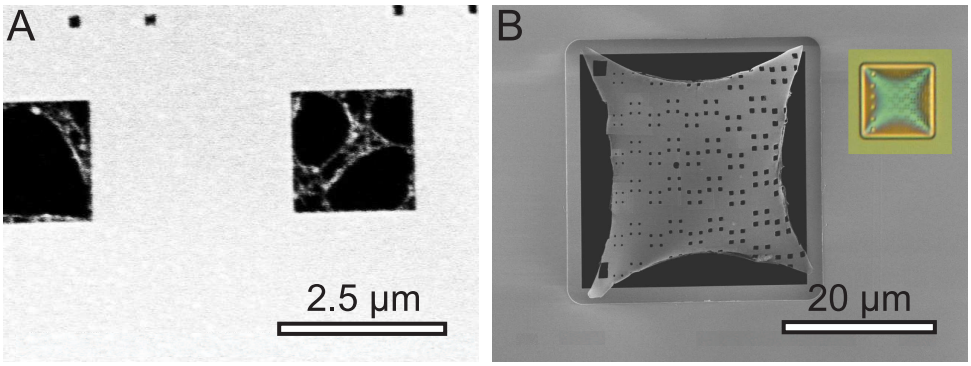


Figure 7.4: Issues with patterning membranes: A) Fragments of substrate or re-deposited fluorine-based polymers bridging pores. B) Result of the over-etching of a SiN membrane (Inset shows an optical image of SiN membrane with clear optical contrast due to differences in stress and strain of the membrane)

the etching mixture.[378] I also observed the features of too fast etching process, when the entire membrane was partially or even fully etched (Fig. 7.4B). RIE rate is sensitive to traces of contamination in chamber and to small differences in etching parameters such as temperature, power or pressure.[377, 378, 380] It is highly likely that the observed differences in the etching process would be limited by using system dedicated to a single etching chemistry.[378]

7.1.2 Fabrication of Suspended Graphene Tunnel Junctions

After developing the process for the scalable fabrication of pores with sizes commensurate with the size of graphene constrictions I designed and patterned gold electrodes aligned with suspended SiN membrane using the EBL process. Because the acquired SiN membranes did not have any registration markers I divided the gold patterning process into two steps. First, I used the EBL system set to low current of 100 nA to find the membrane and pattern the registration markers, which were subsequently

developed and evaporated with Cr 10 nm-thick adhesion layer and Au 70 nm layer. In the second lithography, step these markers were used to pattern electrodes with a large EBL current of 10 µA. The exposure of the entire pattern using low current settings would take too much time. The second EBL step was also followed by a metallization step. I obtained membranes with eight electrode pairs (Fig. 7.5A-B). Subsequently I prepared 200 nm large pores aligned with the electrodes using the previously described method. The last fabrication step was graphene transfer and patterning of the graphene constrictions. This was achieved using the process described in Chapter 2, with the only modification being application of E-spacer to reduce the broadening of the EBL-patterned features resulting from the substrate charging effects.

Examples of patterned devices are plotted in Fig. 7.5C and E. They show acceptable alignment of the graphene constrictions with the pores. Out of 48 patterned devices I found that 24 are conductive with the expected resistance of 3 kΩ after all the fabrication steps. I applied the typical electroburning procedure described in Chapter 2, obtaining 9 successfully formed devices. The sign of success was measurement of a tunnelling IV curve. Recorded curves were similar to curves obtained for normal supported devices (Fig. 7.5D and F). A few repeated voltage sweeps revealed that current levels are stable.

These are preliminary results showing feasibility of wafer-scale fabrication of suspended GTJs aligned with nanopores. Further research is necessary to confirm if the tunnelling gap (the narrowest point of the constriction) is suspended over the pore or whether it is formed over the substrate. Low yield of successfully formed

tunnel junctions (19 %) indicates that electroburning routine should be improved to increase the success rate by fine-tuning the electroburning parameters. Finally, the stability of these devices in liquid environments as well as their noise performance should be investigated.

7.2 Three Terminal Graphene Devices

Motivation for Side-Gate Further advances in DNA sequencing could be obtained by the implementation of a three-terminal measurement system. It has been proposed that inclusion of a gate electrode could enhance differentiation between nucleobases by the onset of resonant transport giving rise to larger current values and overall higher differences in signal between different bases.[362, 366] Such enhancement in molecular fingerprinting has been shown in aqueous environment in STM configuration using global Ag/AgCl gate reference electrode[385]

The efficient DNA sequencing demands high parallelization of the measurements on a single chip.[247, 386–388] However, the transport in nanoscale devices is sensitive to the atom-scale structural differences between such devices.[364] Therefore a different gating level may be necessary for different devices on the same chip in order to tune the energy levels into resonant transport. A global liquid gate[212, 389] may be insufficient to provide resonant transport in all devices. Instead, a local dedicated gate, capable of individually tuning the transport through an array of devices can be beneficial. Here I develop one such approach showing gating operation in three terminal all-graphene devices.

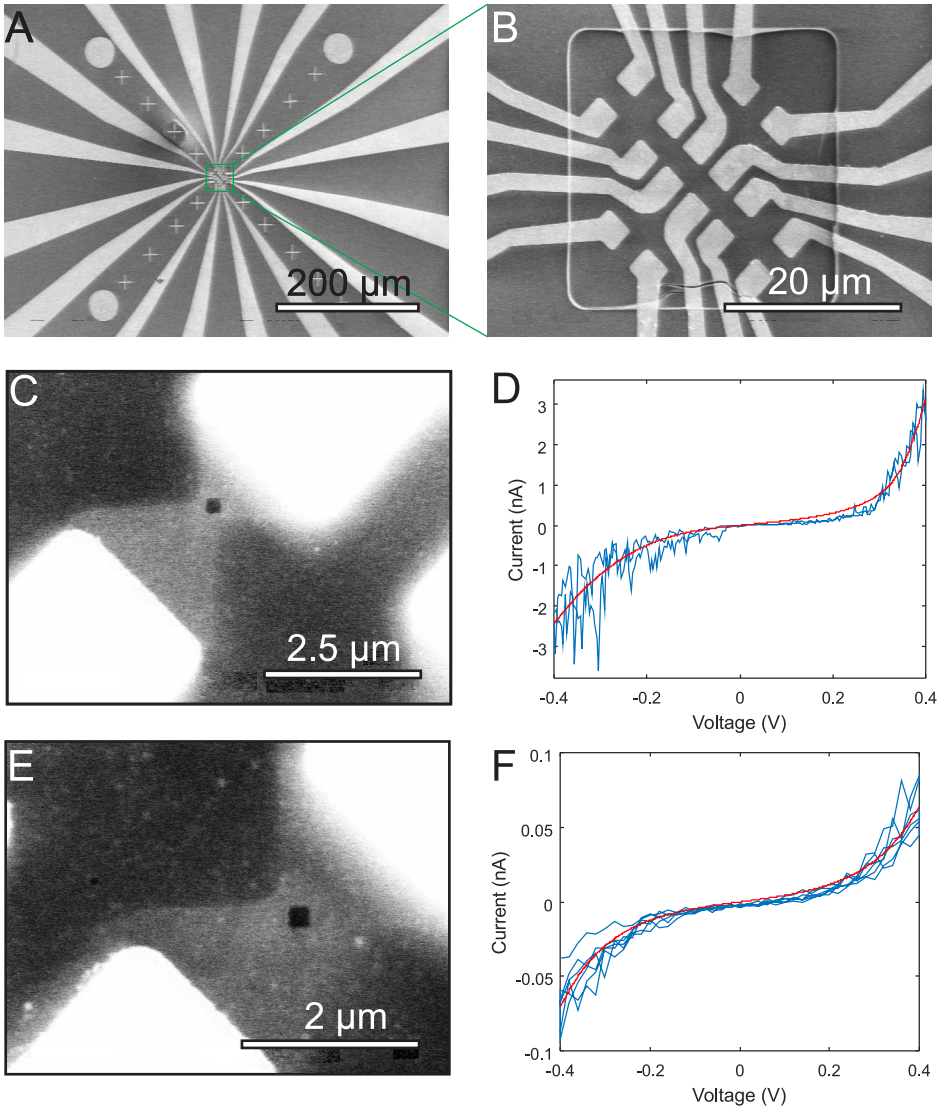


Figure 7.5: SEM images of suspended graphene devices: A-B) Gold electrodes aligned with the suspended SiN membrane. C and E) Images of graphene devices aligned with the nanopore. D and F) Tunnelling curves obtained for the imaged devices (Red lines correspond to Simmons model fit).

The geometry of a DNA strand translocating through a nanopore is stabilised by the presence of electric field driving in-plane tunnelling current. The effect is the larger the higher is the ratio of the in-plane electric field to the transmembrane electric field.[294] The in-plane electric field is expected to align the molecules with the junction, decreasing the number of available geometries and therefore reducing spread of probed current values.[294] Such effects were simulated to happen on the time scales of $\sim 100\,\mathrm{ps}$[294, 390] The same effect of limiting the variability of possible configurations of DNA strand was shown to be induced by a planar electrode sealed in the membrane.[391] Negative voltage applied to such planar electrode was found to shift the distribution of the centre of mass of DNA strand to the middle of the nanopore by means of repulsion of the negatively charge phosphate backbone.[391] Gate voltage can be also used to exert control over the ion flow rate [392] and it was shown that local gate field can control the DNA capture rate[393] and decrease the translocation rates enhancing detection of single nucleobases.[394]

Other advances in the tunnelling sequencing could include the sequencing of a given DNA strand translocating through a series of tunnelling electrodes. Increasing the number of such electrode pairs and analysis of the cross-correlation of the signals decreases the sequencing error exponentially with the number of tunnelling junctions.[314, 395] Detection of a sequence series of tunnelling electrodes is much more effective compared to the decreasing the translocation rate, which allows for longer averaging time in a single junction.[314, 395] I note that such multiple-junction readout could be realized in a series of GTJs located in a nanometric channel.

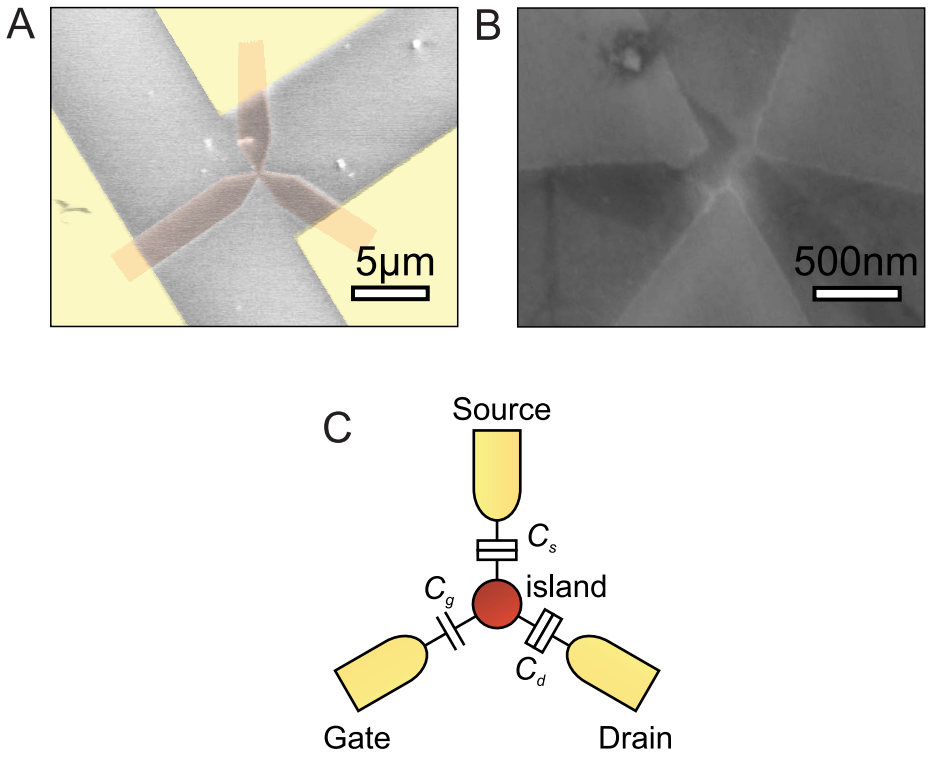


Figure 7.6: Structure of three-terminal graphene transistors. SEM images showing the A) overall geometry and B) constriction area of the devices. C) Schematic diagram of a electric model used to explain observation of the Coulomb blockade.

7.2.1 Fabrication of Three Terminal Devices

In order to equip the graphene devices with a side-gate electrode I altered the geometry of the EBL-fabricated structures so that it contains three interconnected graphene electrodes (Fig. 7.6A). The fabrication process is the same as the process described in Chapter 2. The graphene ribbons at the connection point are constricted in order to facilitate electroburning (Fig. 7.6B). The gate terminal (G) is slightly narrower (200 nm) compared to the width of the source-drain (S-D) channel in order to ensure that the gate distance is sufficiently large to prevent the gate-current.

7.2.2 Electroburning of Three Terminal Devices

After EBL step devices are electroburnt in order to break the graphene constrictions. The first electroburning step is performed by applying feedback-controlled bias between gate and shorted source-drain electrodes. This process results in the formation of a tunnelling gap between gate electrode and source-drain channel (G-SD gap). This is evident from the transition from the linear IV curve before this first electroburning step to a non-linear Simmons-type curve after (Fig. 7.7A). The feedback parameters are similar to those described in chapter 2. Subsequently I perform the second electroburning step by applying feedback-controlled voltage to the S-D electrodes (Fig. 7.7B). Again I observe the transition from linear S-D IV curves, as measured after G-SD electroburning step, to nonlinear tunnelling IV curves (Fig. 7.7C).

The yield of successfully burned devices is $\sim 70\,\%$ for both electroburning steps. The mean tunnelling distance after first electroburning step is $d_{G-SD} = 1.6 \pm 0.7\,\mathrm{nm}$, for 103 devices as caluclated on the basis of Simmons fit of tunnelling I-V curves (Appendix A). The mean tunnelling distance after second electroburning step is $d_{S-D} = 1.8 \pm 0.8\,\mathrm{nm}$, for 71 successfully burned devices. I did not observe any correlation between d_{G-SD} and d_{S-D}. Interestingly, after the second electroburning step the G-SD current decreased beyond detection limit, which I interpret as further reduction in the tunnelling distance d_{G-SD} after S-D gap electroburning (Fig. 7.7C). This might be related to the fact that the narrowest region of the S-D junction after its electroburning lies in the middle of channel, which means that the S-G and D-G electrode distance increased. This feature is beneficial for the practical application of the devices as G-SD leakage current would afflict results.

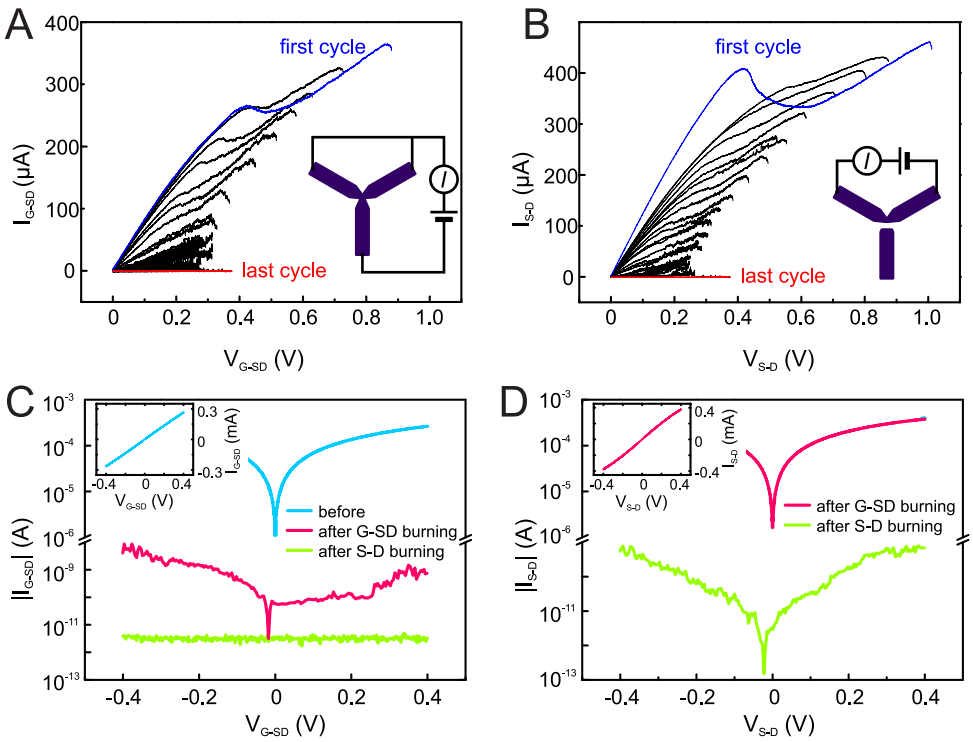


Figure 7.7: Electroburning of three terminal devices: A) IV curves for the first step of electroburning the G-SD gap. B) IV curves for the second step of electroburning the S-D gap. C) IV curves recorded for applied G-SD voltage before first electroburning step, after first electroburning step and after second electroburning step. D) IV curves recorded for applied S-D voltage before and after second electroburning step.

7.2.3 Gating at 77 K and Room Temperature

Subsequently, I proceed to the characterisation of the gating behaviour of the three terminal devices. It is known that electroburning process may lead to the formation of intrinsic graphene quantum dots (QDs).[86, 396] Their nanometer size is expected to govern the electron transport by means of large electrostatic charging energy of such QD and resulting single electron transport. Indeed, I observed features of the QDs in $\sim 10\,\%$ of devices showing S-D tunnelling current. I make this observation by means of measuring current stability diagrams in the function of source-drain (V_{SD}) and gate voltage (V_G), Fig. 7.8A. Clear features of Coulomb blockade were observed with regions of high current due to single electron tunnelling (SET), and low Coulomb blocked region current.

Slopes of the high conductance region in Fig. 7.8A can be used to asses relative capacitance of the electrodes (Fig. 7.6C) as $C_S = 14C_G$ and $C_D = 20C_G$.[397] I can also calculate the lever arm given as[397]

$$\alpha_G = \frac{C_G}{C_G + C_S + C_D}, \tag{7.1}$$

which quantifies the shift of the Fermi level as a function of the gate voltage. The obtained value of $\alpha = 0.03$ is 2-3 times larger than the values of back gate coupling on a 300 nm-thick SiO_2/Si substrate.[398] This gate coupling is however much lower than typically obtained lever arm values for a liquid gate, which is close to unity.[399, 400] I observe significant leakage currents of $I_L = 0.1\,\mathrm{nA}$ at $V_G > 2.5\,\mathrm{V}$, what indicates that the maximum possible energy level shift is $\Delta E = \alpha_G V_G = \pm 0.75\,\mathrm{meV}$

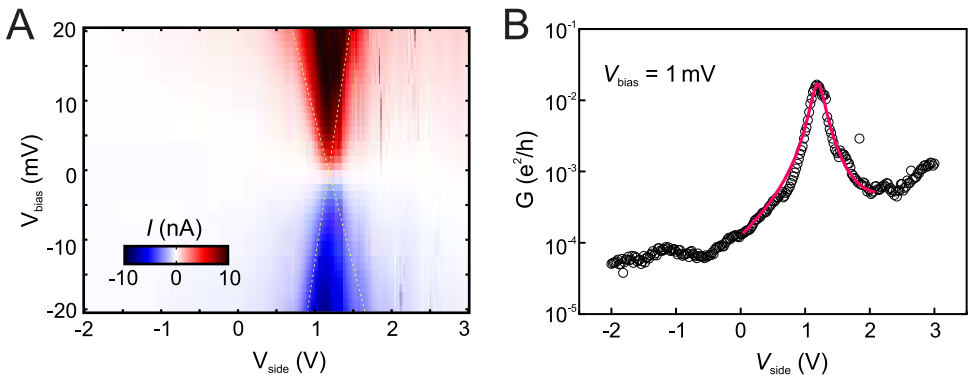


Figure 7.8: Side-gate effect on transport at 77 K. A) Stability diagram showing Coulomb blockade and the region of SET (dashed lines). B) Differential conductance for a gate trace recorded at constant bias, with a fit to resonant Lorentzian peak.

I also fit the differential conductance peak (Fig. 7.8B) with a Breit-Wigner formula[401],

$$G = \frac{2e^2}{h}\left(\frac{1}{\Gamma_S}+\frac{1}{\Gamma_D}\right)^{-1}\frac{h^2\Gamma}{\alpha^2(V_0-V_G)^2+(h\Gamma/2)^2}, \tag{7.2}$$

where V_0 is the centre of the peak and $\Gamma = \Gamma_S + \Gamma_D$ is a sum of tunnelling rates to S and D electrodes. The obtained value of coupling strength $h\Gamma = 6\,\mathrm{meV}$ is larger than thermal energy $kT = 0.2\,\mathrm{eV}$. This indication encourages me to investigate gating action at room temperature.

A stability diagram recorded at room temperature is shown in Fig. 7.9A. The evident observation of high and low conductive regions (Fig. 7.9B) implies that the addition energy is sufficient to dominate transport even at high temperatures and that the gate coupling is sufficient to shift the QD energy level. Interestingly comparing the slopes of the edges of SET region I obtain higher gate coupling constant of $\alpha = 0.26$. I attribute this change to the shift in local electrostatic potential due

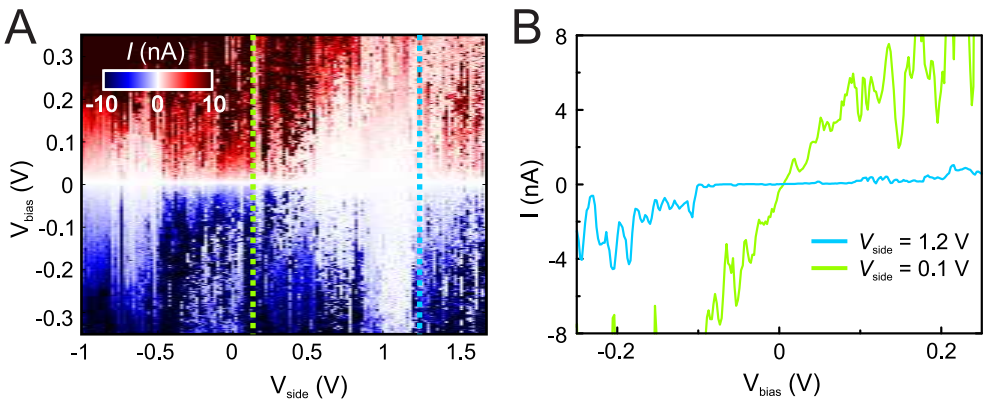


Figure 7.9: Side-gate effect on transport at room temperature. A) Stability diagram showing Coluomb blockade. B) IV curves, corresponding to dashed lines in Fig. A taken as crossections of the stability diagram in the SET and Coulomb blocked regions.

to a possible rearrangement of the SiO_2 charge traps upon increasing temperature.

I expect that such three terminal all-graphene transistors would form an ultimate sequencing platform when aligned with the RIE-fabricated nanopores in thin SiN membranes. Such system would allow for the control over DNA translocation because of the nanopore constriction and concurrently the gate electrode could stabilise the strand geometry and allow to probe the resonant transport through the bases.

Chapter 8

Summary

In this thesis I investigated possible applications and limits to performance of GTJs fabricated by feedback-controlled electroburning. A particular focus was on the characterisation of response of GTJs to environmental factors influencing electron transport in the devices.

I have investigated RTSs observed in GTJs at cryogenic temperature. The analysis of the signals indicated that the RTSs are generated by charge traps located in the underlying substrate. The switching mechanism relies on changing position of a charge carrier between two adjacent charge traps in the course of tunnelling or thermal excitation over a potential barrier. The change of the position of a charge carrier alters the local electrostatic potential and in the effect gates the tunnelling barrier.

The linear scaling of the current step amplitude with the mean tunnelling current indicates that current is just a method of detecting the fluctuations in the tunnelling

barrier, however it does not induce the switching. The analysis of correlations in the amplitude of consecutive current steps in GTJs allows for the observation of Coulomb repulsive interactions between charge carriers. The sensing of RTSs arising due to just a single trap implies that GTJs constitute a localized probe, which is sensitive to its closest environment and is able to detect signals generated by single electrons.

The thermal activation of a larger number of charge traps at room temperature leads to the vanishing features of RTS. The Gaussian distribution of energy barrier values related to the increased number of thermally activated charge traps, leads to the observation of the lognormal current distribution. The $1/f$ noise spectrum emerges as a superposition of larger number of Lorentzian peaks. The normalized noise amplitude values have a low variability range, however its value $\alpha = 10^{-3} - 10^{0}$ is much higher compared to graphene FETs. This observation is perceived as another indication of the sensitivity of GTJs to the local environment. The low scatter of the normalized noise amplitude values means that the observed noise is generated by the electrostatic fluctuations in the environment, that is similar for all of the devices.

The observed noise level is a factor limiting the sensitivity of GTJs in prospective biosensing applications. The increased measurement bandwidth, necessary to probe faster translocation events, and longer measurement duration, necessary to perform longer DNA strand reads, unavoidably lead to the increased level of accumulated noise power, which increases the amplitude of detectable signals. Noise levels observed in GTJs lead to the detectable signal limit on the order of $1 - 100\,\mathrm{nA}$, depending on the measurement duration, bandwidth, baseline current and expected SNR.

Measurements of tunnelling currents in the water environment resulted in the decrease of the tunnelling current at given voltage and increase in the electric noise level, compared to the GTJs in a dry state. I attribute these observations to the formation of EDL of polarized water molecules at the graphene-water interface. The water molecule dipoles oriented in order to screen the electric field of graphene electrodes, result in the effective increase in the tunnelling barrier, while the fluctuations in the structure of the EDL vary the electrostatic potential, leading to the increased noise levels. I observed rare events of fast RTS ($\sim$ ms) in GTJs measured in water, which have never been observed in dry devices. These effects can be attributed to the formation of transient charge traps induced by water molecules at the graphene-water interface. The duration of these signals, sufficient to detect them, is presumably the effect of stabilisation of the charge traps by the stable nanoconfined water clusters.

By using water solutions of nucleoside triphosphates I demonstrated that GTJs have biosensing capability. 10 nM concentrations were found to generate current peaks with a characteristic steep rise slope and a flat plateau. The detected peaks were forming peak bursts, separated by regions with no peaks. Each of the bursts can be interpreted as a single analyte molecule binding event, and the consecutive peaks within the burst can be attributed to the molecule rearrangement in the junction. Advantages of the graphene electrodes are evident from the detection of nucleotides at low concentrations and long dwell times of current peaks. These two features are on par with those reported for purposely functionalized gold junctions. This is an indication of dominant $\pi - \pi$ stacking interaction between nucleotides and graphene.

The comparison of signals recorded in solutions of different nucleosides, guanine

and thymine, proved that different nucleobases generate sizeable tunnelling signals, however the differences in the peak height and duration distributions varied more between different devices, than between different molecules measured with the same device. Despite demonstrating large amplitude signals allowing for the detection of nucleotides, the unambiguous discrimination between their different kind still has to be demonstrated. One of obstacles for the nucleobase discrimination in the current setup may be the random diffusion of the analyte molecules by Brownian motions in the vicinity of a junction. I assume that constricting the nucleobases in the junction would lead to the limited number of molecular configurations and would result in a lower spread of the detected signal values, allowing for the nucleobase discrimination.

As an outlook I demonstrated the fabrication protocol of suspended GTJs aligned with a nanopore, which would allow to direct the translocation of a molecule between the graphene electrodes. These devices have to be further examined to confirm their stability in liquid environment, and to characterise their low-frequency noise levels, which should be lower for the suspended devices compared to the devices fully supported on a substrate. It may be also necessary to improve the alignment of the GTJs with the nanopores. I also showed a method of fabrication of all-graphene three-terminal devices with a local side-gate, which can be used in classical molecular electronics, but they can be also applied to facilitate the discrimination between nucleotides by gating the analyte and allowing to probe the resonant transport. The advantage of the side-gate electrode is the higher gating coupling compared to the global back-gate electrode, and the possibility of gating individual devices, as opposed to back-gate and liquid gate electrodes.

GTJs can constitute an efficient biosensing platform due to their high sensitivity to the local electrostatic environment, atomic thickness allowing to form focused tunnelling probes, and low screening making them sensitive to the local gating effects, which can facilitate sensing. The specificity of analyte interactions can be further improved by the designed functionalization of the edges of GTJs. Sensing of DNA strands is just one of the envisaged applications of GTJs, it will be equally interesting to perform biosensing and sequencing experiments on linear protein and carbohydrate sequences, which currently are not possible with the classical methods.

Appendices

Appendix A

Tunnelling Distance and Simmons Model

Discontinuity between graphene ribbons results in the potential barrier between two graphene leads. Electrons can overcome this barrier either if their thermal energy is higher than the potential barrier or if distance between graphene electrodes is sufficiently small, which allows for tunnelling.[15]

The WKB approximation can be used to obtain the probability of tunnelling through the barrier $V(x)$ for electrones with incident kinetic energy element $E_x = \frac{mv_x^2}{2}$. It takes the form of[15]

$$D(E_x) = exp\left(-\frac{4\pi}{h}\int_{s_1}^{s_2}[2m(V(x)-E_x)]^{1/2}\right), \tag{A.1}$$

where m is electron mass. This expression can be further used to obtain the number

of electrons tunnelling through the barrier[15]

$$N = \int_0^{v_m} v_x n(v_x) D(E_x) dv_x = \frac{1}{m} \int_0^{E_m} n(v_x) D(E_x) dE_x, \tag{A.2}$$

where transition is made from the domain of velocity v_x to energy E_x, and $n(v_x)$ denotes the numeric concentration of electrons with velocities in the range $[v_x, v_x + dx]$.[15] The number of electrons with velocity in the range $[v_x, v_x + dx; v_y, v_x + dy; v_z, v_x + dz]$ is given as[15]

$$n(v) dv_x dv_y dv_z = \frac{2m^4}{h^3} f(E) dv_x dv_y dv_z, \tag{A.3}$$

where

$$f(E) = \frac{1}{\exp\left(-\frac{E-\mu}{kT}\right) + 1} \tag{A.4}$$

is Fermi distribution at temperature T and with the electrochemical potential μ. The distribution of electrons with a given velocity in the direction v_x may be obtained by integrating over all velocity values in the direcctions v_y and v_z[15]

$$n(v_x) = \frac{2m^4}{h^3} \int \int_{-\infty}^{\infty} f(E) dv_y dv_z = \frac{4\pi m^3}{h^3} \int_0^{\infty} f(E) dE_r, \tag{A.5}$$

where the last formula is expressed in polar coordinates with

$$\begin{aligned} v_r^2 &= v_y^2 + v_z^2 \\ E_r &= \frac{m v_r^2}{2} \end{aligned} \tag{A.6}$$

Combining equations A.2 and A.5 the current density is given as[15]

$$j = eN = \frac{4\pi m^2 e}{h^3} \int_0^{E_m} D(E_x) dE_x \int_0^{\infty} f(E) dE_r \tag{A.7}$$

In equilibrium the net currents flowing from left to right j_l and vice versa j_r average out $j_l = -j_r$. However, if there is any voltage applied, there is also a difference in energy distribution between electrons in the left and right leads, giving rise to the net current[15, 402]

$$j = j_l(E) - j_r(E + eV) = \frac{4\pi m^2 e}{h^3} \int_0^{E_m} D(E_x) dE_x \int_0^{\infty} [f(E) - f(E + eV)] dE_r \tag{A.8}$$

Subsequently the profile of barrier $V(x)$ can be expressed with respect to the lead work function η as[15]

$$V(x) = \eta + \phi(x). \tag{A.9}$$

The mean barrier height over the tunnelling distance $\Delta s = x_2 - x_1$ is equal to[15]

$$\overline{\phi} = \frac{1}{\Delta s} \int_{x1}^{x_2} \phi(x) dx \tag{A.10}$$

Using these parameters the density of tunnelling current can be expressed as[15]

$$j = \left(\frac{e}{2\pi h \Delta s^2}\right) \left\{ \overline{\phi} \exp\left(-\frac{4\pi \Delta s}{h} \sqrt{2m\overline{\phi}}\right) - (\overline{\phi} + eV) \exp\left(-\frac{4\pi \Delta s}{h} \sqrt{2m(\overline{\phi} + eV)}\right) \right\} \tag{A.11}$$

It indicates that the density of tunnelling current can be obtained knowing the av-

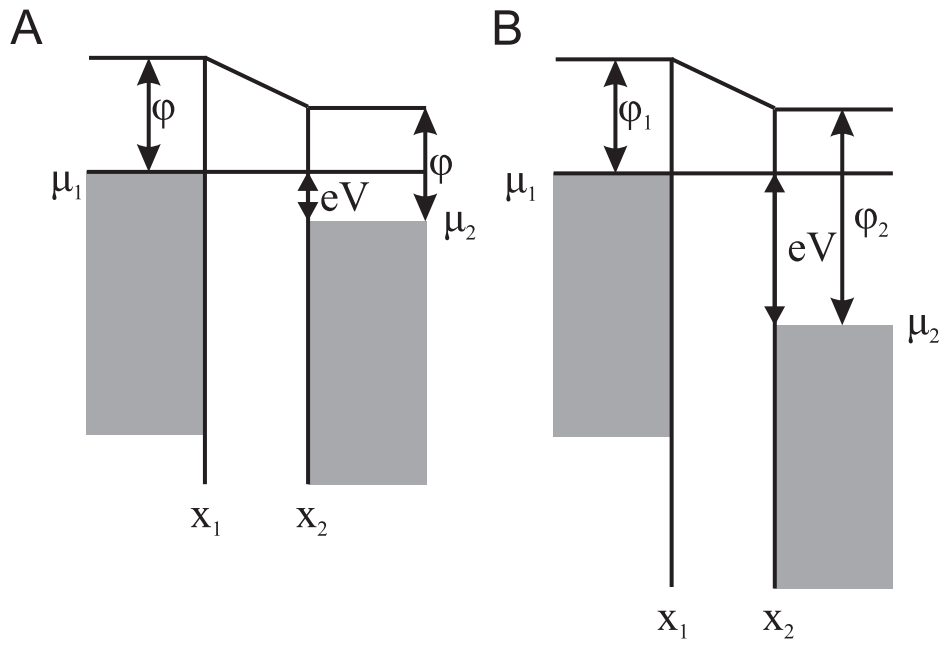


Figure A.1: Diagram of the potential barrier in a biased tunnel junction with A) equal work functions $\phi_1 = \phi_2 = \phi$ and B) different work functions ϕ_1 and ϕ_2.

erage barrier height, without the information of its exact profile.[15]

A couple of cases of this general formula can be deduced. For low voltages ($V \approx 0$) it predicts linear ohmic dependence on voltage[15–18, 403]

$$j = \frac{(2m)^{\frac{1}{2}}}{\Delta s}\left(\frac{e}{h}\right)^2 \overline{\phi}^{\frac{1}{2}} V \exp\left(-\frac{4\pi\Delta s}{h}\sqrt{2m\overline{\phi}}\right). \tag{A.12}$$

In the case of a rectangularr barrier ϕ the intermediate voltage range ($eV < \phi$)

current density can be expressed as [15, 16, 18, 403]

$$j = \left(\frac{e}{2\pi h s^2}\right)\left\{\left(\phi - \frac{eV}{2}\right)\exp\left[-\frac{4\pi s}{h}\sqrt{2m\left(\phi - \frac{eV}{2}\right)}\right] - \left(\phi + \frac{eV}{2}\right)\exp\left[-\frac{4\pi s}{h}\sqrt{2m\left(\phi + \frac{eV}{2}\right)}\right]\right\} \tag{A.13}$$

For the purpose of fitting of experimental tunnelling IV curves, following the method used by Prins *et al.* for fitting tunnelling curves in GTJs I use the simplified formula taking two assumptions[90]; firstly the low temperature form of Fermi distribution ($kT < \mu_1,\ \mu_2,\ \phi(x)$) is assumed, leading to integral

$$\int_0^{\infty} [f_1(E) - f_2(E)]dE = \int_{\mu_2}^{\mu_1} dE. \tag{A.14}$$

The second assumption is a triangular profile of the tunnelling barrier[90]

$$\phi(x) = \phi_1 + (\phi_2 - \phi_1)\frac{x - x_1}{x_2 - x_1} \tag{A.15}$$

The fitting algorithm uses two different formulas. If $E_x < \phi_1,\ \phi_2$ the exponent of tunnelling probability can be expressed as[90]

$$\int_{x_1}^{x_2} \sqrt{\phi(x) - E_x}dx = (x_2 - x_1)\frac{2}{3}\frac{(\phi_2 - E_x)^{\frac{3}{2}} - (\phi_1 - E_x)^{\frac{3}{2}}}{\phi_2 - \phi_1}. \tag{A.16}$$

In the case of $\phi_1 < E_x < \phi_2$[90],

$$\int_{x_1}^{x_2} \sqrt{\phi(x) - E_x}dx = (x_2 - x_1)\frac{2}{3}\frac{(\phi_2 - E_x)^{\frac{3}{2}}}{\phi_2 - \phi_1}. \tag{A.17}$$

Appendix B

Calculations of Noise Spectra

In general a signal measured in an electronic system can be treated as a function of time $x(t)$. Applying the Fourier transform to such signal allows for transition from the time domain into frequency domain[138]

$$X(\omega) = \int_{-\infty}^{\infty} x(t) exp(-i\omega t) dt. \tag{B.1}$$

This function provides information about the spectral rather than temporal distribution of the fluctuations, *i.e.* which flutctuation freqencies are occurring more or less commonly.[138] Also reverse operation of calculating the signal in the time domain by applying the inverse Fourier transform to the function of frequency is possible,

$$x(t) = \frac{1}{2\pi} \int_{-\infty}^{\infty} X(\omega) exp(i\omega t) d\omega. \tag{B.2}$$

Using the Parseval's theorem the following equation can be obtained[138]

$$\int_{-\infty}^{\infty} x(t)x^*(t)exp(-i\omega t)dt = \frac{1}{2\pi}\int_{-\infty}^{\infty} X(\omega)X^*(\omega)exp(i\omega t)d\omega, \tag{B.3}$$

which shows the relation between the product of signal $x(t)$, its conjugate and its Fourier transformed counterpart. Further, assuming that $x(t)$ signal is non-zero only in a limited, symmetric time range $\left[-\frac{T}{2}, \frac{T}{2}\right]$, the expression can be written in an alternative form[138],

$$\int_{-\infty}^{\infty} \left[x_T(t)\right]^2 dt = \frac{1}{2\pi}\int_{-\infty}^{\infty} \left|X_T(\omega)\right|^2 d\omega, \tag{B.4}$$

where $x_T(t)$ denotes the part of spectrum with non-zero amplitude of oscillations. The former expression is also equal to the summed energy of the oscillations[138]. The average power can be calculated by normalising the total energy with the duration of the fluctuation signal[138]

$$\lim_{T\to\infty}\frac{1}{T}\int_{-\infty}^{\infty} \left[x_T(t)\right]^2 dt = \lim_{T\to\infty}\frac{1}{2\pi}\int_{0}^{\infty} \frac{2\left|X_T(\omega)\right|^2 d\omega}{T}. \tag{B.5}$$

In this expression it is sufficient to limit integration to the positive frequencies and account for the total energy by multiplying the expression by a factor of two.[138] As the last step in order to obtain the average PSD averaging over the statistical

ensemble can be performed[138]:

$$S(\omega) = \lim_{T\to\infty} \frac{\overline{2\left|X(\omega)\right|^2}}{T}. \tag{B.6}$$

Alternatively the noise spectrum can be calculated on the basis of autocorrelation function $c(\tau)$ which is a measure of the correlation in the signal fluctuations at different time instants. In the case of a process with time independent value distribution (stationary process) is defined as[138]

$$c(\tau) \equiv \langle x(t)x(t+\tau)\rangle = \lim_{T\to\infty} \frac{1}{T} \int_{\frac{-T}{2}}^{\frac{T}{2}} x(t)x(t+\tau)dt, \tag{B.7}$$

where averaging is performed for all time values t. It can be shown that the autocorrelation function and noise PSD are directly related by the pair of Fourier transforms according to the Wiener-Khintchine theorem[138]

$$c(\tau) = \frac{1}{2\pi} \int_0^\infty S(\omega)\cos\omega\tau d\omega \tag{B.8}$$

$$S(\omega) = 4\int_0^\infty c(\tau)\cos\omega\tau d\tau. \tag{B.9}$$

In the effect the knowledge about any of the $x(t), S(\omega), c(\tau)$ allows to calculate two remaining functions (although as stated before inverse Fourier transform does not allow to obtain the $I-t$ trace unambiguously[136]).

Appendix C

Scalling of ΔI Amplitude and Emergent $1/f$ noise

Usually in models of $1/f$ noise emerging from the superposition of Lorentzian peaks it is assumed that dwell times are distributed uniformly on a logarithmic scale ($t = 10^{-n},\ n = 1,\ 2,\ 3,\ 4, ...$) and $\Delta I = const$ for all of the Lorentzians (as in Fig. 5.1). However, as I show in Fig. C.1 different scaling trends of ΔI can lead to a noise spectrum with slope close to one. I consider here four basic scenarios, namely $\Delta I \sim n$, $\Delta I \sim \frac{1}{n}$, $\Delta I \sim \exp(-n)$ and $\Delta I \sim \exp\{n\}$, which give rise to slopes $\alpha = 1.091$, $\alpha = 1.188$, $\alpha = 1.408$ and $\alpha = 0.653$ respectively (Fig C.1 A-D). In particular $\Delta I \sim \frac{1}{n}$ and $\Delta I \sim \exp(-n)$ scaling models would be intuitively in agreement with a model of a tunnel junction gated by a charge traps. Lower spacing between them would lead to the faster switching kinetics however the effect on switching amplitude would be lower.

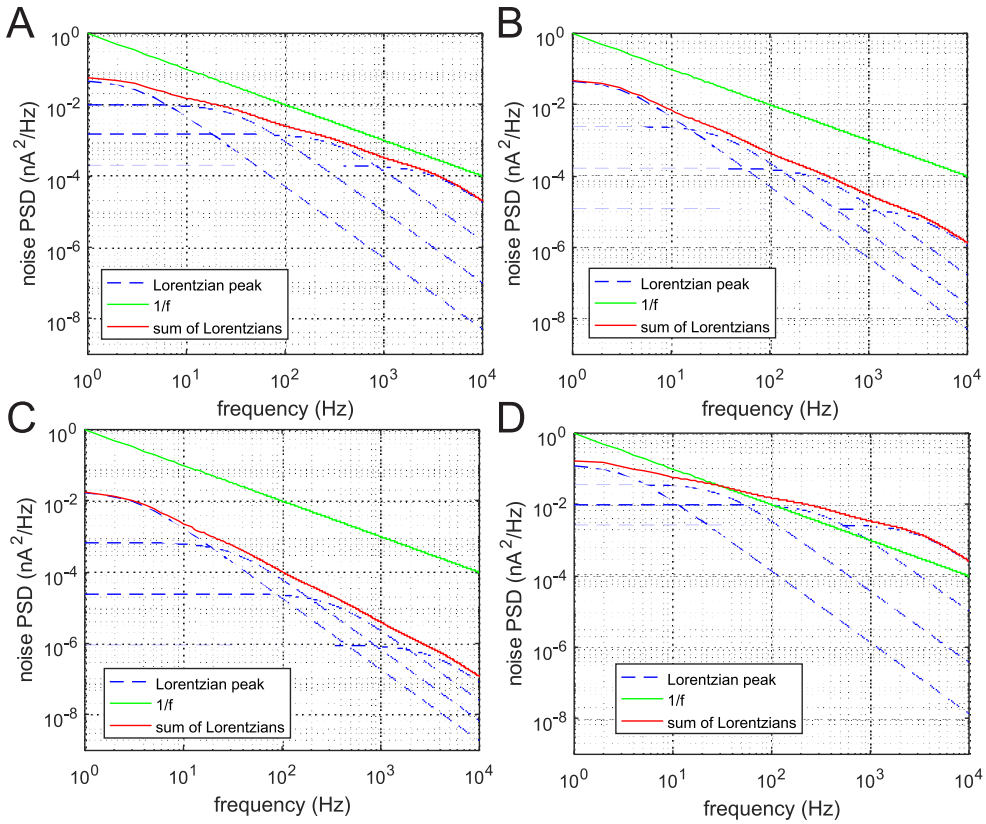


Figure C.1: Different scenarios of scaling Lorentzian noise amplitude A) $\Delta I \sim n$, slope $\alpha = 1.091$ B) $\Delta I \sim \frac{1}{n}$, $\alpha = 1.188$ C) $\Delta I \sim \exp(-n)$, $\alpha = 1.408$, D) $\Delta I \sim \exp\{n\}$, $\alpha = 0.653$.

In general a Lorentzian formula taking into account the current amplitude scaling function $g(n)$ can be written in the form $S(n) = \frac{2[g(n)\Delta I]^2 10^{-n}}{4+(2\pi f 10^{-n})}$. Taking the logarithm it leads to $\log S(n,f) = 2\log(g(n)) + \log\left[\frac{2\Delta I^2 10^{-n}}{4+(2\pi f 10^{-n})}\right] = 2\log S_g(n) + \log S(f)$. In the effect conditions for ΔI scaling with n are gentle, all the functions meeting criterion $|\frac{\Delta S_g(n)}{\Delta n}| \ll |\frac{dS(f)}{df}|$, $n = 1,\ 2,\ 3,\ 4, \ldots$ will introduce only slight deviation from the $1/f$ noise slope.

Appendix D

Limits of Change Point Detection – Simulations

I investigate here the reliability of CPD method, which I use to identify moments of transition between two current states. As it was said 'This is the most crucial and delicate stage of the analysis'[136] and therefore I put special emphasis on preventing any artefacts arising from the application of this method to the analysis of the experimental $I - t$ traces. For this purpose I simulate TLF traces of $\pm 1\,\mathrm{nA}$ amplitude with an exponential distribution of dwell times τ in the range $1 - 100\,\mathrm{ms}$ with known number of switching events (10000). To make such trace more similar to experimental data I superimpose over it white noise of a given amplitude, constant for the duration of the entire trace.

At first I will look at the influence of superimposed white noise amplitude on the detection capability of CPD method. For this purpose to the simulated trace

consisting of 10000 switching events I add a simulated white noise $I - t$ trace, with different noise amplitudes $-20\,\mathrm{dB}$, $-10\,\mathrm{dB}$, $0\,\mathrm{dB}$, $10\,\mathrm{dB}$. Fragments of the resulting traces are presented in Fig. D.1. As can be seen there the CPD method is fairly robust against the high noise level, being able to distinguish between simulated steps and fluctuations due to white noise. In the case of $0\,\mathrm{dB}$ white noise (simulation there resembles signal typically obtained in the measurements) few additional detection events triggered artificially by noise and short levels skipped because of being buried in noise can be observed. At $10\,\mathrm{dB}$ noise amplitude the white noise starts to dominate the signal and CPD method fails to reproduce the original signal.

In Fig. D.2 I present ΔI step correlation histograms obtained for traces with different white noise levels. As expected, higher white noise levels do not introduce additional correlations. They only lead to the wider distribution of ΔI values. However centres of the point clusters are not shifted, and there are no additional point clusters. Only in the case of $10\,\mathrm{dB}$ trace the high noise level obscures simulated TLF and there are erroneously detected multiple $(\Delta I_{up,1}, \Delta I_{up,2})$ or $(\Delta I_{down,1}, \Delta I_{down,2})$ events.

The second test of the reliability of the CPD method was achieved by varying the maximum allowed number of change point fed to the CPD algorithm. This parameter is important as it defines the number of segments into which signal is divided. I generated a test signal with 10000 switching events and $-10\,\mathrm{dB}$ noise amplitude, and subsequently I performed CPD with different numbers of change points $(10000, 15000, 25000, 50000, 100000$ and $5000)$. Fragments of simulated traces are presented in Fig. D.3 As can be seen in Fig. D.3B,C a slight increase of allowed

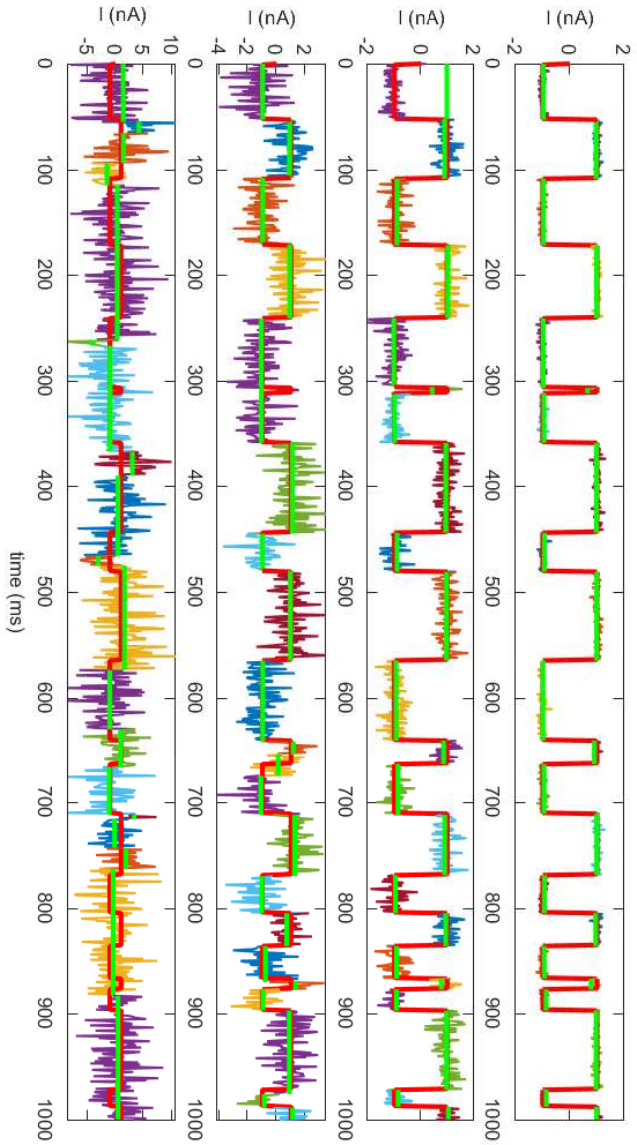


Figure D.1: Detection of current steps in simulated TLF with different noise levels signals by CPD method. Total number of simulated steps is 1000. Noise levels are A) −20 dB B) −10 dB C) 0 dB D) 10 dB.

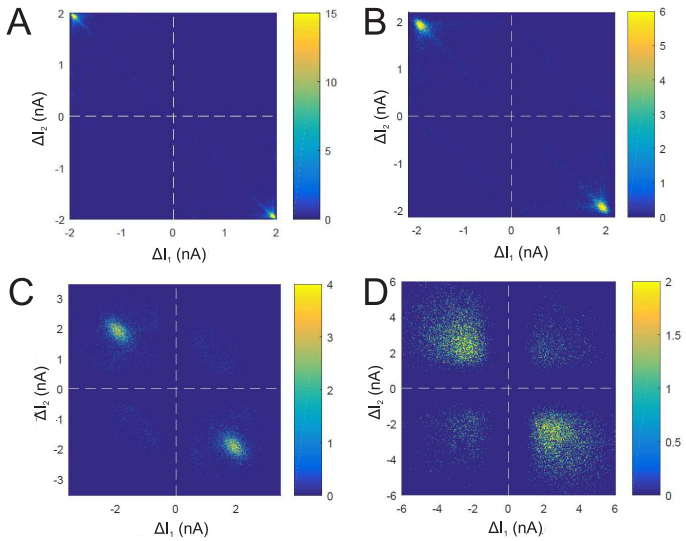


Figure D.2: Distribution of ΔI step correlations for simulated TLF signals with different white noise levels: A) −20 dB B) −10 dB C) 0 dB D) 10 dB. Current steps where dettectd using CPD algorithm with set correct number of change points(10000).

number of change points above the number of simulated steps allows the algorithm to detect the vertical lines connecting points as separate levels. Further increase of the allowed number of change points leads to even further discrepancies. It can be seen in Fig. D.3D that now even slight fluctuations in current due to the white noise are detected as separate levels.

In Fig. D.4 I present diagrams of ΔI step correlations for corresponding traces analyzed with varying number of change points. The increase of allowed number of points by 50 % already introduces significant artefacts (Fig. D.4B), which were not present in the simulated signal. They seemingly correspond to the incorrectly detected switching events, because the additional ΔI point clusters lie on or close to 0 axes. Further increase in the number of allowed change points makes this issue

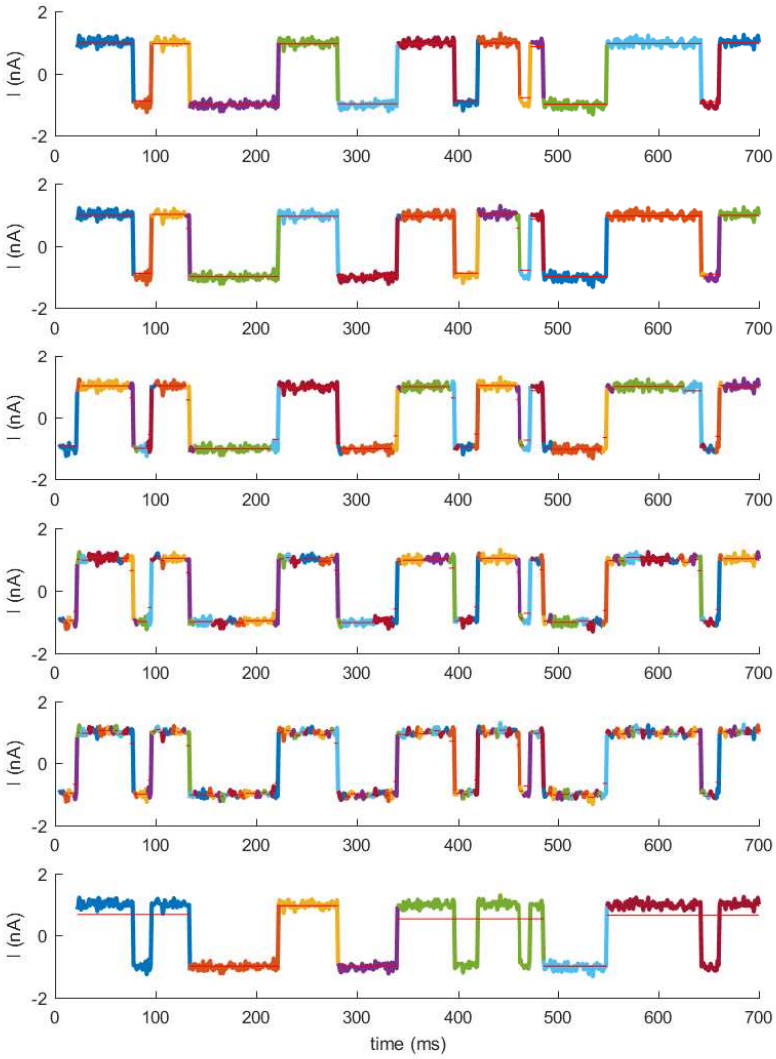


Figure D.3: Detection of current steps in simulated TLF signals by Change Point Detection method. Total number of simulated steps is 1000 while number of maximum allowed change point number in CPD algorithm is A) 10000 B) 15000 C) 25000 D) 50000 E) 100000 F) 5000.

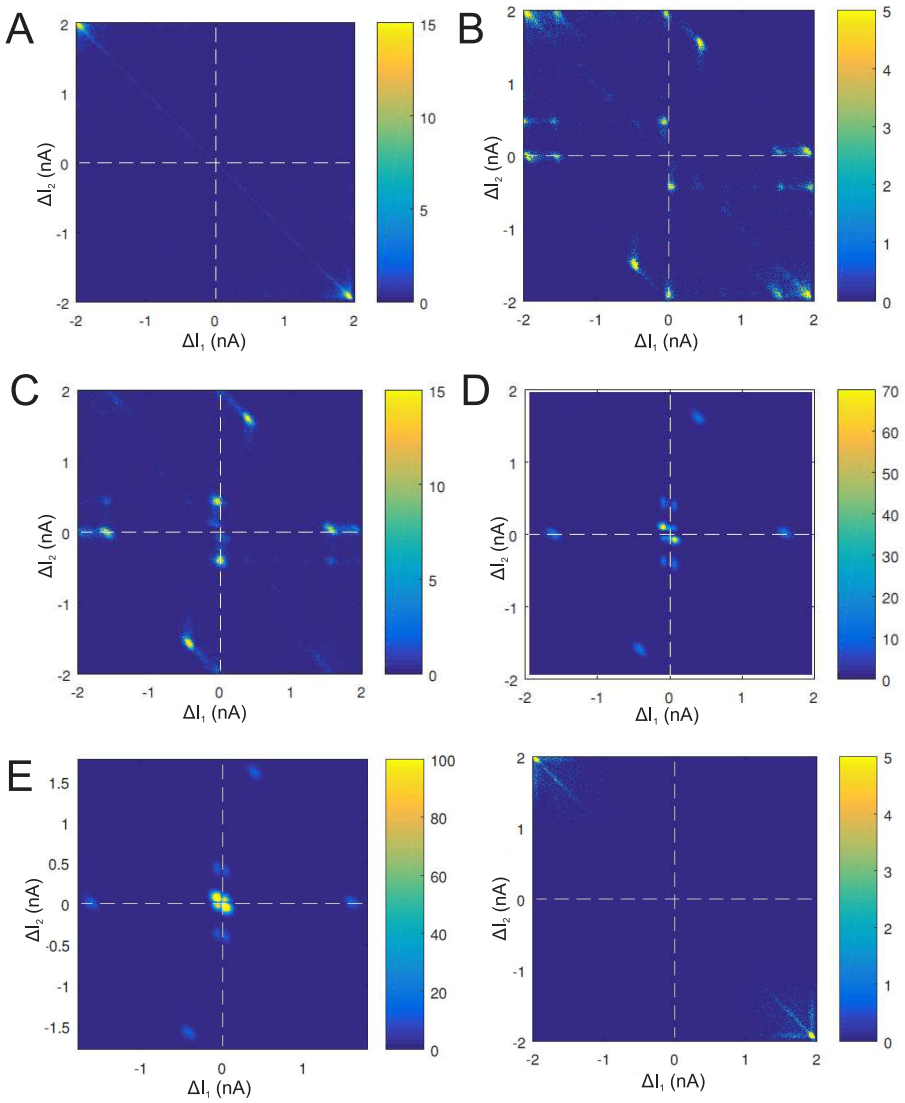


Figure D.4: Distribution of ΔI step correlations for simulated TLF signals detected with different number of maximum change points in CPD algorithm: A) 10000 B) 15000 C) 25000 D) 50000 E) 100000 F) 5000, while the simulated number of steps was 10000.

even more serious. And finally for 10 times higher number of allowed change points (Fig. D.4E) the most populated point clusters are these close to 0 point, indicating

that the majority of the detected current steps are these within real current steps, triggered by high white noise level and not real switching events.

Oppositely in Fig. D.3F and Fig. D.4F I show results of CPD with lower than simulated number of allowed change points (5000). Clustering of the data points is not afflicted by this underpopulation (CPD is still more likely to divide signal into regions with extremely differing mean values). However from $I - t$ traces it can be clearly seen that many of the real current levels are missed and merged into single current level (Fig. D.3F).

On this basis I would like to stress how important is setting the correct number of change points, obtained by noise spectrum fit, into the CPD algorithm. Providing accurate number will help in successful level detection even in the case of a noisy signal.

Appendix E

Limits of Change Point Detection – Experimental traces

Besides checking the influence of of number of allowed change points on the simulated traces another possible test is to perform similar analysis on the experimental data with TLF fluctuation. On the basis of Lorentzian fit to noise spectrum I obtain value of corner frequency f_0 which allows me to calculate expected number of switching events in the trace fragment of duration t as $N = tf_0/2$.

At first I look at $I - t$ traces separated into separate current levels by CPD with different N. In Fig. E.1 I plot a trace fragment showing correctly identified current levels with large ΔI values and erroneously detected current steps with low ΔI levels. The obtained number of switching events in 10 s trace was $N = 156$. I discern between correctly and incorrectly identified traces on the basis of ΔI value following each of the levels. The reference level is set by the lower border ΔI_{max} of the

highly populated quadrants with large current steps in the ΔI correlation histograms (Fig. E.3), that is levels correctly identified by CPD fulfil criterion $\Delta I > |\Delta I_{max}|$, while the opposite is true for the erroneously identified levels $\Delta I < |\Delta I_{max}|$.

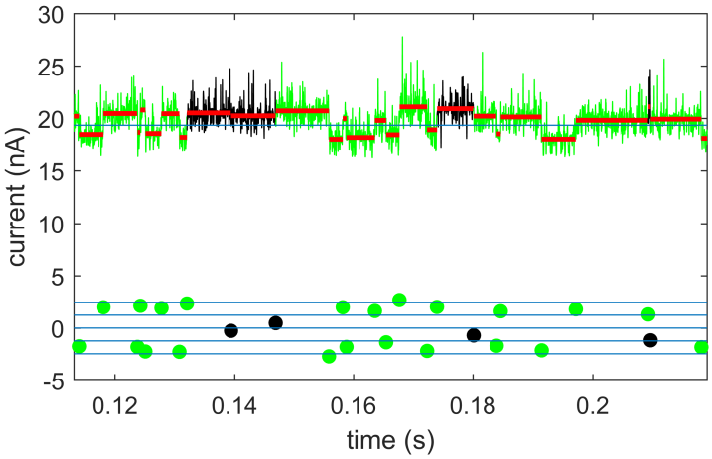


Figure E.1: Discerning real an erroneous current steps. Dot symbols show the value of calculated ΔI values between consecutive levels in a function of time. Horizontal reference lines correspond to 0 nA, $\pm\Delta I_{max}$ and $\pm 2\Delta I_{max}$ current. Transitions with $\Delta I > |\Delta I_{max}|$ values are identified as real switching events (green markers) while transitions with values $\Delta I < |\Delta I_{max}|$ are treated as incorrectly identified ones (black markers). In the plot I also show fragment of the trace with the same colour code – black trace for the mistaken detection and green for the correct detection. Red lines indicate the mean current for each level.

As can be seen from the plots in Fig. E.2 the number of the incorrectly detected events is minimized for the number of points allowed in the CPD equal to number of points obtained from the corner frequency of fitted Lorentzian noise spectrum (Fig. E.2B). Deviation from this number in any direction, *i.e.* decrease or increase of the allowed number of change points exacerbates the fit quality, as evident from the increasing number of incorrectly detected points.

Finally I will look at the ΔI correlation histograms obtained from the same trace

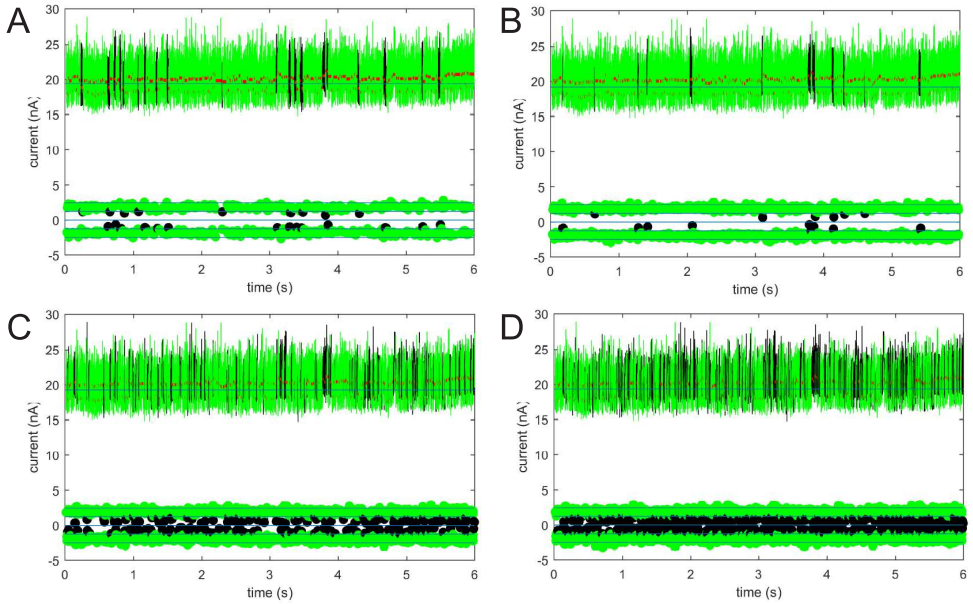


Figure E.2: Effect of maximum number of points in CPD method on correct recognition of current steps. Each of the panels shows trace fragments with separated current levels with marked mean current level for each of them (red lines) and markers denoting values of ΔI occurring after each of the steps. There is a common color code for the traces and fragments, in there are shown correctly identified current steps ($\Delta I > |\Delta I_{max}|$) and in erroneously identified levels in black ($\Delta I < |\Delta I_{max}|$). The estimated number of transitions in the current trace is $156\,\mathrm{s}^{-1}$. The panels show results of CPD analysis with A) 75 B) 156 C) 250 and D) 350 maximum allowed change numbers.

analysed by CPD method with different number of allowed change points. As can be seen in Fig. E.3 the correct and lower number of change points lead to proper ΔI correlation histograms with only two main clusters of points. However increasing the number of allowed change points introduces additional point clusters. This is caused by erroneous separation of the trace into non-physical current steps. This artificial current clusters are analogous to artefacts introduced in the analysis of the simulated samples with overestimated parameters in the previous section.

Therefore, on the basis of trace and ΔI clustering analysis I can conclude that expected relation between Lorentzian corner frequency and number of expected switching events occurring over the time is correct and CPD analysis leads to the correct separation of the signal into separate current levels.

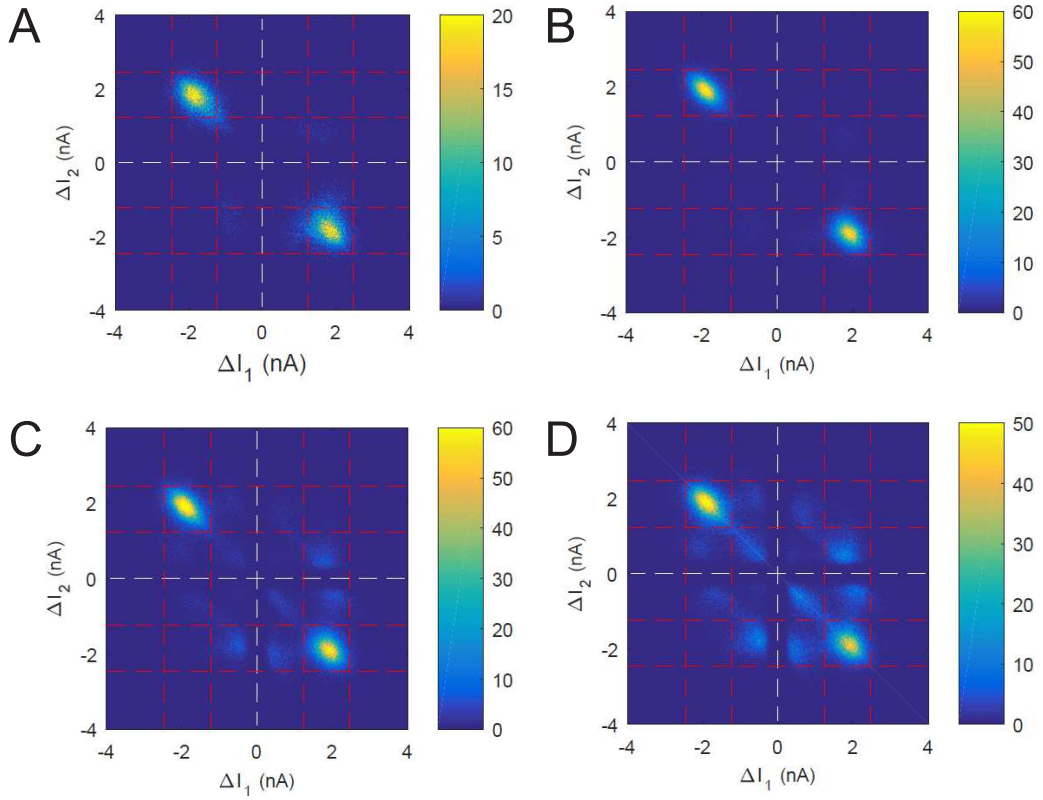


Figure E.3: Here I plot ΔI correlation histograms for the same current trace analyzed by CPD method with different number of allowed change points. The panels show results of CPD analysis with A) 75 B) 156 C) 250 and D) 350 maximum allowed change numbers, while the expected number of channge points was 156.

Appendix F

Measuremnt Circuit and Electronics

A nanopore equivalent circuit can be presented as a resistor representing the pore resistance to ionic current R_M in parallel with a capacitor corresponding to the capacitance of a nanopore C_M (Fig. F.1A).[123, 236] The wiring resistance R_S and capacitance C_S can be also included. Signal is generated by the current source I_S.[123, 236] In the case of a lossy dielectric medium another resistor in parallel with a capacitor may be added.[230] The resistance and capacitance values of the nanopore system give rise to the complex impedance of the form[236]

$$\begin{aligned} X_M &= \frac{R_M + R_S + fR_MC_MR_S}{1 + af + bf^2} \\ a &= R_MC_M + C_SR_M + C_SR_S \\ b &= R_MR_SC_MC_S. \end{aligned} \tag{F.1}$$

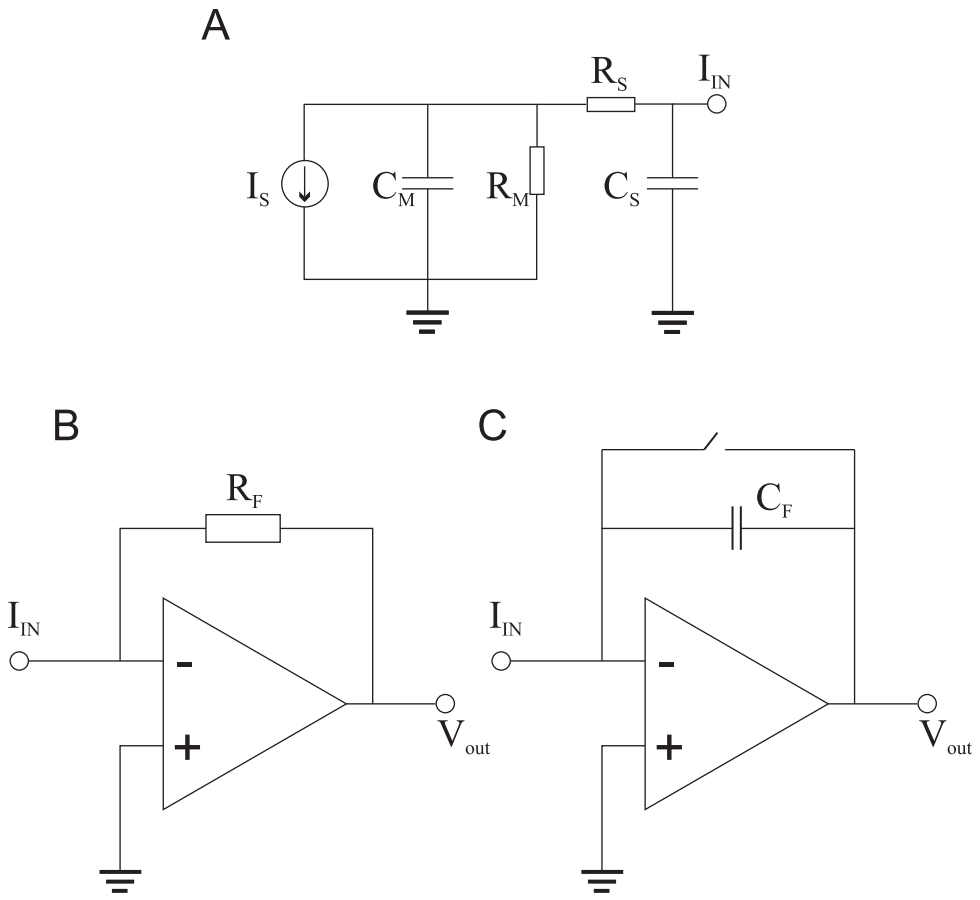


Figure F.1: Electronic circuit model of A) nanopore and amplifier and feedback loops with a B) resistor and C) capacitor feedback elements.[236]

This formula can be used to calculate the noise spectrum of a nanopore system as $S_M = \frac{4kT}{\mathrm{Re}\{X_M\}}$.[234, 236] This is a good approximation of high and intermediate frequency noise[236], however it does not account for the low frequency $1/f$ noise.[230]

The amplification of signals in nanosensing systems is achieved with an operational amplifier (op-amp), where the signal is fed through a negative terminal and with a negative feedback loop, which should yield a linear relation to the device current thanks to the linear feedback element.[120, 123, 236] This geometry allows

for voltage clamping, *i.e.* applying constant voltage by an alternating current flowing through the feedback element.[236] Feedback elements used in the amplifier circuit include resistors (Fig. F.1B) and capacitors (Fig. F.1C).[123, 236]

In the case of a resistor feedback element signal can be read as output voltage

$$V_{OUT} = -I_{IN} R_F.$$

The typically used resistance value of the feedback resistor is equal to 100 MΩ.[233] The drawback of the resistance feedback might be the large resistance value necessary for current detection, which leads to large resistor noise and in the effect necessity to limit the measurement bandwidth. It is also difficult to fabricate large resistance elements in CMOS technology, and such resistors can also introduce large capacitances.[234]

A possible variation is to use a capacitor as a feedback element in an integrator circuit (Fig. F.1C).[123, 236] The feedback is realised through charging of the capacitor C_F by I_{IN} current, which leads to the voltage output V_{OUT} being proportional to the I_{IN} current and the integration time T[236],

$$V_{OUT}(T) = \frac{\int_0^T I(t)dt}{C_F}. \tag{F.2}$$

The flow of current with a set polarity charging the C_F cannot continue for ever and therefore when its maximum charge value is reached it has to be reset to zero by shorting C_F. This is a drawback of such feedback mechanism because current cannot be recorded continuously. The problem is more serious in systems with large

I_{IN} currents (*e.g.* tunnel junctions) as reset in their case has to be more often.

List of Figures

2.1 Structure of a GTJ 20

2.2 Device Fabrication process 24

2.3 Electroburning of GTJs 26

3.1 Emerging TLF and Lorentzian noise spectrum in GTJs 30

3.2 Schematic of flicker and white noise spectrum. 32

3.3 Schematic profile of RTS with marked characteristic parameters, the current step amplitude and the dwell times of *up* and *down* level. . . 35

3.4 Lorentzian noise PSD profile 38

3.5 Different mechanisms of charge carrier number ΔN fluctuations . . . 44

3.6 Mechanism of conductance change in the oxide-based RRAM devices 48

3.7 Dependence of the normalized noise amplitude in graphene on gate voltage ($S(V_G)$) 52

3.8 hBN − grph − hBN stack structure with a reduced noise level 55

3.9 Scanning Noise Microscopy of graphene edges 58

3.10 TLF in a SAM with diluted electroactive ferrocene molecules 60

3.11 TLF in Au MCBJ with benzenditihol molecule 62

3.12 TLF in MCBJ molecular systems in liquid environment 63
3.13 TLF in GTJs due to pseudorotaxane complexation reaction 65
3.14 TLF in molecule-functionalized single CNT devices 66

4.1 RTN spectra of tunnelling current in Graphene Tunnel Junctions . . 69
4.2 Fitted white noise contribution of PSD spectrum for a Graphene Tunnel Junction 71
4.3 Fitted $1/f$ noise contribution of PSD spectrum for a Graphene Tunnel Junction 72
4.4 Fitted Lotrentzian noise contribution of PSD spectrum for a Graphene Tunnel Junction 73
4.5 RTS observed in a GTJ at 77 K and 180 mV$bias$ 76
4.6 Properties of local baseline current 77
4.7 FWHM of locale baseline current plotted versus current 78
4.8 ΔI level analysis in Graphene Tunnel Junction signal 80
4.9 Distribution of dwell times τ 81
4.10 Comparison of dwell time values obtained by noise and trace analysis 82
4.11 Separation of the noise in graphene tunnel junction into separate contributions 85
4.12 White noise analysis 86
4.13 ΔI point clusters 90
4.14 Example of ΔI point cluster plot 92
4.15 ΔI cluster asymmetry analysis 93

4.16 Asymmetry factor of the point distribution for *up* and *down* point clusters 95
4.17 Contour plot of non-rotated ΔI point clusters with bivariate Gaussian distribution 96
4.18 Simulated distribution of $(\Delta I_1, \Delta I_2)$ points 98
4.19 White noise and $1/f$ noise as a function of temperature 101
4.20 Temperature dependence of TLF 103
4.21 Energy difference between *up* and *down* states 104
4.22 $(\Delta I_1, \Delta I_2)$ point correlation histogram for TLF measured in graphene tunnel junction at 4.2 K 107
4.23 Analysis of asymmetry of $(\Delta I_1, \Delta I_2)$ point clusters in the function of temperature 108
4.24 Simulated IV curves showing influence of the point charge potential . 113
4.25 Current switching due to multiple fluctuators 116
4.26 Separation of the asymmetric tunnelling IV into 2 symmetric curves . 118
4.27 Long-duration TLF measurements 120

5.1 Emergence of $1/f$ noise from the superposition of TLFs 123
5.2 $1/f$ noise spectrum of GTJs at room temperature 125
5.3 Tunnelling current in GTJs at room temperature 127
5.4 Lognormal fitting parameters for current distribution at room temperature 129
5.5 6 h long $I - t$ traces recorded at room temperature 131
5.6 Fitting of $1/f$ noise spectra recorded at room temperature 133

5.7 Pseudo-Hooge parameter values 135
5.8 Noise spectrum in nanopore measurements 136
5.9 Multilayer dielectric stack used to reduce the capacitance of nanopore membrane 141
5.10 Noise levels in Femto DPLCA-200 amplifier 143
5.11 Noise in Axopatch 200b 146
5.12 High frequency noise in GTJs 147
5.13 Signal amplitude in nanopore measurements 150
5.14 Current standard deviation in a GTJ as a function of measurement time 153
5.15 Idealised $1/f$ noise spectra and resulting detection limits in graphene tunnel junctions 154
5.16 2D maps of signal detection limits 157

6.1 DNA nucleotide structures 160
6.2 Density of states distribution of nucleotides 162
6.3 Resistive pulse sensing in organic and inorganic nanopores 165
6.4 Diagram of a PCB and flow cell for liquid measurements 168
6.5 Planar and nonlinear diffusion modes 170
6.6 Parasitic currents in electrodes insulated with SiO_2, PMMA insulation and without insulation in dry, DI water and buffer solution environment 172
6.7 Chip insulation 175
6.8 non-contact mode AFM images of an opening in the PMMA insulation layer 176
6.9 Water nanostructure at graphene interface 180

6.10 Diagram of Electric Double Layer 182
6.11 Tunnelling IV curves in ambient and water environments 187
6.12 Slopes of noise spectra recorded for dry devices and in water environment 188
6.13 Noise comparison for Tunnel junctions measured in dry conditions and in water 190
6.14 Noise spectra and tunnelling current $I - t$ traces in dry and water environment 192
6.15 Recognition tunnelling signals recorded with a universal reader molecule 195
6.16 Tunnelling signals in DNA solutions 197
6.17 Tunnelling electrodes aligned with a nanopore 199
6.18 Examples of tunnelling signals of stochastically trapped DNA in MCBJ junctions 201
6.19 Tunnelling signal in 10 nM dGTP solution 205
6.20 Signal peaks in dGTP solution 207
6.21 Noise spectrum in water and dGTP solutions 209
6.22 Features of nucleotide signal peaks 211
6.23 Tunnelling signal in 10 nM dTTP solution 212
6.24 Comparison of current signal in 100 nM dTTP and dGTP solution . . 214
6.25 Comparison of peak amplitude-duration histograms for signals in dTTP and dGTP solutions 216

7.1 SiN membrane 220
7.2 SiN membrane RIE etching rate analysis 222
7.3 Nanopores patterned in SiN by RIE 225

7.4 Issues with patterning membranes 226
7.5 Suspended GTJs 229
7.6 Structure of three-terminal graphene devices 231
7.7 Electroburning of three terminal devices 233
7.8 Side-gate effect on transport at 77 K 235
7.9 Side-gate effect on transport at room temperature 236

A.1 Diagram of potential barrier 246

C.1 Scaling of Lorentzian ΔI amplitude 253

D.1 Detection of current steps in simulated TLF signals with different noise levels by CPD method 256
D.2 Distribution of ΔI step correlations for simulated TLF signals with different white noise levels 257
D.3 Detection of current steps in simulated TLF signals by Change Point Detection method 258
D.4 Distribution of ΔI step correlations for simulated TLF signals detected with different number of maximum change points in CPD algorithm 259

E.1 Discerning real an erroneous current steps 262
E.2 Effect of maximum number of points in CPD method on correct recognition of current steps 263
E.3 ΔI correlation histograms for different numbers of allowed change points in CPD analysis 264

F.1 Electronic circuit model of a nanopore and amplifier feedback loops . 266

Bibliography

1. Aviram, A. & Ratner, M. Molecular rectifiers. *Chem. Phys. Lett.* **29,** 277–283 (1974).
2. Ratner, M. A brief history of molecular electronics. *Nat. Nanotechnol.* **8,** 378–381 (2013).
3. Park, J. *et al.* Coulomb blockade and the Kondo effect in single-atom transistors. *Nature* **417,** 722–725 (2002).
4. Bogani, L. & Wernsdorfer, W. Molecular spintronics using single-molecule magnets. *Nat. Mater.* **7,** 179–186 (2008).
5. Yu, L. H. & Natelson, D. The Kondo Effect in C60 Single-Molecule Transistors. *Nano Lett.* **4,** 79–83 (2004).
6. Koch, J. & Von Oppen, F. Franck-Condon blockade and giant Fano factors in transport through single molecules. *Phys. Rev. Lett.* **94,** 206804 (2005).
7. Burzuri, E. *et al.* Franck-condon blockade in a single-molecule transistor. *Nano Lett.* **14,** 3191–3196 (2014).
8. Leturcq, R. *et al.* Franck-Condon blockade in suspended carbon nanotube quantum dots. *Nat. Phys.* **5,** 327–331 (2009).
9. Waldrop, M. M. The chips are down for Moore's law. *Nature* **530,** 144–147 (2016).
10. Smit, R. H. M. *et al.* Measurement of the conductance of a hydrogen molecule. *Nature* **419,** 906–909 (2002).
11. Schirm, C *et al.* A current-driven single-atom memory. *Nat. Nanotechnol.* **8,** 645–648 (2013).
12. Aradhya, S. V. & Venkataraman, L. Single-molecule junctions beyond electronic transport. *Nat. Nanotechnol.* **8,** 399–410 (2013).

13. Zwolak, M. & Di Ventra, M. Colloquium: Physical approaches to DNA sequencing and detection. *Rev. Mod. Phys.* **80,** 141–165 (2008).

14. Agah, S., Zheng, M., Pasquali, M. & Kolomeisky, A. B. DNA sequencing by nanopores: advances and challenges. *J. Phys. D. Appl. Phys.* **49,** 413001 (2016).

15. Simmons, J. G. Generalized Formula for the Electric Tunnel Effect between Similar Electrodes Separated by a Thin Insulating Film. *J. Appl. Phys.* **34,** 1793–1803 (1963).

16. Simmons, J. G. Electric Tunnel Effect between Dissimilar Electrodes Separated by a Thin Insulating Film. *J. Appl. Phys.* **488,** 2581 (1963).

17. Simmons, J. G. Low-voltage current-voltage relationship of tunnel junctions. *J. Appl. Phys.* **34,** 238–239 (1963).

18. Simmons, J. G. Generalized thermal J-V characteristic for the electric tunnel effect. *J. Appl. Phys.* **35,** 2655–2658 (1964).

19. Osorio, E. a., Bjørnholm, T, Lehn, J.-M., Ruben, M & van der Zant, H. S. J. Single-molecule transport in three-terminal devices. *J. Phys. Condens. Matter* **20,** 374121 (2008).

20. Thijssen, J. M. & Van Der Zant, H. S. J. Charge transport and single-electron effects in nanoscale systems. *Phys. Status Solidi Basic Res.* **245,** 1455–1470 (2008).

21. Perrin, M. L., Burzurí, E. & van der Zant, H. S. J. Single-molecule transistors. *Chem. Soc. Rev.* **44,** 902–919 (2015).

22. Hines, T. *et al.* Transition from tunneling to hopping in single molecular junctions by measuring length and temperature dependence. *J. Am. Chem. Soc.* **132,** 11658–11664 (2010).

23. Vazquez, H. *et al.* Probing the conductance superposition law in single-molecule circuits with parallel paths. *Nat. Nanotechnol.* **7,** 663–667 (2012).

24. Artes, J. M., Li, Y., Qi, J., Anantram, M. & Hihath, J. Conformational gating of DNA conductance. *Nat. Commun.* **6,** 8870 (2015).

25. Gerhard, L. *et al.* An electrically actuated molecular toggle switch. *Nat. Commun.* **8,** 14672 (2017).

26. Magyarkuti, A., Adak, O., Halbritter, A. & Venkataraman, L. Electronic and Mechanical Characteristics of Stacked Dimer Molecular Junctions. *Nanoscale* **10,** 3362–3368 (2018).

27. Leary, E. *et al.* Incorporating single molecules into electrical circuits. The role of the chemical anchoring group. *Chem. Soc. Rev.* **1,** 920–942 (2015).

28. Li, C. Z. *et al.* Quantized tunneling current in the metallic nanogaps formed by electrodeposition and etching Quantized tunneling current in the metallic nanogaps formed by electrodeposition and etching. *Appl. Phys. Lett.* **77,** 3995 (2000).

29. Wu, B. H., Ivie, J. A., Johnson, T. K. & Monti, O. L. A. Uncovering hierarchical data structure in single molecule transport. *J. Chem. Phys.* **146,** 092321 (2017).

30. Garner, M. H. *et al.* Comprehensive suppression of single-molecule conductance using destructive σ -interference. *Nature* **558,** 415–419 (2018).

31. Stroscio, J. A. & Celotta, R. J. Controlling the Dynamics of a Single Atom in Lateral Atom Manipulation. *Science (80-.).* **306,** 242–247 (2004).

32. Lock, D., Rusimova, K. R., Pan, T. L., Palmer, R. E. & Sloan, P. a. Atomically resolved real-space imaging of hot electron dynamics. *Nat. Commun.* **6,** 8365 (2015).

33. Pawlak, R. *et al.* Design and Characterization of an Electrically Powered Single Molecule on Gold. *ACS Nano* **11,** 9930–9940 (2017).

34. Garrido Torres, J. A., Simpson, G. J., Adams, C. J., Fruchtl, H. A. & Schaub, R. On-demand final state control of a surface-bound bistable single molecule switch. *Nano Lett.* **18,** 2950–2956 (2018).

35. Wang, K. *et al.* Measurement and understanding of single-molecule break junction rectification caused by asymmetric contacts. *J. Chem. Phys.* **141,** 054712 (2014).

36. Capozzi, B. *et al.* Single-molecule diodes with high rectification ratios through environmental control. *Nat. Nanotechnol.* 1–7 (2015).

37. Capozzi, B. *et al.* Mapping the Transmission Functions of Single-Molecule Junctions. *Nano* **16,** 39493954 (2016).

38. Ahmed, T. *et al.* Electronic fingerprints of DNA bases on graphene. *Nano Lett.* **12,** 927–931 (2012).

39. Blum, A. S. *et al.* Molecularly inherent voltage-controlled conductance switching. *Nat. Mater.* **4,** 167–172 (2005).

40. He, J., Lin, L., Zhang, P. & Lindsay, S. Identification of DNA basepairing via tunnel-current decay. *Nano Lett.* **7,** 3854–3858 (2007).

41. Huang, S. *et al.* Recognition tunneling measurement of the conductance of DNA bases embedded in self-assembled monolayers. *J. Phys. Chem. C* **114,** 20443–20448 (2010).

42. Korshoj, L. E., Afsari, S., Khan, S., Chatterjee, A. & Nagpal, P. Single Nucleobase Identification Using Biophysical Signatures from Nanoelectronic Quantum Tunneling. *Small* **13,** 1603033 (2017).

43. Albrecht, T. *et al.* Scanning tunneling spectroscopy in an ionic liquid. *J. Am. Chem. Soc.* **128,** 6574–6575 (2006).

44. Guo, S., Manuel, J. & Díez-pérez, I. Electrochemically-gated single-molecule electrical devices. *Electrochim. Acta* **110,** 741–753 (2013).

45. Hirsch, B. E., McDonald, K. P., Tait, S. L. & Flood, A. H. Physical and chemical model of ion stability and movement within the dynamic and voltage-gated STM tipsurface tunneling junction. *Faraday Discuss.* **00,** 1–14 (2017).

46. Nogues, C., Cohen, S. R., Daube, S., Apter, N. & Naaman, R. Sequence dependence of charge transport properties of DNA. *J. Phys. Chem. B* **110,** 8910–8913 (2006).

47. Chang, S. *et al.* Tunnelling readout of hydrogen-bonding-based recognition. *Nat. Nanotechnol.* **4,** 297–301 (2009).

48. Livshits, G. I. *et al.* Long-range charge transport in single G-quadruplex DNA molecules. *Nat. Nanotechnol.* **9,** 1040–1046 (2014).

49. Xu, B. & Dubi, Y. Negative differential conductance in molecular junctions: an overview of experiment and theory. *J. Phys. Condens. Matter* **27,** 263202 (2015).

50. Zhang, L., Zhang, J. & Ulstrup, J. Electrochemical single-molecule conductivity of duplex and quadruplex DNA. *Curr. Opin. Electrochem.* **7,** 66–74 (2018).

51. Wu, Z., Wu, S., Oberholzer, S, Steinacher, M & Calame, M. Scaling of 1/f noise in tunable break junctions. *Phys. Rev. B* **78,** 235421 (2008).

52. Sydoruk, V. A. *et al.* Noise and transport characterization of single molecular break junctions with individual molecule. *J. Appl. Phys.* **112,** 014908 (2012).

53. Xiang, D., Jeong, H., Lee, T. & Mayer, D. Mechanically Controllable Break Junctions for Molecular Electronics. *Adv. Mater.* **25,** 4845–4867 (2013).

54. Perrin, M. L. *et al.* Large negative differential conductance in single-molecule break junctions. *Nat. Nanotechnol.* **9,** 830–834 (2014).

55. Frisenda, R. *et al.* Kondo Effect in a Neutral and Stable All Organic Radical Single Molecule Break Junction. *Nano Lett.* **15,** 3109–3114 (2015).

56. Chen, R & Natelson, D. Evolution of shot noise in suspended lithographic gold break junctions with bias and temperature. *Nanotechnology* **27,** 245201 (2016).

57. Li, R. *et al.* Switching of Charge Transport Pathways via Delocalization Changes in Single-molecule Metallacycles Junctions. *J. Am. Chem. Soc.* **139,** 14344–14347 (2017).

58. Morikawa, T., Yokota, K., Tsutsui, M. & Taniguchi, M. Fast and low-noise tunnelling current measurements for single-molecule detection in electrolyte solution using insulator-protected nanoelectrodes. *Nanoscale* **9,** 4076–4081 (2017).

59. Li, B. T., Hu, W. & Zhu, D. Nanogap Electrodes. *Adv. Mater.* **22,** 286–300 (2010).

60. Ohshiro, T. *et al.* Single-Molecule Electrical Random Resequencing of DNA and RNA. *Sci. Rep.* **2,** 1–7 (2012).

61. Arima, A., Tsutsui, M., Morikawa, T., Yokota, K. & Taniguchi, M. Fabrications of insulator-protected nanometer-sized electrode gaps. *J. Appl. Phys.* **115,** 114310 (2014).

62. Muthusubramanian, N. *et al.* Insulator-protected mechanically controlled break junctions for measuring single-molecule conductance in aqueous environments. *Appl. Phys. Lett.* **109,** 012102 (2016).

63. Wu, S. *et al.* Molecular junctions based on aromatic coupling. *Nat. Nanotechnol.* **3,** 569–574 (2008).

64. Wang, Q. *et al.* Single-Atom Switches and Single-Atom Gaps Using Stretched Metal Nanowires. *ACS Nano* **10,** 9695–9702 (2016).

65. Liu, R. *et al.* Fabricating Atom-Sized Gaps by Field-Aided Atom Migration in Nanoscale Junctions. *Phys. Rev. Appl.* **9,** 54023 (2018).

66. Xiang, D. *et al.* Three-terminal single-molecule junctions formed by mechanically controllable break junctions with side gating. *Nano Lett.* **13,** 2809–2813 (2013).

67. Johnston, D. E., Strachan, D. R. & Johnson, A. T. C. Parallel Fabrication of Nanogap Electrodes. *Nano Lett.* **7,** 2774–2777 (2007).

68. Hoffmann-Vogel, R. Electromigration and the structure of metallic nanocontacts. *Appl. Phys. Rev.* **4,** 031302 (2017).

69. Mangin, A, Anthore, A, Rocca, M. L. D., Boulat, E & Lafarge, P. Transport through metallic nanogaps in an in-plane three-terminal geometry. *J. Appl. Phys.* **105,** 014313 (2013).

70. O'Neill, K., Osorio, E. A. & Van Der Zant, H. S. Self-breaking in planar few-atom au constrictions for nanometer-spaced electrodes. *Appl. Phys. Lett.* **90,** 133109 (2007).

71. Tsutsui, M., Shoji, K., Taniguchi, M. & Kawai, T. Formation and self-breaking mechanism of stable atom-sized junctions. *Nano Lett.* **8,** 345–349 (2008).

72. Van Der Zant, H. S. *et al.* Molecular three-terminal devices: Fabrication and measurements. *Faraday Discuss.* **131,** 347–356 (2006).

73. Boussaad, S *et al.* Discrete tunneling current fluctuations in metal water metal tunnel junctions. *J. Chem. Phys.* **118,** 8891 (2003).

74. Bellisario, D. O. *et al.* Experimental Observation of Real Time Molecular Dynamics Using Electromigrated Tunnel Junctions. *J. Phys. Chem. C* **121,** 22550–22558 (2017).

75. Geim, A. K. & Novoselov, K. S. The rise of graphene. *Nat. Mater.* **6,** 183–191 (2007).

76. A. K. Geim. Graphene : Status and Prospects. *Science (80-.).* **324,** 1530–1534 (2009).

77. Katsnelson, M. I., Novoselov, K. S. & Geim, A. K. Chiral tunneling and the Klein paradox in graphene. *Nat. Phys.* **2,** 620–625 (2006).

78. Bolotin, K. I., Ghahari, F., Shulman, M. D., Stormer, H. L. & Kim, P. Observation of the fractional quantum Hall effect in graphene. *Nature* **462,** 196–199 (2009).

79. Bolotin, K. I. *et al.* Ultrahigh electron mobility in suspended graphene. *Solid State Commun.* **146,** 351–355 (2008).

80. Mayorov, A. S. *et al.* Micrometer-scale ballistic transport in encapsulated graphene at room temperature. *Nano Lett.* **11,** 2396–2399 (2011).

81. Schwierz, F. Graphene transistors. *Nat. Nanotechnol.* **5,** 487–496 (2010).

82. Li, X, Wang, X, Zhang, L, Lee, S & Dai, H. Chemically Derived Ultrasmooth Graphene Nanoribbon Semiconductors. *Science (80-.).* **319,** 1229–1232 (2008).

83. Stampfer, C *et al.* Tunable graphene single electron transistor. *Nano Lett.* **8,** 2378–2383 (2008).

84. Stampfer, C. *et al.* Energy gaps in etched graphene nanoribbons. *Phys. Rev. Lett.* **102,** 1–4 (2009).

85. Wang, L. J. *et al.* A graphene quantum dot with a single electron transistor as an integrated charge sensor. *Appl. Phys. Lett.* **97,** 262113 (2010).

86. Barreiro, A., Zant, H. S.J.V. D., Vandersypen, L. M. K. & van der Zant, H. S. J. Quantum Dots at Room Temperature carved out from Few-Layer Graphene. *Nano Lett.* **12,** 6096–6100 (2012).

87. Lau, C. S., Mol, J. A., Warner, J. H. & Briggs, G. A. D. Nanoscale control of graphene electrodes. *Phys. Chem. Chem. Phys.* **16,** 20398–20401 (2014).

88. Nef, C. *et al.* High-yield fabrication of nm-size gaps in monolayer CVD graphene. *Nanoscale* **6,** 7249–7254 (2014).

89. Cao, Y. *et al.* Building high-throughput molecular junctions using indented graphene point contacts. *Angew. Chemie - Int. Ed.* **51,** 12228–12232 (2012).

90. Prins, F. *et al.* Room-temperature gating of molecular junctions using few-layer graphene nanogap electrodes. *Nano Lett.* **11,** 4607–4611 (2011).

91. Mol, J. A. *et al.* Graphene-porphyrin single-molecule transistors. *Nanoscale* **7,** 13181–13185 (2015).

92. Ullmann, K. *et al.* Single-Molecule Junctions with Epitaxial Graphene Nanoelectrodes. *Nano Lett.* **15,** 3512–3518 (2015).

93. Lau, C. S. *et al.* Redox-Dependent Franck Condon Blockade and Avalanche Transport in a Graphene Fullerene Single-Molecule Transistor. *Nano Lett.* **16,** 170–176 (2016).

94. Island, J. O. *et al.* Fabrication of hybrid molecular devices using multi-layer graphene break junctions. *J. Phys. Condens. Matter* **26,** 474205 (2014).

95. Gu, C., Su, D., Jia, C., Ren, S. & Guo, X. Building nanogapped graphene electrode arrays by electroburning. *RSC Adv.* **8,** 6814–6819 (2018).

96. Chen, Y. Nanofabrication by electron beam lithography and its applications: A review. *Microelectron. Eng.* **135,** 57–72 (2015).

97. Guo, X. *et al.* Covalently Bridging Gaps in Single-Walled Carbon Nanotubes with Conducting Molecules. *Science (80-.).* **311,** 356–359 (2006).

98. Whalley, A. C., Steigerwald, M. L., Guo, X. & Nuckolls, C. Reversible switching in molecular electronic devices. *J. Am. Chem. Soc.* **129,** 12590–12591 (2007).

99. Loh, K. P., Bao, Q., Ang, P. K. & Yang, J. The chemistry of graphene. *J. Mater. Chem.* **20,** 2277 (2010).

100. Jia, X., Campos-Delgado, J., Terrones, M., Meunier, V. & Dresselhaus, M. S. Graphene edges: a review of their fabrication and characterization. *Nanoscale* **3,** 86–95 (2011).

101. Rudnev, A. V. *et al.* Stable anchoring chemistry for room temperature charge transport through graphite-molecule contacts. *Sci. Adv.* **3,** e1602297 (2017).

102. Kaplan, A. *et al.* Current and future directions in electron transfer chemistry of graphene. *Chem. Soc. Rev.* **46,** 4530–4571 (2017).

103. Bell, D. C., Lemme, M. C., Stern, L. A., Williams, J. R. & Marcus, C. M. Precision cutting and patterning of graphene with helium ions. *Nanotechnology* **20.** doi:10.1088/0957-4484/20/45/455301. arXiv: 0905.4407 (2009).

104. Roy, S. *et al.* Direct Electrical Measurements on Single-Molecule Genomic DNA Using Single-Walled Carbon Nanotubes. *Nano Lett.* **8,** 26–30 (2008).

105. Wei, D. *et al.* Real time and in situ control of the gap size of nanoelectrodes for molecular devices. *Nano Lett.* **8,** 1625–1630 (2008).

106. Jiang, Z., Mihovilovic, M., Chan, J. & Stein, D. Fabrication of nanopores with embedded annular electrodes and transverse carbon nanotube electrodes. *J. Phys. Condens. Matter* **22.** doi:10.1088/0953-8984/22/45/454114 (2010).

107. Thiele, C. *et al.* Controlled fabrication of single-walled carbon nanotube electrodes by electron-beam-induced oxidation. *Appl. Phys. Lett.* **99,** 97–100 (2011).

108. Xu, G., Zhang, Y., Duan, X., Balandin, A. A. & Wang, K. L. Variability effects in graphene: Challenges and opportunities for device engineering and applications. *Proc. IEEE* **101,** 1670–1688 (2013).

109. Ivanov, A. P. *et al.* DNA tunneling detector embedded in a nanopore. *Nano Lett.* **11,** 279–285 (2011).

110. Ivanov, A. P., Freedman, K. J., Kim, M. J., Albrecht, T. & Edel, J. B. High precision fabrication and positioning of nanoelectrodes in a nanopore. *ACS Nano* **8,** 1940–1948 (2014).

111. Qi, P. *et al.* Miniature organic transistors with carbon nanotubes as quasi-one-dimensional electrodes. *J. Am. Chem. Soc.* **126,** 11774–11775 (2004).

112. Marquardt, C. W. *et al.* Electroluminescence from a single nanotube-molecule-nanotube junction. *Nat. Nanotechnol.* **5,** 863–867 (2010).

113. Lumetti, S. *et al.* Single-molecule devices with graphene electrodes. *Dalt. Trans.* **45,** 16570–16574 (2016).

114. Lumetti, S, Martini, L & Candini, A. Fabrication and characterization of nanometer-sized gaps in suspended few-layer graphene devices. *Semicond. Sci. Technol.* **32,** 024002 (2017).

115. Xu, Q. *et al.* Single Electron Transistor with Single Aromatic Ring Molecule Covalently Connected to Graphene Nanogaps. *Nano Lett.* **17,** 5335–5341 (2017).

116. Guan, J. *et al.* Direct single-molecule dynamic detection of chemical reactions. *Sci. Adv.* **4,** eaar2177 (2018).

117. Zhang, G., Zhu, D. & Guo, X. Thermally Activated Tunneling Transition in a Photoswitchable Single-Molecule Electrical Junction. *J. Phys. Chem. Lett.* **8,** 2849–2854 (2017).

118. Postma, H. W. C. Rapid sequencing of individual DNA molecules in graphene nanogaps. *Nano Lett.* **10,** 420–425 (2010).

119. Uram, J. D., Ke, K. & Mayer, M. L. Noise and bandwidth of current recordings from submicrometer pores and nanopores. *ACS Nano* **2,** 857–872 (2008).

120. Rosenstein, J. K. & Shepard, K. L. Temporal resolution of nanopore sensor recordings. *Conf. Proc. Annu. Int. Conf. IEEE Eng. Med. Biol. Soc.* 4110–4113 (2013).

121. Balan, A. *et al.* Improving signal-to-noise performance for DNA translocation in solid-state nanopores at MHz bandwidths. *Nano Lett.* **14,** 7215–7220 (2014).

122. Heerema, S. J. *et al.* 1/f noise in graphene nanopores. *Nanotechnology* **26,** 74001 (2015).

123. Gu, Z., Wang, H., Ying, Y.-L. & Long, Y.-T. Ultra-low noise measurements of nanopore-based single molecular detection. *Sci. Bull.* **62,** 1245–1250 (2017).

124. Parkin, W. M. & Drndic, M. Signal and noise in FET-nanopore devices. *ACS Sensors,* acssensors.7b00708 (2018).

125. Lin, Y. M. & Avouris, P. Strong suppression of electrical noise in bilayer graphene nanodevices. *Nano Lett.* **8,** 2119–2125 (2008).

126. Cheng, Z., Li, Q., Li, Z., Zhou, Q. & Fang, Y. Suspended Graphene Sensors with Improved Signal and Reduced Noise. *Nano Lett.* **10,** 1864–1868 (2010).

127. Rumyantsev, S, Liu, G, Stillman, W, Shur, M & Balandin, a. a. Electrical and noise characteristics of graphene field-effect transistors: ambient effects, noise sources and physical mechanisms. *J. Phys. Condens. Matter* **22,** 395302 (2010).

128. Heller, I. *et al.* Charge noise in graphene transistors. *Nano Lett.* **10,** 1563–1567 (2010).

129. Kaverzin, A. A., Mayorov, A. S., Shytov, A. & Horsell, D. W. Impurities as a source of 1/f noise in graphene. *Phys. Rev. B* **85,** 075435 (2012).

130. Liu, G., Rumyantsev, S., Shur, M. & Balandin, A. A. Graphene thickness-graded transistors with reduced electronic noise. *Appl. Phys. Lett.* **100,** 033103 (2012).

131. Sun, N. *et al.* Electrical noise and transport properties of graphene. *J. Low Temp. Phys.* **172,** 202–211 (2013).

132. Liu, G., Rumyantsev, S., Shur, M. S. & Balandin, A. A. Origin of 1 / f noise in graphene multilayers : Surface vs . volume. *Appl. Phys. Lett.* **102,** 093111 (2013).

133. Amar, A., Lozes, R. L., Sasaki, Y., Davis, J. C. & Packard, R. E. Fabrication of submicron apertures in thin membranes of silicon nitride. *J. Vac. Sci. Technol. B Microelectron. Nanom. Struct.* **11,** 259 (1993).

134. Fan, Y., He, K., Tan, H., Speller, S. & Warner, J. H. Crack-Free Growth and Transfer of Continuous Monolayer Graphene Grown on Melted Copper. *Chem. Mater.* **26,** 4984–4991 (2014).

135. Sheng, Y., Rong, Y., He, Z., Fan, Y. & Warner, J. H. Uniformity of large-area bilayer graphene grown by chemical vapor deposition. *Nanotechnology* **26,** 395601 (2015).

136. Yuzhelevski, Y., Yuzhelevski, M. & Jung, G. Random telegraph noise analysis in time domain. *Rev. Sci. Instrum.* **71,** 1681 (2000).

137. Zhang, Z. *et al.* New Insights into the Amplitude of Random Telegraph Noise in Nanoscale MOS Devices. *2017 IEEE Int. Reliab. Phys. Symp.* 3C–3.1–3C–3.5. (2017).

138. Kirton, M. J. & Uren, M. J. Noise in solid-state microstructures: A new perspective on individual defects, interface states and low-frequency (1/f) noise. *Adv. Phys.* **38,** 367–468 (1989).

139. Balandin, A. A. Low-frequency 1 f noise in graphene devices. *Nat. Nanotechnol.* **8,** 549–555 (2013).

140. Simoen, E. & Claeys, C. On the flicker noise in submicron silicon MOSFETs. *Solid. State. Electron.* **43,** 865–882 (1999).

141. Weissman, M. B. 1F Noise and Other Slow, Nonexponential Kinetics in Condensed Matter. *Rev. Mod. Phys.* **60,** 537–571 (1988).

142. Keshner, M. 1/F Noise. *Proc. IEEE* **70,** 212–218 (1982).

143. Voss, R. 1/f (Flicker) Noise: A Brief Review. *33rd Annu. Symp. Freq. Control,* 40–46 (1979).

144. Van der Ziel, A. Flicker Noise in Electronic Devices. *Adv. Electron. Electron Phys.* **49,** 225–297 (1979).

145. Dutta, P. & Horn, P. M. Low-frequency fluctuations in solids: 1/f noise. *Rev. Mod. Phys.* **53,** 497–516 (1981).

146. Song, Y. & Lee, T. Electronic Noise Analyses on Organic Electronic Devices. *J. Mater. Chem. C* **5,** 7123–7141 (2017).

147. Karimi, M. A. *et al.* Shot Noise of 1,4-Benzenedithiol Single-Molecule Junctions. *Nano Lett.* **16,** 1803–1807 (2016).

148. Kim, Y., Song, H., Kim, D., Lee, T. & Jeong, H. Noise Characteristics of Charge Tunneling via Localized States in Metal-Molecule-Metal Junctions. *ACS Nano* **4,** 4426–4430 (2010).

149. Machlup, S. Noise in Semiconductors: Spectrum of a TwoParameter Random Signal. *J. Appl. Phys.* **25,** 341–343 (1954).

150. Kandiah, K., Deighton, M. O. & Whiting, F. B. A physical model for random telegraph signal currents in semiconductor devices. *J. Appl. Phys.* **66,** 937–948 (1989).

151. Hooge, F. 1/f Noise Sources. *IEEE Trans. Electron Devices* **41,** 1926–1935 (1994).

152. McWhorter, A. *1/f Noise and Related Surface Effects in Germanium* (Massachusetts Institute of Technology, MASSACHUSETTS, 1955).

153. Jayaraman, R. & Sodini, C. G. A 1 /f Noise Technique to Extract the Oxide Trap Density Near the Conduction Band Edge of Silicon. *IEEE Trans. Electron Devices* **36,** 1773 (1989).

154. Fu, H.-S. & Sah, C.-T. Theory and experiments on surface 1/f noise. *IEEE Trans. Electron Devices* **19,** 273–285 (1972).

155. Liefrink, F., Dijkhuis, J. I. & van Houten, H. Low-Frequency Noise in Quantum Point Contacts. *Semicond. Sci. Technol.* **9,** 2178–2189 (1994).

156. Rogers, C. *et al.* Electron trap states and low frequency noise in tunnel junctions. *IEEE Trans. Magn.* **23,** 1658–1661 (1987).

157. Kohlstedt, H., Gundlach, K. H. & Kuriki, S. Electric forming and telegraph noise in tunnel junctions. *J. Appl. Phys.* **73,** 2564–2568 (1993).

158. Choi, S., Yang, Y. & Lu, W. Random telegraph noise and resistance switching analysis of oxide based resistive memory. *Nanoscale* **6,** 400–404 (2014).

159. Song, Y. *et al.* Origin of multi-level switching and telegraphic noise in organic nanocomposite memory devices. *Sci. Rep.* **6,** 33967 (2016).

160. Novoselov, K. *et al.* Electric Field Effect in Atomically Thin Carbon Films. *Science (80-.).* **306,** 666–669 (2004).

161. Kim, K. S. *et al.* Large-scale pattern growth of graphene films for stretchable transparent electrodes. *Nano Lett.* **9,** 30–35 (2009).

162. Dong, X., Shi, Y., Huang, W., Chen, P. & Li, L. J. Electrical detection of DNA hybridization with single-base specificity using transistors based on CVD-grown graphene sheets. *Adv. Mater.* **22,** 1649–1653 (2010).

163. Bianchi, M. *et al.* Scaling of graphene integrated circuits. *Nanoscale* **7,** 8076–8083 (2015).

164. Rumyantsev, S., Liu, G., Shur, M. S., Potyrailo, R. A. & Balandin, A. A. Selective gas sensing with a single pristine graphene transistor. *Nano Lett.* **12,** 2294–2298 (2012).

165. Boggild, P. *et al.* Mapping the electrical properties of large-area graphene. *2D Mater.* **4,** 042003 (2017).

166. Bae, S. *et al.* Roll-to-roll production of 30-inch graphene films for transparent electrodes. *Nat. Nanotechnol.* **5,** 574–578 (2010).

167. Robinson, J. T., Perkins, F. K., Snow, E. S., Wei, Z. & Sheehan, P. E. Reduced Graphene Oxide Molecular Sensors. *Nano Lett.* **8,** 3137–3140 (2008).

168. Liu, F. *et al.* Giant random telegraph signals in the carbon nanotubes as a single defect probe. *Appl. Phys. Lett.* **86,** 163102 (2005).

169. Liu, F., Member, S., Wang, K. L., Li, C. & Zhou, C. Study of Random Telegraph Signals in Single-Walled Carbon Nanotube Field Effect Transistors. *IEEE Trans. Nanotechnol.* **5,** 441–445 (2006).

170. Liu, F., Bao, M., Wang, K. L., Zhang, D. & Zhou, C. Coulomb attractive random telegraph signal in a single-walled carbon nanotube. *Phys. Rev. B - Condens. Matter Mater. Phys.* **74,** 035438–1 (2006).

171. Setiadi, A. *et al.* Room-temperature discrete-charge-fluctuation dynamics of a single molecule adsorbed on a carbon nanotube. *Nanoscale* **9,** 10674–10683 (2017).

172. Stolyarov, M. A., Liu, G., Rumyantsev, S. L., Shur, M. & Balandin, A. A. Suppression of 1/ f noise in near-ballistic h -BN-graphene- h- BN heterostructure field-effect transistors. *Appl. Phys. Lett.* **107,** 023106 (2015).

173. Pal, A. N. & Ghosh, A. Resistance noise in electrically biased bilayer graphene. *Phys. Rev. Lett.* **102,** 126805 (2009).

174. Schedin, F *et al.* Detection of individual gas molecules adsorbed on graphene. *Nat. Mater.* **6,** 652–5 (2007).

175. Liu, G. *et al.* Low-frequency electronic noise in the double-gate single-layer graphene transistors. *Appl. Phys. Lett.* **95,** 033103 (2009).

176. Shao, Q. *et al.* Flicker noise in bilayer graphene transistors. *IEEE ELECTRON DEVICE Lett.* **30,** 288–290 (2009).

177. Pal, A. N. & Ghosh, A. Ultralow noise field-effect transistor from multilayer graphene. *Appl. Phys. Lett.* **95,** 082105 (2009).

178. Xu, G. *et al.* Low-noise submicron channel graphene nanoribbons. *Appl. Phys. Lett.* **97,** 073107 (2010).

179. Xue, J. *et al.* Scanning tunnelling microscopy and spectroscopy of ultra-flat graphene on hexagonal boron nitride. *Nat. Mater.* **10,** 282–285 (2011).

180. Liu, Z., Suenaga, K., Harris, P. J. F. & Iijima, S. Open and closed edges of graphene layers. *Phys. Rev. Lett.* **102,** 015501 (2009).

181. Qiu, H., Wang, H. & Ke, F. Low frequency noise in the unstable contact region of Au-to-Au microcontact for microelectromechanical system switches. *Appl. Phys. Lett.* **104,** 254102 (2014).

182. Hossain, M. Z., Rumyantsev, S., Shur, M. S. & Balandin, A. A. Reduction of 1/f noise in graphene after electron-beam irradiation. *Appl. Phys. Lett.* **102,** 153512 (2013).

183. Pumera, M., Ambrosi, A., Bonanni, A., Chng, E. L. K. & Poh, H. L. Graphene for electrochemical sensing and biosensing. *Trends Anal. Chem.* **29,** 954–965 (2010).

184. Shao, Y. *et al.* Graphene based electrochemical sensors and biosensors: A review. *Electroanalysis* **22,** 1027–1036 (2010).

185. Brockdorf, K. *et al.* Imaging of edge inactive layer in micro-patterned graphene monolayer. *Mater. Lett.* **211,** 183–186 (2018).

186. Chen, Y.-C. *et al.* Molecular bandgap engineering of bottom-up synthesized graphene nanoribbon heterojunctions. *Nat. Nanotechnol.* **10,** 156–160 (2015).

187. Lörtscher, E. Wiring molecules into circuits. *Nat. Nanotechnol.* **8,** 381–4 (2013).

188. Xu, G. *et al.* Edge effect on resistance scaling rules in graphene nanostructures. *Nano Lett.* **11,** 1082–1086 (2011).

189. Cai, J *et al.* Atomically precise bottom-up fabrication of graphene nanoribbons. *Nature* **466,** 470–473 (2010).

190. Banhart, F., Kotakoski, J. & Krasheninnikov, A. V. Structural defects in graphene. *ACS Nano* **5,** 26–41 (2011).

191. Vicarelli, L., Heerema, S. J., Dekker, C. & Zandbergen, H. W. Controlling Defects in Graphene for Optimizing the Electrical Properties of Graphene Nanodevices. *ACS Nano* **9,** 3428–3435 (2015).

192. Avouris, P. & Dimitrakopoulos, C. Graphene: synthesis and applications. *Mater. Today* **15,** 86–97 (2012).

193. Dauber, J., Terres, B., Volk, C., Trellenkamp, S. & Stampfer, C. Reducing disorder in graphene nanoribbons by chemical edge modification. *Appl. Phys. Lett.* **104,** 083105 (2014).

194. Lee, H. *et al.* Nanoscale Direct Mapping of Noise Source Activities on Graphene Domains. *ACS Nano* **10,** 10135–10142 (2016).

195. Sung, M. G. *et al.* Scanning Noise Microscopy on Graphene Devices. *ACS Nano* **11,** 8620–8628 (2011).

196. Krittayavathananon, A. *et al.* Improving Single-Carbon-NanotubeElectrode Contacts Using Molecular Electronics. *J. Phys. Chem. Lett.* **8,** 3908–3911 (2017).

197. Arielly, R., Vadai, M., Kardash, D., Noy, G. & Selzer, Y. Real-Time Detection of Redox Events in Molecular Junctions. *J. Am. Chem. Soc.* **136,** 2674–2680 (2014).

198. Schwarz, F. *et al.* Field-induced conductance switching by charge-state alternation in organometallic single-molecule junctions. *Nat. Nanotechnol.* **11,** 170–177 (2016).

199. Gaudenzi, R. *et al.* Redox-Induced Gating of the Exchange Redox-Induced Gating of the Exchange Interactions in a Single Organic Diradical. *ACS Nano* **11,** 5879–5883 (2017).

200. Island, J. O. *et al.* Proximity-Induced Shiba States in a Molecular Junction. *Phys. Rev. Lett.* **118,** 117001 (2017).

201. Xiang, D *et al.* Noise characterization of metal-single molecule contacts Noise characterization of metal-single molecule contacts. *Appl. Phys. Lett.* **106,** 063702 (2015).

202. Brunner, J., González, M. T., Schönenberger, C. & Calame, M. Random telegraph signals in molecular junctions. *J. physics. Condens. matter* **26,** 474202 (2014).

203. Grutter, L. *et al.* Resonant tunnelling through a C60 molecular junction in a liquid environment. *Nanotechnology* **16,** 2143–2148 (2005).

204. Klein, H., Leoni, T., Zoubkoff, R., Leoni, T. & Saul, A. Conductance fluctuations in gold point contacts : an atomistic picture. *Nanotechnology* **23,** 235707 (2012).

205. Tsutsui, M., Kurokawa, S. & Sakai, A. Bias-induced local heating in atom-sized metal contacts at 77 K. *Appl. Phys. Lett.* **90,** 133121 (2007).

206. Sperl, A, Kröger, J & Berndt, R. Direct observation of conductance fluctuations of a single-atom tunneling contact. *Phys. Rev. B* **81,** 035406 (2010).

207. Kihira, Y., Shimada, T., Matsuo, Y., Nakamura, E. & Hasegawa, T. Random telegraphic conductance fluctuation at Au-pentacene-Au nanojunctions. *Nano Lett.* **9,** 1442–1446 (2009).

208. Wen, H. *et al.* Complex formation dynamics in a single-molecule electronic device. *Sci. Adv.* **2,** e1601113 (2016).

209. *Change Point Detection* 2017. `https://uk.mathworks.com/help/signal/ref/findchangepts.html` (2017).

210. Adak, O. *et al.* Flicker Noise as a Probe of Electronic Interaction at Metal Single Molecule Interfaces. *Nano Lett.* **15,** 4143–4149 (2015).

211. Yeh, S.-s., Chang, W.-y. & Lin, J.-j. Probing nanocrystalline grain dynamics in nanodevices. *Sci. Adv.* **3,** e1700135 (2017).

212. Sharf, T. *et al.* Single Electron Charge Sensitivity of Liquid-Gated Carbon Nanotube Transistors. *Nano Lett.* **14,** 4925–4930 (2014).

213. Halbritter, A. *et al.* Regular atomic narrowing of Ni, Fe, and v nanowires resolved by two-dimensional correlation analysis. *Phys. Rev. Lett.* **105,** 266805 (2010).

214. Magyarkuti, A. *et al.* Temporal correlations and structural memory effects in break junction measurements. *J. Chem. Phys.* **146,** 092319 (2017).

215. Maneglia, Y. & Bauza, D. Extraction of slow oxide trap concentration profiles in metaloxidesemiconductor transistors using the charge pumping method. *J. Appl. Phys.* **79,** 4187–4192 (1996).

216. Ralls, S. K. *et al.* Discrete Resistance Switching in Submicrometer Silicon Inversion Layers: Individual Interface Traps and Low-Frequency (1/f?) Noise. *Phys. Rev. Lett.* **52,** 228–231 (1984).

217. Behfar, K. & Naghdabadi, R. Nanoscale vibrational analysis of a multi-layered graphene sheet embedded in an elastic medium. *Compos. Sci. Technol.* **65,** 1159–1164 (2005).

218. Erickson, K. *et al.* Determination of the local chemical structure of graphene oxide and reduced graphene oxide. *Adv. Mater.* **22,** 4467–4472 (2010).

219. Brenner, D. W. *et al.* A second-generation reactive empirical bond order (REBO) potential energy expression for hydrocarbons. *J. Phys. Condens. Matter* **14,** 783–802 (2002).

220. Duplock, E. J., Scheffler, M. & Lindan, P. J. Hallmark of perfect graphene. *Phys. Rev. Lett.* **92,** 225502 (2004).

221. Boukhvalov, D. W., Katsnelson, M. I. & Lichtenstein, A. I. Hydrogen on graphene: Electronic structure, total energy, structural distortions and magnetism from first-principles calculations. *Phys. Rev. B - Condens. Matter Mater. Phys.* **77,** 035427 (2008).

222. Palmer, N., Campuzano, J., Richardson, N. & King, D. Adsorption of ammonia on graphene. *Nanotechnology* **20,** 245501 (2009).

223. Martínez-Galera, A. & Gomez-Rodriguez, J. M. Surface Diffusion of Simple Organic Molecules on Graphene on Pt (111). *J. Phys. Chem. C* **115,** 23036–23042 (2011).

224. Le, D., Kara, A., Schröder, E., Hyldgaard, P. & Rahman, T. S. Physisorption of nucleobases on graphene: a comparative van der Waals study. *J. Phys. Condens. Matter* **24,** 424210 (2012).

225. Ishii, A., Yamamoto, M., Asano, H. & Fujiwara, K. DFT calculation for adatom adsorption on graphene sheet as a prototype of carbon nano tube functionalization. *J. Phys. Conf. Ser.* **100,** 052087 (2008).

226. Gong, J. R. in *Graphene Simul.* chap. DFT Calcul (InTech, 2011).

227. Standley, B. *et al.* Graphene-Based Atomic-Scale Switches. *Nano Lett.* **8,** 3345–3349 (2008).

228. Liu, F. & Wang, K. L. Correlated Random Telegraph Signal and Low-Frequency Noise in Carbon Nanotube Transistors. *Nano Lett.* **8,** 147–151 (2008).

229. Costanzi, B. N. & Dahlberg, E. D. Emergent 1/f Noise in Ensembles of Random Telegraph Noise Oscillator. *Phys. Rev. Lett.* **119,** 097201 (2017).

230. Smeets, R. M. M., Keyser, U. F., Dekker, N. H. & Dekker, C. Noise in solid-state nanopores. *Proc. Natl. Acad. Sci.* **105,** 417–421 (2008).

231. Rosenstein, J. K., Wanunu, M., Merchant, C. A., Drndic, M. & Shepard, K. L. Integrated nanopore sensing platform with sub-microsecond temporal resolution. *Nat. Methods* **9,** 487–494 (2012).

232. Wen, C. *et al.* Generalized Noise Study of Solid-State Nanopores at Low Frequencies. *ACS Sensors* **2,** 300–307 (2017).

233. Rosenstein, J., Ray, V., Drndic, M. & Shepard, K. L. Solid-state nanopores integrated with low-noise preamplifiers for high-bandwidth DNA analysis. *Proc. 2011 IEEE/NIH Life Sci. Syst. Appl. Work. LiSSA 2011,* 59–62 (2011).

234. Shekar, S. *et al.* Measurement of DNA translocation dynamics in a solid-state nanopore at 100 ns temporal resolution. *Nano Lett.* **16,** 4483–4489 (2016).

235. Rosenstein, J., Sorgenfrei, S. & Shepard, K. L. Noise and bandwidth performance of single-molecule biosensors. *Proc. Cust. Integr. Circuits Conf.* 1–7 (2011).

236. Kim, D., Goldstein, B., Tang, W., Sigworth, F. J. & Culurciello, E. Noise analysis and performance comparison of low current measurement systems for biomedical applications. *IEEE Trans. Biomed. Circuits Syst.* **7,** 52–62 (2013).

237. Rosenstein, J. & Shepard, K. L. High-throughput biology in the time domain: Improving temporal resolution of single-molecule sensors. *ISCAS 2012 - 2012 IEEE Int. Symp. Circuits Syst.* 2291–2294 (2012).

238. Siwy, Z. & Fuliński, A. Origin of 1/f alpha Noise in Membrane Channel Currents. *Phys. Rev. Lett.* **89,** 158101 (2002).

239. Nandigana, V. V. R. & Aluru, N. R. 1/f Pink Chaos in Nanopores. *RSC Adv.* **7,** 46092–46100 (2017).

240. Smeets, R. M. M., Keyser, U. F., Wu, M. Y., Dekker, N. H. & Dekker, C. Nanobubbles in solid-state nanopores. *Phys. Rev. Lett.* **97,** 1–4 (2006).

241. Smeets, R. M. M., Dekker, N. H. & C, D. Low-frequency noise in solid-state nanopores. *Nanotechnology* **20,** 095501 (2009).

242. Zhirnov, V., Zadegan, R. M., Sandhu, G. S., Church, G. M. & Hughes, W. L. Nucleic acid memory. *Nat. Mater.* **15,** 366–370 (2016).

243. Lindsay, S. Biochemistry and semiconductor electronicsthe next big hit for silicon? *J. Phys. Condens. Matter* **24,** 164201 (2012).

244. Muthukumar, M. Mechanism of DNA transport through pores. *Annu. Rev. Biophys. Biomol. Struct.* **36,** 435–450 (2007).

245. Van Dorp, S., Keyser, U. F., Dekker, N. H., Dekker, C. & Lemay, S. G. Origin of the electrophoretic force on DNA in solid-state nanopores. *Nat. Phys.* **5,** 347–351 (2009).

246. Keyser, U. F. Controlling molecular transport through nanopores. *J. R. Soc. Interface* **8,** 1369–1378 (2011).

247. Bayley, H. Sequencing single molecules of DNA. *Curr. Opin. Chem. Biol.* **10,** 628–637 (2006).

248. Lander, E. S. *et al.* Initial sequencing and analysis of the human genome. *Nature* **409,** 860–921 (2001).

249. Yokota, K., Tsutsui, M. & Taniguchi, M. Electrode-embedded nanopores for label-free single-molecule sequencing by electric currents. *RSC Adv.* **4,** 15886 (2014).

250. Steinbock, L. J. & Radenovic, a. The emergence of nanopores in next-generation sequencing. *Nanotechnology* **26,** 074003 (2015).

251. Zwolak, M. & Di Ventra, M. Electronic signature of DNA nucleotides via transverse transport. *Nano Lett.* **5,** 421–424 (2005).

252. Shapir, E. *et al.* Electronic structure of single DNA molecules resolved by transverse scanning tunnelling spectroscopy. *Nat. Mater.* **7,** 68–74 (2008).

253. Ryndyk, D. A. *et al.* Scanning Tunneling Spectroscopy of Single DNA Molecules. *ACS Nano* **3,** 1651–1656 (2009).

254. Tanimoto, S., Tsutsui, M., Yokota, K. & Taniguchi, M. Dipole effects on the formation of molecular junctions. *Nanoscale Horizons* **1,** 399–406 (2016).

255. Im, J. *et al.* Electronic single-molecule identification of carbohydrate isomers by recognition tunnelling. *Nat. Commun.* **7,** 13868 (2016).

256. Fyta, M. Threading DNA through nanopores for biosensing applications. *J. Phys. Condens. Matter* **27,** 273101 (2015).

257. Bayley, H. & Martin, C. R. Resistive-Pulse Sensing - From Microbes to Molecules. *Chem. Rev.* **100,** 2575–2594 (2000).

258. Branton, D. *et al.* The potential and challenges of nanopore sequencing. *Nat. Biotechnol.* **26,** 1146–1153 (2008).

259. Venkatesan, B. M. & Bashir, R. Nanopore sensors for nucleic acid analysis. *Nat. Nanotechnol.* **15,** 615–624 (2003).

260. Miles, B. N. *et al.* Single molecule sensing with solid-state nanopores: novel materials, methods, and applications. *Chem. Soc. Rev.* **42,** 15–28 (2012).

261. Schneider, G. F. *et al.* Tailoring the hydrophobicity of graphene for its use as nanopores for DNA translocation. *Nat. Commun.* **4,** 2619 (2013).

262. Kasianowicz, J. J., Brandin, E, Branton, D & Deamer, D. W. Characterization of individual polynucleotide molecules using a membrane channel. *Proc. Natl. Acad. Sci. U. S. A.* **93,** 13770–13773 (1996).

263. Burns, J. R., Stulz, E. & Howorka, S. Self-assembled DNA nanopores that span lipid bilayers. *Nano Lett.* **13,** 2351–2356 (2013).

264. Burns, J. R. *et al.* Lipid-bilayer-spanning DNA nanopores with a bifunctional porphyrin anchor. *Angew. Chemie - Int. Ed.* **52,** 12069–12072 (2013).

265. Zhang, X. *et al.* Characterization of Interstrand DNA-DNA Cross-Links Using the a-Hemolysin Protein Nanopore. *ACS Nano* **9,** 11812–11819 (2015).

266. Clarke, J. *et al.* Continuous base identification for single-molecule nanopore DNA sequencing. *Nat. Nanotechnol.* **4,** 265–270 (2009).

267. Ayub, M., Stoddart, D. & Bayley, H. Nucleobase Recognition by Truncated α Hemolysin Pores. *ACS Nano* **9,** 7895–7903 (2015).

268. Howorka, S, Cheley, S & Bayley, H. Sequence-specific detection of individual DNA strands using engineered nanopores. *Nat. Biotechnol.* **19,** 636–639 (2001).

269. Manrao, E. a. *et al.* Reading DNA at single-nucleotide resolution with a mutant MspA nanopore and phi29 DNA polymerase. *Nat. Biotechnol.* **30,** 349–353 (2012).

270. Schneider, G. F. *et al.* DNA Translocation through Graphene Nanopores. *Nano Lett.* **10,** 3163–3167 (2010).

271. Dimitrov, V *et al.* Nanopores in solid-state membranes engineered for single molecule detection. *Nanotechnology* **21,** 065502 (2010).

272. Bai, J. *et al.* Fabrication of sub-20 nm nanopore arrays in membranes with embedded metal electrodes at wafer scales. *Nanoscale* **6,** 8900–8906 (2014).

273. Dekker, C. Solid-state nanopores. *Nat. Nanotechnol.* **2,** 209–215 (2007).

274. Wu, M. Y., Krapf, D., Zandbergen, M., Zandbergen, H. & Batson, P. E. Formation of nanopores in a SiN/SiO2 membrane with an electron beam. *Appl. Phys. Lett.* **87,** 113106 (2005).

275. Arcadia, C. E., Reyes, C. C. & Rosenstein, J. K. In Situ Nanopore Fabrication and Single-Molecule Sensing with Microscale Liquid Contacts. *ACS Nano* **11,** 4907–4915 (2017).

276. Venkatesan, B. M., Shah, A. B., Zuo, J. M. & Bashir, R. DNA sensing using nanocrystalline surface-enhanced Al2O 3 nanopore sensors. *Adv. Funct. Mater.* **20,** 1266–1275 (2010).

277. Pud, S. *et al.* Mechanical Trapping of DNA in a Double-Nanopore System. *Nano Lett.* **16,** 8021–8028 (2016).

278. Larkin, J. *et al.* Slow DNA transport through nanopores in hafnium oxide membranes. *ACS Nano* **7,** 10121–10128 (2013).

279. Wei, R., Pedone, D., Zürner, A., Döblinger, M. & Rant, U. Fabrication of metallized nanopores in silicon nitride membranes for single-molecule sensing. *Small* **6,** 1406–1414 (2010).

280. Li, J *et al.* Ion-beam sculpting at nanometre length scales. *Nature* **412,** 166–169 (2001).

281. Cai, Q., Ledden, B., Krueger, E., Golovchenko, J. a. & Li, J. Nanopore sculpting with noble gas ions. *J. Appl. Phys.* **100,** 024914 (2006).

282. Fologea, D., Uplinger, J., Thomas, B., Mcnabb, D. S. & Li, J. Slowing DNA Translocation in a Solid-State Nanopore. *Nano Lett.* **5,** 1734–1737 (2005).

283. Smeets, R. M. M. Salt-dependence of ion transport and DNA translocation through solid-state nanopores. *Nano Lett.* **6,** 89–95 (2006).

284. Anderson, B. N., Muthukumar, M. & Meller, A. PH tuning of DNA translocation time through organically functionalized nanopores. *ACS Nano* **7,** 1408–1414 (2013).

285. Krishnakumar, P. *et al.* Slowing DNA translocation through a nanopore using a functionalized electrode. *ACS Nano* **7,** 10319–10326 (2013).

286. Krstic, P., Ashcroft, B. & Lindsay, S. Physical model for recognition tunneling. *Nanotechnology* **26,** 84001 (2015).

287. Merchant, C. a. *et al.* DNA translocation through graphene nanopores. *Nano Lett.* **10,** 2915–2921 (2010).

288. Garaj, S *et al.* Graphene as a subnanometre trans-electrode membrane. *Nature* **467,** 190–193 (2010).

289. Feng, J. *et al.* Identification of single nucleotides in MoS2 nanopores. *Nat. Nanotechnol.* **10,** 1070–1076 (2015).

290. Wells, D. B., Belkin, M., Comer, J. & Aksimentiev, A. Assessing graphene nanopores for sequencing DNA. *Nano Lett.* **12,** 4117–4123 (2012).

291. Garaj, S., Liu, S., Golovchenko, J. a. & Branton, D. Molecule-hugging graphene nanopores. *Proc. Natl. Acad. Sci. U. S. A.* **110,** 12192–121966 (2013).

292. Arjmandi-tash, H., Belyaeva, L. A. & Schneider, F. Single molecule detection with graphene and other two-dimensional materials: nanopores and beyond. *Chem. Soc. Rev.* **45,** 476–493 (2016).

293. Oeffelen, L. V. *et al.* Ion Current Rectification , Limiting and Overlimiting Conductances in Nanopores. *PLoS One* **10,** e0124171 (2015).

294. Lagerqvist, J., Zwolak, M. & Di Ventra, M. Influence of the environment and probes on rapid DNA sequencing via transverse electronic transport. *Biophys. J.* **93,** 2384–2390 (2007).

295. Tsutsui, M., Taniguchi, M., Yokota, K. & Kawai, T. Identifying single nucleotides by tunnelling current. *Nat. Nanotechnol.* **5,** 286–290 (2010).

296. Huang, S. *et al.* Identifying single bases in a DNA oligomer with electron tunnelling. *Nat. Nanotechnol.* **5,** 868–873 (2010).

297. Robinson, D. A. The electrical properties of metal microelectrodes. *Proc. IEEE* **56,** 1065–1071 (1968).

298. Joshkin, V, Lagally, M & Weide, D. V. D. Double layer based electronic nanodevices fabricated on silicon nanoneedles. *J. Appl. Phys.* **100,** 084329 (2006).

299. Heinze, J. Ultramicroelectrodes in Electrochemistry. *Angew. Chemie Int. Ed. English* **32,** 1268–1288 (1993).

300. Fan, F. R. & Bard, A. *STM on wet insulators: electrochemistry or tunneling?* 1995. doi:10.1126/science.270.5243.1849.

301. Schmickler, W. Electronic Effects in the Electric Double Layer. *Chem. Rev.* **96,** 3177–3200 (1996).

302. Doi, K. *et al.* Nonequilibrium Ionic Response of Biased Mechanically Controllable Break Junction (MCBJ) Electrodes. *J. Phys. Chem.* **118,** 3758–3765 (2014).

303. Healy, K. *et al.* Fabrication and characterization of nanopores with insulated transverse nanoelectrodes for DNA sensing in salt solution. *Electrophoresis* **33,** 3488–3496 (2012).

304. Nagahara, L. A., Thundat, T & Lindsay, S. M. Preparation and characterization of STM tips for electrochemical studies. *Rev. Sci. Instrum.* **60,** 3128 (1989).

305. Bach, C. E. *et al.* Effective Insulation of Scanning Tunneling Microscopy Tips for Electrochemical Studies Using an Electropainting Melhod. *J. Electrochem. Soc.* **140,** 1281–1284 (1993).

306. Slevin, C. J., Gray, N. J., Macpherson, J. V., Webb, M. A. & Unwin, P. R. Fabrication and characterisation of nanometre-sized platinum electrodes for voltammetric analysis and imaging. *Electrochem. commun.* **1,** 282–288 (1999).

307. Krapf, D. *et al.* Fabrication and Characterization of Nanopore-Based Electrodes with Radii down to 2 nm. *Nano Lett.* **6,** 105–109 (2006).

308. Sarwat, S. G. *et al.* Scaling limits of graphene nanoelectrodes. *Nano Lett.* **17,** 3688–3693 (2017).

309. Li, W., Tan, C., Lowe, M., Abruna, H. D. & Ralph, D. C. Electrochemistry of Individual Monolayer Graphene Sheets. *ACS Nano* **5,** 2264–2270 (2011).

310. Banerjee, S. *et al.* Electrochemistry at the edge of a single graphene layer in a nanopore. *ACS Nano* **7,** 834–843 (2013).

311. Bonanni, A., Ambrosi, A., Chua, C. K. & Pumera, M. Oxidation debris in graphene oxide is responsible for its inherent electroactivity. *ACS Nano* **8,** 4197–4204 (2014).

312. Li, X., Li, L., Wang, Y., Li, H. & Bian, X. Wetting and interfacial properties of water on the defective graphene. *J. Phys. Chem. C* **117,** 14106–14112 (2013).

313. Neek-amal, M., Peeters, F. M., Grigorieva, I. V. & Geim, A. K. Commensurability Effects in Viscosity of Nanoconfined Water. *ACS Nano* **10,** 3685–3692 (2016).

314. Pedersen, J. N., Boynton, P., Ventra, M. D., Jauho, A.-P. & Flyvbjerg, H. Classification of DNA nucleotides with transverse tunneling currents. *Nanotechnology* **28,** 015502 (2016).

315. Rungger, I., Chen, X., Schwingenschlogl, U. & Sanvito, S. Finite-bias electronic transport of molecules in a water solution. *Phys. Rev. B - Condens. Matter Mater. Phys.* **81,** 235407 (2010).

316. Daiguji, H. Ion transport in nanofluidic channels. *Chem. Soc. Rev.* **39,** 901–911 (2010).

317. Salvo, P. *et al.* Graphene-based devices for measuring pH. *Sensors Actuators, B Chem.* **256,** 976–991 (2018).

318. Brüesch, P. & Christen, T. The electric double layer at a metal electrode in pure water. *J. Appl. Phys.* **95,** 2846–2856 (2004).

319. Ma, K. *et al.* Understanding the graphene-based electric double layer from dielectric perspective: A density functional study. *Chem. Phys. Lett.* **677,** 137–142 (2017).

320. Uesugi, E., Goto, H., Eguchi, R., Fujiwara, A. & Kubozono, Y. Electric double-layer capacitance between an ionic liquid and few-layer graphene. *Sci. Rep.* **3,** 1595 (2013).

321. Grüter, L., Gonzlez, M. T., Huber, R., Calame, M. & Schonenberger, C. Electrical Conductance of Atomic Contacts in Liquid Environments. *Small* **1,** 1067–1070 (2005).

322. Dong, X., Xia, Y., Zhu, G. & Zhang, B. Molecular sensing with the tunnel junction of an Au nanogap in solution. *Nanotechnology* **18,** 395502 (2007).

323. Prokopuk, N., Son, K. a. & Waltz, C. Electron tunneling through fluid solvents. *J. Phys. Chem. C* **111,** 6533–6537 (2007).

324. Prokopuk, N. & Son, K.-A. Tunneling Junctions as Molecular Sensors. *ECS Trans.* **16,** 411–417 (2008).

325. Luka-Guth, K. *et al.* Role of solvents in the electronic transport properties of single-molecule junctions. *Beilstein J. Nanotechnol.* **7,** 1055–1067 (2016).

326. Cao, H., Jiang, J., Ma, J. & Luo, Y. Temperature-dependent statistical behavior of single molecular conductance in aqueous solution. *J. Am. Chem. Soc.* **130,** 6674–6675 (2008).

327. Ghane, T., Kleshchonok, A., Gutierrez, R. & Cuniberti, G. Modeling of Solvent Effects in the Electrical Response of π Stacked Molecular Junctions. *J. Phys. Chem. C* **119,** 20201–20109 (2015).

328. Fatemi, V., Kamenetska, M., Neaton, J. B. & Venkataraman, L. Environmental control of single-molecule junction transport. *Nano Lett.* **11,** 1988–1992 (2011).

329. Kotiuga, M., Darancet, P., Arroyo, C. R., Venkataraman, L. & Neaton, J. B. Adsorption-Induced Solvent-Based Electrostatic Gating of Charge Transport through Molecular Junctions. *Nano Lett.* **15,** 4498–4503 (2015).

330. Tanaka, H. & Kawai, T. Scanning tunneling microscopy imaging and manipulation of DNA oligomer adsorbed on Cu(111) surfaces by a pulse injection method. *J. Vac. Sci. Technol. B Microelectron. Nanom. Struct.* **15,** 602–604 (1997).

331. Tanaka, H., Hamai, C., Kanno, T. & Kawai, T. High-resolution scanning tunneling microscopy imaging of DNA molecules on Cu(111) surfaces. *Surf. Sci.* **432,** 611–616 (1999).

332. Tanaka, H. & Kawai, T. Partial sequencing of a single DNA molecule with a scanning tunnelling microscope. *Nat. Nanotechnol.* **4,** 518–522 (2009).

333. Afsari, S. *et al.* Quantum Point Contact Single-Nucleotide Conductance for DNA and RNA Sequence Identification. *ACS Nano* **11,** 11169–11181 (2017).

334. Lindsay, S. *et al.* Recognition tunneling. *Nanotechnology* **21,** 262001 (2010).

335. Chang, S. *et al.* Chemical recognition and binding kinetics in a functionalized tunnel junction. *Nanotechnology* **23,** 235101 (2012).

336. Zhao, Y. *et al.* Single-molecule spectroscopy of amino acids and peptides by recognition tunnelling. *Nat. Nanotechnol.* **9,** 466–473 (2014).

337. Chang, S. *et al.* Palladium electrodes for molecular tunnel junctions. *Nanotechnology* **23,** 425202 (2012).

338. Biswas, S. *et al.* Universal Readers Based on Hydrogen Bonding or π π Stacking for Identification of DNA Nucleotides in Electron Tunnel Junctions. *ACS Nano* **10,** 11304–11316 (2016).

339. Albrecht, T., Slabaugh, G., Alonso, E. & Al-Arif, S. M. R. Deep learning for single-molecule science. *Nanotechnology* **28,** 423001 (2017).

340. Fanget, A. *et al.* Nanopore integrated nanogaps for DNA detection. *Nano Lett.* **14,** 244–249 (2013).

341. Di Ventra, M. & Taniguchi, M. Decoding DNA, RNA and peptides with quantum tunnelling. *Nat. Nanotechnol.* **11,** 117–126 (2016).

342. Lagerqvist, J, Zwolak, M & Di Ventra, M. Fast DNA Sequencing via transverse electronic transport. *Nano Lett.* **6,** 779–782 (2006).

343. Gierhart, B. C. *et al.* Nanopore with transverse nanoelectrodes for electrical characterization and sequencing of DNA. *Sensors Actuators B 132* **132,** 593–600 (2008).

344. Fischbein, M. D. & Drndic, M. Sub-10 nm Device Fabrication in a Transmission Electron Microscope. *Nano Lett.* **7,** 1329–1337 (2007).

345. Maleki, T, Mohammadi, S & Ziaie, B. A nanofluidic channel with embedded transverse nanoelectrodes. *Nanotechnology* **20,** 105302 (2009).

346. Spinney, P. S., Collins, S. D., Howitt, D. G. & Smith, R. L. Fabrication and characterization of a solid-state nanopore with self-aligned carbon nanoelectrodes for molecular detection. *Nanotechnology* **23,** 135501 (2012).

347. Menard, L. D., Mair, C. E., Woodson, M. E., Alarie, J. P. & Ramsey, J. M. A device for performing lateral conductance measurements on individual double-stranded DNA molecules. *ACS Nano* **6,** 9087–9094 (2012).

348. Tsutsui, M., Taniguchi, M. & Kawai, T. Single-molecule identification via electric current noise. *Nat. Commun.* **1,** 135–138 (2010).

349. Tsutsui, M. *et al.* Electrical Detection of Single Methylcytosines in a DNA Oligomer. *J. Am. Chem. Soc.* **133,** 9124–9128 (2011).

350. Tsutsui, M. *et al.* Single-molecule sensing electrode embedded in-plane nanopore. *Sci. Rep.* **1,** 1–6 (2011).

351. Tsutsui, M. *et al.* Transverse electric field dragging of DNA in a nanochannel. *Sci. Rep.* **2,** 1–7 (2012).

352. Ohshiro, T. *et al.* Detection of post-translational modifications in single peptides using electron tunnelling currents. *Nat. Nanotechnol.* **9,** 835–840 (2014).

353. Pang, P. *et al.* Fixed-Gap Tunnel Junction for reading DNA nucleotides. *ACS Nano* **8,** 11994–12003 (2014).

354. Prasongkit, J. *et al.* Theoretical assessment of feasibility to sequence DNA through interlayer electronic tunneling transport at aligned nanopores in bilayer graphene. *Sci. Rep.* **5,** 17560 (2015).

355. Nishino, T., Shiigi, H., Kiguchi, M. & Nagaoka, T. Specific singlemolecule detection of glucose in a supramolecularly designed tunnel junction. *Chem. Commun.* **53,** 5212–5215 (2017).

356. Shearer, C. J., Slattery, A. D., Stapleton, A. J., Shapter, J. G. & Gibson, C. T. Accurate thickness measurement of graphene. *Nanotechnology* **27,** 125704 (2016).

357. Prasongkit, J., Grigoriev, A., Pathak, B., Ahuja, R. & Scheicher, R. H. Transverse conductance of DNA nucleotides in a graphene nanogap from first principles. *Nano Lett.* **11,** 1941–1945 (2011).

358. Katkov, V. L., Isaeva, O. G. & Osipov, V. a. Resonant Tunneling In Graphene-DNA Base-Graphene Junctions. *J. Phys. Conf. Ser.* **393,** 012026 (2012).

359. Zhao, Q. *et al.* Nanopore-based DNA analysis via graphene electrodes. *J. Nanomater.* **2012,** 31850 (2012).

360. Agapito, L. a., Gayles, J., Wolowiec, C. & Kioussis, N. AviramRatner rectifying mechanism for DNA base-pair sequencing through graphene nanogaps. *Nanotechnology* **23,** 135202 (2012).

361. Jeong, H. *et al.* Quantum interference in DNA bases probed by graphene nanoribbons. *Appl. Phys. Lett.* **103,** 023701 (2013).

362. Shukla, V., Jena, N. K., Grigoriev, A. & Ahuja, R. Prospects of Graphene-hBN Heterostructure Nanogap for DNA Sequencing. *ACS Appl. Mater. Interfaces* **9,** 39945–39952 (2017).

363. Prasongkit, J., Grigoriev, A., Pathak, B., Ahuja, R. & Scheicher, R. H. Theoretical study of electronic transport through dna nucleotides in a double-functionalized graphene nanogap. *J. Phys. Chem. C* **117,** 15421–15428 (2013).

364. He, Y. *et al.* Enhanced DNA sequencing performance through edge-hydrogenation of graphene electrodes. *Adv. Funct. Mater.* **21,** 2674–2679 (2011).

365. Saha, K. K., Drndić, M. & Nikolić, B. K. DNA base-specific modulation of microampere transverse edge currents through a metallic graphene nanoribbon with a nanopore. *Nano Lett.* **12,** 50–55 (2012).

366. Paulechka, E., Wassenaar, T. A., Kroenlein, K., Kazakov, A. & Smolyanitsky, A. Nucleobase-functionalized graphene nanoribbons for accurate high-speed DNA sequencing. *Nanoscale* **8,** 1861–1867 (2016).

367. Avdoshenko, S. M. *et al.* Dynamic and electronic transport properties of DNA translocation through graphene nanopores. *Nano Lett.* **13,** 1969–1976 (2013).

368. Girdhar, A., Sathe, C., Schulten, K. & Leburton, J.-P. Graphene quantum point contact transistor for DNA sensing. *Proc. Natl. Acad. Sci.* **110,** 16748–16753 (2013).

369. Patel, H. N. *et al.* DNA-graphene interactions during translocation through nanogaps. *PLoS One* **12,** 0171505 (2017).

370. Banerjee, S. *et al.* Slowing DNA Transport Using Graphene-DNA Interactions. *Adv. Funct. Mater.* **25,** 936–946 (2015).

371. Grant, A. W., Hu, Q.-H. & Kasemo, B. Transmission electron microscopy windows for nanofabricated structures. *Nanotechnology* **15,** 1175–1181 (2004).

372. Storm, A. J., Chen, J. H., Ling, X. S., Zandbergen, H. W. & Dekker, C. Fabrication of solid-state nanopores with single-nanometre precision. *Nat. Mater.* **2,** 537–540 (2003).

373. Wanunu, M. *et al.* Rapid electronic detection of probe-specific microRNAs using thin nanopore sensors. *Nat. Nanotechnol.* **5,** 807–814 (2010).

374. Yang, J. *et al.* Rapid and precise scanning helium ion microscope milling of solid-state nanopores for biomolecule detection. *Nanotechnology* **22.** doi:10.1088/0957-4484/22/28/285310 (2011).

375. Rauf, S., Shiddiky, M. J. A., Asthana, A. & Dimitrov, K. Fabrication and characterization of gold nanohole electrode arrays. *Sensors Actuators B Chem.* **173,** 491–496 (2012).

376. Petrossian, L. *et al.* Fabrication of Cylindrical Nanopores and Nanopore Arrays in Silicon-On-Insulator Substrates. *J. Microelectromechanical Syst.* **16,** 1419–1428 (2007).

377. Jansen, H., Gardeniers, H. & Boer, M. D. A survey on the reactive ion etching of silicon in microtechnology. *J. Micromechanics Microengineering* **6,** 14–28 (1996).

378. Kaspar, P. *et al.* Silicon nitride hardmask fabrication using a cyclic CHF 3 -based reactive ion etching process for vertical profile nanostructures. *J. vac* **28,** 1179 (2010).

379. Nabar, B. P., Celik-Butler, Z., Dennis, B. H. & Billo, R. E. A nanoporous silicon nitride membrane using a two-step lift-off pattern transfer with thermal nanoimprint lithography. *J. Micromechanics Microengineering* **22,** 045012 (2012).

380. Kuo, Y. Reactive Ion Etching of PECVD Amorphous Silicon and Silicon Nitride Thin Films with Fluorocarbon Gases. *J. Electrochem. Soc* **137,** 1235–1239 (1990).

381. Gribov, N. N., Theeuwen, S. J.C. H., Caro, J & Radelaar, S. A new fabrication process for metallic point contacts. *Microeleetronic Eng.* **35,** 317–320 (1997).

382. Rommel, M. *et al.* Sub-10 nm resolution after lift-off using HSQ / PMMA double layer resist. *Microelectron. Eng.* **110,** 123–125 (2013).

383. Vlassiouk, I., Apel, P. Y., Dmitriev, S. N., Healy, K. & Siwy, Z. S. Versatile ultrathin nanoporous silicon nitride membranes. *Proc. Natl. Acad. Sci.* **106,** 21039–21044 (2009).

384. Koh, A. L., Mccomb, D. W., Maier, S. A., Low, H. Y. & Yang, J. K. W. Sub-10 nm patterning of gold nanostructures on silicon-nitride membranes for plasmon mapping with electron energy-loss spectroscopy. *J. Vac. Sci. Technol. B Microelectron. Nanom. Struct.* **28,** C6O45 (2010).

385. Tao, N. J. Probing potential-tuned resonant tunneling through redox molecules with scanning tunneling microscopy. *Phys. Rev. Lett.* **76,** 4066–4069 (1996).

386. Wheeler, D. A. *et al.* The complete genome of an individual by massively parallel DNA sequencing. *Nature* **452,** 872–876 (2008).

387. Lemay, S. G. Nanopore-based biosensors: The interface between ionics and electronics. *ACS Nano* **3,** 775–779 (2009).

388. Jain, T., Rasera, B. C. & Guerrero, R. J. S. Microfluidic multiplexing of solid-state nanopores. *J. Phys. c* **29,** 484001 (2017).

389. Yuan, H. *et al.* Electrostatic and Electrochemical Nature of Liquid-Gated Electric-Double-Layer Transistors Based on Oxide Semiconductors. *J. Am. Chem. Soc* **132,** 18402–18407 (2010).

390. Krems, M., Zwolak, M., Pershin, Y. V. & Di Ventra, M. Effect of noise on DNA sequencing via transverse electronic transport. *Biophys. J.* **97,** 1990–1996 (2009).

391. Qiu, H., Girdhar, A., Schulten, K. & Leburton, J.-p. Electrically Tunable Quenching of DNA Fluctuations in Biased Solid-State Nanopores. *ACS Nano* **10,** 4482–4488 (2016).

392. Hu, N., Ai, Y. & Qian, S. Field effect control of electrokinetic transport in micro/nanofluidics. *Sensors Actuators, B Chem.* **161,** 1150–1167 (2012).

393. Paik, K. H. *et al.* Control of DNA capture by nanofluidic transistors. *ACS Nano* **6,** 6767–6775 (2012).

394. Ren, R. *et al.* Nanopore extended field-effect transistor for selective single-molecule biosensing. *Nat. Commun.* **8,** 586 (2017).

395. Boynton, P., Balatsky, A. V., Schuller, I. K. & Di Ventra, M. Improving sequencing by tunneling with multiplexing and cross-correlations. *J. Comput. Electron.* **13,** 794–800 (2014).

396. Moser, J. & Bachtold, A. Fabrication of large addition energy quantum dots in graphene. *Appl. Phys. Lett.* **95,** 173506 (2009).

397. Hanson, R., Kouwenhoven, L. P., Petta, J. R., Tarucha, S. & Vandersypen, L. M. Spins in few-electron quantum dots. *Rev. Mod. Phys.* **79,** 1217–1265 (2007).

398. Jacobsen, A., Simonet, P., Ensslin, K. & Ihn, T. Finite-bias spectroscopy of a three-terminal graphene quantum dot in the multilevel regime. *Phys. Rev. B - Condens. Matter Mater. Phys.* **89,** 165413 (2014).

399. Kay, N. J. *et al.* Single-molecule electrochemical gating in ionic liquids. *J. Am. Chem. Soc.* **134,** 16817–16826 (2012).

400. Wang, F. *et al.* Ionic Liquid Gating of Suspended MoS 2 Field Effect Transistor Devices. *Nano Lett.* **15,** 5284–5288 (2015).

401. Beenakker, C. W. J. Theory of Coulomb-blockade oscillations in the conductance of a quantum dot. *Phys. Rev. B* **44,** 1646–1656 (1991).

402. Arakawa, N., Otaka, Y. & Shiiki, K. Evaluation of barrier height and thickness in tunneling junctions by numerical calculation on tunnel probability. *Thin Solid Films* **505,** 67–70 (2006).

403. Simmons, J. G. Potential barrier and emission-limited current flow between closely spaced pararell metal electrodes. *J. Appl. Phys.* **35,** 2472–2481 (1964).